

JOINT TRANSPORTATION RESEARCH PROGRAM

INDIANA DEPARTMENT OF TRANSPORTATION
AND PURDUE UNIVERSITY



Load and Resistance Factor Design of Bridge Foundations Accounting for Pile Group–Soil Interaction



**Fei Han, Jeehee Lim, Rodrigo Salgado,
Monica Prezzi, Mir Zaheer**

RECOMMENDED CITATION

Han, F., Lim, J., Salgado, R., Prezzi, M., & Zaheer, M. (2015). *Load and resistance factor design of bridge foundations accounting for pile group-soil interaction* (Joint Transportation Research Program Publication No. FHWA/IN/JTRP-2015/24). West Lafayette, IN: Purdue University. <http://dx.doi.org/10.5703/1288284316009>

AUTHORS

Fei Han

Jeehee Lim

Graduate Research Assistants
Lyles School of Civil Engineering
Purdue University

Monica Prezzi, PhD

Professor of Civil Engineering
Lyles School of Civil Engineering
Purdue University

Rodrigo Salgado, PhD

Professor of Civil Engineering
Lyles School of Civil Engineering
Purdue University
(765) 494-5030
salgado@purdue.edu
Corresponding Author

Mir Zaheer, PE

Supervisor, Geotechnical Design Services
Indiana Department of Transportation

ACKNOWLEDGMENTS

The work presented here resulted from considerable work done over the years by the authors and other former students who have worked on LRFD development at Purdue University. Discussions with Dr. Sang Inn Woo are appreciated. Some of the pile design methods for which resistance factors are proposed have not yet appeared in print, but they are described in technical reports or are else detailed herewith. The assistance of the JTRP staff and, in particular, the support received from INDOT technical staff and the Study Advisory Committee members (Naveed Burki, Keith Hoernschemeyer, Athar Khan, Scott Ludlow, Barry Partridge, and Mir Zaheer) is much appreciated. The authors are also thankful for the continuous support received from the project administrator, Dr. Barry Partridge, and the business owner, Mr. Athar Khan.

JOINT TRANSPORTATION RESEARCH PROGRAM

The Joint Transportation Research Program serves as a vehicle for INDOT collaboration with higher education institutions and industry in Indiana to facilitate innovation that results in continuous improvement in the planning, design, construction, operation, management and economic efficiency of the Indiana transportation infrastructure. <https://engineering.purdue.edu/JTRP/index.html>

Published reports of the Joint Transportation Research Program are available at <http://docs.lib.purdue.edu/jtrp/>.

NOTICE

The contents of this report reflect the views of the authors, who are responsible for the facts and the accuracy of the data presented herein. The contents do not necessarily reflect the official views and policies of the Indiana Department of Transportation or the Federal Highway Administration. The report does not constitute a standard, specification, or regulation.

COPYRIGHT

Copyright 2015 by Purdue University. All rights reserved.
Print ISBN: 978-1-62260-404-3
ePUB ISBN: 978-1-62260-405-0

1. Report No. FHWA/IN/JTRP-2015/24	2. Government Accession No.	3. Recipient's Catalog No.	
4. Title and Subtitle Load and Resistance Factor Design of Bridge Foundations Accounting for Pile Group–Soil Interaction		5. Report Date November 2015	6. Performing Organization Code
7. Author(s) Fei Han, Jeehee Lim, Rodrigo Salgado, Monica Prezzi, Mir Zaheer		8. Performing Organization Report No. FHWA/IN/JTRP-2015/24	
9. Performing Organization Name and Address Joint Transportation Research Program Purdue University 550 Stadium Mall Drive West Lafayette, IN 47907-2051		10. Work Unit No.	11. Contract or Grant No. SPR-3636
12. Sponsoring Agency Name and Address Indiana Department of Transportation State Office Building 100 North Senate Avenue Indianapolis, IN 46204		13. Type of Report and Period Covered Final Report	
15. Supplementary Notes Prepared in cooperation with the Indiana Department of Transportation and Federal Highway Administration.		14. Sponsoring Agency Code	
16. Abstract <p>Pile group foundations are used in most foundation solutions for transportation structures. Rigorous and reliable pile design methods are required to produce designs whose level of safety (probability of failure) is known. By utilizing recently developed, advanced, two-surface plasticity constitutive models, rigorous finite element analyses are conducted. These analyses are for axially loaded single piles and pile groups with several pile-to-pile distances in various group configurations installed in sandy and clayey soil profiles. The analyses shed light on the relationships between the global response of the pile-soil system (development of shaft and base resistances) and the behavior of local soil elements (e.g., shear band formation). The influence of the group configuration, pile-to-pile spacing, soil profile, and pile head settlement on the group effects are studied. Mechanisms of pile-soil-pile interactions in pile groups are revealed. Pile efficiencies for individual piles and the overall pile group are reported for use in pile group design. The instrumentation, installation, and static and dynamic testing of a closed-ended, driven pipe pile in Marshall County, Indiana is documented. The test results along with two other case histories are used to verify the new Purdue pile design method. Probabilistic analyses are performed to develop resistance factors for the load and resistance factor design, LRFD, of pile groups considering both displacement and non-displacement piles, various soil profiles, and two target probabilities of failure. The pile design equations, pile group efficiencies and resistance factors together form the LRFD pile design framework. Two step-by-step design examples are provided to demonstrate the LRFD pile design procedures for single piles and pile groups.</p>			
17. Key Words pile groups, pile group-soil interaction, group efficiencies, group effect, piling, pile resistance, pile group design, load and resistance factor design, LRFD		18. Distribution Statement No restrictions. This document is available to the public through the National Technical Information Service, Springfield, VA 22161.	
19. Security Classif. (of this report) Unclassified	20. Security Classif. (of this page) Unclassified	21. No. of Pages 94	22. Price

EXECUTIVE SUMMARY

LOAD AND RESISTANCE FACTOR DESIGN OF BRIDGE FOUNDATIONS ACCOUNTING FOR PILE GROUP-SOIL INTERACTION

INTRODUCTION

Pile group foundations are used in most foundation solutions for transportation structures. Traditionally, design of pile group foundations has been performed in the United States using working stress design (WSD), which uses a single value factor for safety to account for the uncertainties in pile design. A method that would enable designs to reflect uncertainties in a more precise manner and be associated with a target probability of failure would be advantageous with respect to WSD. Recognizing this, the Federal Highway Administration (FHWA) mandated that load and resistance factor design (LRFD) be used for designing the foundations of all bridge structures initiated after September 2007. In LRFD, load variability is reflected in load factors applied by multiplication to the loads the foundations must carry, and resistance variability is reflected in resistance factors applied by multiplication to the foundation resistances. If load and resistance factors are determined using reliability analysis, it is possible to link them to a probability of failure. In order to develop a comprehensive and reliable LRFD pile design framework, it is necessary to have clear, detailed, and accurate understandings of the mechanism of resistance development in pile groups. This report contains a number of analyses that provide insights into pile group response that were not previously available. It then uses these analyses to develop a first iteration of an LRFD design framework for pile groups.

FINDINGS

To evaluate the axial load response of single piles and pile groups, finite element (FE) simulations are performed with advanced, two-surface plasticity constitutive models for soils. The finite element simulations are realistic not only because of the use of realistic soil models, but also because they enable behavior that would be observed in reality. For example, mesh configurations are such that the FE analyses can capture the highly localized deformation (formation of shear bands) along the pile shafts and near the pile bases.

Analyses for single piles successfully capture the development (initial build up, softening, and achievement of critical/residual states) of shear stresses in the soil. The analyses shed light on the relationships between the global response of the pile-soil system (development of shaft and base resistances) and the behavior of local soil elements and shear band formation. The analyses provide insight into the effect of embedment depth into stiff bearing layers on axially loaded nondisplacement piles in sand and clay. The obtained resistances show good agreement with Purdue design equations for nondisplacement piles installed in sand and clay.

Based on the simulation results for pile groups, we found that group effects are almost negligible for small pile groups (1×2 , 1×3 , and 2×2 pile groups) due to intense localization of deformation along the pile shafts. In contrast, individual piles at different locations (center, corner, or side) in a large pile group (e.g., 4×4) respond differently to the axial load applied on top of

the pile group. Mechanisms of pile-soil-pile interactions in pile groups are revealed by correlating the change of local state variables (e.g., stresses, void ratio, and pore pressure) to the resistance mobilization in individual piles. Due to these group interactions, pile efficiencies (defined as the ratio between the resistance developed by an individual pile in a group to the resistance that it would develop as a single pile) are different for different individual piles in a pile group. Since the mechanisms of the resistance mobilization, as well as the group interactions, are different along the pile shafts and near the pile bases, the pile efficiencies for shaft and base resistances are considered separately. It is found that pile efficiencies depend on the soil profile, pile spacing, pile group configuration, pile head settlement, position of pile in the group (center, corner, or side), pile diameter, and embedment length. Additional analyses are required to reliably assess the impact of these factors on the pile efficiencies for large pile groups (larger than 4×4).

As part of a validation effort for design equations presented in the report, a closed-ended pipe pile was carefully instrumented with two types (electrical-resistance and vibrating-wire) of strain gauges, driven in a sandy soil profile and load tested (both static and dynamic) in Marshall County, Indiana. The test results were interpreted in terms of load-settlement response, residual loads, development of shaft and base resistance, and set-up effects. The measured pile bearing capacities, along with the test results of two other case histories, were used to validate the new Purdue pile design method, which was improved in this report to take shaft degradation effects into account for displacement piles in sand. Very good agreement was found between the measured and estimated resistances.

Rigorous reliability analyses were performed using Monte Carlo simulations based on the new Purdue pile design equations to produce different resistance factors for shaft and base resistances, respectively. We considered single piles, both non-displacement and displacement piles, in sand and clay with practical ranges of soil properties, soil profiles, pile dimensions, various ratios between live loads and dead loads, and different target probability of failures. The optimal resistance factors determined using the reliability analyses were then adjusted to values that could be used with the load factors suggested by AASHTO. Calculated equivalent factors of safety also provided a general sense of how the same design methods would be used in WSD. We recommend that the resistance factors for single piles be used for small pile groups due to the negligible group effect in small pile groups. For large pile groups, further research is required to quantify uncertainties and variabilities related to the group effects and soil profiles.

IMPLEMENTATION

Single pile and pile group design examples show that the proposed pile design methods are straightforward and easy to implement in simple spreadsheet programs. While much work remains to be done in this topic, the report advances considerably the understanding of both single and pile group load response and how they should be designed for transportation infrastructures. Further studies are required to understand and quantify the effects of pile driving on the soil surrounding the piles as a function of pile diameter and pile length and how changes in soil density and state due to pile installation affect the pile group interaction factors.

CONTENTS

1. INTRODUCTION	1
1.1 Background	1
1.2 Report Structure	1
2. NUMERICAL ANALYSES OF SINGLE PILES IN SAND	1
2.1 Finite Element Analysis	1
2.2 Results and Discussion	3
3. NUMERICAL ANALYSES OF PILE GROUPS IN SAND	8
3.1 Finite Element Analysis	8
3.2 Results and Discussion	9
3.3 Group Efficiency	13
3.4 4 × 4 Pile Group	14
4. NUMERICAL ANALYSES OF SINGLE PILES IN CLAY	20
4.1 Introduction	20
4.2 Finite Element Analysis	20
4.3 Analyses Results	23
4.4 Conclusions	32
5. NUMERICAL ANALYSES OF PILE GROUPS IN CLAY	32
5.1 Finite Element Analysis	32
5.2 Results and Discussion for Small Pile Groups	33
5.3 4 × 4 Pile Group	38
6. PILE LOAD TEST	39
6.1 Introduction	39
6.2 Site Description	40
6.3 Test Pile Instrumentation	40
6.4 Pile Driving and Dynamic Testing	42
6.5 Static Load Test	43
6.6 Pile Load Test Results	43
6.7 Load Capacity Predictions	46
6.8 Additional Verification of Pile Design Methods	50
6.9 Summary and Conclusions	51
7. LRFD OF PILE GROUPS	55
7.1 Introduction	55
7.2 LRFD Framework	56
7.3 Pile Group Resistance Equations	56
7.4 Live Load/Dead Load Ratio for Transportation Structures	59
7.5 Assessment of Uncertainties	59
7.6 Reliability Analysis	60
7.7 Practical Cases Considered	64
7.8 Reliability Analyses Results	64
7.9 Conclusions	72
8. DESIGN RECOMMENDATIONS	74
8.1 Pile Design Equations	74
8.2 Recommended Resistance Factors	74
8.3 Pile Efficiencies for Individual Piles in Pile Group	74
8.4 Pile Group Design Method	74
8.5 Design Examples	77
9. IMPLEMENTATION	79
9.1 Pile Design Excel Spreadsheet Program Tool	79
9.2 Web-Based Pile Design Tool	79
9.3 Conclusions	83
REFERENCES	83

LIST OF TABLES

Table	Page
Table 2.1 List of Parameters Used in the Simulations for Sands	2
Table 3.1 Number of Elements Used in the FE Simulations for Different Small Pile Group Configurations	9
Table 3.2 Efficiency for Individual Piles in a 4×4 Pile Group Installed in Ottawa Sand (%)	19
Table 4.1 List of Parameters Used in the Simulations for Clays	21
Table 4.2 Base, Shaft and Total Resistance of Pile at $10\%-B$ of Pile Top Settlement with Various Soil-Pile Interface Element Thickness, where B = Pile Diameter	23
Table 4.3 Comparison of Unit Base Resistances for Single Pile in NC LC and NC BBC Obtained from FE Analysis and Design Method	27
Table 5.1 Efficiency for Individual Piles in a 4×4 Pile Group Installed in Normally Consolidated London Clay (%)	39
Table 6.1 Soil Profile at the Test Site	40
Table 6.2 Design Methods for Driven Piles in Sand	47
Table 6.3 Design Methods for Driven Piles in Clay	48
Table 6.4 Input Variables Required for Pile Design Methods	49
Table 6.5 Degradation Terms Used in the Design Methods for Calculation of Unit Shaft Resistance in Sand	49
Table 6.6 Soil Properties Used in the Predictions	50
Table 6.7 Comparisons between the Measured and Predicted Bearing Capacities	50
Table 6.8 Comparison of the Estimated Average Unit Limit Shaft Resistance, q_{sL} (kPa), with the Measured Values between Each Pair of Neighboring Strain Gauges	52
Table 6.9 Soil Profile at the Load Test Site in Lagrange County, Indiana	53
Table 6.10 Comparison of the Predicted Ultimate Base Resistances with the Measured Value of Pile Load Test in Lagrange County, Indiana	53
Table 6.11 Soil Profile at the Load Test Site in Jasper County, Indiana	54
Table 6.12 Comparison of Predicted Ultimate Base Resistances with the Measured Value of Pile Load Test in Jasper County, Indiana	55
Table 7.1 Unit Shaft Resistance of Drilled Shafts and Driven Piles in Sand or Clay	58
Table 7.2 Unit Base Resistance of Drilled Shafts and Driven Piles in Sand or Clay	59
Table 7.3 Summary of Uncertainty Assessment	60
Table 7.4 Various Pile Dimensions Considered in Reliability Analyses	66
Table 7.5 Code-Adjusted Base and Shaft Resistance Factors, RF_b^{code} and RF_s^{code} , for $LF_{DL}^{code} = 1.25$ and $LF_{LL}^{code} = 1.75$, and Different Drilled Shafts in Sand for CPT-Based Design Method	69
Table 7.6 Code-Adjusted Base and Shaft Resistance Factors, RF_b^{code} and RF_s^{code} , for $LF_{DL}^{code} = 1.25$ and $LF_{LL}^{code} = 1.75$, and Drilled Shafts in Sand for SPT-Based Design Method	69
Table 7.7 Code-Adjusted Base and Shaft Resistance Factors, RF_b^{code} and RF_s^{code} , for $LF_{DL}^{code} = 1.25$ and $LF_{LL}^{code} = 1.75$, and Drilled Shafts in Clay	70
Table 7.8 Code-Adjusted Base and Shaft Resistance Factors, RF_b^{code} and RF_s^{code} , for $LF_{DL}^{code} = 1.25$ and $LF_{LL}^{code} = 1.75$, and Driven Piles in Sand	73
Table 7.9 Code-Adjusted Base and Shaft Resistance Factors, RF_b^{code} and RF_s^{code} , for $LF_{DL}^{code} = 1.25$ and $LF_{LL}^{code} = 1.75$, and Driven Piles in Clay	74
Table 7.10 Recommended Code-Adjusted Resistance Factors for Pile Group Design for Drilled Shafts and Driven Piles in Sand and Clay with $LF_{DL}^{code} = 1.25$ and $LF_{LL}^{code} = 1.75$	74
Table 8.1 CPT-Based Pile Design Equations for Drilled Shafts and Driven Piles in Sand or Clay	75
Table 8.2 Recommended Code-Adjusted Resistance Factors for Pile Group Design for Drilled Shafts and Driven Piles in Sand and Clay with $LF_{DL}^{code} = 1.25$ and $LF_{LL}^{code} = 1.75$	75

Table 8.3 Efficiency (as a Percentage) for Individual Piles in a 4 × 4 Pile Group Installed in Sand	76
Table 8.4 Efficiency (as a Percentage) for Individual Piles in a 4 × 4 Pile Group Installed in Normally Consolidated London Clay	76
Table 8.5 Nominal and Factored Resistances Calculated for a Few Assumed Pile Lengths for Single Pile Design	77
Table 8.6 Nominal and Factored Resistances Calculated for a Few Assumed Pile Lengths for Pile Group Design	78
Table 9.1 Applicable Design Methods in Web-Based Design Tool	81

LIST OF FIGURES

Figure	Page
Figure 2.1 Mesh configuration for three-dimensional FE analysis	2
Figure 2.2 Trial meshes used near the pile base: (a) square pattern elements with the size of 4 cm and (b) square pattern elements with the size of 3 mm	3
Figure 2.3 Effect of mesh density near pile base on normalized base resistance, q_b/q_c , at different levels of relative settlement, s/B	3
Figure 2.4 Soil response near the pile base when relative settlement, s/B , at the pile head is equal to 10%: (a) shear strain (b) void ratio (c) pressure (d) shear stress	4
Figure 2.5 Normalized unit base resistance, q_b/q_c , mobilized in sands with different relative densities: (a) plotted against relative settlement, s/B , at the pile head and (b) plotted against relative settlement, s/B , at the pile base	5
Figure 2.6 Dilation that occurs in shear band elements. Shear band is shown thicker with respect to the pile than would normally be observed	5
Figure 2.7 Dilation profile of the shear band in the horizontal direction along depth for a 10 m (= 32.8 ft) long, 0.3 m (= 1 ft) diameter pile pre-installed in Ottawa sand with $D_R = 50\%$ and $D_R = 80\%$	6
Figure 2.8 Total shaft resistance vs. relative settlement at the pile head	6
Figure 2.9 Profiles of unit shaft resistance along depth at several relative settlement levels ($L = 10\text{ m} = 32.8\text{ ft}$, $B = 0.3\text{ m} = 1\text{ ft}$, $D_R = 80\%$)	6
Figure 2.10 Comparison of load-settlement curves for a 10 m (= 32.8 ft) long non-displacement pile with $B = 0.3\text{ m} (= 1\text{ ft})$ embedded in Ottawa sand with $D_R = 50\%$ and $D_R = 80\%$	7
Figure 2.11 One-dimensional axisymmetric finite-element analyses simulating centrifuge tests	7
Figure 2.12 Values of β obtained from the one-dimensional axisymmetric analyses compared with the centrifuge test data	8
Figure 3.1 Load-settlement curves for simple soil constitutive models: (a) linear-elastic model and (b) Mohr-Coulomb model	8
Figure 3.2 FE analysis of the 1×3 pile group: (a) planes of symmetry for the pile group and (b) the simulation domain and its boundary conditions	9
Figure 3.3 Mesh configuration for three-dimensional FE analysis of a 1×3 pile group	9
Figure 3.4 Effect of group configuration on the load-settlement curves	10
Figure 3.5 Comparison of the response of an individual pile to axial load in a 2×2 pile group with that for a single pile installed in medium dense, $D_R = 50\%$, Ottawa sand	10
Figure 3.6 Location of soil elements at the points being considered for a 2×2 pile group: (a) in the vertical direction and (b) in the horizontal plane	11
Figure 3.7 Development of shear band in a 2×2 pile group: (a) vertical settlement at the ground surface in the center of the pile group and (b) shear strain of an element next to the pile shaft at $4B$ below the ground surface	11
Figure 3.8 Group effects considering a soil element in the vicinity of the pile shaft and at $4B$ below the ground surface for a 2×2 pile group in terms of: (a) the radial stress (b) the shear stress and (c) the void ratio	12
Figure 3.9 Group effects near the pile base in a 2×2 pile group in terms of: (a) the vertical displacement; (b) the radial stress; (c) the mean stress in-between piles and (d) the shear stress next to the pile shaft	12
Figure 3.10 Comparison of profiles of limit unit shaft resistance for a single pile and an individual pile in a 2×2 pile group with $s_{cc} = 2B$ embedded in: (A) medium dense sand and (b) dense sand	13
Figure 3.11 Dependency of the group efficiency on the relative settlement s/B at the pile head	14
Figure 3.12 Efficiency for (a) the shaft resistance and (b) the base resistance of an individual pile in the 1×2 pile group	14
Figure 3.13 Efficiency for (a) the shaft resistance and (b) the base resistance of an individual pile in the 2×2 pile group	15
Figure 3.14 Efficiency for (a) the shaft resistance and (b) the base resistance of the center pile in the 1×3 pile group	15
Figure 3.15 Efficiency for (a) the shaft resistance and (b) the base resistance of the side pile in the 1×3 pile group	15
Figure 3.16 Tolerable movements for bridge foundations	16
Figure 3.17 The three types of piles and the symmetric conditions in a 4×4 pile Group	16
Figure 3.18 The simulation domain and boundary conditions used in the symmetric analysis of the 4×4 pile group	16
Figure 3.19 Mesh configuration for the three dimensional FE analysis of the 4×4 pile group	17

Figure 3.20 Load-settlement curves for a single pile and individual piles in a 4×4 pile group with $s_{cc} = 2B$ installed in: (a) and with $D_R = 50\%$ and (b) sand with $D_R = 80\%$	17
Figure 3.21 Development of the unit shaft resistance in: (a) center pile in sand with $D_R = 50\%$; (b) center pile in sand with $D_R = 80\%$; (c) side pile in sand with $D_R = 50\%$; (d) side pile in sand with $D_R = 80\%$; (e) corner pile in sand with $D_R = 50\%$; (f) corner pile in sand with $D_R = 80\%$ in a 4×4 pile group at different vertical settlements at the pile heads	18
Figure 3.22 Shaft resistance efficiency of individual piles in a 4×4 pile group installed in Ottawa sand with: (a) $D_R = 50\%$ and (b) $D_R = 80\%$ at different settlement levels	19
Figure 3.23 Base resistance efficiency of individual piles in a 4×4 pile group installed in Ottawa sand with: (a) $D_R = 50\%$ and (b) $D_R = 80\%$ at different settlement levels	19
Figure 4.1 Mesh configuration and boundary conditions for (a) 2D and (b) 3D FE analyses where $L =$ pile length and $B =$ pile diameter	22
Figure 4.2 Initial void ratio, e_o , and initial soil unit weight, γ_o , profiles for normally consolidated London clay	23
Figure 4.3 Contours of (a) shear strain, ε_{xy} (b) shear stress, σ_{xy} (c) equivalent plastic strain, ε_{eq}^p (d) plastic dissipation, D_p , in normally consolidated London Clay near pile base at 10% of relative settlement at pile head	24
Figure 4.4 Contours of (a) shear strain, ε_{xy} (b) shear stress, σ_{xy} (c) equivalent plastic strain, ε_{eq}^p (d) plastic dissipation, D_p , in normally consolidated Boston Blue Clay near pile base at 10% of relative settlement at pile head	25
Figure 4.5 Base resistances of 10-m-long (33-ft-long) nondisplacement piles with 0.3 m (= 1 ft) diameter installed in normally consolidated London Clay (LC) and normally consolidated Boston Blue Clay (BBC)	26
Figure 4.6 Base resistances of 10-m-long (33-ft-long) nondisplacement piles with 0.3 m (= 1 ft) diameter installed in overconsolidated London Clay (LC) with OCR = 10	26
Figure 4.7 Total shaft resistance of nondisplacement pile in normally consolidated London Clay (LC), normally consolidated Boston Blue Clay (BBC) and overconsolidated London Clay (LC) with OCR = 10 versus relative settlement at pile head	27
Figure 4.8 Profiles of (a) cross-sectional load, (b) unit shaft resistance and (c) excess pore water pressure along depth at several relative settlement levels for nondisplacement pile with $L = 10$ m (= 32.8 ft) and $B = 0.3$ m (= 1 ft) in NC LC	28
Figure 4.9 Profiles of (a) cross-sectional load, (b) unit shaft resistance and (c) excess pore water pressure along depth at several relative settlement levels for nondisplacement pile with $L = 10$ m (= 33 ft) and $B = 0.3$ m (= 1 ft) in NC BBC	29
Figure 4.10 Profiles of (a) cross-sectional load and (b) unit shaft resistance along depth at several relative settlement levels for nondisplacement pile with $L = 10$ m (= 33 ft) and $B = 0.3$ m (= 1 ft) in OC LC with OCR = 10	30
Figure 4.11 Load-settlement curves for 10 m (= 33 ft) along nondisplacement pile with pile diameter $B = 0.3$ m (= 1 ft) installed in normally consolidated (NC) London Clay, NC Boston Blue Clay and overconsolidated (OC) London Clay (OCR = 10)	31
Figure 4.12 Pile resistances of nondisplacement pile installed in soft clay over stiff clay with different embedment depths	31
Figure 4.13 Comparison between 2D and 3D FE analyses: (a) applied loads at pile head and (b) base and shaft resistances with respect to relative settlement of pile head	32
Figure 5.1 FE Analysis of the 1×3 pile group: (a) planes of symmetry for the pile group and (b) the simulation domain and its boundary conditions	33
Figure 5.2 Mesh configuration for three-dimensional FE analysis of a 1×3 pile group	33
Figure 5.3 Effect of group configuration on the load-settlement curves	34
Figure 5.4 Effect of pile-to-pile spacings on the load-settlement curves	34
Figure 5.5 Comparison of the response of an individual pile to axial load in a 2×2 pile group with that for a single pile	34
Figure 5.6 Location of soil elements at the points being considered for a 2×2 pile group: (a) in the vertical direction and (b) in the horizontal plane	34
Figure 5.7 Group effects in a 2×2 pile group with $s_{cc} = 2B$ as a function of relative settlement at the pile head for soil elements at the pile midlength: (a) vertical displacement of a soil element in the center of the pile group; (b) shear stress on the pile shaft and (c) mean stress for a soil element in the center of the pile group	35
Figure 5.8 Comparison of profiles of limit unit shaft resistance for a single pile and an individual pile in a 2×2 pile group with $s_{cc} = 2B$ in London Clay with OCR = 1	35
Figure 5.9 Dependency of the group efficiency on the relative settlement s/B at the pile head	35
Figure 5.10 Efficiency for (a) the shaft resistance and (b) the base resistance of an individual pile in small pile groups	36

Figure 5.11 The three types of piles and the symmetric conditions in a 4×4 pile group	36
Figure 5.12 The simulation domain and boundary conditions used in the symmetric analysis of the 4×4 pile group	36
Figure 5.13 Mesh configuration for the three-dimensional FE analysis of the 4×4 pile group	37
Figure 5.14 Load-settlement curves for a single pile and individual piles in a 4×4 pile group with $s_{cc} = 2B$ installed in London Clay with $OCR = 1$	37
Figure 5.15 Development of (a) shaft resistance and (b) base resistance for a single pile and individual piles in a 4×4 pile group with $s_{cc} = 2B$ installed in London Clay with $OCR = 1$	37
Figure 5.16 Efficiency for (a) shaft resistance and (b) base resistance of individual piles in a 4×4 pile group	38
Figure 6.1 Results of the SPTs and CPTs performed at the test site	40
Figure 6.2 Dimensions of the test pile and layout of strain gauges on the two segments of the test pile: (a) dimensions of the cross section of the test pile, (b) layout of strain gauges on the top pile segment, and (c) layout of strain gauges on the bottom pile segment	41
Figure 6.3 Pile instrumentation: (a) vibrating-wire strain gauges arc-welded to the pipe pile surface; (b) electrical-resistance strain gauges glued onto the pipe pile surface, protected by multilayers of waterproofing coatings; (c) strain gauge cables collected in a bundle and guided by nuts welded onto the pipe pile surface; (d) angled steel channels and tapered base cover welded to the pipe pile to protect all strain gauges and cables	42
Figure 6.4 Details of the two-segment pile driving process: (a) guiding ring and mineral wool layers used for splicing of the two pipe pile segments and heat isolation, respectively; (b) rebar hook used to fasten cables originating from the bottom pile segment inside the top pile segment; and (c) welded pile segments	42
Figure 6.5 Pile driving resistance versus depth	43
Figure 6.6 Load application system at the pile head and deflectometers supported by reference beams	43
Figure 6.7 Load-settlement curves at the pile head: (a) complete load-settlement history of load test; (b) load-settlement curve after unloading with measured settlement at pile head reset to zero	44
Figure 6.8 Residual load and axial load profiles accounting for the residual loads at the ultimate load level	44
Figure 6.9 Load-transfer curves (without accounting for the residual loads)	45
Figure 6.10 Measured limit shaft resistance along the pile	46
Figure 6.11 The effect of the shaft degradation term on predictions of the unit shaft resistance in sand: (a) the degradation term calculated according to the design methods considered vs. depth; and (b) the value of the degradation term normalized with respect to its maximum value (at the pile base) vs. depth	49
Figure 6.12 Comparison of the unit limit shaft resistance q_{sL} obtained from the static load test (considering the residual load) with those estimated using: (a) Purdue-CPT method; (b) ICP method; (c) UWA method; (d) NGI method; and (d) Fugro method	51
Figure 6.13 Results of CPTs performed at the pile load test site	52
Figure 6.14 Comparison of the unit limit shaft resistance, q_{sL} , obtained from the static load test (not accounting for residual loads) with those estimated using: (a) Purdue-CPT method; (b) ICP method; (c) UWA method; (d) NGI method; and (d) Fugro method	53
Figure 6.15 Results of CPTs performed at the pile load test site	54
Figure 6.16 Comparison of the unit limit shaft resistance q_{sL} obtained from the static load test (not accounting for residual loads) with those estimated using: (a) Purdue-CPT method; (b) ICP method; (c) UWA method; (d) NGI method; and (d) Fugro method	55
Figure 7.1 Flow chart of Monte Carlo simulations	62
Figure 7.2 Soil profiles for sand: (a) (1) – (2); (b) (3) – (5); and (c) (6) where $D_{R,mean,i}$ = mean relative density of i^{th} layer, B = pile diameter, and L_p = pile length	65
Figure 7.3 Soil profiles for clay: (a) (1); and (b) (2) where $s_{u,mean}$ = mean undrained shear strength of clay, $\sigma'_{v0,mean}$ = mean effective initial vertical stress, OCR = overconsolidation ratio, B = pile diameter, and L_p = pile length	65
Figure 7.4 Optimal resistance and load factors with various pile dimensions: (a) critical-state friction angle and (b) K_0 for CPT-based design method	66
Figure 7.5 Optimal resistance and load factors with various soil profiles for CPT-based design method	67

Figure 7.6 Optimal resistance and load factors with various pile dimensions for CPT-based design method	67
Figure 7.7 Optimal resistance and load factors with various LL/DL for CPT-based design method	67
Figure 7.8 (a) Factor of safety and (b) optimal resistance and load factors versus probability of failure for CPT-based design method	68
Figure 7.9 Optimal load and resistance factors with various (a) $\phi_{c,mean}$ and (b) K_0	70
Figure 7.10 Optimal load and resistance factors with various soil profiles	71
Figure 7.11 Optimal load and resistance factors for various pile diameter B_{mean} with (a) pile length, $L_p = 10$ m (= 33 ft); (b) $L_p = 20$ m (= 66 ft); and (c) $L_p = 30$ m (= 98 ft)	72
Figure 7.12 Optimal load and resistance factors for various B_{mean}/L_p	73
Figure 7.13 Optimal load and resistance factors for various LL/DL	73
Figure 7.14 Optimal load and resistance factors with various probability of failure, p_f	73
Figure 8.1 Results of CPTs performed at the test site of the project on U.S.	31 76
Figure 8.2 Result of CPT performed at the test site of the project on U.S.	52 78
Figure 9.1 Pile design Excel spreadsheet program tool	80
Figure 9.2 Selection of pile design equations and the result output	80
Figure 9.3 Web-based pile design tool	81
Figure 9.4 Calculation example of web-based pile design tool: (a) input data (b) calculation results	82

1. INTRODUCTION

1.1 Background

The two trends currently in place in pile design can and must progress together: the design of pile foundations using a simple form of reliability-based design called Load and Resistance Factor Design, LRFD, and the rigorous analysis of the loading of pile foundations using sophisticated computational methods. LRFD has been mostly implemented by the industry and DOTs through calibrations of current practices using Working Stress Design, WSD, also known as Allowable Stress Design, ASD; however, this practice does not enable realization of the advantages offered by LRFD. These advantages include specific accounting of uncertainties in the soil, foundation element and loading and the ability to design for specific values of probability of failure.

The other trend is the rigorous analysis of pile foundations. This trend is recent and has been enabled by the development of rigorous constitutive models (Chakraborty, Salgado, & Loukidis, 2013; Dafalias & Manzari, 2004; Levasseur, Malécot, Boulon, & Flavigny; Ling & Yang, 2006; Loukidis & Salgado, 2009; Rouainia & Muir wood, 2000; Stallebrass & Baudet, 2004; Woo & Salgado, 2015) and of computational methods capable of dealing with the complexities (strong nonlinearity, deformation localization) of this type of analysis (Chakraborty, Salgado, Basu, & Prezzi, 2013; Loukidis & Salgado, 2008; Pucker & Grabe, 2012; Qiu, Hencke, & Grabe, 2011; Wang et al., 2015; Wang, Randolph, & White, 2013). While some work has been done for single piles (Basu, Loukidis, Prezzi, & Salgado, 2011; Loukidis & Salgado, 2008; Mascarucci, Miliziano, & Mandolini, 2014), no work of this type has yet been done for pile groups. Design of pile groups has relied to a great extent on results of elastic analyses done years back. These analyses are unable to capture the evolution of stresses, strains and displacements in the soil around the piles, thus leading to an erroneous load-settlement response.

In this report, we use recently developed constitutive models to perform single pile and pile group analysis with the goal of proposing an LRFD methodology. While much work remains to be done in this topic, the report advances considerably the understanding of both single and pile group load response and how they should be designed for transportation infrastructures.

1.2 Report Structure

Chapter 2 and Chapter 3 present the results of rigorous finite-element analyses, using recently developed advanced, two-surface plasticity constitutive models, of single piles installed in sandy and clayey soil profiles, respectively. The analyses shed light on the relationships between the global response of the pile-soil system (development of shaft and base resistances)

and the behavior of local soil elements (e.g., shear band formation).

In Chapter 4 and Chapter 5, the results of the finite-element analyses of small (e.g., 2×2 pile group) and large (e.g., 4×4 pile group) pile groups installed in sand and clay, respectively, are reported. The effects of the pile group configuration, pile-to-pile spacing, and soil profile on the group interactions are studied. Pile efficiencies for individual piles and the overall pile group are reported.

Chapter 6 reports the instrumentation, installation, and static and dynamic testing of a closed-ended, driven pipe pile in Marshall County, Indiana. Pile resistance estimated by the Purdue CPT method, along with several other design methods, is compared with that obtained from the pile load test. Two other case histories are also used to validate the Purdue CPT pile design method.

Chapter 7 presents the systematic probabilistic analyses performed to develop resistance factors for the LRFD of pile groups considering displacement and nondisplacement piles, a range of soil conditions, and two values of target probability of failure.

Chapter 8 summarizes the design equations and the resistance factors for drilled shafts and driven piles in sandy and clayey soil profiles. Design examples are provided as references.

Chapter 9 presents developed design tools in this project, which INDOT can utilize and already utilizes.

2. NUMERICAL ANALYSES OF SINGLE PILES IN SAND

2.1 Finite Element Analysis

2.1.1 Constitutive Model

The advanced two-surface plasticity constitutive model developed by Loukidis and Salgado (2009) is used herewith. Based on critical-state soil mechanics, the model captures the mechanical response of sands under various loading conditions. A user-defined model subroutine VUMAT, which can be implemented in ABAQUS/Explicit (SIMULIA, 2012), was coded in FORTRAN to describe the constitutive relations. The constitutive model was calibrated for both clean Toyoura sand and Ottawa sand, with model parameters listed in Table 2.1. Since the pile stiffness is significantly greater than that of the soil, the pile is simulated as a linear-elastic material, with Young's modulus $E = 30$ GPa.

2.1.2 Analysis Configuration

Figure 2.1 shows the configuration of the mesh for the three-dimensional, finite-element analysis prepared in Abaqus/CAE 6.12-1 (SIMULIA, 2012); it has a total number of about 26000 8-noded, linear brick, hexahedral elements. The unit limit shaft resistance is very sensitive to the mesh configuration (Loukidis &

TABLE 2.1
List of Parameters Used in the Simulations for Sands.

	Parameter symbol	Parameter value		Test used for calibration
		Toyoura sand	Ottawa sand	
Small-strain parameters	ν	0.15	0.15*	Tests using local strain transducers, or isotropic compression or 1D compression tests with unloading path
	C_g	900	611	Bender element or resonant column tests
	n_g	0.40	0.437	Bender element or resonant column tests
	γ_1	0.001	0.00065	Resonant column tests or TX tests with local strain measurements
Critical state	α_1	0.40	0.47	Undrained TX compression tests
	Γ_c	0.934	0.78	TX compression tests
	λ	0.019	0.081	TX compression tests
	ζ	0.70	0.20	TX compression tests
Bounding surface	M_{cc}	1.27	1.21	TX compression tests
	k_b	1.5	1.9	TX compression tests
Dilatancy	D_0	0.90	1.31	TX compression tests
	k_d	2.8	2.2	TX compression tests
Plastic modulus	h_1	1.62	2.20	TX compression tests
	h_2	0.254	0.240	TX compression tests
	e_{lim}	1.00	0.81	TX compression tests
	μ	2.0	1.2	Undrained TX compression tests
Stress-induced anisotropy	c_1	0.72	0.71	TX extension tests
	c_2	0.78	0.78	SS or other plane-strain tests
	n_s	0.35	0.35	SS or other plane-strain tests
Inherent anisotropy	α	0.29	0.31	TX compression tests
	k_h	0.11	0.39	TX compression tests
Yield surface	m	0.05	0.05	

*Assumed value.

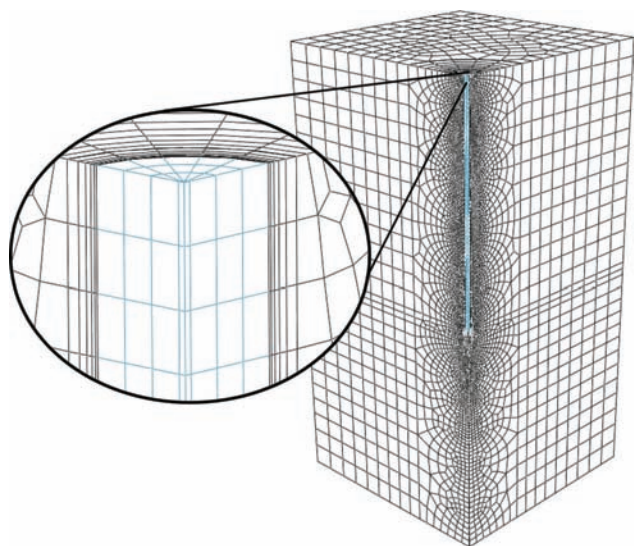


Figure 2.1 Mesh configuration for three-dimensional FE analysis.

Salgado, 2008; Mascarucci et al., 2014), particularly to the thickness of the soil elements adjacent to the pile (Tehrani et al., 2015). According to Loukidis and Salgado (2008), a realistic shear band thickness t_s of the order of $10D_{50}$ (2 mm for Toyoura sand and 4 mm for

Ottawa sand) should be used as the thickness of the elements adjacent to the pile (Alshibli & Sture, 1999; Rechenmacher, Abedi, & Chupin, 2010; Uesugi & Kishida, 1987).

Given the substantial roughness of the pile shaft and the cementation at the soil-pile interface due to grouting that is commonly used for nondisplacement piles, shearing along the pile shaft is assumed to happen within the soil adjacent to the pile instead of at the pile-soil interface. Perfect contact, which means the common nodes of the soil and pile are tied to each other with respect to all degrees of freedom, was assumed at the pile-soil interface. So long as there is no drilling mud contamination of the soil around the pile, the soil may be assumed to be the original *in situ* soil. The density of the sand is determined by the specific gravity and the relative density D_R being considered.

After equilibrium between the predefined stress field and the gravity applied to the whole domain is achieved through a geostatic step, velocities are applied at the pile head. Since the constitutive model used in the current FE analysis is rate-independent, a relatively high loading rate could be applied as long as it did not generate dynamic effects in the pile-soil system. The loading applied at the pile top was smoothed such that the loading rate gradually increased from zero to the desired velocity within the first second. A velocity $v = 2$ mm/s was taken

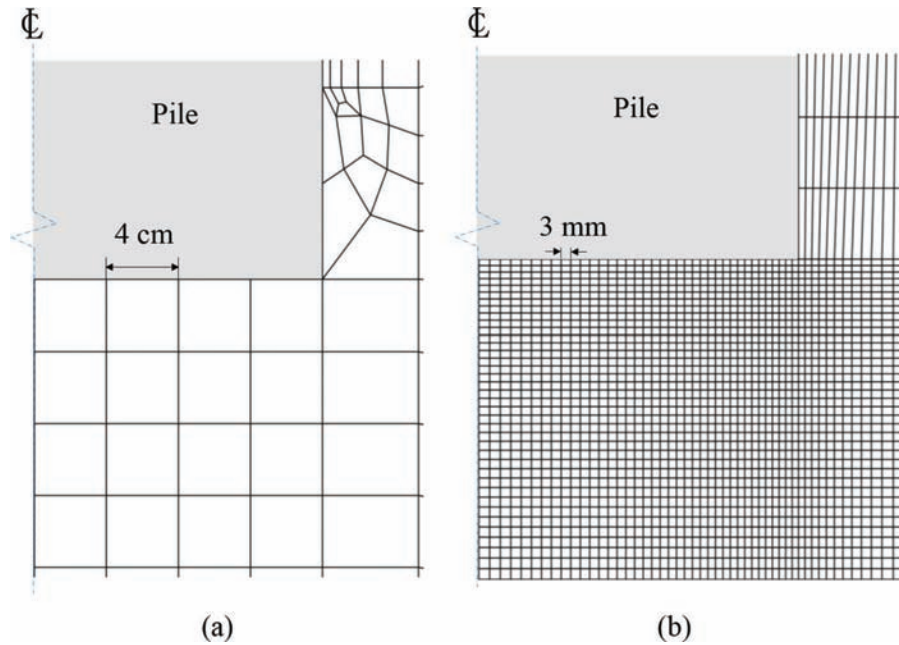


Figure 2.2 Trial meshes used near the pile base: (a) square pattern elements with the size of 4 cm and (b) square pattern elements with the size of 3 mm.

as the final loading velocity. As commonly done in design practice (Fleming, Weltman, Randolph, & Elson, 2008; Jardine, Chow, Overy, & Standing, 2005; Lehane, Schneider, & Xu, 2005; Randolph, 2003; Salgado, 2008), the ultimate resistance is defined as the load at a relative settlement $s/B = 10\%$ at the pile head. Thus, the pile was loaded until the final settlement at the pile head was equal to $0.1B$.

2.2 Results and Discussion

2.2.1 Base Resistance

In order to properly simulate the soil response to the pile moving downwards and obtain realistic predictions of the base resistance, a suitable mesh should be used near the pile base. A mesh that is too coarse is not able to capture the complex response of the soil near the pile base. Too fine a mesh would lead to excessive computational time, extreme element distortion and unrealistic localization of shear strain.

Figure 2.2 shows examples of square-pattern meshes with sizes of 4 cm and 3 mm, respectively, attempted for use near the pile base. Axisymmetric simulations, which are equivalent to the three-dimensional simulations, were used to test the performance of these meshes. The results are shown in Figure 2.3. The base resistance is usually normalized with respect to the cone resistance, q_c , at the depth where the pile base is located (Lee, 1999; Lee & Salgado, 1999; Simonini, 1996). The cone resistance can be determined by using the formula proposed in Salgado and Prezzi (2007) based on cavity

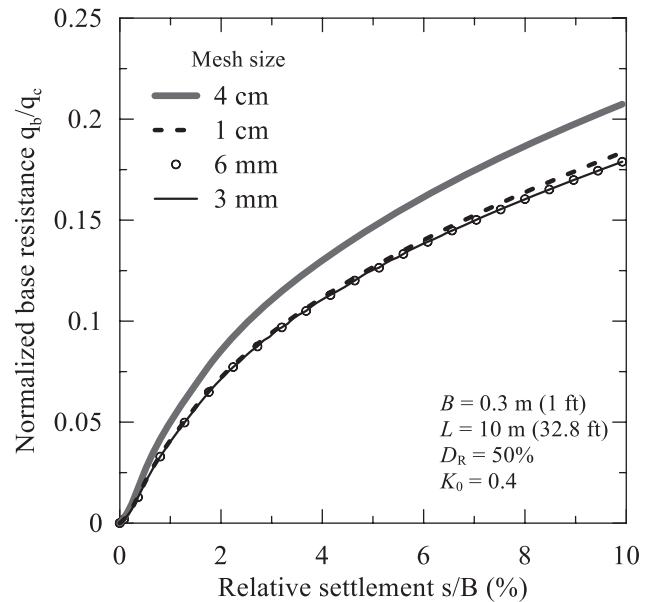


Figure 2.3 Effect of mesh density near pile base on normalized base resistance, q_b/q_c , at different levels of relative settlement, s/B .

expansion analysis, expressed as:

$$\frac{q_c}{P_A} = 1.64 \exp[0.1041c + (0.0264 - 0.0002c)D_R] \left(\frac{\sigma'_h}{P_A}\right)^{0.841 - 0.0047D_R} \quad (2.1)$$

where ϕ_c = critical-state friction angle; σ'_h = the horizontal effective stress; q_c = cone resistance and P_A = reference stress = 100 kPa. Substituting into Equation 2.1,

$D_R = 50\%$, which corresponds to a unit weight $\gamma = 15.95 \text{ kN/m}^3$, critical-state friction angle for Ottawa sand $\phi_c = 30^\circ$ (Loukidis, 2006) and $K_0 = 0.4$, as used in the FE simulations, q_c can be determined to be 7.87 MPa at the location of the pile base ($z = 10 \text{ m}$).

From Figure 2.3, we can clearly see that using a mesh size of 4 cm overestimates, by a large amount, the base resistance, while the analysis results almost coincide with each other when a 3 mm and 6 mm mesh size are used. Thus, 6 mm was selected as the element size around the pile base for the sake of computational efficiency without affecting the analysis results. The sum of the upward load, Q_b , acting on the pile base and shaft resistance, Q_s , acting along the pile shaft is balanced by the axial load, Q_t , applied at the pile head plus the self-weight of the pile. This equilibrium of the forces that the pile is subjected to is expressed as follows:

$$Q_b + Q_s = Q_t + W_{pile} \quad (2.2)$$

The unit base resistance, q_b , reported here refers to the net unit base resistance:

$$q_b = \frac{Q_b - W_{pile}}{A_b} \quad (2.3)$$

where A_b is the area of the pile base, q_b measures the amount of extra resistance that the pile base can provide beyond the initial resistance required to balance the pile self-weight. Thus, q_b always starts from zero (see Figure 2.3). Equation 2.2 and Equation 2.3 result in $Q_t = q_b A_b + Q_s$.

Figure 2.4 illustrates the soil response near the base of a 10-meter-long circular pile with a diameter equal to 0.3 m (1 ft) pre-installed in sand with $D_R = 50\%$ when the pile head is pushed down 30 mm (10% B). With the fine mesh and the advanced constitutive model, the analysis successfully captures the shear strain localization that develops starting from the pile base corner and extending towards the pile's central axis with a small angle with respect to the vertical direction, as shown in Figure 2.4(a). Similar features were found in calibration chamber tests by using the Digital Image Correlation technique (Arshad, Tehrani, Prezzi, & Salgado, 2014; Tehrani et al., 2015). The shearing in a dilative sand is always accompanied by an increasing volume or greater void ratio. Bearing in mind that the initial void ratio, e_0 , for Ottawa sand with $D_R = 50\%$ is equal to 0.63, the colored area in Figure 2.4(b), with $e > 0.63$, undergoes dilation induced by the localized shearing. The pattern

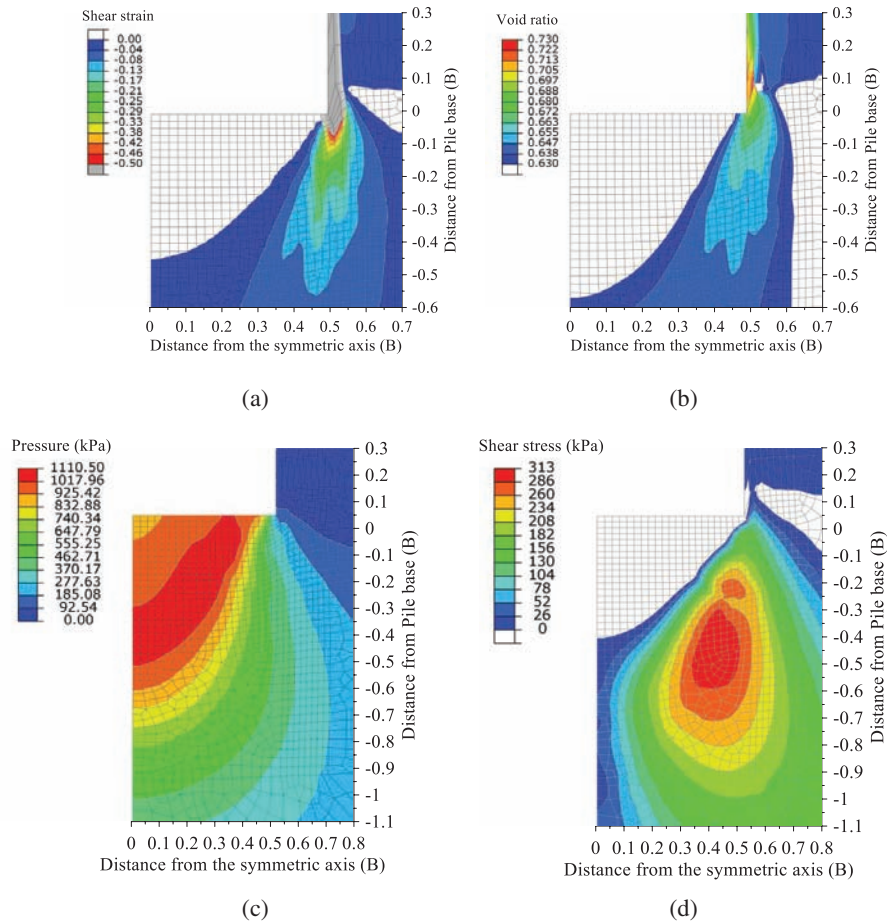


Figure 2.4 Soil response near the pile base when relative settlement, s/B , at the pile head is equal to 10%: (a) shear strain (b) void ratio (c) pressure (d) shear stress.

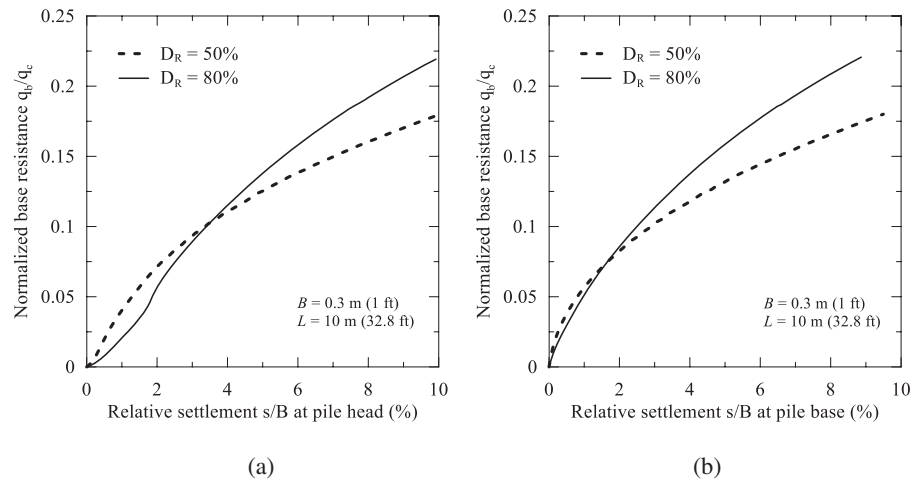


Figure 2.5 Normalized unit base resistance, q_b/q_c , mobilized in sands with different relative densities: (a) plotted against relative settlement, s/B , at the pile head and (b) plotted against relative settlement, s/B , at the pile base.

and magnitude of the shear strain and dilation match well with each other. As shown in Figure 2.4(c), there is large mean stress increase below the pile base and within a cone-shaped surface, where the void ratio decreases (soil contracts), see Figure 2.4 (b), and minimal shearing is observed, see Figure 2.4(a). Figure 2.4(d) shows the profile of the in-plane shear stress, which aligns closely with the direction of the shear strain localization. The largest shear stress is observed near the boundary between dilation and contraction in Figure 2.4(b). These findings shed light upon the shearing mechanism near the pile base. (1) A cone-shaped shear surface reaching down 0.4-0.6B below the pile base is already well developed at 10% relative settlement, with the soil contracting under very large mean effective stresses. (2) The soil outside the conical volume is pushed downwards and to the side, and significant shearing localizes along the cone-shaped failure surface. The pile base resistance is highly dependent on the soil properties in the region extending down to the depth of 0.6B at $w/B = 0.1$.

Figure 2.5(a) compares the normalized unit base resistance, q_b/q_c , developed by a 10 m (= 32.8 ft) long pile with $B = 0.3 \text{ m (= 1 ft)}$ installed in sands with $D_R = 50\%$ and $D_R = 80\%$. The normalized unit base resistance in dense sand, $D_R = 80\%$, is greater than that in medium dense sand, $D_R = 50\%$, at both 5% and 10% relative settlement levels. It is worth mentioning that in Figure 2.5(a), which is plotted against relative settlement at the pile head, there is a noticeable change of slope in the resistance-settlement curves that occurs, especially in the dense sand, when the relative settlement is about 2%. This is because, at the beginning of loading, the load applied at the pile head is first balanced by the shaft resistance until transfer of the load to the pile base gradually starts. The change of slope vanishes if the base resistance is plotted against the settlement at the pile base, as shown in Figure 2.5(b).

2.2.2 Dilation along the Pile Shaft

Figure 2.6 shows that an element adjacent to the pile (magnified for illustration), expands (dilates) in the horizontal direction when being sheared as the pile moves downwards. The dilation of the shear band element is important to understand the development of the unit shaft resistance. The dilation of the shear band elements adds an extra horizontal normal stress increment to the initial horizontal effective stress, σ'_{ho} , and, consequently, leads to a greater shear resistance than would be developed without any dilation (as in loose sand). As the shearing continues, the shear band elements reach critical state, dilation stops, and the shaft resistance stabilizes to a constant value.

The level of the dilation, defined as negative volumetric strain, can also be represented by the horizontal strain in the shear band elements since the source of the

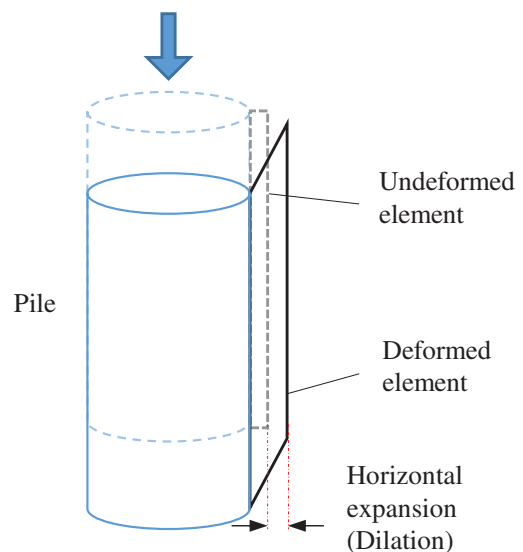


Figure 2.6 Dilation that occurs in shear band elements. Shear band is shown thicker with respect to the pile than would normally be observed.

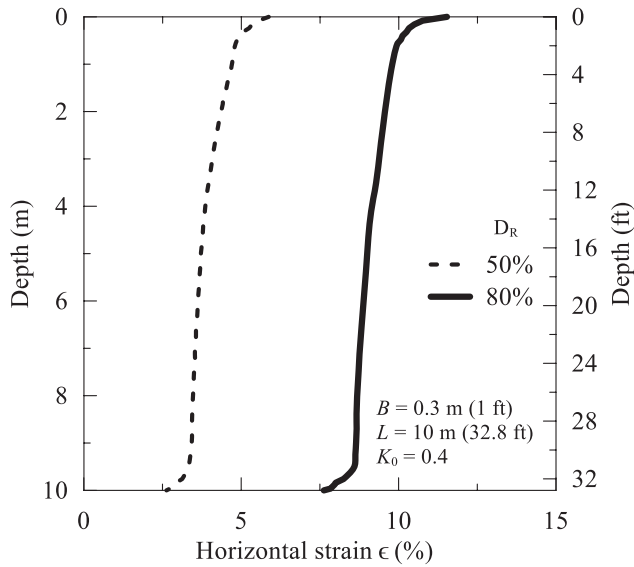


Figure 2.7 Dilation profile of the shear band in the horizontal direction along depth for a 10 m (= 32.8 ft) long, 0.3 m (= 1 ft) diameter pile pre-installed in Ottawa sand with $D_R = 50\%$ and $D_R = 80\%$.

volumetric strain in these elements is mainly from the horizontal expansion. Figure 2.7 compares the profiles of dilation in the shear band in the horizontal direction along depth for a 10 m (= 32.8 ft) long, 0.3 m (= 1 ft) diameter pile pre-installed in Ottawa sand with $D_R = 50\%$ and $D_R = 80\%$. Dilation of the shear band elements in dense sand, $D_R = 80\%$, is about twice as much as that in medium dense sand, $D_R = 50\%$. Less dilation is found at greater depth, where the confining stress is greater.

2.2.3 Shaft Resistance

Figure 2.8 shows the development of the total shaft resistance for a 10-m-long nondisplacement pile with diameter equal to 0.3 m (= 1 ft) embedded in Ottawa sand with $D_R = 50\%$ and $D_R = 80\%$. In both cases, the shaft resistance increases non-linearly as the pile is pushed down until a peak shaft resistance is developed when the relative settlement is in the 1–2% range. The shaft resistance then decreases and tends to stabilize as the soil elements near the pile-soil interface reach the critical-state. A more obvious peak in the shaft resistance is found in dense sand, $D_R = 80\%$. Since dilatancy of sand increases with relative density, as indicated in an earlier section, at the ultimate load level, $s/B = 10\%$, the shaft resistance mobilized in dense sand is almost twice as much as that developed in medium dense sand.

The unit shaft resistance mobilized on the pile surface may be calculated by differentiating the profile of the axial load along depth, then dividing it by the pile perimeter, πB . Figure 2.9 presents the profile of the unit shaft resistance mobilized in dense sand, $D_R = 80\%$, along depth at a few representative levels of relative settlement. The development of the unit shaft resistance

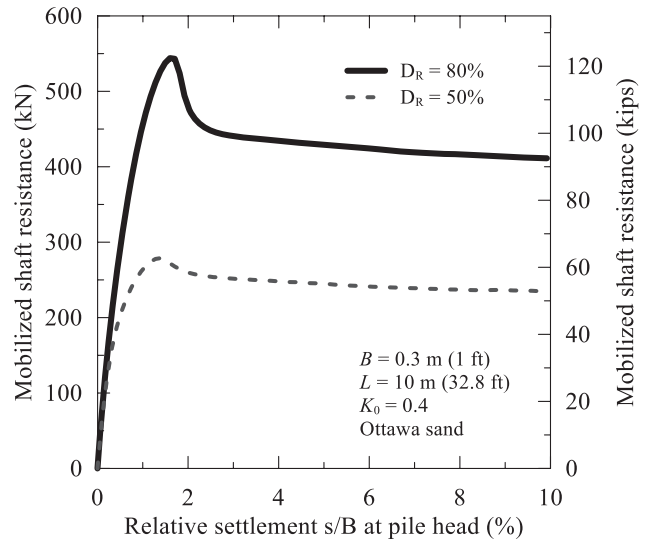


Figure 2.8 Total shaft resistance vs. relative settlement at the pile head.

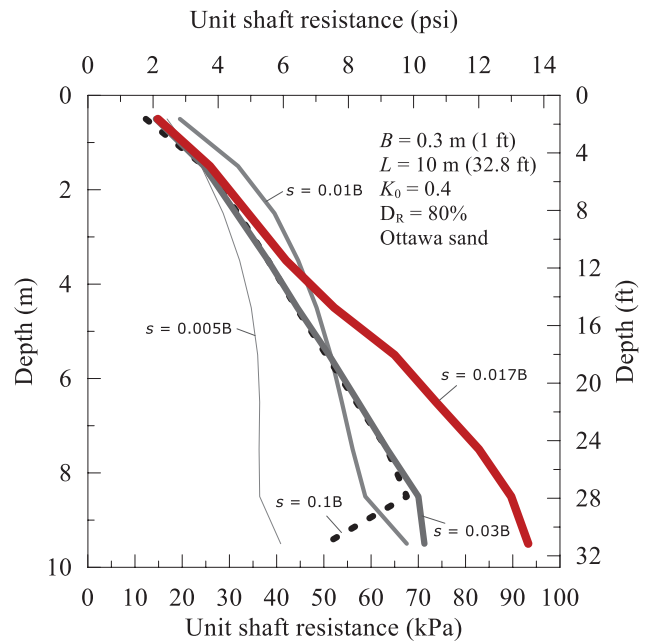


Figure 2.9 Profiles of unit shaft resistance along depth at several relative settlement levels ($L = 10 \text{ m} = 32.8 \text{ ft}$, $B = 0.3 \text{ m} = 1 \text{ ft}$, $D_R = 80\%$).

along depth is consistent with the trend of the shaft resistance-settlement curve. The unit shaft resistance gradually increases at both shallow and deep locations down the pile until the soil at a shallower depth first reaches the peak resistance when $s/B = 1\%$. Then, the shear resistance further down the pile continues to develop until it reaches peak resistance, when $s/B = 1.7\%$, while the soil at the shallower depth undergoes a softening process. Critical state is reached throughout the pile length when the pile head settlement is about $0.03B$, after which, the profile of the unit shaft resistance along depth barely changes, except near the pile

base. As the pile base moves down, it tends to move the soil elements near the pile base corner downwards, from $5B$ above the pile base to the pile base, decreasing the confining stress and bringing down the unit shaft resistance significantly in that region. This leads to a slight decrease in the total shaft resistance, even when most of the soil elements near the piles shaft have reached the critical-state. See Figure 2.8.

2.2.4 Load-Settlement Curve

Figure 2.10 compares the load-settlement curves developed by a 10 m (= 32.8 ft) long nondisplacement pile with $B = 0.3$ m (= 1 ft) embedded in Ottawa sand with $D_R = 50\%$ and $D_R = 80\%$. Since the base resistance increases monotonically with pile head settlement, the shape of the load-settlement curves follows that of the shaft resistance. An obvious peak total resistance is developed in the dense sand while the peak almost disappears in the medium dense sand. It should be noted that the peak in the load-settlement curves will not be observed if load is applied in a load-controlled manner, as normally used in engineering practice. This is because in a typical static load test, the load is always applied incrementally. If the applied load tends to decrease, when softening occurs, testers should increase the pressure in the hydraulic jack to maintain the load until it stabilizes. In contrast, loading in a displacement-controlled manner was used in the present analysis.

2.2.5 Comparison with Centrifuge Tests

Fioravante (2002) and Colombi (2005) reported data from centrifuge tests on 245- mm-long (9.6 inch),

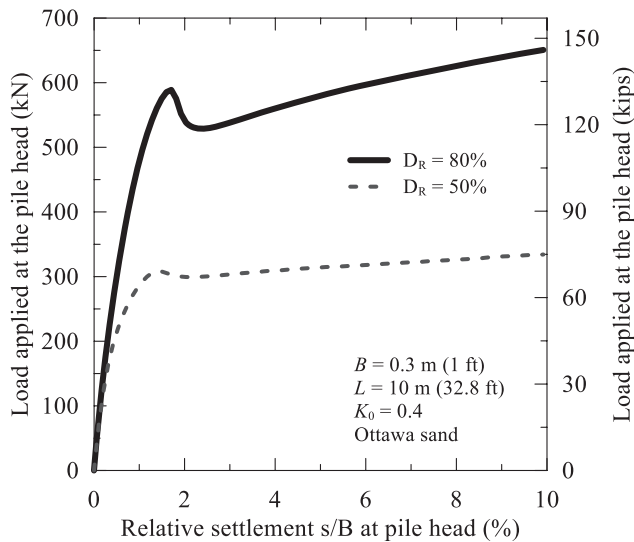


Figure 2.10 Comparison of load-settlement curves for a 10 m (= 32.8 ft) long nondisplacement pile with $B = 0.3$ m (= 1 ft) embedded in Ottawa sand with $D_R = 50\%$ and $D_R = 80\%$.

closed-ended nondisplacement model piles, which were made from 10-mm-diameter (0.4 inch) aluminum alloy pipes. The model piles were pre-installed in medium dense, $D_R = 66\%$, and dense, $D_R = 90\%$, Toyoura sand before the axial load was applied to the pile head in the target acceleration field.

Figure 2.11 shows the schematic configuration for the one-dimensional analysis, which analyzes the response of a surrounding soil disc, represented by a row of 4-noded, quadrilateral, axisymmetric elements with a total width of $20B$, to the axial loading of the pile (Loukidis & Salgado, 2008). Initial vertical and horizontal stresses corresponding to the depth being considered were applied to all the elements. Each pair of nodes lying in the same vertical line are tied together such that both the vertical and horizontal displacements of the two nodes are the same. With the nodes tied, only two forms of motion/deformation were allowed: the shearing along the vertical direction and the contraction or dilation in the radial direction. The pile being pushed down was simulated by applying vertical displacement or velocity to the left-most vertical boundary, where the horizontal displacement was kept equal to be zero. The right-most boundary is fixed in both directions.

Analyses were performed at several vertical stress levels representing different depths in the ground. The actual diameter of 10 mm of the model pile was used, and the shear band thickness, $t_s = 8D_{50} = 1.5$ mm, was assigned to the left-most element. Constitutive model parameters calibrated for Toyoura sand in Table 2.1 were used in the FE analyses.

Widely used in practice, the β method relates the unit limit shaft resistance, q_{sL} , to the initial vertical stress, σ'_{v0} , at the depth being considered by:

$$q_{sL} = K\sigma'_{v0} \tan \delta = \beta\sigma'_{v0} \quad (2.4)$$

where K = coefficient of lateral earth pressure = σ'_h / σ'_{v0} , δ = soil-pile interface friction angle. The values of β at different depths in the centrifuge tests were back-calculated from q_{sL} and σ'_{v0} . As shown in Figure 2.12, the simulation results are in good agreement with the test data.

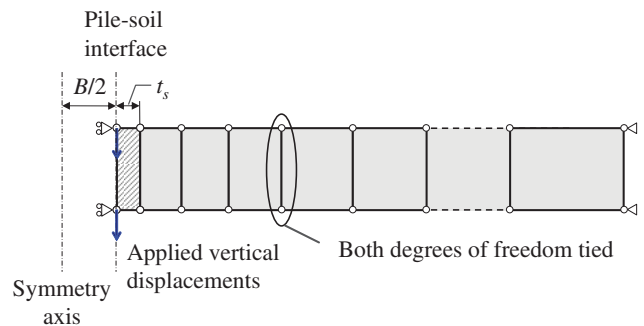


Figure 2.11 One-dimensional axisymmetric finite-element analyses simulating centrifuge tests.

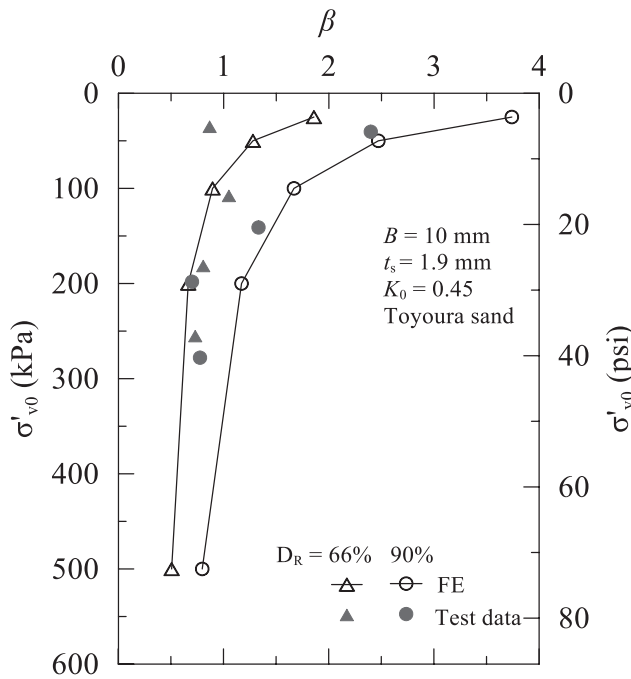


Figure 2.12 Values of β obtained from the one-dimensional axisymmetric analyses compared with the centrifuge test data.

3. NUMERICAL ANALYSES OF PILE GROUPS IN SAND

3.1 Finite Element Analysis

3.1.1 Necessity of the Use of a Realistic Constitutive Model

The use of a realistic constitutive model is necessary. A simple constitutive model, for example, a linear-elastic model or a Mohr-Coulomb model, does not take the intrinsic properties of the soil as model parameters, which

have to be empirically determined for pile design, bringing about uncertainty and arbitrariness in the analyses. These simple constitutive models are not able to capture the simple shear along the pile shaft, the triaxial compression below the pile base and the triaxial extension near the corner of the pile base subjected to axial loading.

In order to demonstrate the importance of the use of a realistic constitutive model, Figure 3.1 compares the load-settlement curve of a single pile and the average load-settlement curves of piles in different pile group configurations when simple constitutive models, the linear-elastic model and the Mohr-Coulomb model, are used for the soil. Neither of the two simple constitutive models is able to properly simulate the pile-soil-pile interaction effects in a pile group since these simple constitutive relations cannot capture the peak resistance, softening and critical-state response observed in a load-settlement curve as pile loading progresses.

Therefore, the advanced two-surface plasticity constitutive model developed by Loukidis and Salgado (2009) is used herewith, with details discussed in 2.1.1.

3.1.2 Analysis Configuration

Four different pile group configurations of interest were analyzed: 1×2 , 1×3 , 2×2 and 4×4 . Given the symmetry in the pile group configurations considered, modeling was required on only one portion of the entire domain. This reduced significantly the number of elements required to perform the analyses, thus, the total computational time. For example, in a 1×3 pile group with three piles in a row, the entire soil-pile domain is symmetric with respect to the two lines of symmetry shown in Figure 3.2(a). Therefore, only one quarter of the whole domain is required modeling. The simulated domain and the boundary conditions for this case are illustrated in Figure 3.2(b).

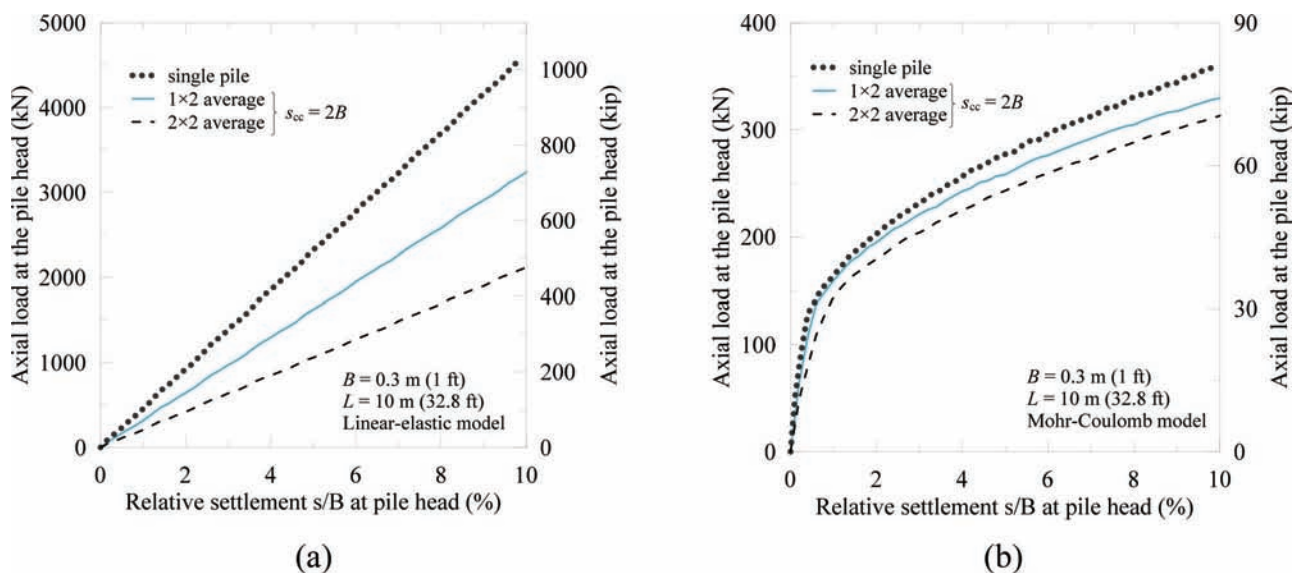


Figure 3.1 Load-settlement curves for simple soil constitutive models: (a) linear-elastic model and (b) Mohr-Coulomb model.

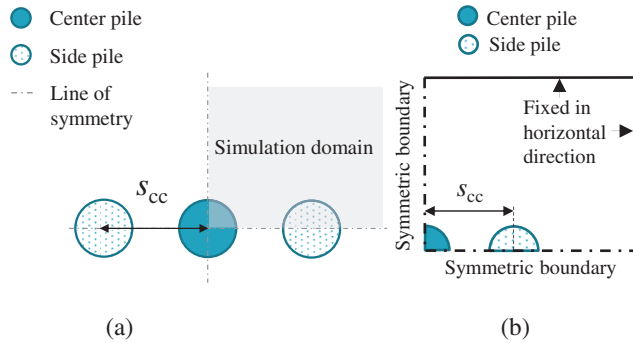


Figure 3.2 FE analysis of the 1×3 pile group: (a) planes of symmetry for the pile group and (b) the simulation domain and its boundary conditions.

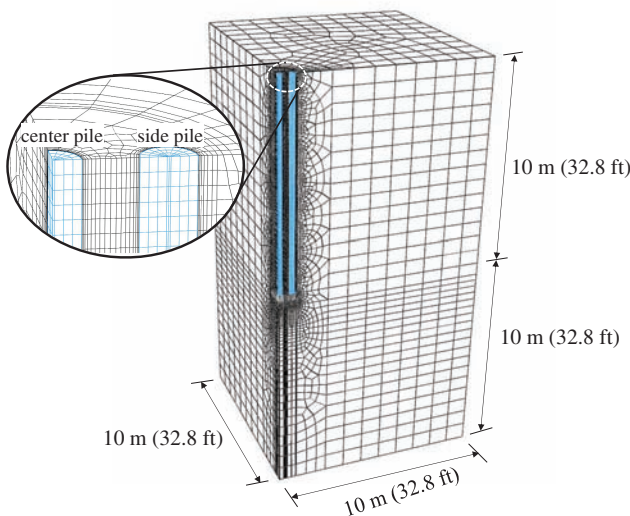


Figure 3.3 Mesh configuration for three-dimensional FE analysis of a 1×3 pile group.

The meshes for the three-dimensional, finite-element analyses were prepared in Abaqus/CAE 6.12-1 (SIMULIA, 2012) and consisted mainly of 8-noded, linear brick, hexahedral elements. Figure 3.3 shows the geometric dimensions of the simulation domain and the mesh configuration for the FE analysis of a 1×3 pile group with center-to-center spacing, $s_{cc} = 2B$. A total number of 54,465 elements were used to generate the mesh. As more complex pile group configurations and greater pile spacings are considered, the number of elements required in the analyses increased significantly, leading to considerably greater computational effort. Table 3.1 summarizes the numbers of elements used for different pile group configurations with various center-to-center pile spacings, s_{cc} .

The limit unit shaft resistance of a pile is very sensitive to the mesh configuration (Loukidis & Salgado, 2008; Mascarucci et al., 2014), particularly to the thickness of the soil elements adjacent to the pile shaft and around the pile base. According to Loukidis and Salgado (2008), a realistic shear band thickness, t_s , of the order of

TABLE 3.1
Number of Elements Used in the FE Simulations for Different Small Pile Group Configurations.

s_{cc}	Group configuration		
	1×2	2×2	1×3
$2B$	35,759	67,052	54,465
$3B$	39,288	74,933	63,865
$4B$	44,676	86,056	71,285

$10D_{50}$ (e.g., 2 mm for Toyoura sand and 4 mm for Ottawa sand) should be used as the thickness of the elements adjacent to the pile (Alshibli & Sture, 1999; Rechenmacher et al., 2010; Uesugi & Kishida, 1987). Given the roughness of the pile shaft, shearing along the pile shaft is assumed to occur within the soil adjacent to the pile instead of right at the pile-soil interface. So long as there is no drilling mud contamination in the soil around the piles, in the case of nondisplacement piles, the stress state of the soil is assumed to be that of the original *in situ* soil. Perfect contact, which means that the common nodes of the soil and pile are tied to each other with respect to all degrees of freedom, was assumed at the pile-soil interface. The density of the sand was determined from the specific gravity and the relative density, D_R , being considered.

Loading was simulated by simultaneously applying the same velocity at each pile head in the pile group after equilibrium between the predefined stress field and the gravity applied to the entire domain is achieved through a geostatic step. Since the constitutive model used in the FE analyses is rate-independent, a relatively high loading rate could be applied on the head of the piles, so long as no dynamic effects were generated in the pile-soil system. The loading applied at the head of the piles was smoothed such that the loading rate gradually increased from zero to the desired velocity, $v = 2$ mm/s, within the first second. The ultimate resistance was defined as the load corresponding to a relative settlement, $s/B = 10\%$, where B = pile diameter at the pile head (Fleming et al., 2008; Jardine et al., 2005; Lehane et al., 2005; Randolph, 2003; Salgado, 2008). The analyses were terminated when the settlements at all pile heads were equal to $0.1B$.

3.2 Results and Discussion

In this section, the three commonly used pile group configurations, one-by-two, one-by-three and two-by-two pile groups, are considered with center-to-center spacings, s_{cc} , varying from $2B$ to $4B$.

3.2.1 Load-Settlement Curves

Figure 3.4 compares the load settlement curve of a single pile with the average load-settlement curves of piles in different group configurations, 1×2 , 1×3 and 2×2 , but with the same center-to-center spacing, $s_{cc} = 2B$, installed in dense Ottawa sand. At the beginning of the loading, the average load-settlement curve is less

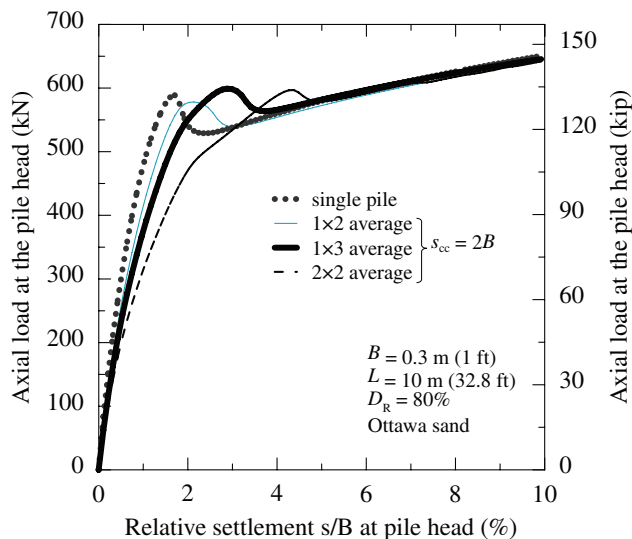


Figure 3.4 Effect of group configuration on the load-settlement curves.

stiff with increasing number of piles in a group, presumably due to greater interaction effects among the piles in the group. As shearing localizes and the shear bands form in the soil adjacent to the shaft of the piles at relative pile head settlements ranging from 1.5% to 4.5%, the degree of interaction between the piles decrease, and the average load-settlement curves tend to merge and become the same as that of a single pile.

It can be inferred that the nature and level of pile-soil-pile interaction in a pile group are different along the shaft and around the base of the piles, since the mechanisms for the mobilization of the shaft and base resistances are different. Figure 3.5 decomposes the total resistance of an individual pile in a 2×2 pile group with pile spacing of $2B$ placed in a medium dense sand into its shaft and base resistances. The resistances for a single pile are also plotted for comparison. The pile-soil and pile-pile interactions are due mainly to interaction along the zone of influence around the shaft of the piles, with minimal group effect found at the base of the piles at an ultimate load level of up to 10% of the pile diameter.

3.2.2 Mechanisms Leading to Interaction Effects along the Shaft of Piles in a Group

A 2×2 pile group installed in medium dense Ottawa sand, $D_R = 50\%$, with center-to-center distance, $s_{cc} = 2B$, is considered. Since group effects result mainly from the interaction that develops as the load is transferred to the soil along the pile shafts in small pile groups, only shaft resistance results are presented in this section.

Representative points at a few locations in a horizontal plane within the 2×2 pile group and at various depths along the piles are selected to investigate the effects of the elemental soil behavior on the global response of the piles to loading. Figure 3.6 shows the locations considered at five depths along the pile length: at the ground surface, $4B$ below the ground surface, at the pile midlength, $6B$

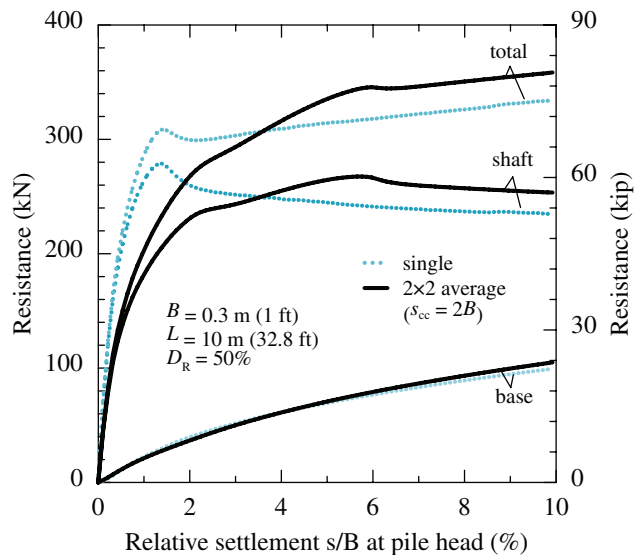


Figure 3.5 Comparison of the response of an individual pile to axial load in a 2×2 pile group with that for a single pile installed in medium dense, $D_R = 50\%$, Ottawa sand.

above the pile base and at the pile base and three locations in the horizontal plane: next to the pile shaft, midway between two side piles and at the center of the 2×2 pile group. The symbols in Figure 3.6 (a) and (b) will be used in combination to describe the location of a soil element at the point being considered. For example, C-III represents the point located in the center of the 2×2 pile group at the pile midlength.

3.2.2.1 Increase of the Confining Stress at a Shallow Depth. Due to the confinement provided by the piles in a pile group, as shown in Figure 3.7(a), the soil between the piles in a 2×2 pile group moves downward together with the surrounding piles, delaying shear strain localization in soil adjacent to the pile shafts (and the formation of shear bands) until s/B is nearly 6%, as shown in Figure 3.7(b). In contrast, for a single pile, shearing takes place almost immediately after loading starts, with shear localization developing even before s/B reaches 1%. At the same s/B level of 1%, settlement of the ground surface at a distance of $\sqrt{2}B$ from the pile center, the same distance considered for the case of the 2×2 pile group, stabilizes. See Figure 3.7(a).

Figure 3.8 (a) and (b) show the radial stress, σ'_h , and shear stress, τ'_{vs} , in a soil element adjacent to the shaft of a pile in a 2×2 pile group, respectively. Because of the greater built-up of radial stresses for the piles in a group than for a single pile, higher peak and critical-state shear stresses result. As shown in Figure 3.8 (c), the dilation, increase in void ratio, in the soil element at location B-I in a pile group is less than that for a single pile because of the greater confining stress at that location. The appearance of the peak shear stress, see Figure 3.8 (b), corresponds to the highest rate of dilation, see Figure 3.8 (c). This happens at a relative settlement, s/B , close to 1% for a single pile and in the 4–5% range for the 2×2 pile group.

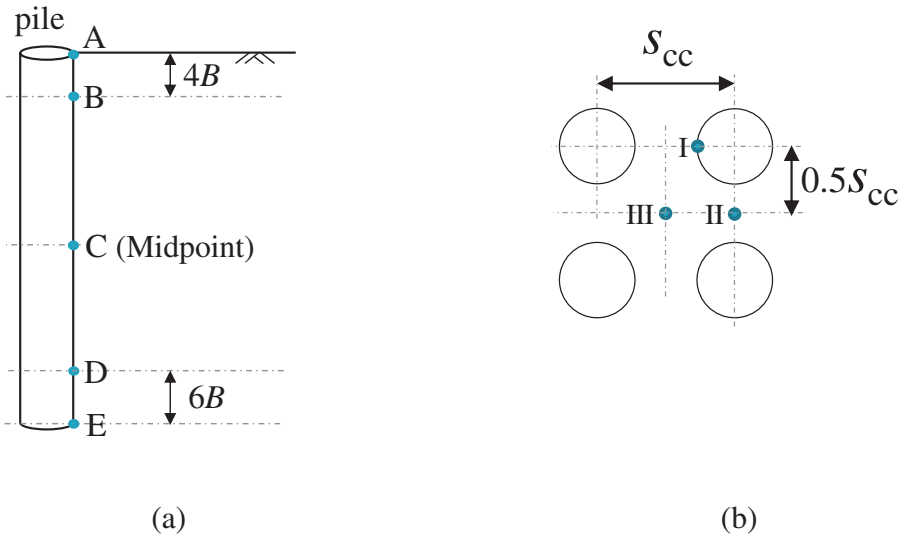


Figure 3.6 Location of soil elements at the points being considered for a 2×2 pile group: (a) in the vertical direction and (b) in the horizontal plane.

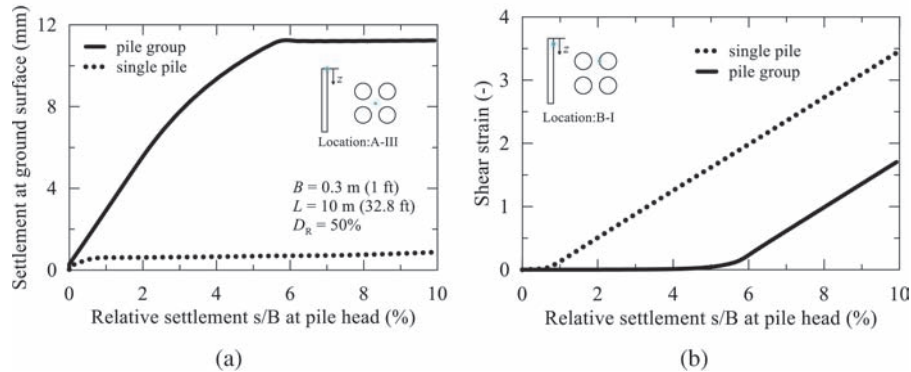


Figure 3.7 Development of shear band in a 2×2 pile group: (a) vertical settlement at the ground surface in the center of the pile group and (b) shear strain of an element next to the pile shaft at $4B$ below the ground surface.

3.2.2.2 The Unloading of the Soil in-between Piles near the Pile Base. Figure 3.9 (a) shows that the soil between piles at the pile base level is dragged downwards together with the neighboring piles, causing unloading of the soil elements near the shaft and slightly above the pile base. The vertical displacement in soil at the same distance ($0.5B$) from the pile surface and the same depth is also plotted for comparison. This is confirmed in Figure 3.9(c), which shows a continuous decrease of the mean stress, p' , at location D-II after the initial build-up. The radial stress, σ'_h , and the shear stress, τ'_s , in soil adjacent to the pile surface subsequently drop, as shown in Figure 3.9(b) and (d).

Figure 3.10(a) shows the profile of the limit unit shaft resistance for an individual pile in the 2×2 pile group and for a single pile installed in medium dense sand, $D_R = 50\%$. The limit unit shaft resistance for a

pile in the 2×2 pile group is greater than that of a single pile at shallow depths, but the opposite is the case near the pile base. This confirms the two mechanisms discussed above: (i) the increase in confinement due to the presence of neighboring piles causes an increase in the unit limit shaft resistance at shallow depths and (ii) the unloading of the soil in-between the piles near the pile base causes a decrease in the limit unit shaft resistance. Figure 3.10(b) shows the same comparison shown in Figure 3.10(a) between a 2×2 pile group and a single pile but placed in dense sand, $D_R = 80\%$. Similar trends result for both medium dense and dense sands; however, the difference between the limit unit shaft resistance profiles is less in dense sand due to the greater tendency for strain localization in denser sand, and thus smaller pile-soil-pile interaction effects.

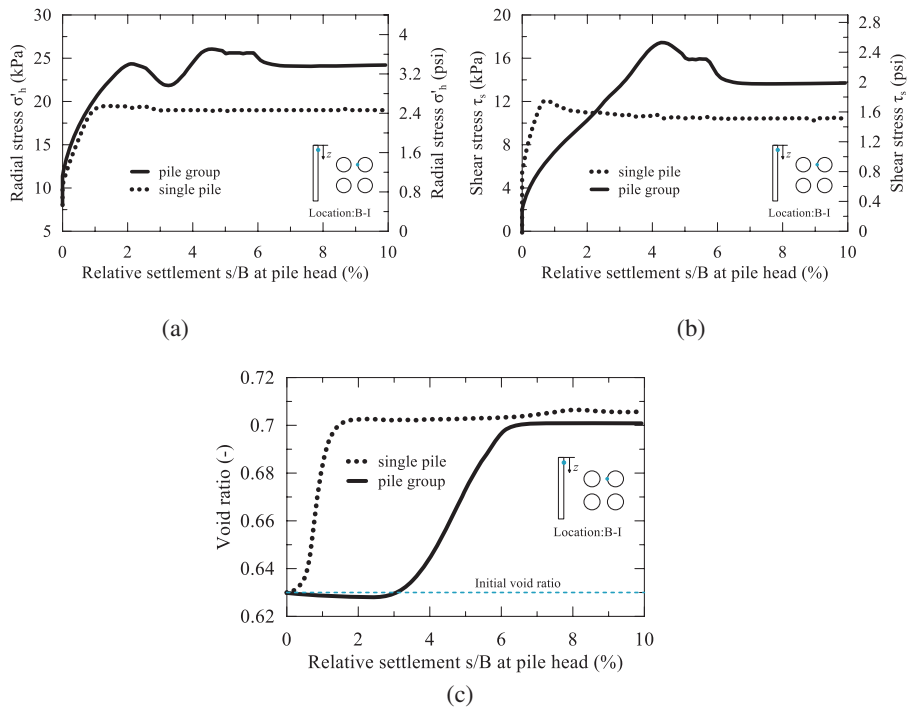


Figure 3.8 Group effects considering a soil element in the vicinity of the pile shaft and at $4B$ below the ground surface for a 2×2 pile group in terms of: (a) the radial stress (b) the shear stress and (c) the void ratio.

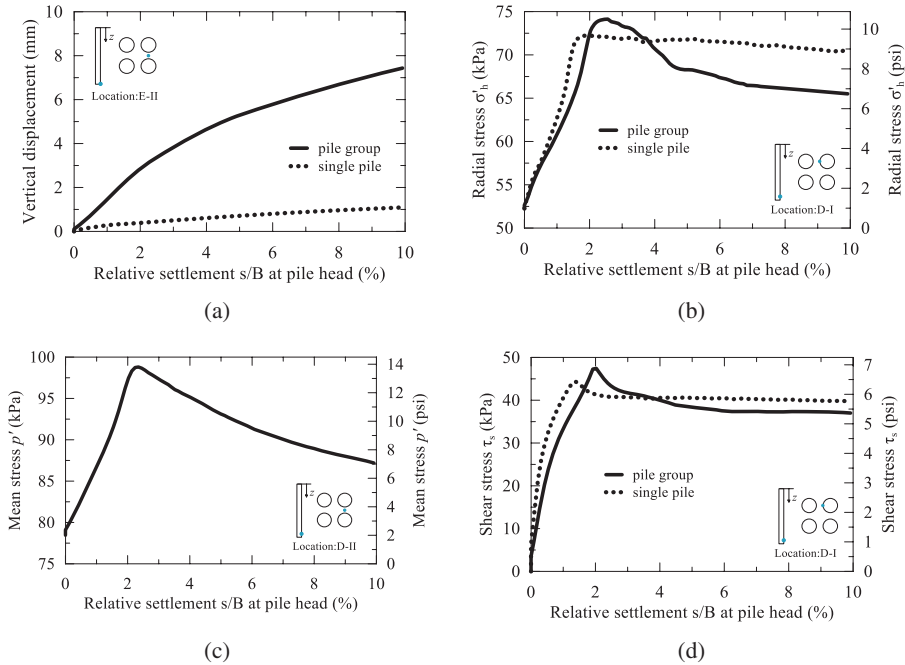


Figure 3.9 Group effects near the pile base in a 2×2 pile group in terms of: (a) the vertical displacement; (b) the radial stress; (c) the mean stress in-between piles and (d) the shear stress next to the pile shaft.

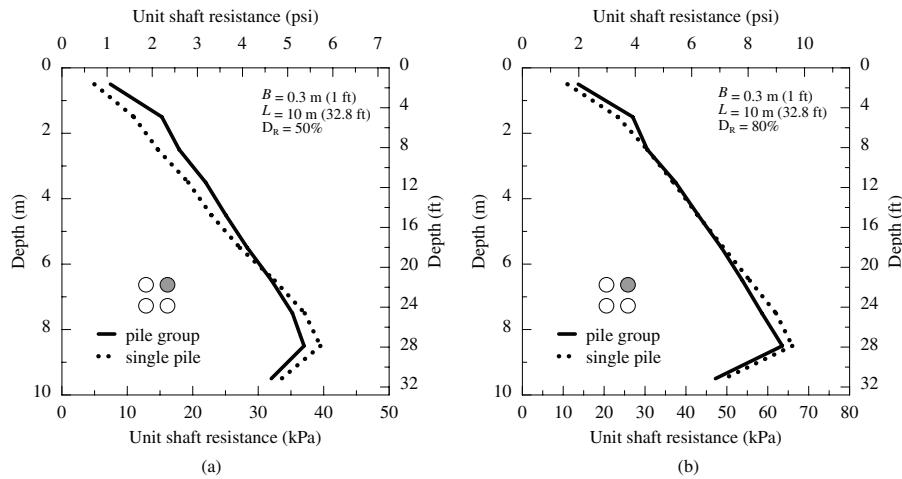


Figure 3.10 Comparison of profiles of limit unit shaft resistance for a single pile and an individual pile in a 2×2 pile group with $s_{cc} = 2B$ embedded in: (A) medium dense sand and (b) dense sand.

3.3 Group Efficiency

Group efficiency, η_g , is defined as the ratio of average resistance developed in individual piles in a pile group to that developed in a single pile with the same diameter and length installed in the same soil profile:

$$\eta_g = \frac{\sum_{i=1}^{n_p} Q_i(s)}{n_p Q(s)} \quad (3.1)$$

where Q_i is the sum of shaft and base resistances developed in the i^{th} pile in a pile group with n_p piles, Q is the resistance developed by a single pile, and s is the settlement at the pile head.

In Equation 3.1, group efficiency, η , is a function of the pile head settlement s because the single pile resistance, $Q = Q(s)$, and the resistance, $Q_i = Q_i(s)$, of each pile in the group are both functions of s . This means that it is not possible to speak of a single pile group efficiency value for a given pile group, this efficiency value depends on the settlement value for which we wish to perform the design.

An alternative manner of considering design of a pile group is to multiply the resistance that a single pile would develop by an efficiency factor to obtain the resistances of the individual piles in the group. This efficiency for the i^{th} pile in a pile group can be expressed as:

$$\eta_i = \frac{Q_i(s)}{Q(s)} \quad (3.2)$$

If the efficiencies of individual piles in a pile group are known, the total resistance, Q_G , developed in the group can be readily calculated as:

$$Q_g = \sum_{i=1}^{n_p} Q(s)\eta_i \quad (3.3)$$

Consider shaft resistance and base resistance separately, since the mechanisms and the magnitudes of the

group interactions are totally different along the shaft and at the pile base. Efficiencies for the shaft resistance, $\eta_{s,i}$, and the base resistance, $\eta_{b,i}$, respectively, of the i^{th} pile in a group can be defined in a similar manner:

$$\eta_{s,i} = \frac{Q_{s,i}(s)}{Q_s(s)}, \quad \eta_{b,i} = \frac{Q_{b,i}(s)}{Q_b(s)} \quad (3.4)$$

where $Q_{s,i}$ and $Q_{b,i}$ are the shaft and base resistances, respectively, developed in the i^{th} pile in the group; Q_s and Q_b are the shaft and base resistances, respectively, developed in a single pile. For group configurations in which every pile has identical response, namely the 1×2 and 2×2 groups, the efficiencies of individual piles are equal to the group efficiency of the entire pile group. According to (3.4), the total resistance developed in the i^{th} pile equals $Q_s(s)\eta_{s,i} + Q_b(s)\eta_{b,i}$, and the total resistance in the pile group then becomes:

$$Q_g = \sum_{i=1}^{n_p} \{Q_s(s)\eta_{s,i} + Q_b(s)\eta_{b,i}\} \quad (3.5)$$

3.3.1 Effect of Relative Settlement Level

Figure 3.11 shows the group efficiency as a function of the relative settlement s/B at the pile head for different pile group configurations in dense Ottawa sand, $D_R = 80\%$. Group efficiency values are initially low, ranging from 65% to 85%, however values increase and reach peak values above 100% at relative settlement levels in the 2-4% range. The efficiencies finally converge to values very close to 100% as soil elements along the pile shaft reach critical state.

3.3.2 Effect of Center-to-Center Pile Spacing

Efficiencies, as defined previously, for individual piles in a pile group are also calculated considering these two types of resistances separately, since the mechanisms of interaction along the shaft and base of

piles in group are completely different. Figure 3.12 to Figure 3.15 show the efficiencies for individual piles at the ultimate load, the load corresponding to $s/B = 10\%$ at the pile head, for several pile group configurations with center-to-center spacing varying from $2B$ to $4B$. As the center-to-center spacing increases, the degree of interaction between the piles in the group decreases. The piles in the group behave similarly to a single pile. The efficiencies tend to be 100% for both the shaft and base resistances when the center-to-center spacing is equal to $4B$. In general, greater interaction effects are found for pile groups in medium dense sand than in dense sand. Efficiency values for base resistance for

almost all of the small-pile-group configurations considered in this study are within the range of $100 \pm 5\%$, indicating minimal group effects near the pile base at ultimate load levels. Efficiency for the shaft resistance is a result of the combined effects of the two mechanisms discussed in the previous section.

1 × 2 Pile Group Efficiency

For 1 × 2 pile group efficiency, see Figure 3.12.

2 × 2 Pile Group Efficiency

For 2 × 2 pile group efficiency, see Figure 3.13.

Pile Efficiency for Center Pile in a 1 × 3 Group

For pile efficiency for a center pile in a 1 × 3 pile group, see Figure 3.14.

Pile Efficiency for Side Pile in a 1 × 3 Group

For pile efficiency for a side pile in a 1 × 3 pile group, see Figure 3.15.

3.4 4 × 4 Pile Group

A 4 × 4 pile group with center-to-center spacing, $s_{cc} = 2B$, installed in Ottawa sand with two different densities, $D_R = 50\%$ and $D_R = 80\%$, was also analyzed to study the group effects in a large pile group.

3.4.1 Tolerable Movements for Bridge Foundations

Based on observations and measurements on hundreds of bridges in Canada and the United States, Bozozuk (1978) summarized these case histories in Figure 3.16 and suggested values for tolerable vertical and horizontal movements for bridge foundations. 50 mm (2 inches), the harmful but tolerable vertical movement,

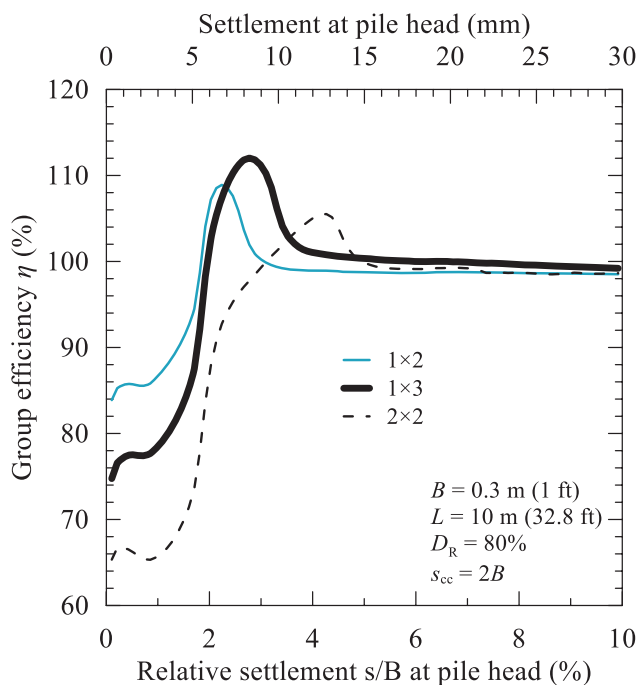
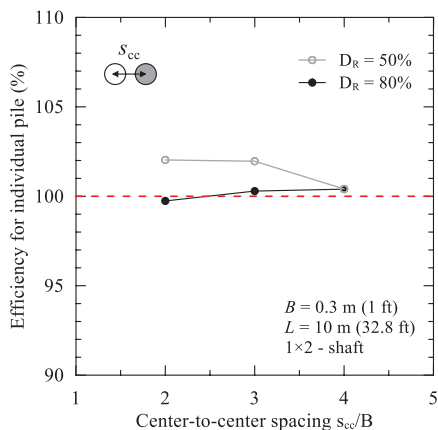
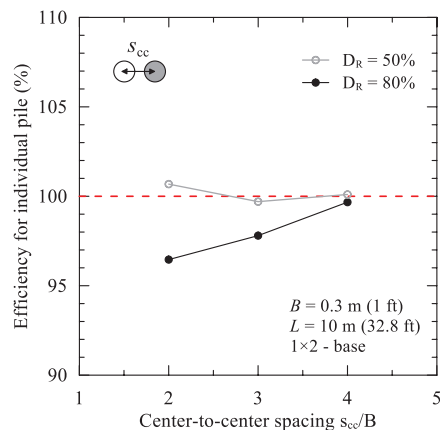


Figure 3.11 Dependency of the group efficiency on the relative settlement s/B at the pile head.



(a)



(b)

Figure 3.12 Efficiency for (a) the shaft resistance and (b) the base resistance of an individual pile in the 1 × 2 pile group.

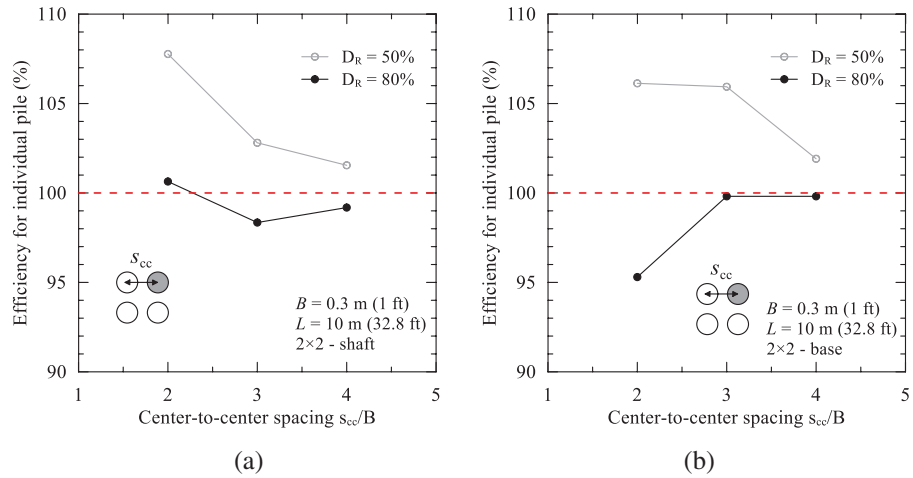


Figure 3.13 Efficiency for (a) the shaft resistance and (b) the base resistance of an individual pile in the 2×2 pile group.

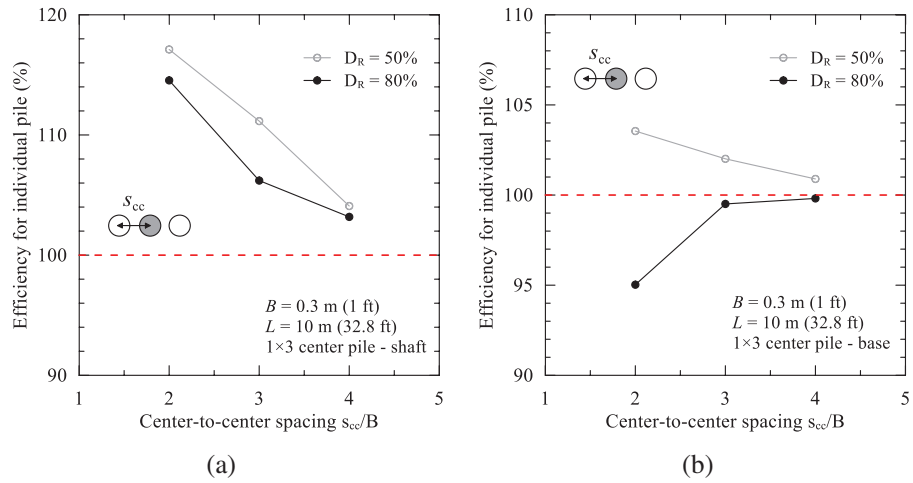


Figure 3.14 Efficiency for (a) the shaft resistance and (b) the base resistance of the center pile in the 1×3 pile group.

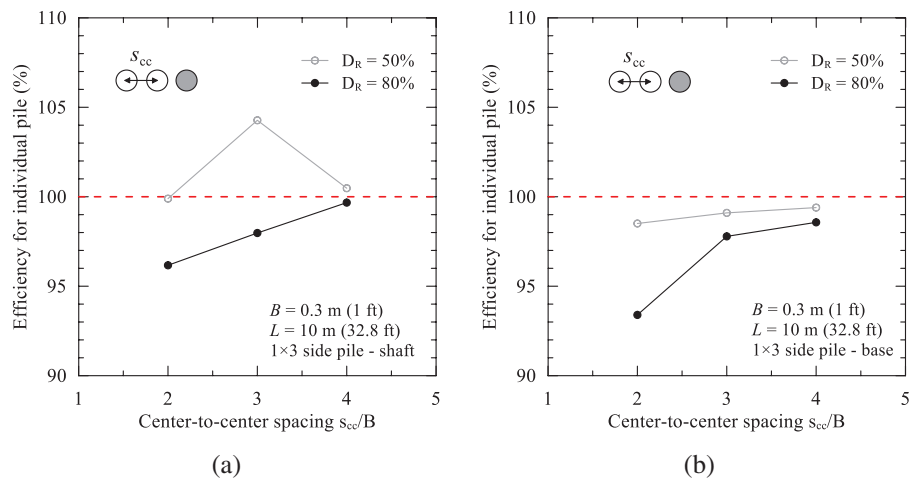


Figure 3.15 Efficiency for (a) the shaft resistance and (b) the base resistance of the side pile in the 1×3 pile group.

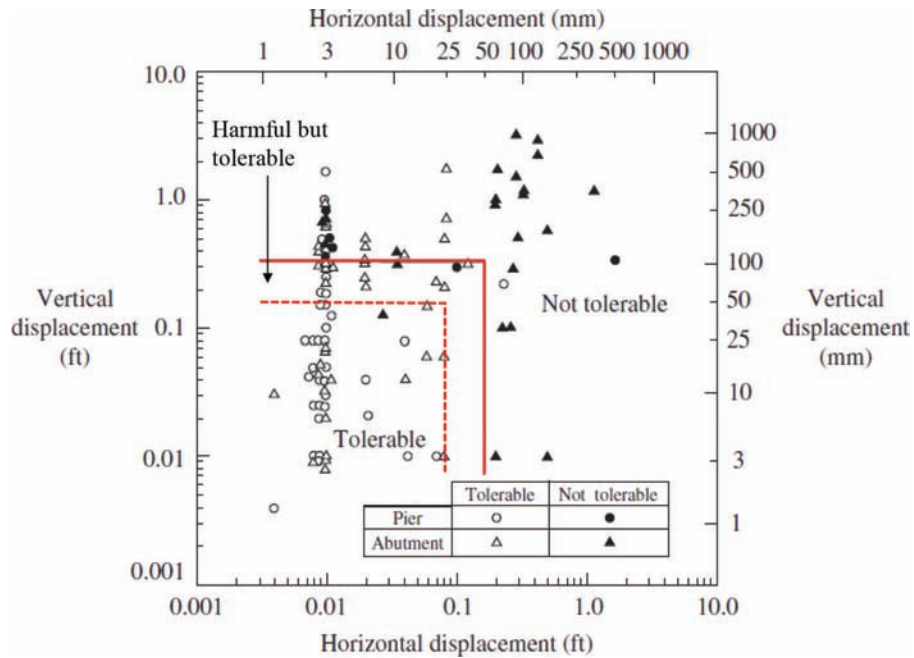


Figure 3.16 Tolerable movements for bridge foundations (Bozozuk, 1978).

will be used as the criterion for the serviceability limit criterion in this report. Group effects, particularly in larger pile groups (e.g., 4 × 4 pile group), will be investigated at various settlement levels up to 50 mm.

3.4.2 Pile Group Configuration

In a 4 × 4 pile group, there are three types of piles: 4 center piles, 8 side piles and 4 corner piles. The responses of any two piles of the same type are identical due to symmetry. Therefore, only three piles, one of each type, will be studied to fully understand the response of a 4 × 4 pile group to axial load. The entire soil-pile domain is symmetric with respect to the three lines of symmetry shown in Figure 3.17. Figure 3.18 shows the simulation domain, which is only one eighth of the entire domain, and the boundary conditions. By considering symmetry, the computational cost of the analyses is greatly reduced.

Figure 3.19 shows the geometric dimensions of the simulation domain and the mesh configuration for the FE analysis of the 4 × 4 pile group with center-to-center spacing, $s_{cc} = 2B$. A total number of 117,713 8-noded, linear brick, hexahedral elements were used in the mesh. Note that in the simulation domain, only one pile of each type is modeled. A vertical velocity of 2 mm/s was applied simultaneously at all pile heads in the pile group until the desired vertical displacement of 50 mm was reached.

3.4.3 Load-Settlement Response

Figure 3.20 shows the load-settlement curves for individual piles in a 4 × 4 pile group in sand with two different densities and those of a single pile placed in

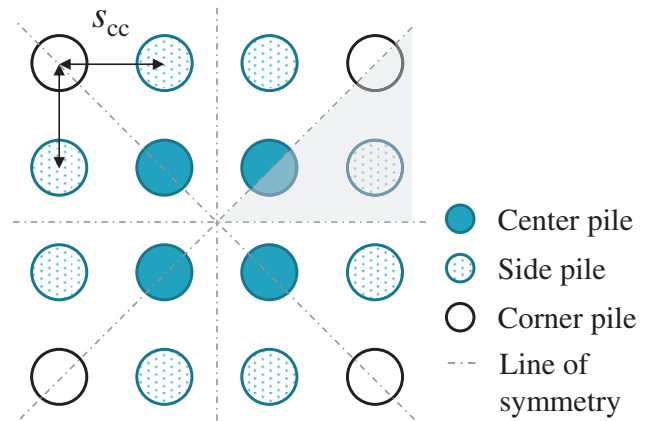


Figure 3.17 The three types of piles and the symmetric conditions in a 4 × 4 pile group.

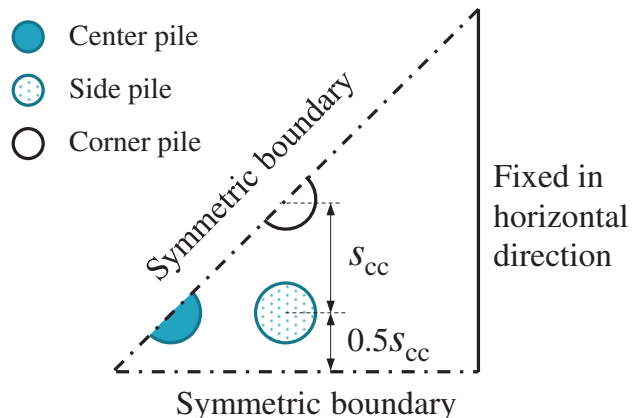


Figure 3.18 The simulation domain and boundary conditions used in the symmetric analysis of the 4 × 4 pile group.

the same soil profiles. The responses of the individual piles to axial load in a large pile group are very different from that of a single pile in the same soil profiles due to greater pile-soil-pile interaction effects. In contrast, in small pile groups, differences in response tend to be less. These effects are dependent on the settlement levels. The resistances developed in individual piles in the pile group are all lower than that developed in a single pile installed in the same soil profile at the beginning of loading. As the settlement increases, the resistances continue to be mobilized in individual piles in the pile group, exceeding that of the single pile.

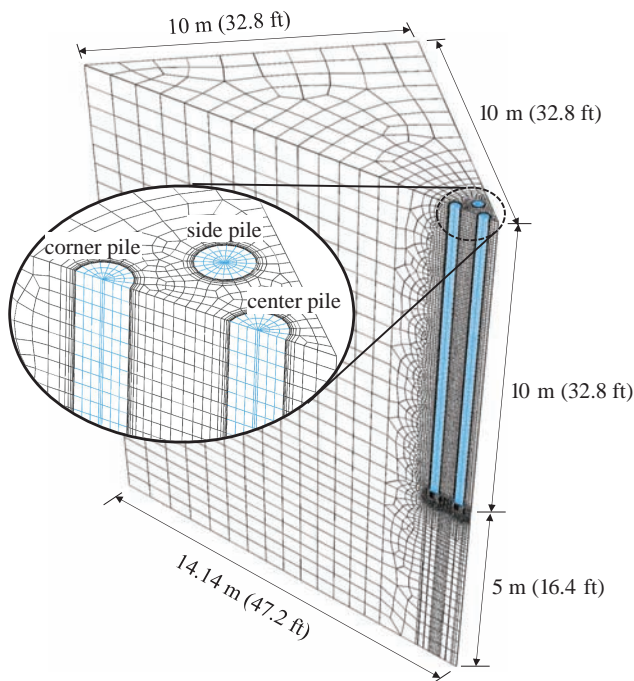


Figure 3.19 Mesh configuration for the three dimensional FE analysis of the 4×4 pile group.

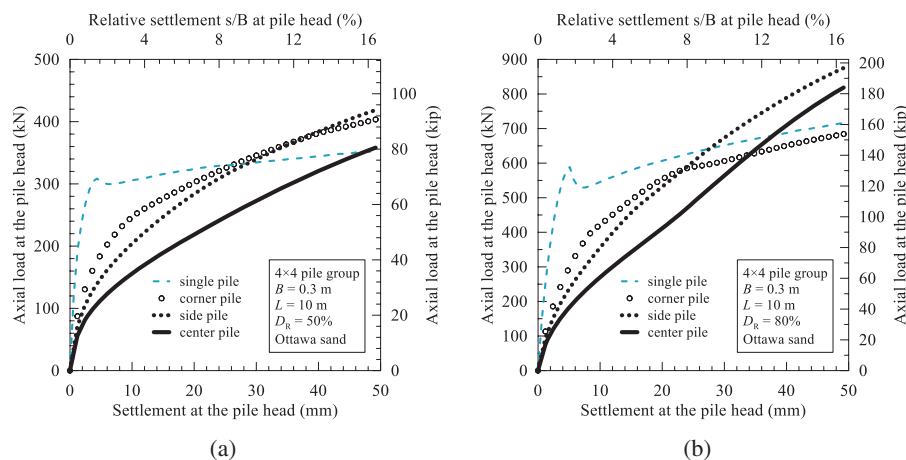


Figure 3.20 Load-settlement curves for a single pile and individual piles in a 4×4 pile group with $s_{cc} = 2B$ installed in: (a) and with $D_R = 50\%$ and (b) sand with $D_R = 80\%$.

3.4.4 Development of the Shaft Resistance

In order to investigate the mobilization of the shaft resistance in individual piles in the 4×4 pile group, Figure 3.21 shows the profiles of the unit shaft resistance mobilized in the three types of individual piles in two different relative densities at different pile head settlements. The profile of the unit shaft resistance developed at $s/B = 10\%$, when the limit shaft resistance is mobilized along the whole length of pile, in a single pile in the same soil profile is also plotted as a reference.

For center piles, the localization of shearing, formation of shear band, in the soil right next to the soil-pile interfaces starts from the two ends of the piles, significantly increasing the unit shaft resistance, to values higher than those that would be developed in a single pile, at these locations. As the settlement continues to increase, the shearing localization moves from the two ends to the middle of the pile. Even at the end of the loading, when $s = 50$ mm, the limit shaft resistance is not fully mobilized in the middle segment of the center piles. Therefore, it can be inferred that the shaft resistance of the center piles will continue to increase, with considerable potential, if the pile group is pushed further into the ground. Among the three types of piles, the corner piles are least affected by the pile-soil-pile interactions, resulting in the most similar profiles of the unit shaft resistance to that of a single pile. The shaft resistance is almost fully mobilized along the pile shaft, leading to very little potential for additional shaft resistance if the pile group is further loaded. The response of the side piles to axial loads is in-between those of the center and corner piles.

3.4.5 Group Efficiency

Figure 3.22 and Figure 3.23 compares the efficiency for both the shaft and base resistances of individual piles in the 4×4 pile group at two different settlements, $s = 30$ mm and $s = 50$ mm. The efficiencies increase as the pile head settlement increases for all cases. When $s = 50$ mm, the efficiency for the shaft resistance is

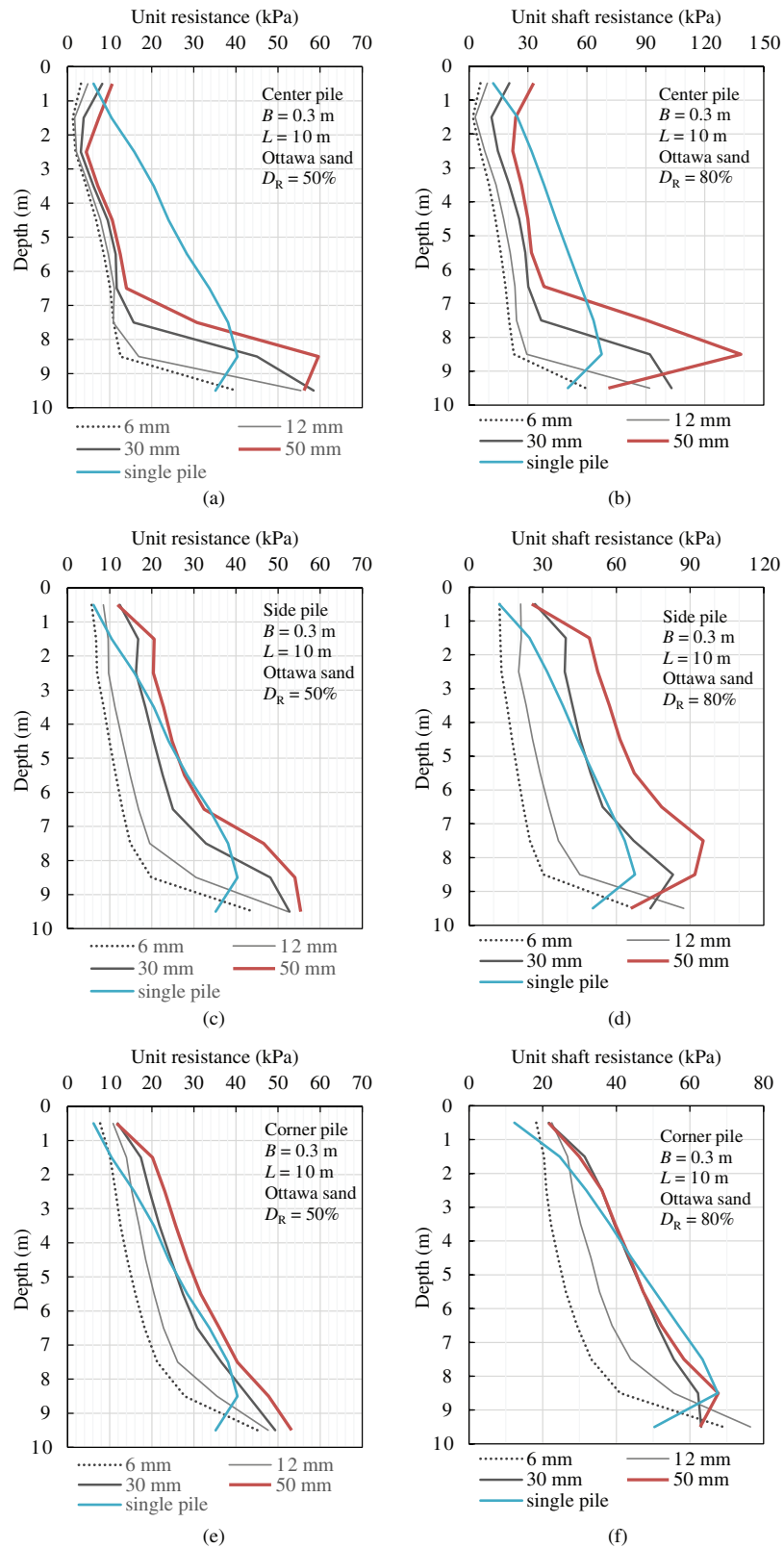


Figure 3.21 Development of the unit shaft resistance in: (a) center pile in sand with $D_R = 50\%$; (b) center pile in sand with $D_R = 80\%$; (c) side pile in sand with $D_R = 50\%$; (d) side pile in sand with $D_R = 80\%$; (e) corner pile in sand with $D_R = 50\%$; (f) corner pile in sand with $D_R = 80\%$ in a 4×4 pile group at different vertical settlements at the pile heads.

generally greater than 100% due to the increasing confining stress in-between piles. Regardless of the relative density, the highest base resistance develops in center piles, while the lowest base resistance develops in the corner piles. Lower efficiencies for the base resistance are found in a denser sand for each type of individual piles.

Table 3.2 summarizes the efficiencies for the shaft resistance, base resistance and total resistance of each individual pile in the 4x4 pile group at two different pile head settlements. The overall group efficiency for the 4x4 pile group is also reported. Generally, higher overall group efficiency for the shaft resistance is found in a denser sand; on the contrary, the

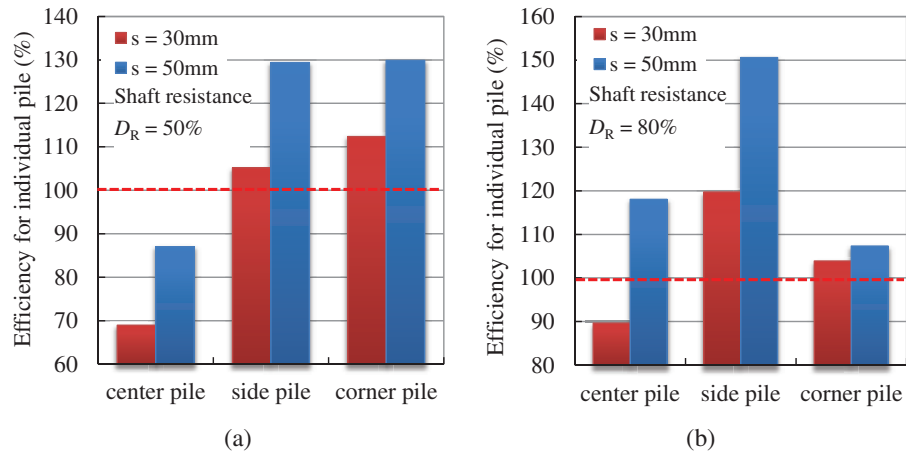


Figure 3.22 Shaft resistance efficiency of individual piles in a 4x4 pile group installed in Ottawa sand with: (a) $D_R = 50\%$ and (b) $D_R = 80\%$ at different settlement levels.

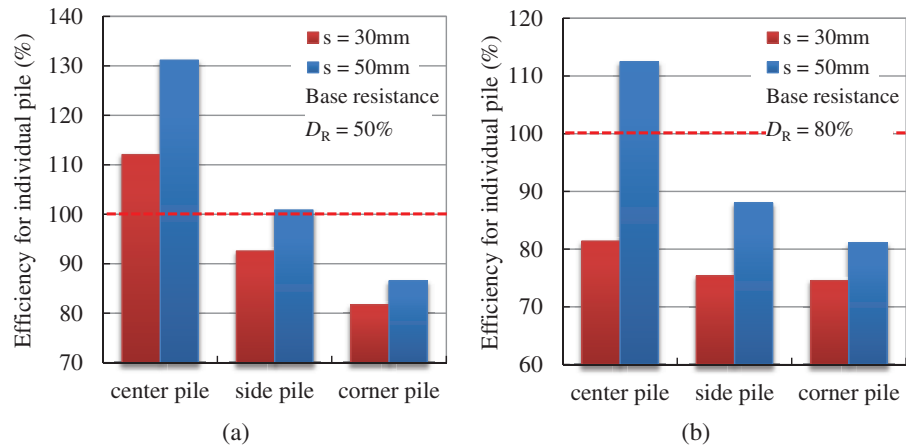


Figure 3.23 Base resistance efficiency of individual piles in a 4x4 pile group installed in Ottawa sand with: (a) $D_R = 50\%$ and (b) $D_R = 80\%$ at different settlement levels.

TABLE 3.2
Efficiency for Individual Piles in a 4x4 Pile Group Installed in Ottawa Sand (%)

		$D_R = 50\%$				$D_R = 80\%$			
		Center pile	Side pile	Corner pile	Group efficiency	Center pile	Side pile	Corner pile	Group efficiency
$s = 30\text{ mm}$	Base	112	93	82	95	81	75	75	77
	Shaft	69	105	112	98	90	120	104	108
	Total	82	101	103	97	87	103	93	97
$s = 50\text{ mm}$	Base	131	101	87	105	112	88	81	92
	Shaft	87	129	130	119	118	151	107	132
	Total	102	119	115	114	116	123	96	114

overall group efficiency for the base resistance is lower in a denser sand. It's interesting to note that the overall group efficiency for total resistance increases from 97% to 114% when the pile head settlement increases from 30 mm to 50 mm in both relative densities.

The analyses of the 4 × 4 pile group can serve as a guide in the design of even larger pile groups (say, a 10 × 10 pile group), since any large pile group consists of center piles, side piles and corner piles, for which the response to loading and mobilization of soil resistances are very different. Thus, piles of different types need to be considered separately for the calculation of the total resistance of a pile in a pile group.

4. NUMERICAL ANALYSES OF SINGLE PILES IN CLAY

4.1 Introduction

Soils that can be classified as clay for the purposes of calculating pile resistance include any soil mixture in which clay or plastic silt dominates. The fraction of clay or plastic silt by weight required for clay to dominate needs not be very large. As little as 10% clay by weight may be sufficient (Salgado, Bandini, & Karim, 2000). Clay dominates if it floats larger particles, so that mechanical response is basically determined by the clay.

In reality, piles in clay are loaded by bridge structures at a rate such that the loading is partially drained but closer to undrained (Basu, Prezzi, Salgado, & Chakraborty, 2014). From a pile design point of view, two types of analyses need to be considered. Undrained analyses, generating a short-term resistance, are used for contractive clays (e.g., NC clay). It is conservative to do so since pile resistance increases with time due to dissipation of positive excess pore pressure. In contrast, fully drained analyses, producing a long-term resistance, are used for dilative clays (e.g., clays with high OCRs). This is conservative since pile resistance decreases with time due to dissipation of negative excess pore pressure. We rely on these simulations and the body of knowledge presently available to update pile resistance estimation equations.

4.2 Finite Element Analysis

4.2.1 Constitutive Model

To simulate axial loading of piles in clay, we used the advanced two-surface constitutive model for clay developed by Chakraborty, Salgado, and Loukidis (2013). The model can capture the mechanical response of clay under multi-axial loading and predicts both drained and undrained behavior from small to large strain levels. The model can also consider the increase in strength at high strain rates and the drop in strength towards a residual value at very large shear strains. The model is formulated in terms of effective stress. Effective stress,

σ'_{ij} , is defined by $\sigma'_{ij} = \sigma_{ij} - u\delta_{ij}$, where σ_{ij} is total stress, u is pore-water pressure and δ_{ij} is Kronecker's delta, equal to 1 if $i = j$, 0 otherwise. In our simulations, the rate of application of load to the pile head after pile installation is high enough to produce an undrained response but sufficiently low for the strain-rate effect on the shear strength of the clay to be negligible. The analyses were, in any case, performed with the rate effects components of the model switched off.

We considered two types of clay—London Clay (LC), which is a high-plasticity clay that has a clear residual state, and Boston Blue Clay (BBC), which is an inorganic clay of low to medium plasticity that does not have a residual state. Table 4.1 shows the model parameters and the values of these parameters used in this study.

4.2.2 Analysis Configurations

The finite-element analyses were performed using ABAQUS/Explicit (SIMULIA, 2012). In order to use the Chakraborty, Salgado, and Loukidis (2013) constitutive model in ABAQUS/Explicit, we developed two user-defined subroutines (VUMAT), which were used for the drained and undrained analyses, respectively, in ABAQUS.

In the undrained analyses, for a given strain increment, the VUMAT updates the stress by adding the updated effective stress to the updated pore water pressure. In fully drained analyses, pore water pressure remains unchanged during loading. The effective stress is updated using the same constitutive relations in both undrained and drained conditions. Pore water pressure is updated by calculating its rate of change, \dot{u} , using:

$$\dot{u} = \frac{K_w}{n} \dot{\epsilon}_v \quad (4.1)$$

where $\dot{\epsilon}_v$ is the volumetric strain rate, K_w is the bulk modulus of water and n is the porosity. During an explicit analysis, the volumetric strain rate is not exactly zero even though the simulation condition is fully undrained. The volumetric strain rate generated during a time increment would correspond to the change in excess pore water pressure given by Equation 4.1. This excess pore water pressure is then added to the pore pressure in the subsequent time increment to suppress the change in volumetric strain during the following time step. This process happens for very small time increments, so the cumulative volumetric strain for the whole simulation is essentially zero.

Porosity, n , can be calculated from $n = e_0 / (1 + e_0)$, where e_0 is the initial void ratio of the clay. Since no drainage and no volume change occurs during loading, n is current throughout the analysis. We assumed K_w to be 2.2GPa ($= 3.2 \times 10^5$ psi) in this study based on Halliday, Resnick, and Walker (2010).

The pile is assumed to be linear with Young's modulus, E , equal to 20 GPa ($= 2.9 \times 10^6$ psi), and Poisson's ratio, ν , equal to 0.2. We assumed non-slip contact between the pile and soil.

TABLE 4.1
List of Parameters Used in the Simulations for Clays.

Model components	Parameters	Parameter values		Test data required
		LC	BBC	
Small-strain (elastic) Poisson's ratio	ν	0.25	0.25	Test using local strain transducers or isotropic consolidation or 1D consolidation with unloading
G_0 correlation parameter	C_g	100	250	Bender element or resonant column tests
Elastic Moduli with degradation (G and K)	ζ	10	5	Isotropic consolidation or 1D consolidation
	κ	0.064	0.036	Isotropic consolidation or 1D consolidation
Normal consolidation line	N	1.07	1.138	Isotropic consolidation or 1D consolidation
	λ	0.168	0.187	Isotropic consolidation or 1D consolidation
Stress anisotropy	$K_{0,NC}$	0.6	0.53	1D consolidation
Shear strength	M_{cc}	0.827	1.305	Triaxial compression tests
	n_s	0.2	0.2	Simple shear or other plane-strain tests
	k_b	0.0	0.0	Triaxial compression tests
	ρ	2.5	2.7	Triaxial compression tests
Dilatancy surface	D_0	1	1	Triaxial compression tests
Flow rule	c_2	0.95	0.95	Simple shear or other plane-strain tests
	ξ	0.31	0.31	1D consolidation followed by unloading to zero deviatoric stress and isotropic consolidation
Hardening	h_0	1.1	1.1	Triaxial compression tests
Residual state	$M_{r,min}$	0.33	—	Ring shear tests
	b_r	0.05	—	Ring shear tests
	Y	0.015	—	Ring shear tests
Yield surface	m	0.05	0.05	

Figure 4.1(a) and (b) show the mesh configuration and boundary conditions for 2D and 3D finite-element analyses, respectively. 4-noded, quadrilateral elements are used for axisymmetric simulation in 2D analysis. 8-noded, brick elements and 6-noded wedge elements are used in the 3D analyses. We consider a 10-m-long (33-ft-long) pile with pile diameter $B = 0.3$ m (= 1.0 ft).

To capture the formation of a shear band in clay near the pile shaft, the thickness of the smallest element next to the pile shaft should match the thickness of the shear band in clay for linear finite elements. According to Chakraborty, Salgado, Basu, et al. (2013), despite clear evidence of the formation of shear bands in clays, the thickness of shear band in clay has not been well defined. Morgenstern and Tchalenko (1967, 1969) observed shear band thicknesses in clay in the 3–4 mm range using direct shear tests on kaolin clay through microscope photographs. Thakur (2007, 2011) measured the shear band as 3–5 mm using particle image velocimetry (PIV) in plane-strain compression tests on a Norwegian quick clay. Andresen and Jostad (2002), Puzrin, Alonso, and Pinyol (2010), and Stamatopoulos and Balla (2010) assumed shear band thickness values to be in the 3–5 mm range. In this study, we assumed the shear band thickness in clay to

be 4 mm (= 0.16 in) and used 4-mm-thick element next to the pile shaft.

To estimate the sensitivity of the results to element size, we performed analyses for 2, 3, 4, and 5-mm-thick elements next to the pile shaft for London clay in axisymmetric analyses. We used 17 kN/m³ (= 108 lb/ft³) for the unit weight of clay. Table 4.2 shows base, shaft and total resistances of the pile at 10% of pile diameter of pile head settlement with various soil-pile interface element thickness. The shaft resistance increases as the interface element thickness increases, but not significantly. The maximum variation in shaft resistance is 6%. No change in base resistance is observed.

The initial soil unit weight, γ_0 , is estimated using:

$$\gamma_0 = \frac{G_s + S e_0}{1 + e_0} \gamma_w \quad (4.2)$$

where G_s is specific gravity of soil solid particles, S is degree of saturation of soil, e_0 is the initial void ratio of soil, and γ_w is the unit weight of water (= 9.81 kN/m³ = 62.5 lb/ft³). According to Ou (2006), $G_s = 2.74$ for London Clay (LC) and 2.775 for Boston Blue Clay (BBC). We assumed that the groundwater table is located at the ground surface and that the clay is fully saturated ($S = 1$). The initial void ratio, e_0 , is estimated using:

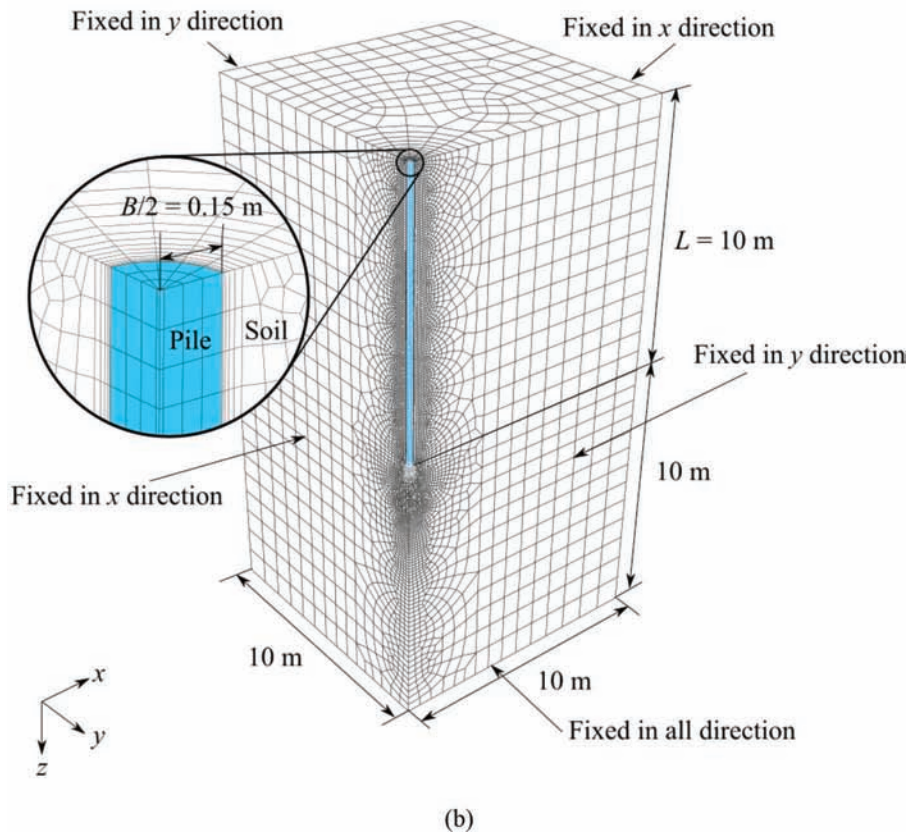
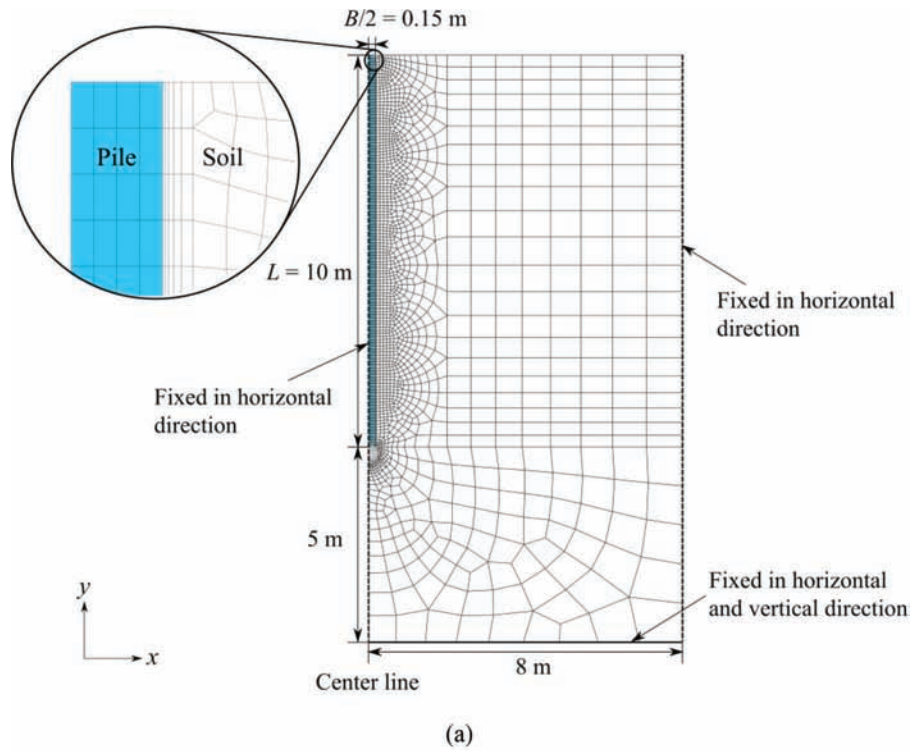


Figure 4.1 Mesh configuration and boundary conditions for (a) 2D and (b) 3D FE analyses where L = pile length and B = pile diameter.

TABLE 4.2

Base, Shaft and Total Resistance of Pile at 10%-*B* of Pile Top Settlement with Various Soil-Pile Interface Element Thickness, where *B* = Pile Diameter.

Interface element thickness (mm (in))	Base resistance (kN (kips))	Shaft resistance (kN (kips))	Total resistance (kN (kips))
2 (0.08)	6 (1.3)	61 (13.7)	67 (15.1)
3 (0.12)	6 (1.3)	63 (14.2)	69 (15.5)
4 (0.16)	6 (1.3)	63 (14.2)	69 (15.5)
5 (0.20)	6 (1.3)	65 (14.6)	71 (16.0)

$$e_0 = N - \lambda \ln\left(\frac{p'_c}{p_A}\right) + \kappa \ln(\text{OCR}) \quad (4.3)$$

where *N* is the void ratio of the clay at the reference pressure $p_A = 100$ kPa (= 14.5 psi), λ and κ are the slopes of the normal consolidation line and unloading-reloading lines in the $e - \ln(p')$ plane, p'_c is the preconsolidation pressure, and OCR is the overconsolidation ratio in terms of mean effective stresses. OCR is defined by p'_c / p'_o , where p'_o is the initial mean effective stress. Figure 4.2 shows e_0 and γ_0 profiles for normally consolidated (NC) London Clay. As shown in Figure 4.2, e_0 and γ_0 vary with depth because e_0 is a function of the initial mean effective stress. In this study, for simplicity, we used an average γ_0 for clay deposits with the same OCR throughout the profile. When we compared the results from FE analyses with results from analysis considering a varying soil unit weight with depth for NC clay, the results were almost the same. The difference between the total resistances of the pile being less than 1%.

The coefficient, K_0 , of earth pressure at rest is assumed to be 0.6 for normally consolidated (NC) LC and 2.28 for overconsolidated (OC) LC with OCR = 10 based on 1D consolidation simulation results

performed by using the Chakraborty, Salgado, and Loukidis (2013) constitutive model. K_0 is defined by $\sigma'_{ho} / \sigma'_{vo}$, where σ'_{ho} is initial horizontal effective stress and σ'_{vo} is initial vertical effective stress. We assumed $K_0 = 0.6$ for NC BBC based on 1D consolidation simulation results performed by using the Chakraborty, Salgado, and Loukidis (2013) constitutive model.

The ultimate resistance is defined as the load required to cause a pile head settlement equal to 10% of the pile diameter *B* (Fleming et al., 2008; Jardine et al., 2005; Lehane et al., 2005; Randolph, 2003; Salgado, 2008).

4.3 Analyses Results

4.3.1 Base Resistances

Figure 4.3 shows axisymmetric analysis results for a 10-m-long (33-ft-long) single pile with pile diameter $B = 0.3$ m (=1 ft) installed in normally consolidated London Clay when the pile head settles 30 mm (= 0.1 ft = 1.2 in = 10% of *B*). Figure 4.3(a)–(d) presents contours of shear strain, ϵ_{xy} , shear stress, σ_{xy} , equivalent plastic strain, $\epsilon^p_{eq} = (2 \epsilon^p_{ij} \epsilon^p_{ij} / 3)^{1/2}$, where ϵ^p_{ij} represents the plastic strain components and plastic

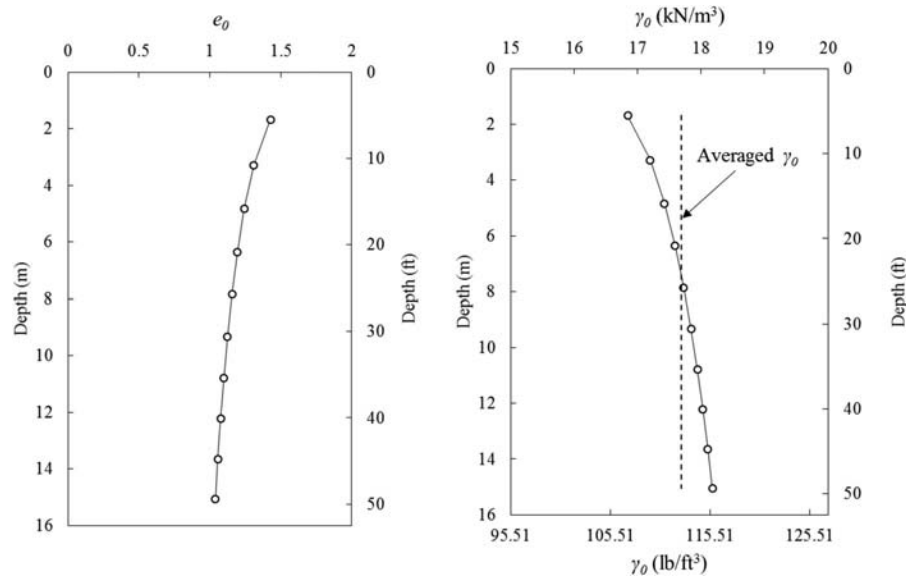


Figure 4.2 Initial void ratio, e_0 , and initial soil unit weight, γ_0 , profiles for normally consolidated London clay.

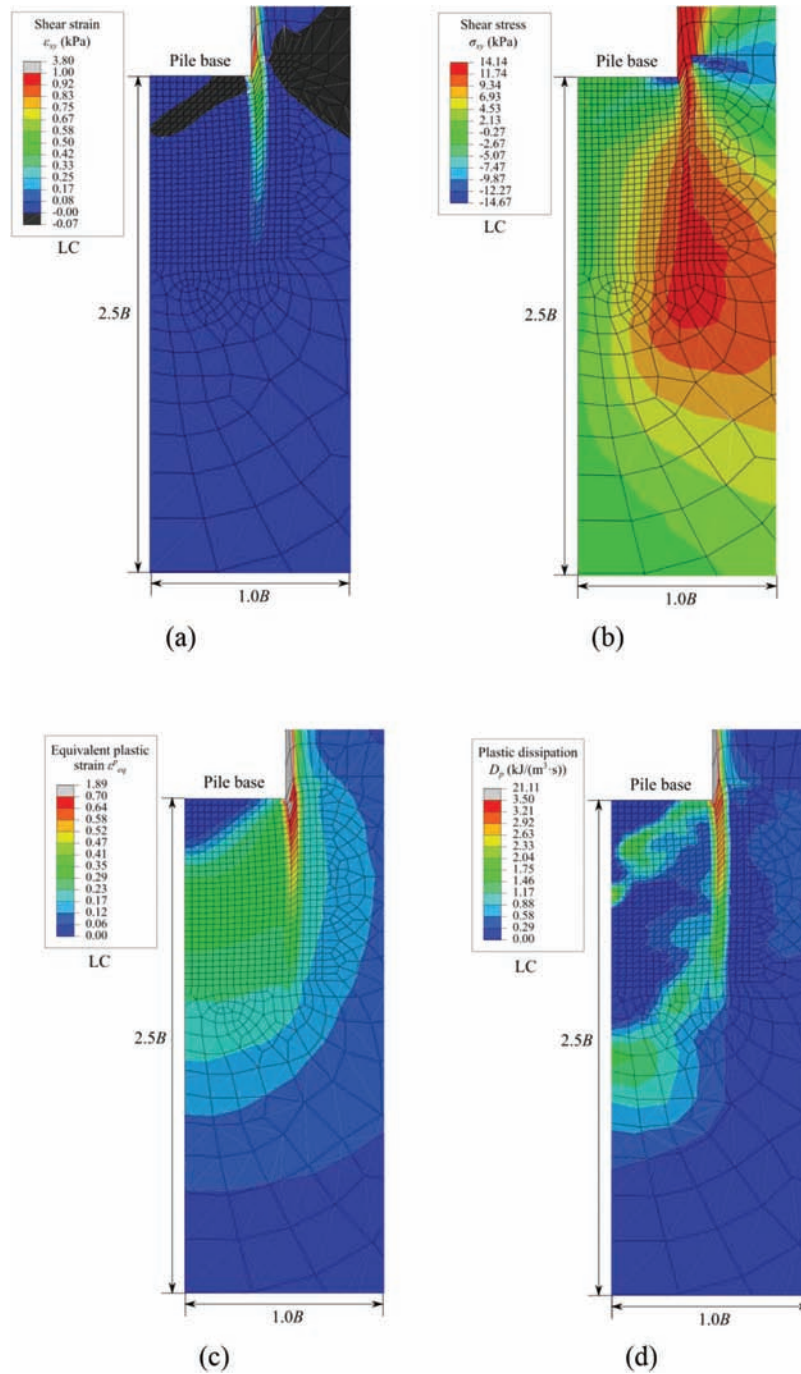


Figure 4.3 Contours of (a) shear strain, ϵ_{xy} (b) shear stress, σ_{xy} (c) equivalent plastic strain, ϵ^p_{eq} (d) plastic dissipation, D_p , in normally consolidated London Clay near pile base at 10% of relative settlement at pile head.

dissipation, D_p , corresponding to that settlement level. D_p is defined as $\sigma_{ij}\dot{\epsilon}^p_{ij}$ where $\dot{\epsilon}^p_{ij}$ represents the plastic strain rate tensor components. The void ratio of the soil does not change during loading under fully undrained conditions.

The contour lines of shear strain shown in Figure 4.3(a) suggest full development of shear bands along the shaft of the pile and along the vertical surface that is roughly a continuation of the pile lateral surface down to a depth of approximately one diameter below

the pile base. There is also an incipient shear band bounding a roughly conical surface that forms below the pile base. Figure 4.3(b) shows that shear stress develops locally in a way that is consistent with the generated shear strain around the pile base.

Figure 4.3(c) shows, like Figure 4.3(a), that plastic strain develops along the pile shaft and along the vertical surface extending approximately vertically from the corner of the pile base where the shear strain is concentrated. Below the pile base, there is almost no

plastic strain generated within a conical wedge of soil below the pile base, which means that this cone-shaped soil volume in contact with the pile base behaves almost like an elastic material that is attached to the pile. Some plastic strain is observed immediately below it, but no strong localization is observed.

The plastic dissipation plot shown in Figure 4.3(d) provides a more clear indication that a shear band is already in the process of forming that will create a cone

of soil attached to the pile base that will move with the pile at plunging. There is also some plastic dissipation further down below that resembles already the type of “shear mechanism” we often see in connection with foundation plunging conditions.

Figure 4.4(a)–(d) show contours of shear strain, ε_{xy} , shear stress, σ_{xy} , equivalent plastic strain, ε_{eq}^p , and plastic dissipation, D_p corresponding to that settlement level. The void ratio of the soil does not change during

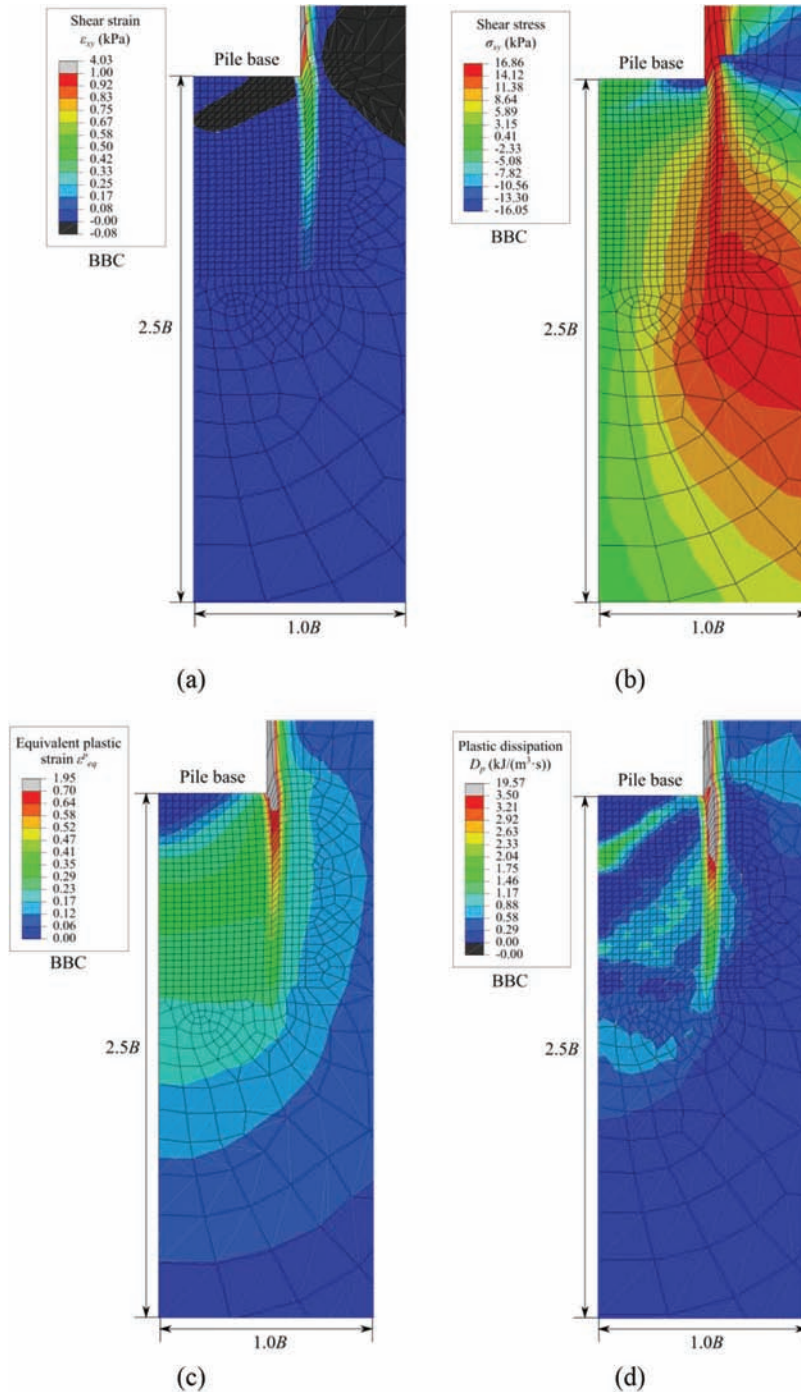


Figure 4.4 Contours of (a) shear strain, ε_{xy} (b) shear stress, σ_{xy} (c) equivalent plastic strain, ε_{eq}^p (d) plastic dissipation, D_p , in normally consolidated Boston Blue Clay near pile base at 10% of relative settlement at pile head.

loading because the simulation is fully undrained. The contours of shear strain, shear stress, equivalent plastic strain and plastic dissipation resemble closely those for London Clay shown in Figure 4.3.

Figure 4.5 shows plots of base resistance with respect to the relative settlement for 10-m-long (33-ft-long) non-displacement piles with diameter equal to 0.3 m (= 1 ft) installed in normally consolidated London Clay and normally consolidated Boston Blue Clay. The base resistance of the pile installed in BBC is greater than that in LC. The ultimate base resistances of the piles installed in LC and BBC are 6.6 kN (= 1.5 kips) and 8.9 kN (= 2.0 kips), respectively. In this chapter, base resistance, $Q_{b,ult}$, is defined as the net ultimate unit base resistance, $q^{net}_{b,ult}$, multiplied by the cross-sectional area of pile base. Ultimate unit base resistance is defined by $q_{b,ult} - q_0$, where $q_{b,ult}$ is ultimate unit base resistance and q_0 is the surcharge (total stress at the pile base level). Figure 4.5 shows that base resistance increases with settlement at a high rate as the relative settlement of the pile head approaches 2% and then continues to increase, but at a lower rate. Because the piles are much stiffer than clay, the load applied at the pile head transfers to the pile base almost directly. The settlements of the pile head and pile base are almost the same during loading, with pile compression minimal during loading.

Figure 4.6 shows plots of base resistance with respect to the relative settlement for 10-m-long (33-ft-long) nondisplacement piles with diameter equal to 0.3 m (= 1 ft) installed in overconsolidated London Clay with overconsolidation ratio, OCR, equal to 10. As for highly overconsolidated clays, negative excess pore pressure is generated during loading due to dilative behavior of the soil; after dissipation of excess pore pressure, the resistance of the pile would decrease. To be conservative, for highly overconsolidated clays, we performed analyses under fully drained conditions. The obtained ultimate

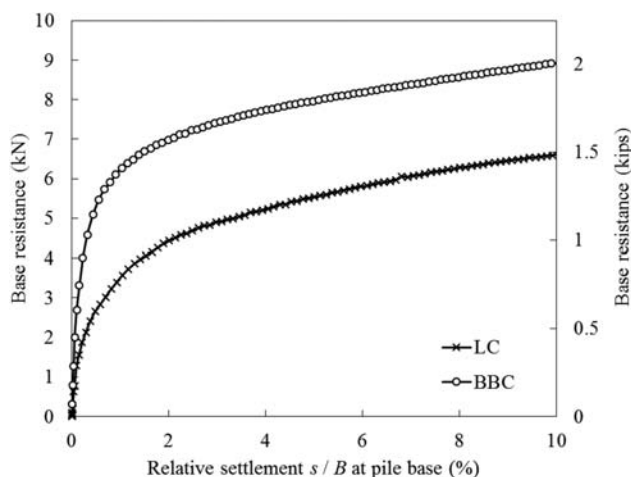


Figure 4.5 Base resistances of 10-m-long (33-ft-long) non-displacement piles with 0.3 m (= 1 ft) diameter installed in normally consolidated London Clay (LC) and normally consolidated Boston Blue Clay (BBC)

base resistances is 54.5 kN (= 12.3 kips). Figure 4.6 shows that base resistance increases with settlement monotonically until the relative settlement reaches to 10%. Similar to results for normally consolidated clays, the load applied at the pile head transfers to the pile base almost directly, so the settlements of the pile head and pile base are almost the same during loading, with pile compression minimal during loading.

Equations for net ultimate unit base resistance, $q^{net}_{b,ult}$, for piles in clay typically use a ratio, N_c , between $q^{net}_{b,ult}$ and undrained shear strength, s_u , of the clay near the pile base. N_c would range from 9 to 10 based on experimental results according to Meyerhof (1951). Salgado (2008) proposed the use of 9.6 as N_c for drilled shafts, nondisplacement piles, in clay based on Hu and Randolph (2002). In order to obtain the value of N_c from our analyses for 10% relative settlement, we performed elemental simulations of triaxial compression (TXC) tests on NC LC and NC BBC samples consolidated isotropically to a confining pressure equal to the mean effective stress at the pile base using the constitutive model developed by Chakraborty, Salgado, and Loukidis (2013). The resulting values of s_u are 12.71 kPa (= 1.84 psi) for NC LC, 16.35 kPa (= 2.37 psi) for NC BBC and 130.6 kPa (= 18.9 psi) for highly OC LC with OCR = 10. Table 4.3 compares $q^{net}_{b,ult}$ and N_c obtained from axisymmetric FE analyses with the value of N_c proposed by Hu and Randolph (2002) and the corresponding value of $q^{net}_{b,ult}$. N_c obtained from the FE analyses are 7.3, 7.7 and 5.9 for NC LC, NC BBC and OC LC, respectively. These values of N_c are about 24%, 20% and 39% lower than the value that has been assumed in the past.

It is likely that FE analysis underestimates the base resistance that would be available to a foundation in a real structure. After 10% of relative settlement of the pile head, we found that positive excess pore water pressure developed below the pile base in both NC clays and negative excess pore water pressure developed in highly OC clays under fully undrained conditions. As

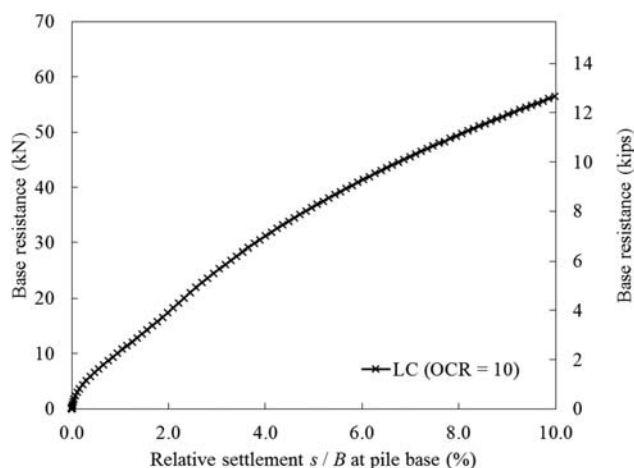


Figure 4.6 Base resistances of 10-m-long (33-ft-long) non-displacement piles with 0.3 m (= 1 ft) diameter installed in overconsolidated London Clay (LC) with OCR = 10.

TABLE 4.3

Comparison of Unit Base Resistances for Single Pile in NC LC and NC BBC Obtained from FE Analysis and Design Method (Salgado, 2008).

Clay type	FE analysis result		Design method (Salgado, 2008)	
	$q^{net}_{b,ult}$ (kPa (psi))	N_c	$q^{net}_{b,ult}$ (kPa (psi))	N_c
NC LC	93 (14)	7.3	122 (18)	9.6
NC BBC	126 (18)	7.7	157 (23)	9.6
OC LC (OCR = 10)	770 (112)	5.9	1241 (180)	9.6

NC LC = normally consolidated London Clay.

NC BBC = normally consolidated Boston Blue Clay.

$q^{net}_{b,ult}$ = net ultimate unit base resistance.

for NC clays, as positive excess pore water pressure dissipates, the clay consolidates and becomes stronger. As for OC clays, as negative excess pore water pressure dissipates, the clay dilates and becomes weaker. By simulating fully undrained conditions for NC clays and fully drained condition for OC clay, we could obtain the lowest resistances of the pile. Depending on the rate of dissipation of excess pore water pressure, the base resistance of a drilled shaft would exceed the values calculated using $N_c = 7.3, 7.7$ or 5.9 .

4.3.2 Shaft Resistances

Figure 4.7 shows the development of total shaft resistances for a 10-m-long (33-ft-long) nondisplacement pile with 0.3 m (= 1 ft) diameter embedded in normally consolidated London Clay (LC), normally consolidated Boston Blue Clay (BBC) and overconsolidated London Clay (LC) with OCR = 10. In NC clays, the shaft resistance response is very stiff until it reaches a peak value at about 1% relative settlement for LC and about 0.5% relative settlement for BBC. In highly OC clay, the shaft resistance increases slowly and reaches a peak value at about 3% of relative settlement. After the peak, the shaft resistance stabilizes for the three piles, with a slight increase with increasing settlement for BBC and a slight decrease with increasing settlement for LC; In OC LC, it decreases more compared with the shaft resistance in NC LC. This drop in resistances for NC and highly OC LC is because, after reaching critical state, the shear strength of LC continuously decreases as it transitions to its residual state at large strain levels. The increase in shaft resistance of the pile in NC BBC is caused by arching effects below the pile base. The ultimate shaft resistances, Q_{sL} , of the pile in NC LC, NC BBC and OC LC are 60 kN (= 13.5 kips), 77 kN (=17.3 kips) and 342 kN (= 77 kips), respectively.

Figure 4.8 shows profiles of axial load, unit shaft resistance and excess pore water pressure along depth for a nondisplacement pile with $L = 10\text{m}$ (= 33 ft) and $B = 0.3\text{m}$ (= 1 ft) installed in NC LC for different values of relative settlement of the pile head (0.5%, 1%, 2%, 3% and 10%). Figure 4.8(a) are load transfer curves, which show the distribution of axial loads with depth. After the peak shaft resistance at 1% relative

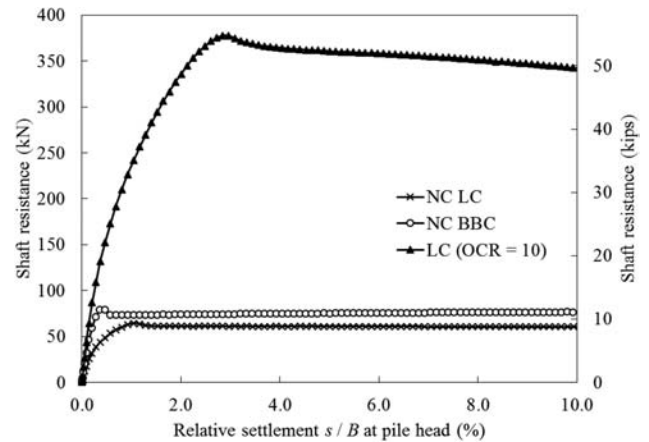


Figure 4.7 Total shaft resistance of nondisplacement pile in normally consolidated London Clay (LC), normally consolidated Boston Blue Clay (BBC) and overconsolidated London Clay (LC) with OCR = 10 versus relative settlement at pile head.

settlement, the clay, in general, softens and stabilizes at around 2% relative settlement. After that, the load transfer curve shifts slightly to the right side parallelly as only the base resistance increases. The development of the unit shaft resistance along depth shown in Figure 4.8(b) is consistent with the curve of total shaft resistance with respect to relative settlement for LC in Figure 4.7. The unit shaft resistance increases along the entire pile length until a peak develops at around 1% relative settlement, after which the unit shaft resistance decreases slightly and then stabilizes. Figure 4.8(b) also shows unit shaft resistance along depth calculated from the equation for drilled shafts in clay proposed by Chakraborty, Salgado, Basu (2013):

$$q_{sL} = \alpha s_u \quad (4.4)$$

$$\alpha = \left(\frac{s_u}{\sigma'_{v0}} \right)^{-0.05} \left[A_1 + (1 - A_1) \exp \left\{ - \left(\frac{\sigma'_{v0}}{p_A} \right) (\phi_c - \phi_{r,min})^{A_2} \right\} \right] \quad (4.5)$$

where ϕ_c is critical-state friction angle, $\phi_{r,min}$ is the minimum residual-state friction angle, $A_1 = 0.4$

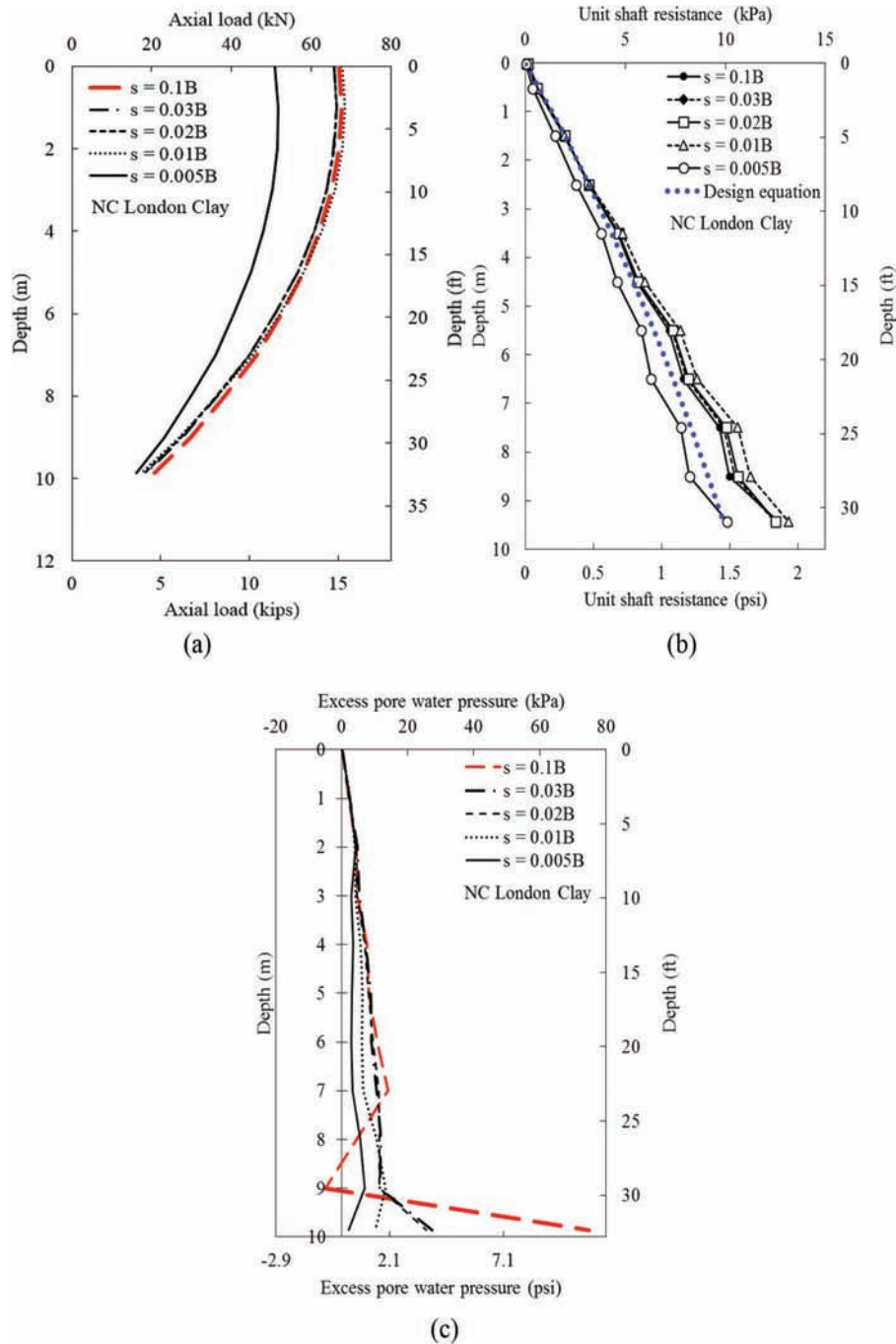


Figure 4.8 Profiles of (a) cross-sectional load, (b) unit shaft resistance and (c) excess pore water pressure along depth at several relative settlement levels for nondisplacement pile with $L = 10$ m ($= 32.8$ ft) and $B = 0.3$ m ($= 1$ ft) in NC LC.

for $\phi_c - \phi_{r,min} = 12^\circ$, $A_1 = 0.75$ for $\phi_c - \phi_{r,min} = 5^\circ$, and A_2 is given by:

$$A_2 = 0.4 + 0.3 \ln \left(\frac{s_u}{\sigma'_{v0}} \right) \quad (4.6)$$

The undrained shear strength, s_u , in Equation 4.4 is defined as the critical-state s_u obtained from isotropically consolidated, undrained TXC tests with the

confining pressure equal to the mean effective stress at the depth under consideration. Accordingly, we obtained s_u near the pile by performing several elemental simulations of undrained TXC tests after isotropic consolidation along the pile using the constitutive model developed by Chakraborty, Salgado, and Loukidis (2013). Simulation results for NC LC yielded a constant value of $ds_u/d\sigma'_{v0} = 0.17$. The unit shaft resistance calculated using the design equation

matches reasonably closely the simulation results for most of the pile length, underpredicting the value from the simulations by 20% or less for depths near the pile base.

Figure 4.8(c) shows depth profiles of excess pore water pressure for relative settlement of the pile head equal to 0.5%, 1%, 2%, 3% and 10%. Until shaft resistance reaches critical state, excess pore water pressure gradually increases for all depths. After reaching critical state, excess pore water pressure seems to stabilize at overall depth. After that, as base resistance

increases, the excess pore water pressure around the pile base increases due to the compressive behavior of soil.

Figure 4.9 shows profiles of axial load unit shaft resistance and excess pore water pressure along depth for a single pile with $L = 10\text{ m}$ ($= 33\text{ ft}$) and $B = 0.3\text{ m}$ ($= 1\text{ ft}$) installed in NC BBC at different relative settlements (0.5%, 1%, 2%, 3% and 10%) at the pile head. The load transfer curves (Figure 4.9(a)) show the distribution of axial loads along the depth at different relative settlements. After the peak shaft resistance at 0.5% relative settlement, the shaft resistance reaches

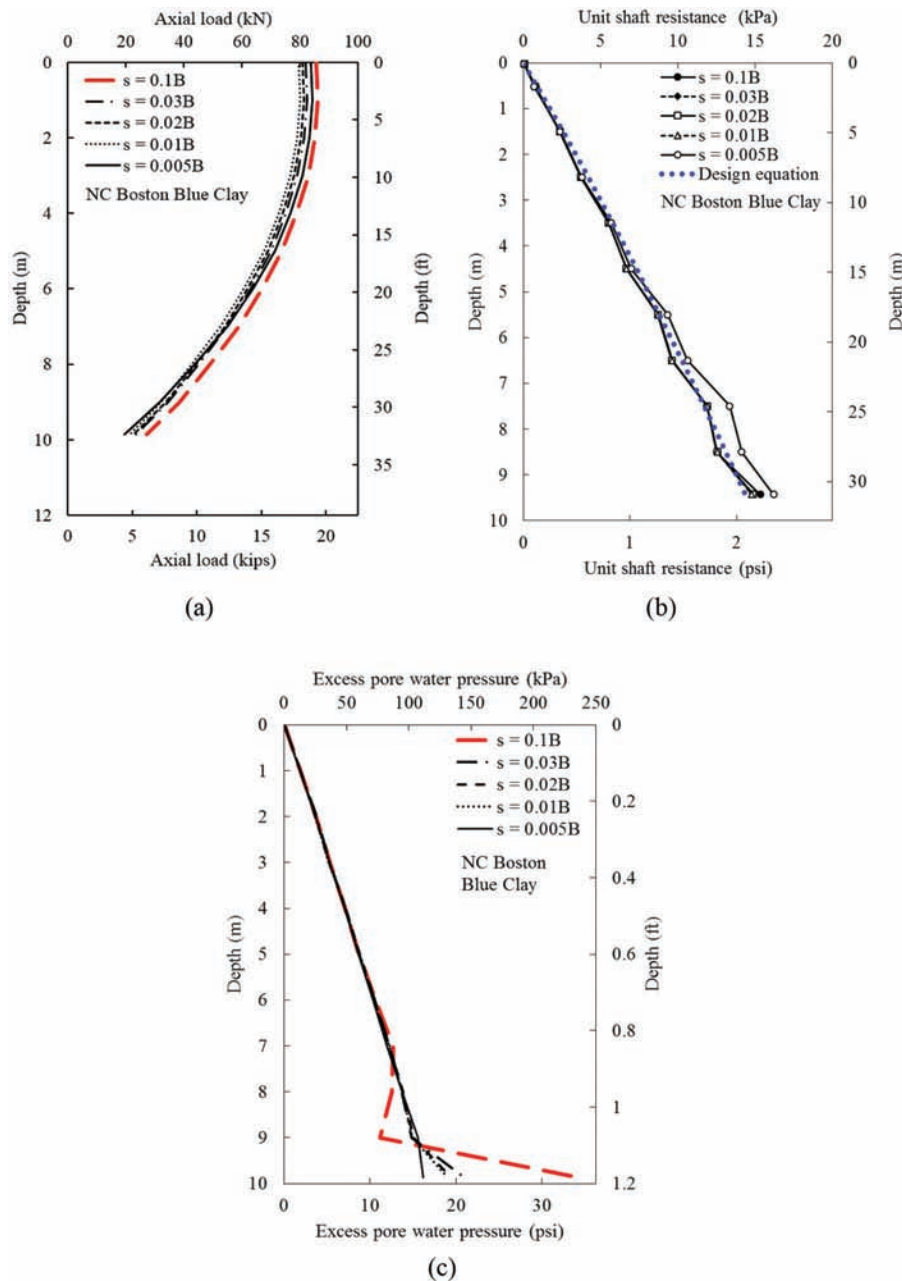


Figure 4.9 Profiles of (a) cross-sectional load, (b) unit shaft resistance and (c) excess pore water pressure along depth at several relative settlement levels for nondisplacement pile with $L = 10\text{ m}$ ($= 33\text{ ft}$) and $B = 0.3\text{ m}$ ($= 1\text{ ft}$) in NC BBC.

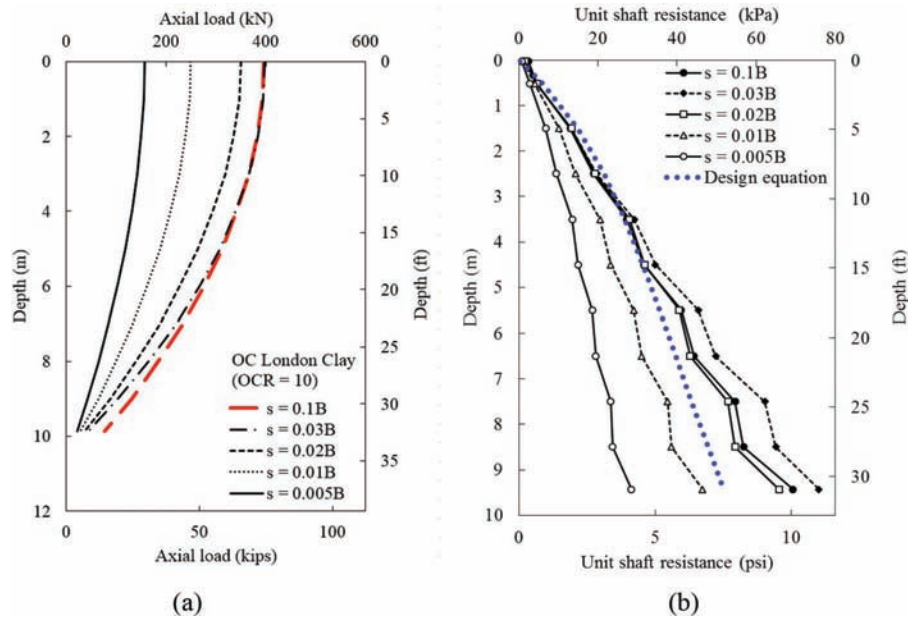


Figure 4.10 Profiles of (a) cross-sectional load and (b) unit shaft resistance along depth at several relative settlement levels for nondisplacement pile with $L = 10$ m (= 33 ft) and $B = 0.3$ m (= 1 ft) in OC LC with OCR = 10.

critical state, which means it is fully mobilized. After that, the load transfer curve shifts to the right as only the base resistance increases. Figure 4.9(b) shows that the unit shaft resistance increases at all depths until a relative settlement of approximately 0.5% is reached, after which the unit shear resistance decreases at all depths before it finally stabilizes. Because BBC does not have a residual state, the unit shaft resistance does not decrease after the soil reaches its critical state along the pile. A very slight increase in unit shaft resistance happens near the pile base due to arching effects around the pile base. Figure 4.9(b) also shows unit shaft resistance calculated from the design equation for drilled shafts in clay (Chakraborty, Salgado, Basu, et al., 2013). The undrained shear strength s_u is calculated by performing elemental simulations for TXC tests after isotropic consolidation using the constitutive model developed by Chakraborty, Salgado, and Loukidis (2013). Based on the simulation results for isotropically consolidated soils with a consolidation stress equal to the mean effective stress in the soil along the depth, we obtain a value of $ds_u/d\sigma'_{v0} = 0.217$ for NC BBC. The unit shaft resistances obtained from the FE analysis and from the design equation are very close along the entire pile length.

Figure 4.9(c) shows a profile of excess pore water pressure along depth at different pile head relative settlements (0.5%, 1%, 2%, 3% and 10%). The excess pore water pressure increases until the shaft resistance reaches critical state at about 0.6% of relative settlement. After that, it stabilizes. After shaft resistance is fully mobilized, as base resistance increases, the excess pore water pressure around the pile base increases significantly, which means that the total mean stress increases in the soil are large. Around $3 \sim 9B$ above the

pile base, the excess pore water pressure decreases as a result of a dilative response.

Figure 4.10 shows profiles of axial load and unit shaft resistance along depth for a single pile with $L = 10$ m (= 33 ft) and $B = 0.3$ m (= 1 ft) installed in OC LC with OCR = 10 for different relative settlements (0.5%, 1%, 2%, 3% and 10%) for the pile head. The load transfer curves (Figure 4.10(a)) show the distribution of axial loads along the depth at different relative settlements. After the peak shaft resistance at 3% relative settlement, the clay at shallow depth softens and stabilizes. After that, the axial loads at the pile head remain almost the same. The base resistance increases and the shaft resistance decreases after that. The development of the unit shaft resistance along depth shown in Figure 4.10(b) is consistent with the curve of total shaft resistance with respect to relative settlement for OC LC in Figure 4.7. The unit shaft resistance increases along the entire pile length until a peak at around 3% relative settlement. Figure 4.10(b) also shows unit shaft resistance calculated from the design equation for drilled shafts in clay (Chakraborty, Salgado, Basu, et al., 2013). The undrained shear strength, s_u , is calculated by performing elemental simulations for TXC tests after isotropic consolidation using the constitutive model developed by Chakraborty, Salgado, and Loukidis (2013). Based on the simulation results for isotropically consolidated soils with a consolidation stress equal to the mean effective stress in the soil along the depth, we obtain a value of $ds_u/d\sigma'_{v0} = 1.73$ for OC LC when OCR = 10. The unit shaft resistances obtained from the FE analysis and from the design equation are reasonably close. The design equation underpredicts the value from the simulations by 25% or less for depths near the pile base.

In both FE analyses for single pile in NC LC and NC BBC, the overall excess pore water pressure near both the pile shaft and base was positive at 10% relative settlement. As these excess pore water pressures dissipate, pile resistances will increase over time, so that the pile resistances calculated using the FE analyses presented in this chapter and the values calculated using the α method with α given by Equation 4.5 are conservative and can be directly used in design.

4.3.3 Load-Settlement Curves

Figure 4.11 shows load-settlement curves for identical nondisplacement piles with length $L = 10$ m (= 33 ft)

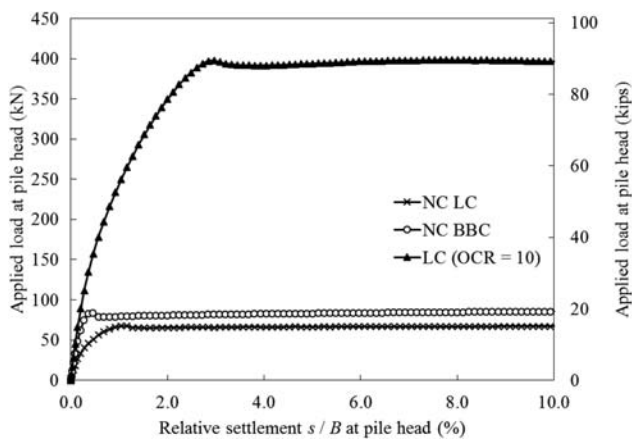


Figure 4.11 Load-settlement curves for 10 m (= 33 ft) long nondisplacement pile with pile diameter $B = 0.3$ m (= 1 ft) installed in normally consolidated (NC) London Clay, NC Boston Blue Clay and overconsolidated (OC) London Clay (OCR = 10).

and pile diameter $B = 0.3$ m (= 1 ft), each installed in NC LC, NC BBC and OC LC with OCR = 10. In these cases, a peak in total resistance is followed by immediate softening and then a fairly stable plateau. The load-settlement curves resemble those for total shaft resistance because the base resistance increases monotonically and has relatively small values for all cases.

4.3.4 Effect of Stiff Bearing Layer

We performed axisymmetric FE analyses of a 10-m-long (33-ft-long) nondisplacement pile with 0.3 m (= 1 ft) diameter installed in a layered soil with a top layer of soft clay (normally consolidated London Clay) over stiff clay (overconsolidated London Clay with OCR = 10) under fully undrained conditions. To estimate the effect of the embedment into the stiff clay layer on pile resistances, we considered five different embedment depths: $-2B$, $-B$, 0 , B , $2B$ and $5B$ (negative embedment meaning the pile is above the stiff clay). We also performed analyses for a single pile in uniform soft clay and in uniform stiff clay.

Figure 4.12 shows total, base and shaft resistances of pile as a function of embedment depth. The base and shaft resistances for the uniform soft clay and $-2B$ to $-B$ of embedment depth are almost the same. As the embedment depth increases from $-B$ to 0 , base resistance increases considerably. As the embedment depth increases from 0 to $5B$, the base resistance does not change much, but the shaft resistance increases almost linearly. Based on the analyses results shown in Figure 4.12, we could conclude that, in theory, the maximum base resistance is reached at 0 embedment depth, but that the gain in shaft resistance as a pile is embedded further in the stiffer clay would justify a larger rather than smaller embedment.

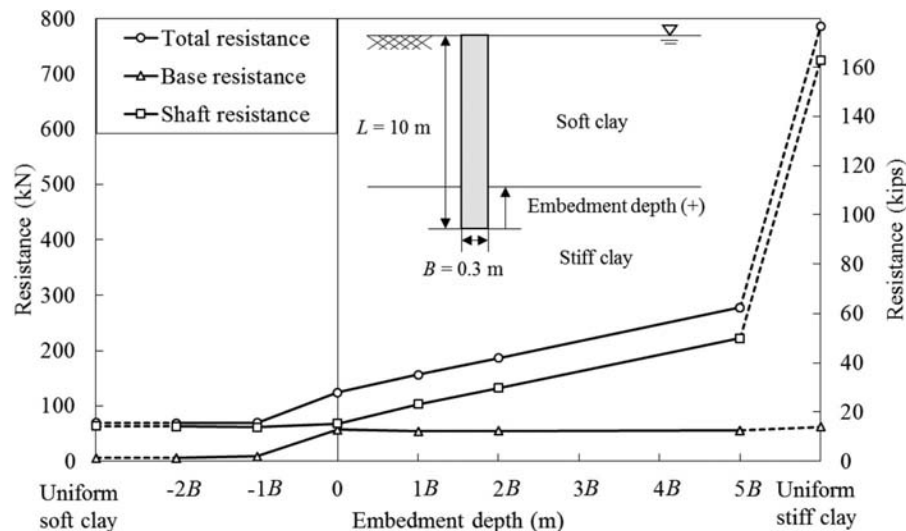
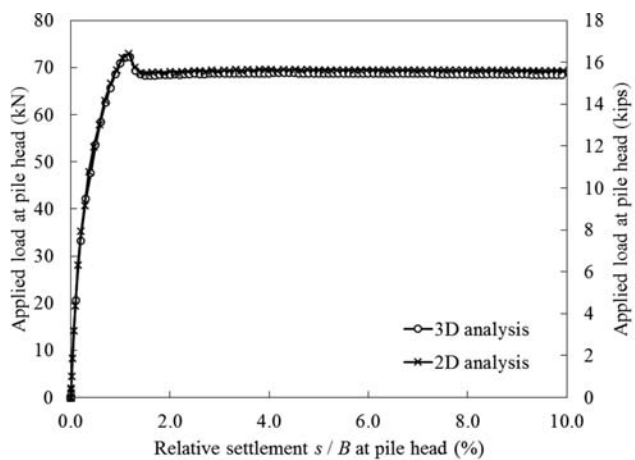


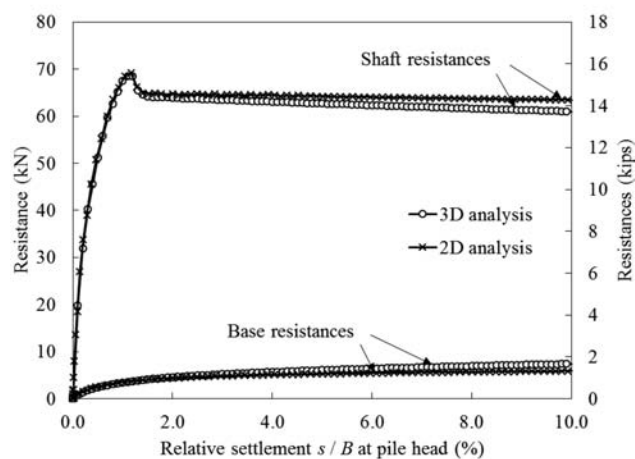
Figure 4.12 Pile resistances of nondisplacement pile installed in soft clay over stiff clay with different embedment depths.

4.3.5 Comparison between 2D and 3D FE Analyses

Figure 4.13 shows the comparison between 2D and 3D analyses results for a 10-m-long (33-ft-long) nondisplacement pile with 0.3 m (= 1 ft) of diameter installed in NC LC. Figure 4.13(a)–(b) compares total resistances, base resistances and shaft resistances obtained from 2D and 3D simulation results with respect to relative settlement. Theoretically, we should obtain the same analyses results because the analyses conditions are the same in 2D and 3D analyses. As shown in Figure 4.13(a), the load-settlement curves obtained from 2D and 3D analyses are almost the same. The difference between total ultimate resistances is about 1 kN (= 0.2 kips). The base and shaft resistances with respect to relative settlements of the pile head in 2D and 3D analyses are also essentially the same, as shown in Figure 4.13(b); the differences in ultimate base and shaft resistances are 1.5 kN (= 0.3 kips) and 2.4 kN (= 0.5 kips), respectively. These small



(a)



(b)

Figure 4.13 Comparison between 2D and 3D FE analyses: (a) applied loads at pile head and (b) base and shaft resistances with respect to relative settlement of pile head.

differences are due to differences in mesh configurations in 2D and 3D analyses. Even though we used the same thickness of the elements near the pile shaft and the base in 2D and 3D analyses, the meshes cannot be completely equivalent.

4.4 Conclusions

Rigorous simulations of the axial loading of single piles in clay using the realistic constitutive model for clay developed by Chakraborty, Salgado, and Loukidis (2013) were performed. The simulations could capture the complex response of the pile loaded in clay under undrained conditions: the development of shear bands around the pile base and shaft, the softening in shaft resistance after a peak is reached for small settlement values, and the development of excess pore water pressure around the pile. Localization of strain can be captured by using fine mesh configurations with the elements near the pile with thickness equal to the expected shear band thickness.

The simulation results show that previously proposed relationships for shaft resistance (Chakraborty, Salgado, Basu, et al., 2013) can be used in design. In addition, new base resistance equations have been proposed based on the results of the simulations. We also explored the effect of the pile embedment depth into a stiff clay layer and, by comparing 2D and 3D analyses results for single pile in clay, have verified that we can perform either 2D or 3D analyses for axially loaded pile foundations in clay.

5. NUMERICAL ANALYSES OF PILE GROUPS IN CLAY

5.1 Finite Element Analysis

5.1.1 Constitutive Model

The advanced two-surface plasticity constitutive model developed in Chakraborty, Salgado, and Loukidis (2013) is used in this study. Parameters used for the constitutive model can be found in Chapter 4.

5.1.2 Analysis Configuration

Three small pile groups (1×2 , 1×3 , 2×2) and a larger pile group (4×4) are considered in this chapter. Only one portion of the entire soil-pile domain needs to be modeled due to symmetry, reducing significantly the number of elements required to perform the analyses and consequently the total computational time. For example, in a 1×3 pile group (with three piles in a row), the entire soil-pile domain is symmetric with respect to the two lines of symmetry shown in Figure 5.1(a). Thus, only one quarter of the whole domain needs to be modeled, with corresponding boundary conditions illustrated in Figure 5.1(b).

Figure 5.2 shows the geometric dimensions of the simulation domain and the mesh configuration for the

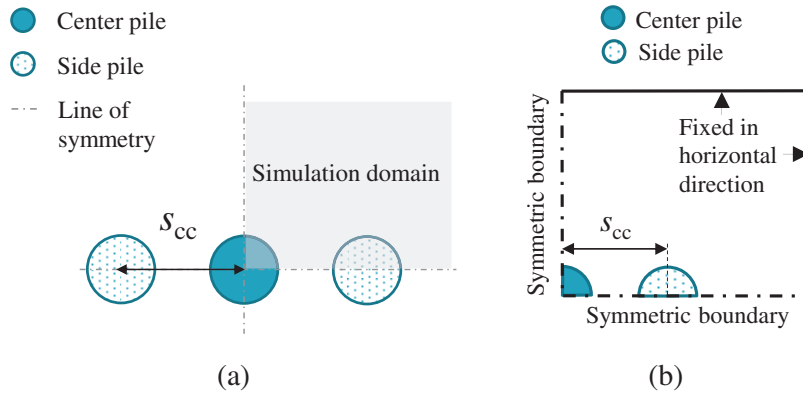


Figure 5.1 FE Analysis of the 1×3 pile group: (a) planes of symmetry for the pile group and (b) the simulation domain and its boundary conditions.

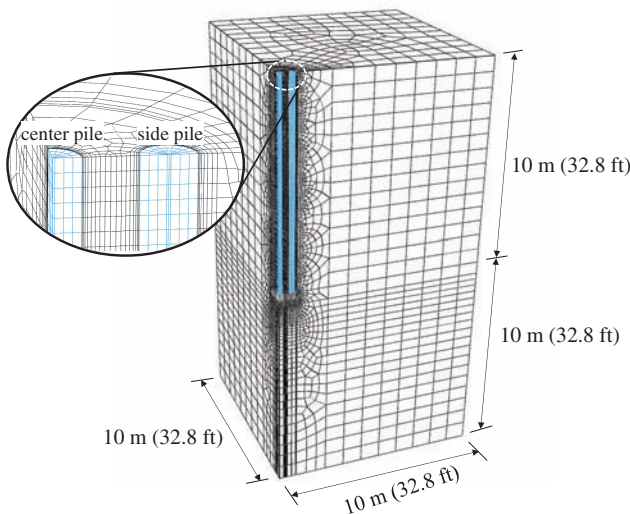


Figure 5.2 Mesh configuration for three-dimensional FE analysis of a 1×3 pile group.

FE analysis of a 1×3 pile group with center-to-center spacing $s_{cc} = 2B$ (B being the pile diameter). The mesh consists of a total number of 54,465, 8-noded, linear brick, hexahedral elements.

The limit unit shaft resistance of a pile depends on the mesh configuration (Chakraborty, Salgado, Basu, 2013; Masarucci et al., 2014; Salgado, 2008), particularly on the thickness of the soil elements adjacent to the pile shaft and around the pile base. As discussed in Chapter 3, a typical shear band thickness ($t_s = 4 \text{ mm}$) for clay (Stamatopoulos & Balla, 2010; Thakur, 2011) is used for the soil elements adjacent to the pile surface. A geostatic step was first used to apply the *in-situ* stress state in the whole domain. The axial loading was then simulated by simultaneously applying the same vertical velocity at each pile head in the pile group. The loading applied at the pile head was smoothed such that the loading rate gradually increased from zero to the desired velocity $v = 2 \text{ mm/s}$ within the first second. As usually done in practice (Fleming et al., 2008; Jardine et al., 2005; Lehane et al.,

2005; Randolph, 2003; Salgado, 2008), the ultimate resistance for a pile was defined as the resistance developed when the relative settlement $s/B = 10\%$ ($B =$ pile diameter) at the pile head. Thus, the vertical velocity was maintained at all pile heads until the pile head settlement reached $0.1B$.

5.2 Results and Discussion for Small Pile Groups

In this section, three commonly used small pile group configurations (one-by-two, one-by-three and two-by-two pile groups) are considered with center-to-center spacings s_{cc} varying from $2B$ to $4B$.

5.2.1 Load-Settlement Curves

Comparisons of load-settlement curves are made between a single pile and piles in the group to show the effects of the group configuration and the pile-to-pile spacing on the degree of group interaction. Figure 5.3 compares the load-settlement curve of a single pile with the average (total load developed in the pile group divided by the number of piles in that group) load-settlement curve of piles in the group for different pile group configurations but with the same center-to-center spacing $s_{cc} = 2B$ installed in normally consolidated London Clay.

When loading starts, the average load-settlement curve is less stiff for a larger pile group due to greater interaction effects. As settlement continues between $0.01B$ and $0.05B$, shearing localizes in the soil adjacent to the pile shafts (with the formation of shear bands), the degree of interaction between the piles decreases, and the average load-settlement curves tend to merge with that for the single pile.

The pile group response to loading also depends on the center-to-center pile spacing s_{cc} . Figure 5.4 compares the average load-settlement curves of a 2×2 pile group with that of a single pile. As the pile spacing increases, the response of the piles becomes similar to that of a single pile. When $s_{cc} = 4B$, the average load-settlement curve of the pile group is almost the same as that of the single pile.

The nature and level of pile-soil-pile interaction in a pile group are different along the shaft and base of the piles. Figure 5.5 decomposes the total resistance of an individual pile in a 2×2 pile group with pile spacing of $2B$ placed in normally consolidated London Clay into its shaft and base resistances; the resistances that would be developed in a single pile are also plotted for comparison. The pile-soil-pile interaction occurs mainly along the zone of influence near the shaft of the piles, with minimal group effects at the base of the piles for loads up to an ultimate load level ($s/B = 10\%$).

5.2.2 Mechanisms Leading to Interaction Effects along the Shaft of Piles in a Group

A 2×2 pile group placed in normally consolidated London Clay with center-to-center spacing $s_{cc} = 2B$ is considered. As shown in the previous section, since group effects result mainly from the interaction that develops as load is transferred to the soil along the shaft of the piles in small pile groups, only shaft resistance results are presented in this section.

Representative points at a few locations in a horizontal plane within the 2×2 pile group and at various depths along the piles are selected for further examination (at these locations, the elemental soil response to loading affects considerably the global response of the piles). Figure 5.6 shows the locations

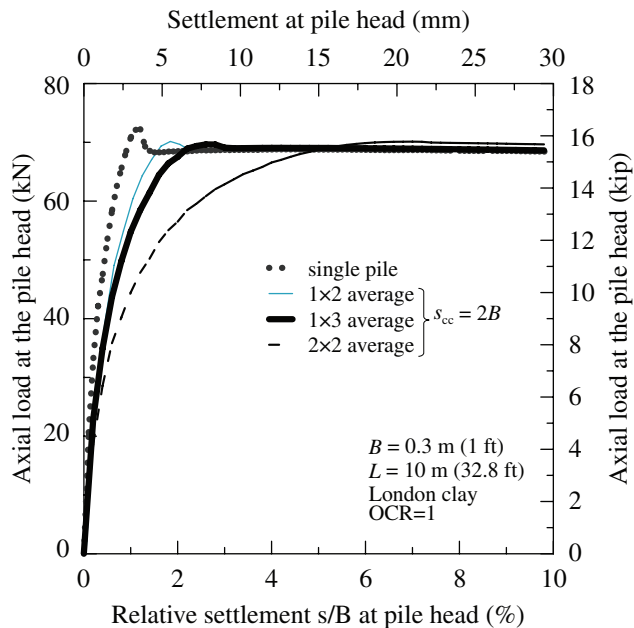


Figure 5.3 Effect of group configuration on the load-settlement curves.

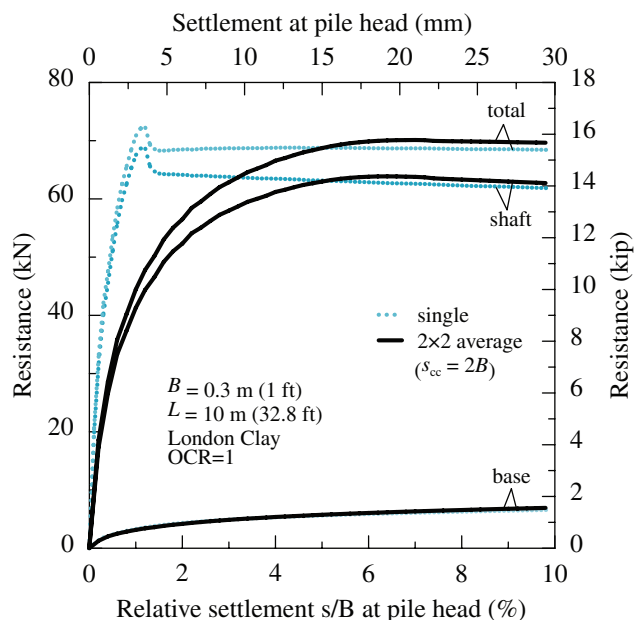


Figure 5.5 Comparison of the response of an individual pile to axial load in a 2×2 pile group with that for a single pile.

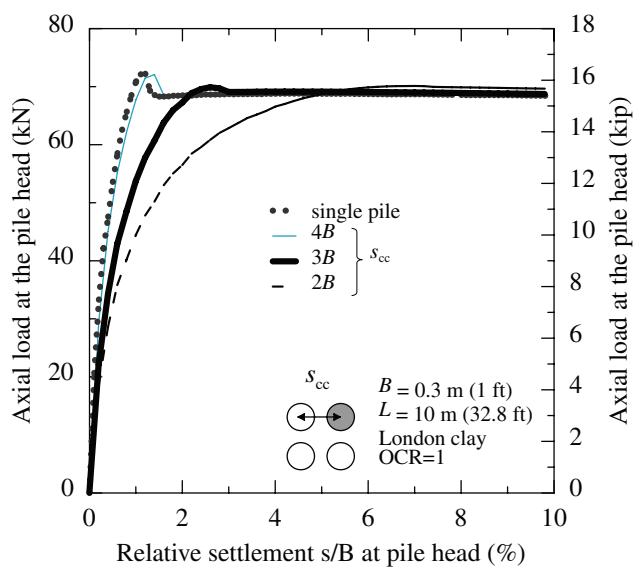


Figure 5.4 Effect of pile-to-pile spacings on the load-settlement curves.

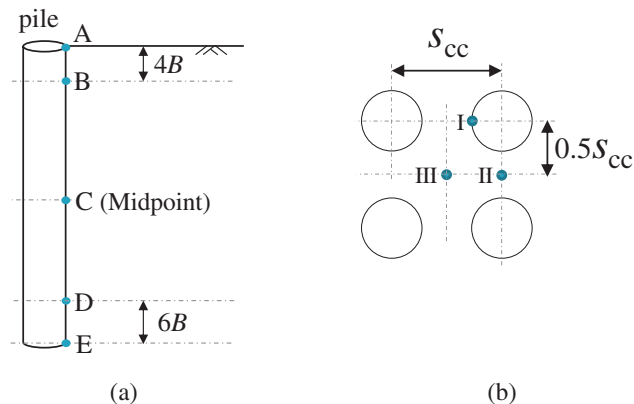


Figure 5.6 Location of soil elements at the points being considered for a 2×2 pile group: (a) in the vertical direction and (b) in the horizontal plane.

considered at five depths along the pile length (at the ground surface, $4B$ below the ground surface, at the pile midlength, $6B$ above the pile base and at the pile base) and three locations in the horizontal plane (next to the

pile shaft, midway between two side piles and at the center of the 2×2 pile group). The symbols in Figure 5.6(a) and (b) will be used in combination to describe the location of a soil element at the point being

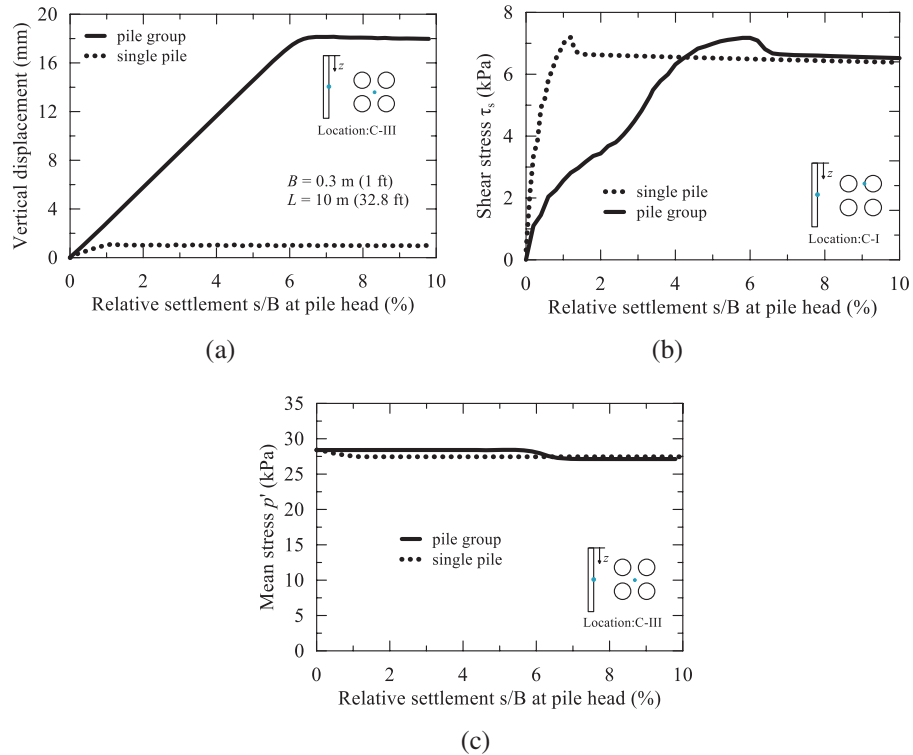


Figure 5.7 Group effects in a 2×2 pile group with $s_{cc} = 2B$ as a function of relative settlement at the pile head for soil elements at the pile midlength: (a) vertical displacement of a soil element in the center of the pile group; (b) shear stress on the pile shaft and (c) mean stress for a soil element in the center of the pile group.

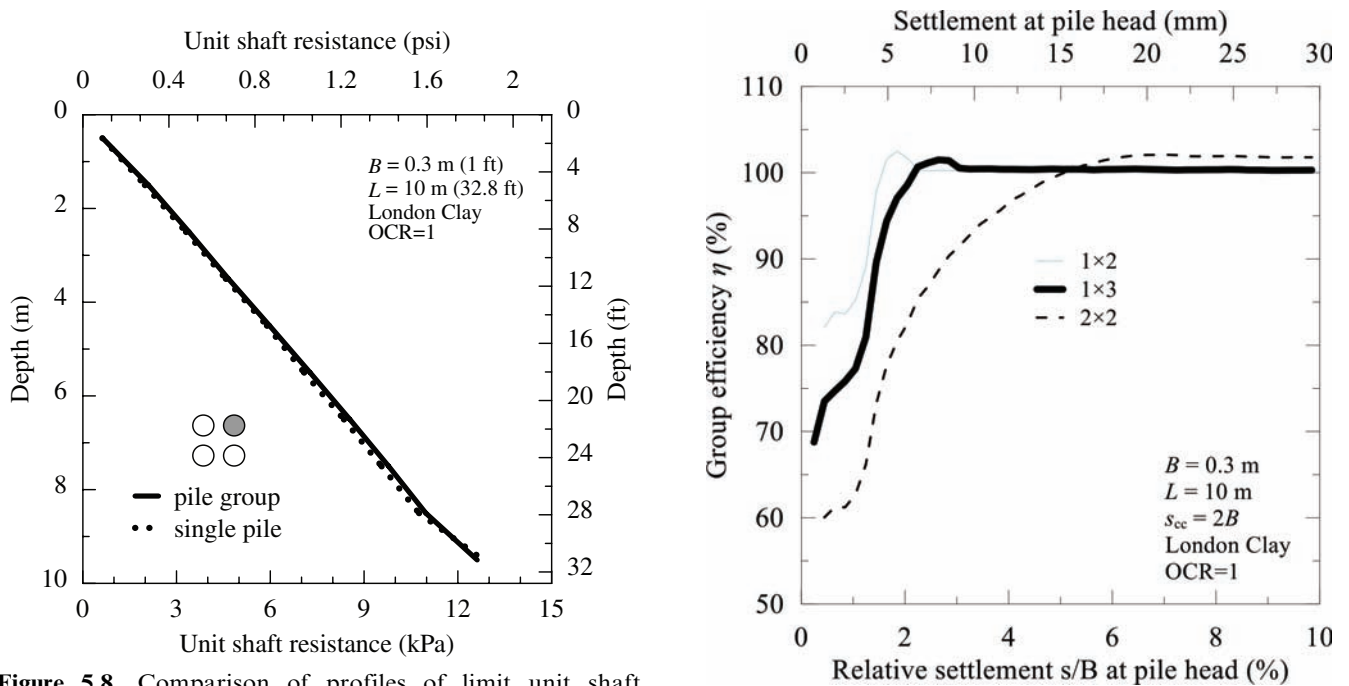


Figure 5.8 Comparison of profiles of limit unit shaft resistance for a single pile and an individual pile in a 2×2 pile group with $s_{cc} = 2B$ in London Clay with $OCR = 1$.

Figure 5.9 Dependency of the group efficiency on the relative settlement s/B at the pile head.

considered. For example, B-II represents the point located halfway between two side piles and at a depth of $4B$ below the ground surface.

A soil element at location C-III first moves downward together with the surrounding piles but ceases to move down at s/B approximately equal to 6%. This happens because, for s/B greater than 6%, there is shear strain localization with the formation of shear bands along the shaft of the piles, with the result that motion localizes there. As shown in Figure 5.7(a), the vertical displacement in soil element at a distance of $\sqrt{2}B$ from the pile center (the same distance considered for the case of the 2×2 pile group) is small and stabilizes early, reflecting the earlier formation of a shear band along the pile shaft. Because of strain localization at the settlement level of 6%, the shear stress in a soil element at the C-I location peaks at the same value of settlement, as seen in Figure 5.7(b), after which the critical state is reached. In contrast, for a single pile, shear localization occurs in an element near the pile at

the same depth at the lower relative settlement level $s/B = 1\%$. Despite the different stress histories observed in soil elements adjacent to a single pile and an individual pile in a pile group, very similar values of shear stresses are reached at critical state. In Figure 5.7(c), the change of the mean effective stress for a soil element at C-III, which reflects the contribution of all the piles in the group, is found to be minimal and the value at the critical state is almost no different from that for a single pile.

Figure 5.8 shows the profiles of the unit shaft resistance mobilized in one of the piles in the 2×2 pile group and in a single pile installed in normally consolidated London Clay for the same soil conditions. There is no appreciable difference between the two.

5.2.3 Group Efficiency

The effects of the relative settlement level and the center-to-center spacing on group efficiency are

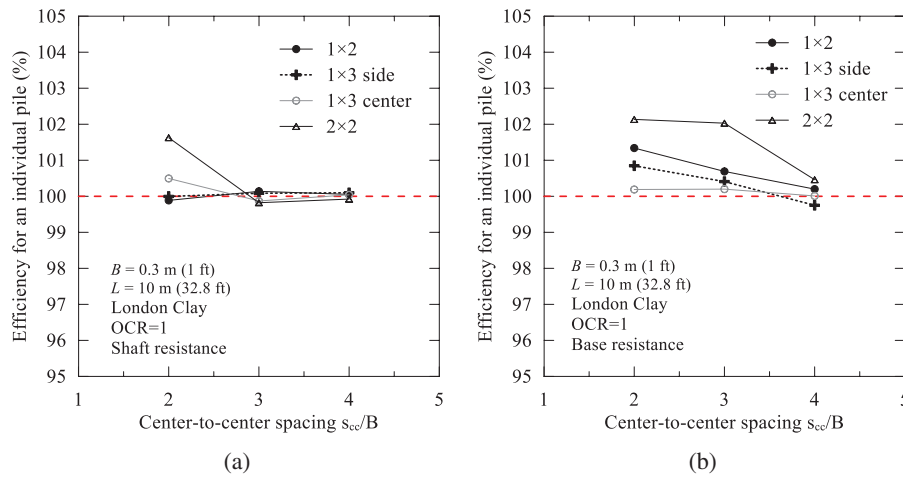


Figure 5.10 Efficiency for (a) the shaft resistance and (b) the base resistance of an individual pile in small pile groups.

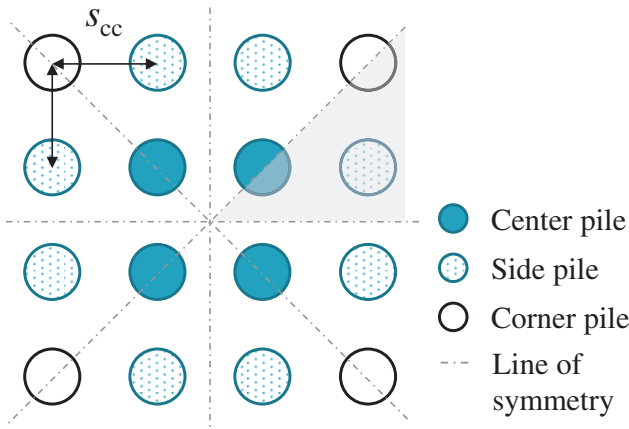


Figure 5.11 The three types of piles and the symmetric conditions in a 4×4 pile group.

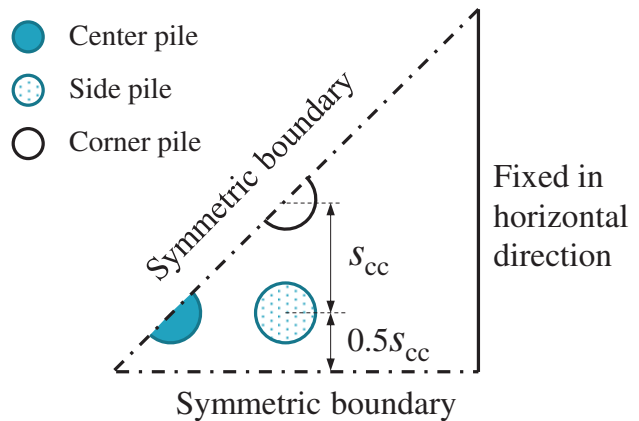


Figure 5.12 The simulation domain and boundary conditions used in the symmetric analysis of the 4×4 pile group.

discussed in this section. The definitions of pile efficiency when part of a group and overall group efficiency can be found in 3.3.

5.2.3.1 Effect of Relative Settlement Level

Figure 5.9 shows the group efficiency for the total resistance as a function of the relative settlement s/B at

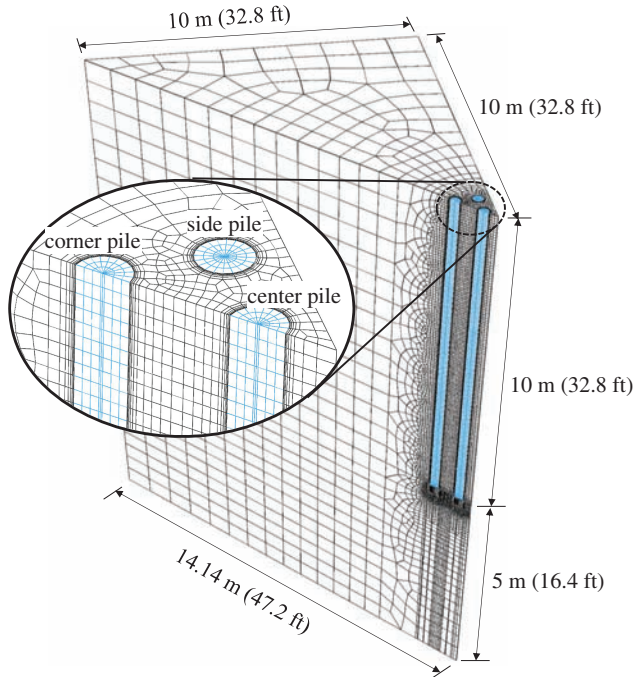


Figure 5.13 Mesh configuration for the three-dimensional FE analysis of the 4×4 pile group.

the pile head for different pile groups in London Clay with $OCR = 1$. Group efficiency values are initially low, ranging from 60% to 85%, increase with the settlement level, and finally converge to values very close to 100% as soil elements along the pile shaft reach critical state. Among the three group configurations being considered, the 2×2 pile group shows the slowest increase in group efficiency, reaching 100% only when s/B is over 5%.

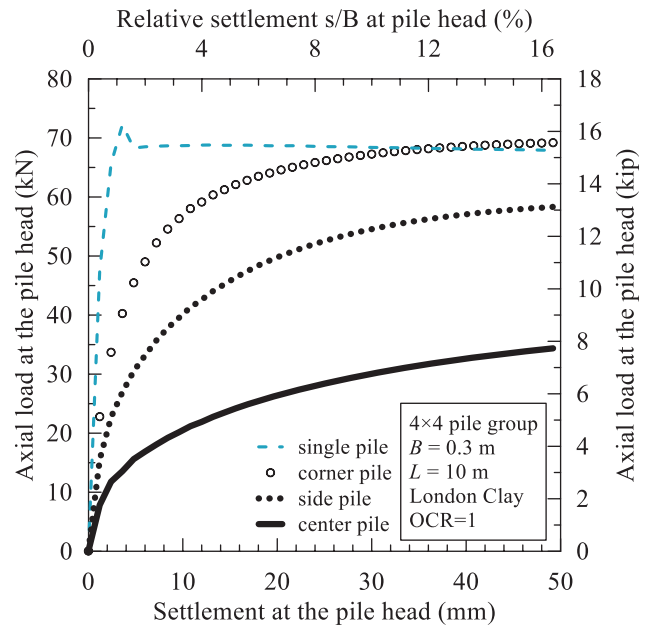


Figure 5.14 Load-settlement curves for a single pile and individual piles in a 4×4 pile group with $s_{cc} = 2B$ installed in London Clay with $OCR = 1$.

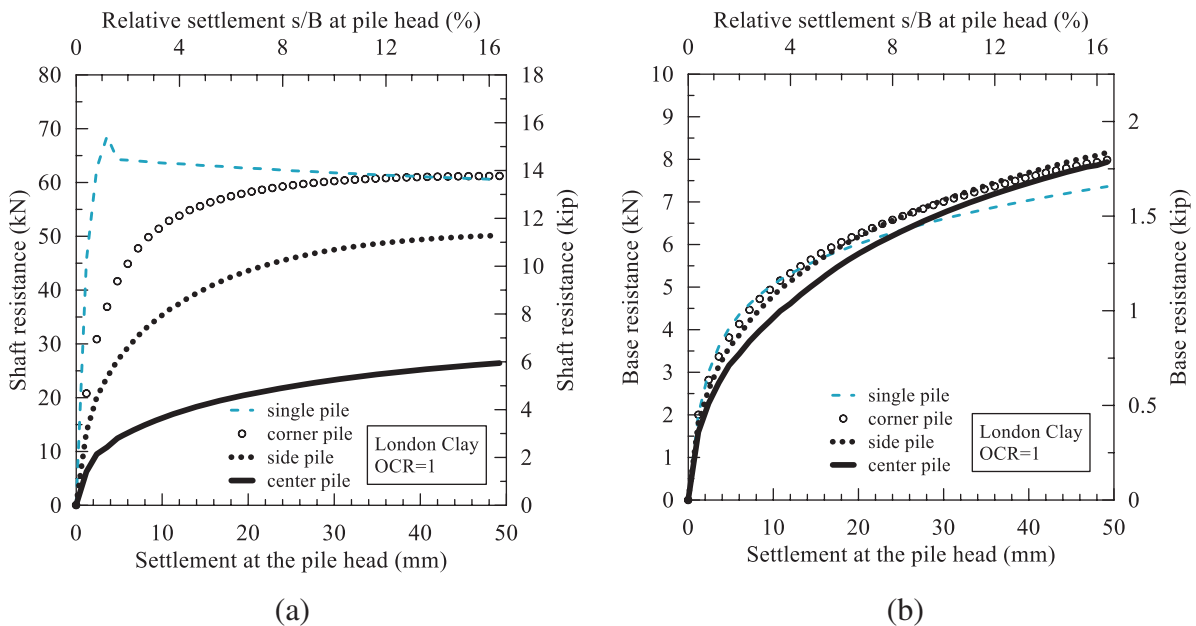


Figure 5.15 Development of (a) shaft resistance and (b) base resistance for a single pile and individual piles in a 4×4 pile group with $s_{cc} = 2B$ installed in London Clay with $OCR = 1$.

5.2.3.2 Effect of Center-to-Center Pile Spacing

Efficiencies of individual piles are also calculated considering the pile shaft and base resistances separately. Figure 5.10 shows the efficiencies at the ultimate load (the load corresponding to $s/B = 10\%$ at the pile head) for individual piles in different pile group configurations with center-to-center spacings s_{cc} varying from $2B$ to $4B$. As s_{cc} increases, the degree of interaction between the piles in the group decreases, as expected. The efficiency tends to 100% for both the shaft and base resistances when the center-to-center spacing is equal to $4B$. Efficiency values at ultimate load levels for both base and shaft resistances for almost all of the configurations considered in this study are within the range of $100 \pm 3\%$, indicating minimal group effects.

5.3 4 × 4 Pile Group

A 4 × 4 pile group with center-to-center spacing $s_{cc} = 2B$ installed in London Clay with OCR=1 was also analyzed to quantify group effects in a large pile group.

5.3.1 Pile Group Configuration

Figure 5.11 shows the three types of piles in a 4 × 4 pile group: 4 center piles, 8 side piles and 4 corner piles. Since the entire soil-pile domain is symmetric with respect to three lines of symmetry (Figure 5.11), the behavior of any two piles of the same type are identical. Thus, only one eighth of the entire domain, containing halves of a center pile and a corner pile and a whole side pile, needs to be modeled, with the associated boundary conditions shown in Figure 5.12. The computational cost of the analyses is greatly reduced in this manner.

Figure 5.13 shows the geometric dimensions of the simulation domain and the mesh configuration for the FE analysis of the 4 × 4 pile group with center-to-center spacing $s_{cc} = 2B$. The mesh contains a total number of 117,713 8-noded, linear brick, hexahedral elements. As discussed in Chapter 3, the tolerable vertical movement of 50 mm will be used as the serviceability limit state criterion. Thus, a vertical velocity of 2 mm/s is applied simultaneously on all pile heads until the pile head settlement s reaches 50 mm.

5.3.2 Load-Settlement Response

Figure 5.14 shows the load-settlement curves for individual piles in the 4 × 4 pile group in normally consolidated London Clay and that of a single pile placed in the same soil profile. The responses of the individual piles to axial load in a large pile group are very different from that of the single pile due to greater pile-soil-pile interaction effects. Among the three types of piles in a 4 × 4 pile group, the center piles show the greatest degree of interaction, leading to the lowest resistances.

Figure 5.15 separates the responses of the pile shaft and the pile base to investigate the mechanism(s) of the group interactions. It is clear that group interactions mainly take place along the pile shaft, while the responses at the pile base in individual piles in the pile group are similar to that of the single pile, resulting in slightly higher base resistance. Soil around the center piles experiences greater confinement and moves downward together with the piles as the load is applied, with less intense shearing

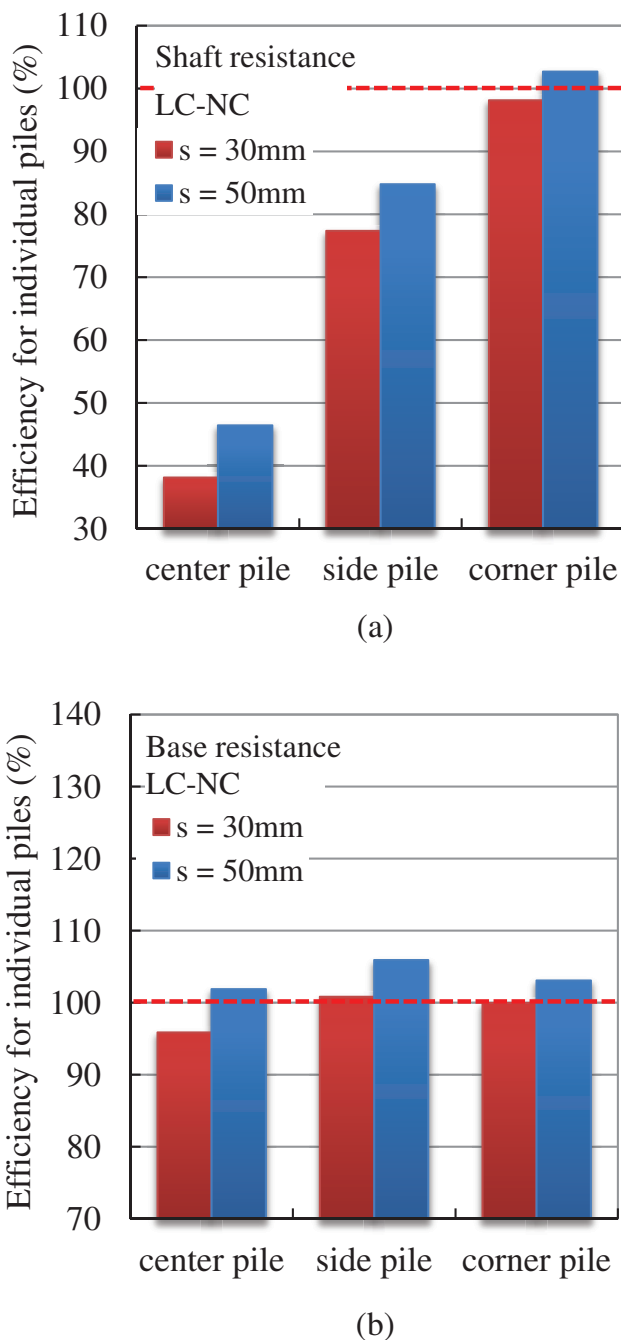


Figure 5.16 Efficiency for (a) shaft resistance and (b) base resistance of individual piles in a 4 × 4 pile group.

TABLE 5.1
Efficiency for Individual Piles in a 4 × 4 Pile Group Installed in Normally Consolidated London Clay (%).

		Center pile	Side pile	Corner pile	Group efficiency
$s = 30 \text{ mm}$	Base	96	101	100	99
	Shaft	38	77	98	73
	Total	44	80	98	75
$s = 50 \text{ mm}$	Base	102	106	103	104
	Shaft	46	85	103	80
	Total	53	87	103	83

localization in the soil right next to the soil-pile interfaces, such that the limit unit shaft resistance is not fully mobilized even when $s = 50 \text{ mm}$. Subjected to the least group effects, only the corner piles are able to mobilize the limit shaft resistance when the pile head settlement s reaches about 35 mm.

5.3.3 Group Efficiency

Figure 5.16 compares the efficiency for both the shaft and base resistances of each of the pile at two different settlement levels. Efficiencies for both the shaft resistance and base resistance increase (by less than 10%) as the pile head settlement increases from 30 mm to 50 mm. When the shaft resistance mobilized by the piles in the 4 × 4 pile group is compared with that of a single pile, it is seen that the shaft resistances developed in individual piles are generally lower than that develops in a single pile; the efficiency is lower than 50% for the center piles, about 85% for the side piles and close to 100% for the corner piles when $s = 50 \text{ mm}$. Efficiencies for the base resistance are close to 100% in most cases. The lowest efficiency is found in the center pile.

Table 5.1 summarizes the efficiencies for the shaft resistance, base resistance and total resistance of each type of individual pile in the 4 × 4 pile group at two different pile head settlements. The overall group efficiency η for the 4 × 4 pile group is also reported. The corner pile behaves similarly to a single pile, producing efficiencies close to 100% for both shaft and base resistances. The efficiencies for the total resistance are much lower than 100% (as low as 44%) in center and side piles, leading to the overall group efficiency of 75% when $s = 30 \text{ mm}$ and 83% when $s = 50 \text{ mm}$.

The analyses of the 4 × 4 pile group are instructive for the design of even larger pile groups (e.g., a 10 × 10 pile group), which consist of center piles, side piles and corner piles. These piles need to be considered separately for the calculation of the total resistance of a large pile group. For example, a pile group larger than 4 × 4 consists of more center piles and side piles, whose efficiencies are much lower than 100% and only 4 corner piles, which have efficiency close to 100%, resulting in an overall group efficiency that is much lower than 100%.

6. PILE LOAD TEST

6.1 Introduction

Driven steel pipe piles are often used as foundations due to their relatively fast and easy installation and large load carrying capacity. Understanding the response of driven piles subjected to axial loading is essential for the development of design methods that can be relied on to accurately predict their bearing capacity in different soil profiles. Yet, results of only a limited number of well-documented, instrumented static load tests on driven pipe piles are available in the literature (Al-Shafei, Cox, & Helfrich, 1994; Bica, Salgado, Kim, Seo, & Prezzi, 2014; Fellenius, Harris, & Anderson, 2004; Kim, Bica, Salgado, Prezzi, & Lee, 2009; Paik, Salgado, Lee, & Kim, 2003; Yen, Lin, Chin, & Wang, 1989). Model pile load tests have also been used to investigate several aspects of the response of piles to loading. However, model pile load tests are not substitutes for full-scale static load tests for two reasons: (i) soil profiles in nature are very complex (model pile load tests in a calibration chamber or centrifuge are generally performed in reconstituted soil samples) and (ii) the response of model piles may differ from that of full-scale piles due to scale effects. Therefore, a large database consisting of high-quality, full-scale static load tests is needed for validation of pile analyses and design methods.

A variety of pile design methods have been proposed to estimate the bearing capacity of driven closed-ended pipe piles. These methods are often grouped into two categories: the direct (*in situ* test-based) design methods and the indirect (soil property-based) design methods. In the direct methods (e.g., the ICP sand method by Jardine et al., 2005; Lehane et al., 2005), the pile resistances are directly correlated with the cone penetration test (CPT) cone resistance q_c (CPT) or the standard penetration test (SPT) blow count N_{SPT} . In contrast, in indirect methods (e.g., Karlsrud, Clausen, & Aas, 2005; the Purdue Clay method by Salgado, Woo, & Kim, 2011), the pile resistances are typically estimated from the critical-state friction angle ϕ_c and relative density D_R for sands and from the plasticity index PI and critical-state and residual-state friction angles for clays; values of these properties can be obtained from the results of *in situ* or laboratory tests.

This chapter reports on the instrumentation, installation, and (static and dynamic) testing of a closed-ended

pipe pile with a diameter equal to 356 mm (14 inch) driven to a depth of 15.4 m (50.5 ft) in a multilayered soil profile. Limit unit shaft resistance and pile driving resistance profiles, load-settlement and load-transfer curves, and residual load profiles are obtained from the load test measurements. In addition, several property-based and CPT-based pile design methods for both sandy and clayey soils are used to estimate the limit shaft and ultimate base resistances of the test pile. Estimates from these design methods are compared with the resistances measured in the static load test.

6.2 Site Description

An instrumented, driven, closed-ended pipe pile was load tested at a bridge construction site located at the intersection of 7th Road with U.S. 31 in Marshall County, Indiana. The test pile will be used in the foundations of a two-span bridge over 7th Road. Two SPTs and two CPTs were performed close to the test pile location before the static load test was performed, with the results shown in Figure 6.1, to obtain soil

profile data for pile capacity predictions. The CPTs were terminated at depths of approximately 16 m (52.5 ft), where a hard layer consisting of a mixture of silt and sand was found. According to the SPT borings, the soil profile consists mainly of layers of medium dense to dense silty sand and stiff to hard silt and sand mixtures. The water table was found at 4.3m (14.1 ft) below the ground surface according to the SPT boring logs, and this depth was confirmed by groundwater monitoring data collected by the Indiana Department of Natural Resources (DNR, 2015). The soil profile at the test site is summarized in Table 6.1.

6.3 Test Pile Instrumentation

The test pile is a steel, closed-ended pipe pile with an outer diameter of 356 mm (14 inch) and a wall thickness of 9.53 mm (0.375 inch); see Figure 6.2(a). The pipe has a cross-sectional area of 103.7 cm² (16.1 inch²). The pile base was closed by a steel plate with a diameter slightly greater than that of the pipe pile. The pile was fabricated by welding, at the construction site, a 6.1-

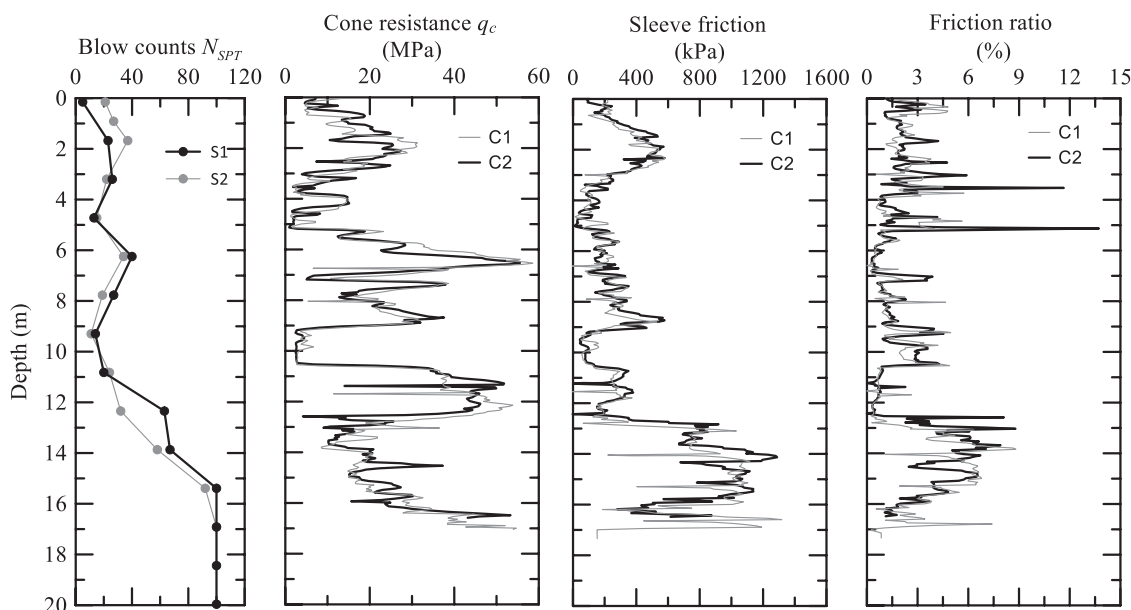


Figure 6.1 Results of the SPTs and CPTs performed at the test site.

TABLE 6.1
Soil Profile at the Test Site.

Layer No.	Depth (m)	Depth (ft)	Soil description	w_c (%)	γ_t (kN/m ³)
1	0–3.4	0–11.2	Stiff to very stiff silt with sand	14.8	19.4
2	3.4–5.2	11.2–17.0	Medium dense silty sand	13.4	21.2
3	5.2–9.1	17.0–29.9	Dense sand	10.5	20.7
4	9.1–10.5	29.9–34.4	Silty clay	14.7	21.5
5	10.5–12.8	34.4–42.2	Dense sand	10.5	20.7
6	12.8–24.7	42.2–81.0	Hard silt with sand	10.8	20.7

NOTE: w_c = natural water content; γ_t = total unit weight.

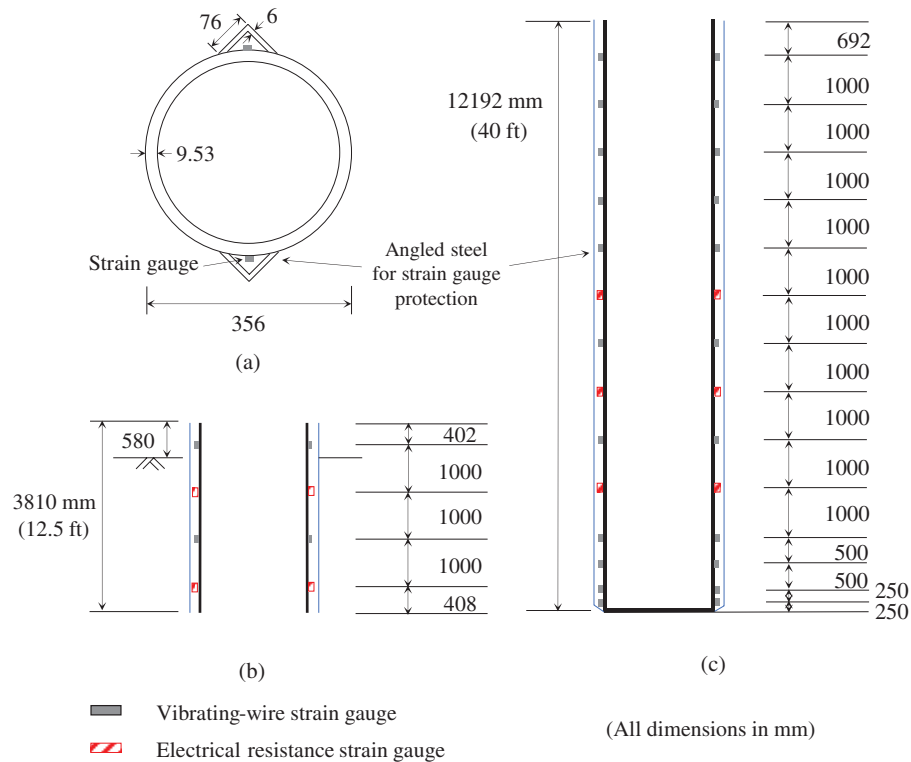


Figure 6.2 Dimensions of the test pile and layout of strain gauges on the two segments of the test pile: (a) dimensions of the cross section of the test pile, (b) layout of strain gauges on the top pile segment, and (c) layout of strain gauges on the bottom pile segment.

m-long (20 ft) top segment and a 12.2-m-long (40 ft) bottom segment (the use of two pipe pile segments was required by limitations in contractor transportation and driving capabilities).

A hybrid instrumentation scheme, with both electrical-resistance strain gauges, which have a quick response time and are inexpensive, and vibrating-wire strain gauges, which are stable in the long term and are resistant to moisture intrusion, was used to measure the axial deformation of the test pile and to obtain the test pile load transfer curves. The strengths and weaknesses of the two types of strain gauges were discussed in detail by Bica et al. (2014). Eight pairs of electrical-resistance strain gauges (Tokyo Sokki Kenyujo Model FLA-6-350-11-3LT) and 13 pairs of vibrating-wire strain gauges (Geokon Model 4000) were attached to opposite sides of the pipe pile segments. However, the top 2.29 m (7.5 ft) of the top pile segment, which had 3 pairs of electrical-resistance strain gauges, was cut off after driving. As a result, only 5 pairs of electrical-resistance strain gauges were in use at the time of the load test.

The layout of the strain gauges on the final 3.8-m-long (12.5 ft) top segment of the test pile is shown in Figure 6.2(b); it includes 2 pairs of electrical-resistance strain gauges and 2 pairs of vibrating-wire strain gauges. The layout of the strain gauges on the 12.2-m-long (40 ft) bottom segment of the test pile is shown in Figure 6.2(c);

it includes 11 pairs of vibrating-wire strain gauges and 3 pairs of electrical-resistance strain gauges.

Figure 6.3 shows the vibrating-wire and electrical-resistance strain gauges attached to the test pile, the bundled strain gauge cables and the instrumented pipe pile ready to be transported to the test site. Since the water table was found to be close to the ground surface (4.3 m below the ground surface) during the site investigation phase of the project and the fact that electrical-resistance strain gauges are susceptible to moisture intrusion damage, three layers of water-proof coatings, including N-1 coating (Neoprene rubber), SB tape and Araldite, were applied over the electrical-resistance gauges and the uninsulated lead wires (Figure 6.3(b)).

All strain gauges and their cables were protected by steel-angled channels welded onto the surface of the pipe pile. The bottom of the channels were covered by a tapered steel base to prevent soil intrusion during pile driving. See Figure 6.3(d). Figure 6.2(a) shows the dimensions of the pile and the angled channels. The strain gauge cables were connected to a data acquisition system consisting of two data loggers, Campbell CR5000 for the electrical-resistance strain gauges and Geokon Micro-800, Model 8025 for the vibrating-wire strain gauges, and one multiplexer, Geokon Model 8032.

6.4 Pile Driving and Dynamic Testing

The test pile was driven by a single-acting impact hammer (APE model D30-32) down to a depth of 15.42 m (50.6 feet) on June 16th, 2014. The hammer had a ram weight of 3,000 kg and a maximum hammer stroke of 3.2 m, generating a maximum rated energy of 94.1 kN•m (69405 lb•ft). After the bottom pile segment was driven into the ground, a steel guiding ring (shown in Figure 6.4(a)), which was used to splice the two pile segments, was welded to its top. The strain gauge cables originating from the bottom pile segment were then

collected and passed through the top pile segment and hung over a rebar hook (see Figure 6.4(b)) welded inside the top pile segment. All cables were covered by multiple layers of mineral wool (see Figure 6.4(a)), which were used to isolate the cables from the heat generated during welding of the splice. With the guiding ring in place, the top pile segment was positioned, aligned and welded to the bottom pile segment (Figure 6.4(c)) and was then driven into the ground.

Figure 6.5 shows the hammer blow counts per foot of pile penetration recorded during driving of the test pile. The hammer blow count, together with the pile

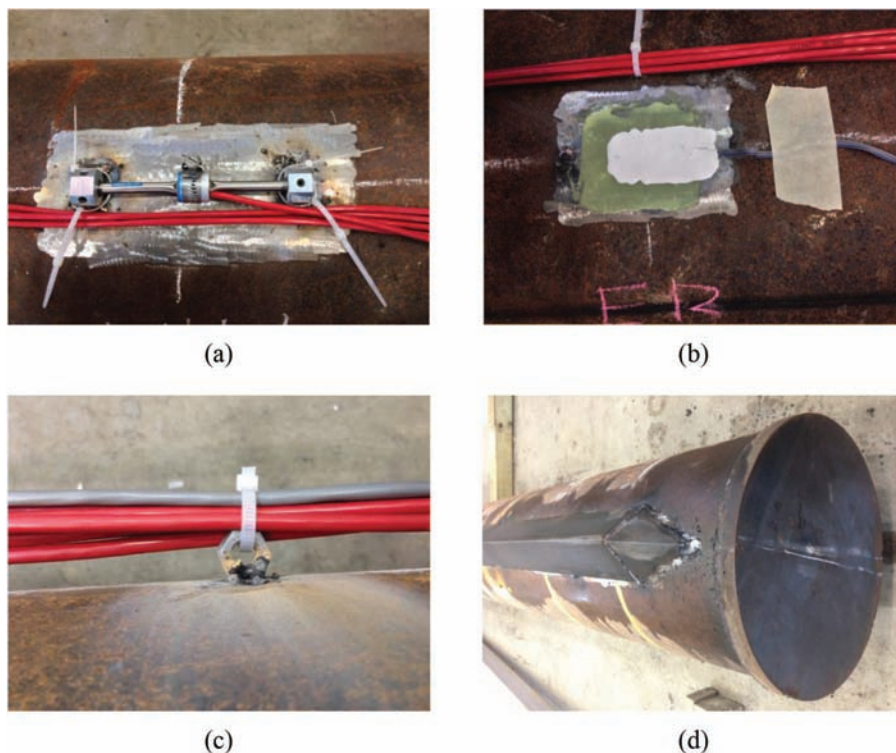


Figure 6.3 Pile instrumentation: (a) vibrating-wire strain gauges arc-welded to the pipe pile surface; (b) electrical-resistance strain gauges glued onto the pipe pile surface, protected by multilayers of waterproofing coatings; (c) strain gauge cables collected in a bundle and guided by nuts welded onto the pipe pile surface; (d) angled steel channels and tapered base cover welded to the pipe pile to protect all strain gauges and cables.

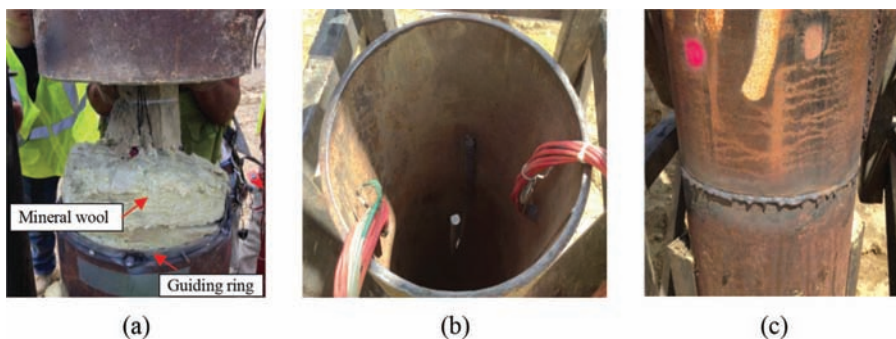


Figure 6.4 Details of the two-segment pile driving process: (a) guiding ring and mineral wool layers used for splicing of the two pipe pile segments and heat isolation, respectively; (b) rebar hook used to fasten cables originating from the bottom pile segment inside the top pile segment; and (c) welded pile segments.

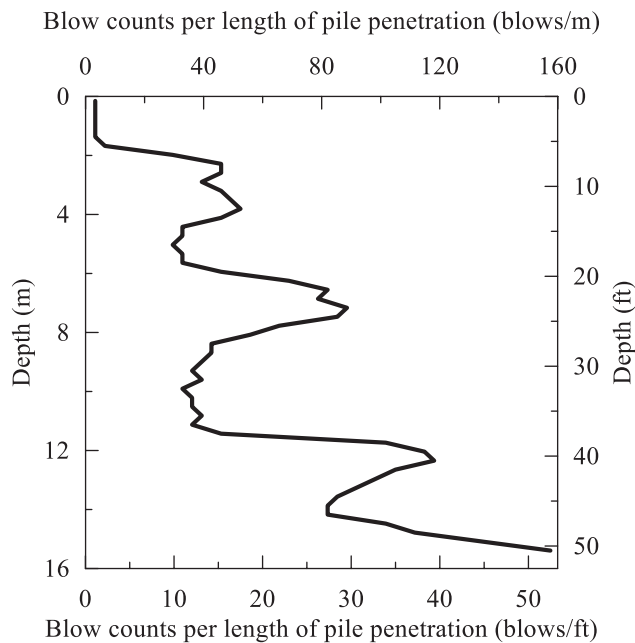


Figure 6.5 Pile driving resistance versus depth.

driving analyzer (PDA), was used to determine whether the desired pile capacity had been reached; once the estimated capacity reached the required value, pile driving was stopped and the redundant top pile segment was cut. The final length of the pile was 16 m (52.5 feet), with 15.42 m (50.6 feet) embedded into the ground.

Dynamic load tests with the pile driving analyzer (PDA) were performed by GRL Engineers, Inc. on the test pile both at the end of the initial driving and during a restrike test on July 8th (22 days after the initial driving). Two strain transducers and two piezoelectric accelerometers were mounted on opposite sides of the test pile outer surface. The ultimate capacities of the pile were estimated using the signal matching program CAPWAP (Pile Dynamics, Inc.).

6.5 Static Load Test

Primco Inc. and GRL Engineers, Inc. performed the static load test on the pile on June 25, 2014 (9 days after the initial pile driving). The Purdue University research team was responsible for the pile instrumentation and data acquisition during testing. The static load was applied vertically on the test pile head by increasing the pressure in a hydraulic jack positioned between the pile and the main reaction beam. The applied load was determined by both a calibrated load cell and a jack pressure gauge. The vertical pile head settlement was monitored by two digital deflectometers positioned diametrically opposite to each other at the test pile head and supported on reference beams (see Figure 6.6).

Initially, the load was applied in increments ranging from 178 kN (40 kip) to 222 kN (50 kip) to a load level of 1868 kN (420 kip). After that, the load increment was reduced to 111 kN (25 kip) until the plunging or limit



Figure 6.6 Load application system at the pile head and deflectometers supported by reference beams.

load was reached. For each loading step, the pile head settlement was recorded at least in two of the following time increments: 1, 2, 5, 10, 20, 30, 40 and 60 minutes. The load at each load step was maintained until the settlement rate calculated from two consecutive pile head settlement readings was less than 0.5mm/hr. In instances in which it took longer than 60 minutes to satisfy this criterion, the next load increment was applied only after the difference in settlement between the current and previous record was less than 5%. After reaching the plunging load of 3394 kN (763 kip), the test pile was unloaded in four equal decrements, with waiting periods of 30 minutes between each of the unloading steps. The data acquisition systems recorded the strain gauge readings at every 60 seconds for the vibrating-wire strain gauges and at every 0.5 seconds for the electrical-resistance strain gauges during the entire load test.

6.6 Pile Load Test Results

6.6.1 Load-Settlement Response

The Young's modulus of the test pile was obtained from the strain gauge measurements from the pair of strain gauges located above the ground level and the records of the load applied at the pile head. The Young's modulus of the pile was determined to be 201 GPa.

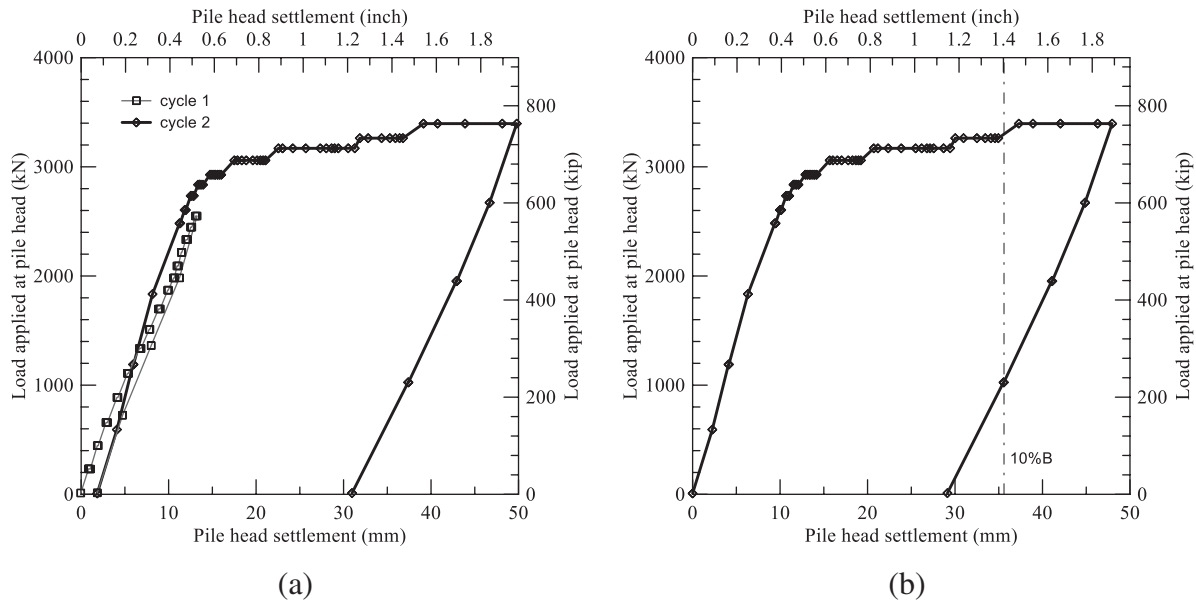


Figure 6.7 Load-settlement curves at the pile head: (a) complete load-settlement history of load test; (b) load-settlement curve after unloading with measured settlement at pile head reset to zero.

Figure 6.7 shows the axial load applied at the pile head versus the pile head settlement curve, with symbols representing intermediate readings taken during the waiting time for stabilization of the settlement caused by each load increment. The load-settlement response was almost linear in the beginning of the loading up to an applied load of 2,900 kN (652 kip) (corresponding to a pile head settlement of 12 mm), after which the slope of the load-settlement curve decreased significantly. The ultimate load, corresponding to a pile head settlement of 10% of the test pile diameter (35.6 mm), was 3275 kN (736 kip). Finally, at an applied load of 3394 kN (763 kip), the pile head settlement increased by 12.7 mm within 20 minutes (a rate significantly higher than the 0.5 mm/hr rate stabilization criterion), indicating that the pile was plunging into the ground with a pile head settlement of 48.3 mm (1.9 inch) at that moment. The unloading section of the load-settlement curve was almost linear and parallel to the initial part of the loading section.

6.6.2 Residual Loads

The mechanism of development of residual loads is well understood and explained in the literature (Alawneh & Malkawi, 2000; Briaud & Tucker, 1984; Fellenius et al., 2004; Seo, Yildirim, & Prezzi, 2009). At the end of a hammer blow, the pile is pushed up due to soil rebound below the pile base and the elastic recovery of the pile. This upward movement is resisted by shaft friction along part of or the entire pile length, leading to compressive residual loads locked in the pile. After driving, the upward residual load at the pile base should be in equilibrium with the downward resultant of the residual shaft loads. In our study, all of the strain gauges were zeroed before initial driving, and the

residual loads were estimated from the strain gauge values measured right before the static load test. Vibrating-wire strain gauges are subject to drifts in zero readings due to the inertial forces during pile driving; electrical-resistance strain gauges, in contrast, are light and small and thus stable during pile driving. Therefore, residual loads were determined only based on the readings from the electrical-resistance strain gauges. All the strain gauges were re-zeroed just before the static load test.

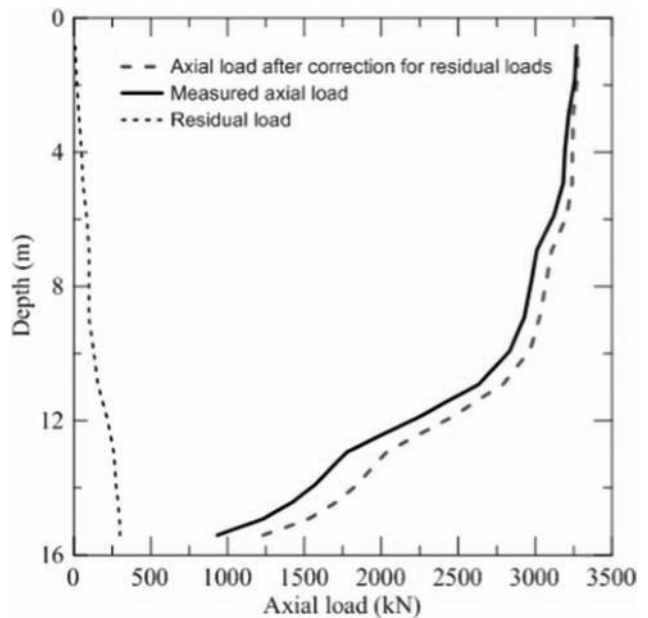


Figure 6.8 Residual load and axial load profiles accounting for the residual loads at the ultimate load level.

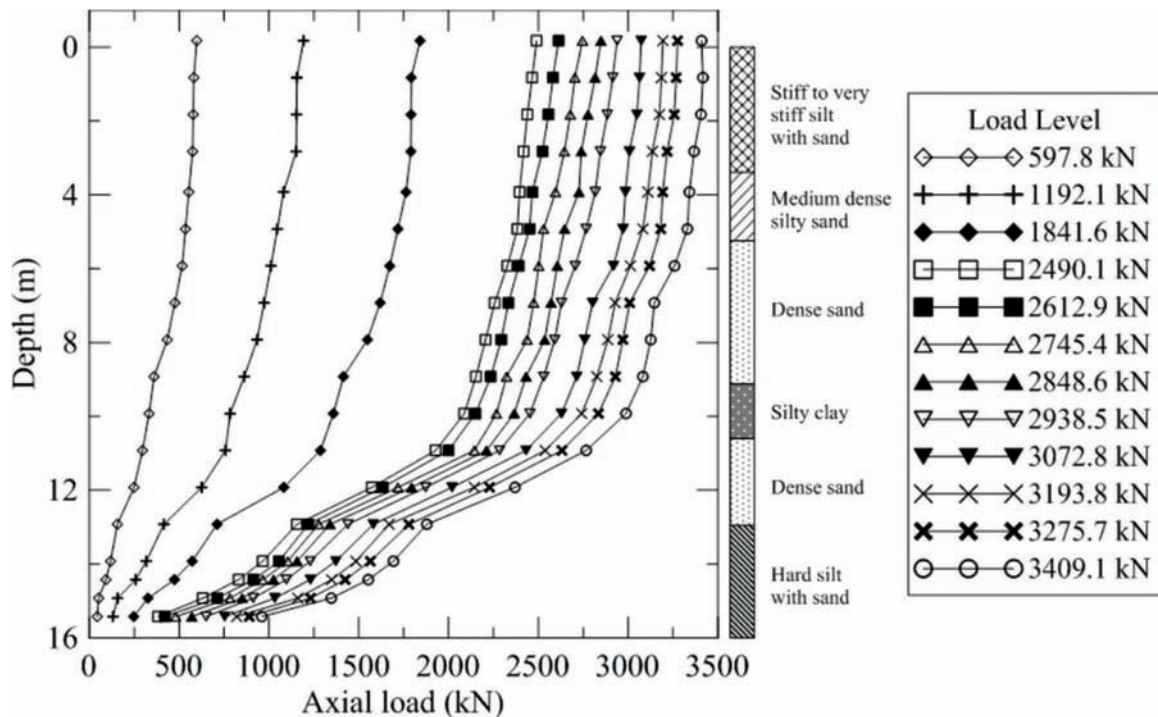


Figure 6.9 Load-transfer curves (without accounting for the residual loads).

Figure 6.8 shows the test pile residual load and axial load profiles accounting for the residual loads at the ultimate load level ($=3,275\text{kN} = 736\text{ kip}$). The actual axial load along the pile is the summation of the residual load estimated from the strain gauge readings taken right before the load test and the load measured using the strain gauges during the load test, bearing in mind that the strain gauges were re-zeroed before the static load test.

During application of the load at the pile head during the static load test, whatever fraction of the applied load reaches different pile length segments is in addition to any locked-in loads and is first used to demobilize any shaft resistance pointing downward due to the locked-in residual loads. As the strain gauges were re-zeroed before load application, the shaft resistance back-calculated from the strain gauge readings has these two components: the residual load recovery and the actual upward-pointing shaft resistance available along the pile length.

The unit shaft resistance available at some depth z depends on the locked, residual shear stress there at the time of the load test. Depending on the extent of pile rebound, upward-pointing residual shaft resistance may develop along a segment of the pile just above the base; for this segment, the actual unit shaft resistance is less than the value that would be obtained from gauge readings after the reset. For the remaining length of the pile shaft, the actual unit shaft resistance is greater than the directly measured values. In the presence of residual load at the pile base, which normally points upwards (in compression), the actual base resistance is greater than

the directly measured value. The residual load does not affect the total load capacity of the pile. It only affects the proportion of the total load that is taken by the shaft and the base of the pile (the total capacity, which is equal to the summation of the two, remains the same).

Much is still being learned about what happens to a pile after driving (Axelsson, 2000; Basu et al., 2014; Bowman & Soga, 2005; Chow, Jardine, Brucy, & Nauroy, 1998; Jardine, Standing, & Chow, 2006; Lee, Kim, Salgado, & Zaheer, 2010; Lim & Lehane, 2014; White & Zhao, 2006; Zhang & Wang, 2015); by the time a pile is loaded by the superstructure that will be built on it, the residual loads may have degraded through the same processes that are suspected to lead to pile set up. Thus, it is important to ascertain what the actual shaft and base resistances are in the absence of residual loads so that they may be considered when making design decisions.

6.6.3 Base and Shaft Capacity

Five pairs of electrical-resistance strain gauges and thirteen pairs of vibrating-wire strain gauges recorded the strain changes at eighteen different locations along the test pile length during the entire static load test; this data was used to obtain the profiles of the axial load distribution along the pile at each and every loading step.

Figure 6.9 shows the depth profiles of the axial loads (load-transfer curves) obtained from the strain gauges along the pile at each loading level. The average unit shaft resistance between two neighboring strain gauges can be calculated as the difference between the axial

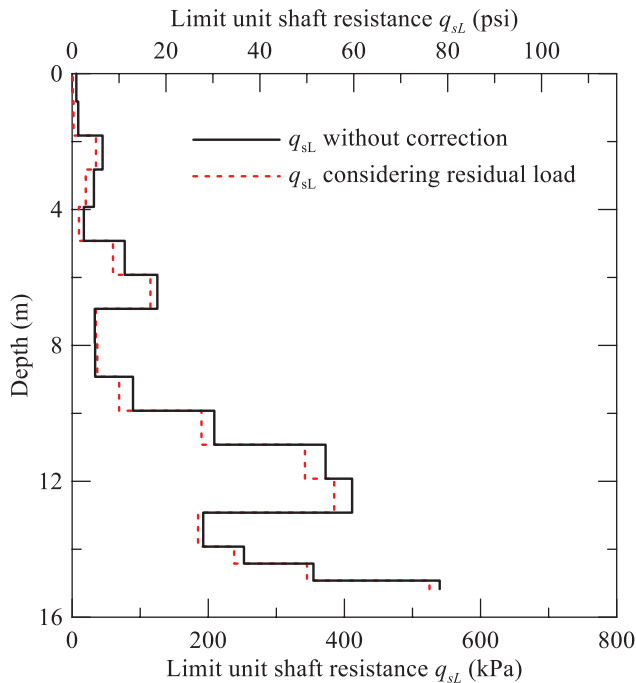


Figure 6.10 Measured limit shaft resistance along the pile.

loads obtained from these two gauges divided by the area of the outer surface of the pipe section between the two gauges. Thus, the slope of these curves indicates the magnitude of the shaft resistance. The profile of the calculated unit shaft resistance along depth both with and without consideration of the residual loads is plotted in Figure 6.10. As discussed in the previous section, the unit shaft resistances accounting for the residual loads are less than the values obtained directly from the strain gauge measurements made during the loading test.

6.7 Load Capacity Predictions

The ultimate bearing capacity Q_{ult} of a single pile is the sum of the ultimate base resistance $Q_{b,ult}$ and the limit shaft resistance Q_{sL} (Salgado, 2008):

$$Q_{ult} = Q_{b,ult} + Q_{sL} = q_{b,ult}A_b + \sum_{i=1}^n q_{sLi}A_{si} \quad (6.1)$$

where $q_{b,ult}$ is the ultimate unit base resistance; A_b is the area of the pile base; q_{sLi} is the unit shaft resistance of layer i ; A_{si} is the area of pile shaft of layer i and n is the number of layers along the pile shaft. A variety of methods, both property-based and *in situ* test-based, are used to estimate the static, axial bearing capacity of piles driven into sandy and clayey soils (e.g., Clausen, Aas, & Karlsrud, 2005; Fleming et al., 2008; Jardine et al., 2005; Karlsrud et al., 2005; Kolk, Baaijens, & Senders, 2005; Kolk & der Velde, 1996; Lehane et al., 2005; Salgado et al., 2011). The equations for some current pile design methods for sandy soil and clayey soil are listed in Table 6.2 and Table 6.3, respectively. Apart from the cone resistance, some of the design methods require basic soil properties for the estimation

of the pile bearing capacity; these are summarized in Table 6.4.

The unit shaft resistance (typically in sandy soils) at a certain depth along the pile decreases as the pile is driven down further from that depth due to a reduction in the normal stress on the pile with the increasing number of hammer blows on the pile (Lehane, Jardine, Bond, & Frank, 1993; Vesic, 1967; White & Bolton, 2002). This phenomenon, known as “friction fatigue,” is accounted for in the design methods by adding a shaft resistance degradation term (see Table 6.5) to the design equations. Note that upper bound values are defined in the ICP and UWA methods to prevent the degradation term from going to infinity near the pile base. Figure 6.11(a) shows the degradation term for the different design methods vs. depth for the pile load test presented in this paper. In Figure 6.11(b), the degradation term is normalized with respect to the maximum value of each method, indicating the rate and magnitude of the degradation of the unit shaft resistance from the pile base towards the pile head; the Fugro and ICP methods produce the fastest and slowest degradation rates, respectively.

The bearing capacity of driven piles may increase with time after pile installation; this increase in capacity is attributed to setup effects (e.g., Axelsson, 2000; Bullock, Schmertmann, McVay, & Townsend, 2005; Chow et al., 1998; Jardine et al., 2006; Lee et al., 2010; White & Zhao, 2006; Zhang & Wang, 2015). Both field tests and some model pile tests have shown that pile setup takes place mainly along the pile shaft (Axelsson, 2000; Bullock et al., 2005; Chow et al., 1998). However, estimation of setup may not yet be done reliably. Researchers have started assigning a time after installation at which their resistance predictions would apply (Table 6.2 and Table 6.3 indicate such times for some methods), but rate and magnitude of set up at this time are simply not known with sufficient accuracy to include them in design methods with an acceptable degree of confidence. Pile setup depends on pile type, installation method and soil profile. Additionally, shaft and base resistances must be treated separately, as their development processes are different, and any time-dependent behavior will also be different.

Table 6.6 summarizes the values of the input variables that were used in pile resistance estimations. In the ICP clay method, the interface friction angle δ_c is recommended to be determined by site-specific ring shear interface tests. In the absence of such test results, a value of 20° was assumed. The plasticity index PI was not used in the NGI method since the clay is an overconsolidated clay with s_u/σ'_{v0} greater than 1.0 (see Table 6.3)

Table 6.7 compares the results of predictions by the different design methods with those obtained from the static and dynamic measurements. Given the emerging consensus that the base resistance changes little with time (Axelsson, 2000; Bullock et al., 2005; Chow et al., 1998; Kim et al., 2009), the Purdue CPT method and the ICP method produced the closest estimates of the

TABLE 6.2
Design Methods for Driven Piles in Sand.

Method and key reference	Limit unit shaft resistance q_{sL}	Ultimate unit base resistance $q_{b,ult}$	Comments
Purdue-CPT (Randolph, 2003; Salgado et al., 2011)	$q_{sL} = K \sigma'_{v0} \tan \delta_c$ $K = K_{\min} + (K_{\max} - K_{\min}) \exp\left(-\alpha \frac{h}{B}\right)$ $K_{\min} = 0.2$ $K_{\max} = 0.02q_c / \sigma'_{v0}$ h is the distance from the depth being considered to the pile base; $K_{\min} = 0.2$; $\alpha = 0.05$	$q_{b,ult} = (1 - 0.0058D_R)q_{cb,avg}$	—
ICP (Jardine et al., 2005)	$q_{sL} = (\sigma'_{rc} + \Delta\sigma'_{rd}) \tan \delta_c$ $\sigma'_{rc} = 0.029q_c \left(\frac{\sigma'_{v0}}{P_A}\right)^{0.13} \left(\frac{h}{R}\right)^{-0.38}$ $\Delta\sigma'_{rd} = 2G\Delta r/R$ $G = q_c [0.0203 + 0.00125\eta + -1.216 \times 10^{-6}\eta^2]^{-1}$ $\eta = q_c (p_A \sigma'_{v0})^{-0.5}$ $\Delta r = 0.02\text{mm}$ for lightly rusted steel piles; h is the distance from the depth being considered to the pile base, $h/R \geq 8$.	$q_{b,ult} = \max[0.3, 1 - 0.5 \log(B/B_{CPT})]q_{cb,avg}$ B_{CPT} is cone diameter = 0.036 m	Intended to predict the pile bearing capacity 10 days after driving for “virgin” piles.
UWA (Lehane et al., 2005)	$q_{sL} = \frac{f}{f_c} \left(\sigma'_{rc} + \frac{4G\Delta r}{B} \right) \tan \delta_c$ $\sigma'_{rc} = 0.03q_c \left[\max\left(\frac{h}{B}, 2\right) \right]^{-0.5}$ $G/q_c = 185 \left[\frac{q_c/P_A}{(\sigma'_{v0}/P_A)^{0.5}} \right]^{-0.75}$ $\Delta r = 0.02 \text{ mm}$ $f/f_c = 1$ for compression and 0.75 for tension	$q_{b,ult} = 0.6q_{cb,avg}$	The method is intended to predict the pile bearing capacity measured 10-20 days after driving.
NGI (Claussen et al., 2005)	$q_{sL} = \max \left[\frac{P_A}{z} \left(\frac{z}{z_{base}} \right)^{0.25} F_{D_R} F_{tip} F_{load} F_{mat}, 0.1\sigma'_{v0} \right]$ $F_{D_R} = 2.1 [D_R^* - 0.1]^{1.7}$ $D_R^* = 0.4 \ln \left[\frac{q_c}{22(\sigma'_{v0} P_A)^{0.5}} \right]$ where z is the depth below the ground surface; z_{base} is the pile base depth; $F_{tip} = 1.6$; $F_{load} = 1.3$ for compression; $F_{mat} = 1.0$ for steel and 1.2 for concrete pile; D_R^* is the nominal relative density, which may be greater than 100%.	$q_{b,ult} = \frac{0.8q_{cb,avg}}{1 + \left\{ 0.4 \ln \left[\frac{q_{cb,avg}}{22(\sigma'_{v0} P_A)^{0.5}} \right] \right\}^2}$ σ'_{v0} is the vertical effective stress at the depth of the pile base.	—
Fugro (Kolk et al., 2005)	$q_{sL} = 0.08q_c \left(\frac{\sigma'_{v0}}{P_A} \right)^{0.05} \left(\frac{h}{R} \right)^{-0.9}$ if $h/R \geq 4$ $q_{sL} = 0.08q_c \left(\frac{\sigma'_{v0}}{P_A} \right)^{0.05} (4)^{-0.9} \left(\frac{h}{4R} \right)$ if $h/R < 4$ h is the distance from the depth being considered to the pile base	$q_{b,ult} = 8.5P_A \left(\frac{q_{cb,avg}}{P_A} \right)^{0.5}$	The method is intended to predict the pile bearing capacity measured about 10 days after driving.

NOTE: ϕ_c is the critical-state friction angle; σ'_{v0} is the initial horizontal effective stress at the depth being considered; B is the pile diameter; R is the pile radius; P_A is the reference stress = 100 kPa; q_c is the representative cone resistance of the soil layer; σ'_{v0} is the initial vertical effective stress at the depth being considered; δ_c is the interface friction angle (ICP and UWA suggest using interface shear tests to determine the value of δ_c ; if not feasible, it can also be estimated from the mean particle size (Jardine et al., 2005; Lehane et al., 2005). δ_c can also be determined from the critical-state friction angle in sand by: $\delta_c = 0.9\phi_c$; Foye, Abou-Jaoude, Prezzi, & Salgado, 2009; Salgado et al., 2011); $q_{cb,avg}$ is the representative cone resistance at the pile base level; this can be obtained by averaging the cone resistances near the pile base level.

TABLE 6.3
Design Methods for Driven Piles in Clay.

Reference	Limit unit shaft resistance q_{sL}	Ultimate unit base resistance $q_{b,ult}$	Comments
Purdue-CPT (Salgado et al., 2011)	$q_{sL} = \alpha s_u$ $\alpha = 1.28 \left(\frac{s_u}{\sigma'_{v0}} \right)^{-0.05} \left[A_1 + (1 - A_1) e^{-\left(\frac{\sigma'_{v0}}{r_1} \right)^{(\phi_c - \phi_{r,min})^2}} \right]$ $A_1 = 0.75$ for $\phi_c - \phi_{r,min} \leq 5^\circ$, 0.4 for $\phi_c - \phi_{r,min} \geq 12^\circ$ and a linearly interpolated value for $5^\circ \leq \phi_c - \phi_{r,min} \leq 12^\circ$ $A_2 = 0.64 + 0.4 \ln \left(\frac{s_u}{\sigma'_{v0}} \right)$	$10s_u$	The method is intended to estimate the shaft resistance after dissipation of the excess pore pressure generated during pile installation.
ICP (Jardine et al., 2005)	$q_{sL} = 0.8K_c \sigma'_{v0} \tan \delta_c$ $K_c = [2.2 + 0.016OCR - 0.870\Delta I_{vy}] OCR^{0.42} \left(\max \left[\frac{h}{R}, 1 \right] \right)^{-0.20}$ $\Delta I_{vy} = \log_{10} S_t$ where OCR is the overconsolidation ratio; h is the distance from the depth being considered to the pile base and S_t is the sensitivity of clay = s_{ur}/s_{ur} , s_{ur} being the undrained shear strength of disturbed samples.	For undrained loading: $q_{b,ult} = 0.8q_{cb,avg}$ For drained loading: $q_{b,ult} = 1.3q_{cb,avg}$	The method is intended to estimate the shaft resistance after dissipation of the excess pore pressure generated during pile installation. Ring shear interface tests are recommended to determine the interface friction angle δ_c .
UWA (Lehane, Li, & Williams, 2013)	$q_{sL} = 0.055q_t \left[\max \left(\frac{h}{R}, 1 \right) \right]^{-0.2}$ <i>or</i> $q_{sL} = \frac{0.023q_t \left[\max \left(\frac{h}{R}, 1 \right) \right]^{-0.2}}{(q_t/\sigma'_{v0})^{0.15}} \tan \delta_c$ h is the distance from the depth being considered to the pile base.	N/A	Two equations were proposed for the shaft resistance and the first one is more reliable. Time effects were not mentioned.
NGI (Karlsrud et al., 2005)	For NC clays with $(s_u/\sigma'_{v0}) < 0.25$: $q_{sL} = \alpha^{NC} s_u$ $\alpha^{NC} = 0.32(PI - 10)^{0.3}$ ($0.20 \leq \alpha^{NC} \leq 1.0$) For OC clays with $(s_u/\sigma'_{v0}) > 1.0$: $q_{sL} = \alpha s_u F_{tip}$ $\alpha = 0.5(s_u/\sigma'_{v0})^{-0.3}$ $F_{tip} = 0.8 + 0.2(s_u/\sigma'_{v0})^{0.5}$ for closed-ended pipe piles ($1.0 \leq F_{tip} \leq 1.25$) For clays with $0.25 < (s_u/\sigma'_{v0}) < 1.0$: α is determined by linear interpolation between the above two cases.	$9s_u$	The calculated shaft resistance corresponds to a time of 100 days after the initial driving. s_u is recommended to be determined from unconsolidated undrained (UU) compression tests.
Fugro (Kolk & der Velde, 1996; Van Dijk & Kolk, 2011)	$q_{sL} = \alpha s_u$ $\alpha = 0.9 \left(\frac{L-z}{B} \right)^{-0.2} (s_u/\sigma'_{v0})^{-0.3} \leq 1$	$q_{b,ult} = 0.7(q_t - \sigma_{v0})$	The method for shaft resistance generally predicts long-term resistance.

NOTE: ϕ_c is the critical-state friction angle; $\phi_{r,min}$ is the minimum residual-state friction angle; PI is the plasticity index; σ'_{v0} is the initial horizontal effective stress at the depth being considered; σ'_{v0} is the initial vertical effective stress at the depth being considered; σ_{v0} is the initial vertical total stress at the depth being considered; L is the pile length; z is the depth being considered; B is the pile diameter; R is the pile radius; q_c is the cone resistance at the depth being considered; $q_t = q_{c+(1-\alpha)u_2}$, where α is the cone area ratio and u_2 is the pore pressure measured behind the cone tip; s_u is the undrained shear strength of clay; δ_c is the interface friction angle.

TABLE 6.4
Input Variables Required for Pile Design Methods.

Design method	Sand				Clay						
	Cone resistance q_c	Critical-state friction angle ϕ_c	Relative density D_R	Interface friction angle δ_c	Cone resistance q_c	Friction angle of clay ϕ_c and $\phi_{r,min}$	Interface friction angle δ_c	Undrained shear strength s_u	Plasticity index PI	Overconsolidation ratio OCR	Sensitivity S_t
Purdue CPT	●	●		○	●	●		○			
ICP	●			●	●		●			●	●
UWA	●			●	●		(●) ^a				
NGI	●		○					●	●		
Fugro	●				●			●			

NOTE: The solid circles indicate variables required for the design methods and the hollow circles indicate variables that can be derived from other variables.

^aTwo equations were proposed in the UWA clay method (Lehane et al., 2013); one of them requires the interface friction angle δ_c as an input variable.

TABLE 6.5
Degradation Terms Used in the Design Methods for Calculation of Unit Shaft Resistance in Sand.

Term	Design methods				
	Purdue	ICP	UWA	NGI	Fugro
	$\exp(-\alpha \frac{h}{B})$	$[\max(\frac{h}{R}, 8)]^{-0.38}$	$[\max(\frac{h}{B}, 2)]^{-0.5}$	$\frac{z}{z_{base}}$	$(\frac{h}{R})^{-0.9}$ if $h/R \geq 4$ $(4)^{-0.9} (\frac{h}{4R})$ if $h/R < 4$
Maximum value at the pile base	1	0.45	0.71	1	0.29

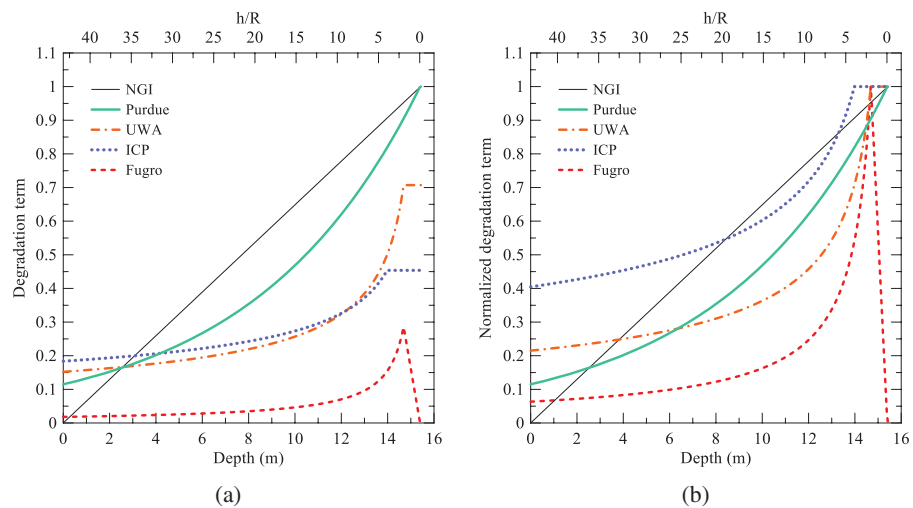


Figure 6.11 The effect of the shaft degradation term on predictions of the unit shaft resistance in sand: (a) the degradation term calculated according to the design methods considered vs. depth; and (b) the value of the degradation term normalized with respect to its maximum value (at the pile base) vs. depth.

TABLE 6.6
Soil Properties Used in the Predictions.

Layer No.	Depth (m)	Depth (ft)	Soil classification for design	w_c (%)	γ_t (kN/m ³)	ϕ_c^a (deg)	δ_c (deg)	$\phi_{r,min}^a$ (deg)	OCR	s_u (kPa)	S_t
1	0–3.4	0–11.2	Sand	14.8	19.4	33	29.7	—	—	—	—
2	3.4–5.2	11.2–17.0	Sand	13.4	21.2	33	29.7	—	—	—	—
3	5.2–9.1	17.0–29.9	Sand	10.5	20.7	33	29.7	—	—	—	—
4	9.1–10.5	29.9–34.4	Clay	14.7	21.5	24	20	12	5.3	200	2.62
5	10.5–12.8	34.4–42.2	Sand	10.5	20.7	33	29.7	—	—	—	—
6	12.8–24.7	42.2–81.0	Sand	10.8	20.7	33	29.7	—	—	—	—

NOTE: w_c is the natural water content; γ_t is the total unit weight; OCR is overconsolidation ratio, which was estimated according to Kulhawy and Mayne (1990): $OCR = k (q_t - \sigma_{vo}) / \sigma'_{vo}$, where an average value of $k = 0.33$ was assumed; s_u is the undrained shear strength, which was estimated using the correlation with CPT: $s_u = (q_t - \sigma_{vo}) / N_k$, where $N_k = 12$ was used; S_t is the sensitivity of clay, which was determined according to Robertson (2009): $S_t = 7.1 / F_r$, where F_r is the normalized friction ratio [$F_r = f_s / (q_t - \sigma_{vo}) 100\%$, f_s being the sleeve friction resistance].

^aAssumed values.

TABLE 6.7
Comparisons between the Measured and Predicted Bearing Capacities.

Test	Time after initial driving (day)	Shaft (kN)	Shaft (kip)	Base (kN)	Base (kip)	Total (kN)	Total (kip)
PDA (CAPWAP) - 1	0.1	752	169	1179	265	1931	434
Ultimate load at a settlement of 10% of the pile diameter ^a	9	2344	527	931	209	3275	736
Ultimate load at a settlement of 10% of the pile diameter ^b	9	2045	460	1230	277	3275	736
PDA (CAPWAP) - 2	22	1807	406	1560	351	3367	757
Design method	Time after installation to which prediction applies (day) ^c						
Purdue-CPT	—	1992	448	1221	274	3213	722
NGI	—	2410	542	1157	260	3567	802
ICP	10	1933	435	1208	272	3141	706
UWA	10–20	1909	429	1443	324	3352	754
Fugro	≈10	1762	396	1312	295	3074	691

^aNot accounting for residual loads.

^bAccounting for residual loads.

^cTime after installation to which prediction applies in sandy soil were reported here since the soil profile mainly consists of sandy soils; see Table 6.3 for those in clayey soils.

base resistance when compared with the static load test results 9 days after pile installation (considering values obtained accounting for the residual load). Most of the design methods produce good estimates of the shaft resistance when compared with the static load test results accounting for the residual load. Figure 6.12 compares the profiles of the unit limit shaft resistance q_{sL} obtained from the static load test considering residual loads with those estimated by different design methods; the same comparisons are summarized in Table 6.8. The signal matching program CAPWAP (Pile Dynamics, Inc.) was also used in the two dynamic load tests to estimate the mobilized pile resistance, as reported in Table 6.7. An increase in the total resistance from 1931 kN (434 kip) to 3367 kN (757 kip) was predicted (GRL Engineers, Inc. 2014) from the end of initial driving to the restrike test 22 days later; 73% of this increase came from the shaft resistance.

6.8 Additional Verification of Pile Design Methods

6.8.1 Pile Load Test in Lagrange County, IN (Paik et al., 2003)

A static load test was performed in Lagrange County, Indiana (Paik et al., 2003) on a closed-ended pipe pile with a diameter of 356 mm driven to a depth of 6.87 m. The soil profile consists of 3 meters of loose gravelly sand with $D_R = 30\%$ over dense gravelly sand with $D_R = 80\%$. Approximately 2 meters of fill material above the ground surface had been removed before the load test such that the soil profile is in an overconsolidated condition. The ground water table was found to be 3m below the ground surface. Figure 6.13 shows the results of CPTs performed at the pile load test site.

Figure 6.14 compares the unit limit shaft resistance q_{sL} estimated using the above-discussed pile design

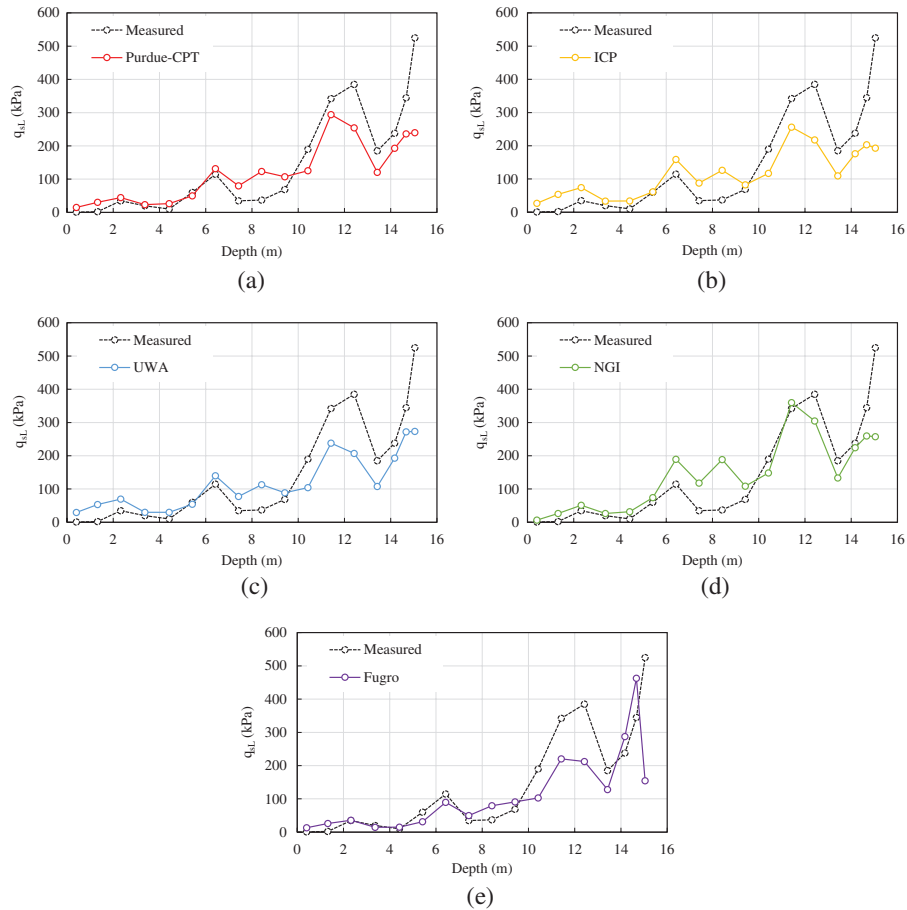


Figure 6.12 Comparison of the unit limit shaft resistance q_{sL} obtained from the static load test (considering the residual load) with those estimated using: (a) Purdue-CPT method; (b) ICP method; (c) UWA method; (d) NGI method; and (e) Fugro method.

methods with that obtained from the static load test. The ICP, Purdue and UWA methods yield the best, most consistent predictions. The ultimate base resistance $Q_{b,ult}$ measured in the static load test is used to verify the design methods for base resistance, with the results compared in Table 6.10. The predictions by the ICP and Purdue methods are very close to the measured value.

6.8.2 Pile Load Test in Jasper County, IN (Kim et al., 2009)

A fully instrumented static load test was undertaken (Kim et al., 2009) on a closed-ended driven pipe pile with diameter of 356 mm (14 inch). The pile was driven to a depth of 17.4 m (57 ft) into a multilayered soil profile, Table 6.11, with alternating layers of sandy, silty and clayey soils. The ground water table was at 1 meter below the ground surface. Figure 6.15 shows the CPT results that were used to estimate the resistance of the test pile.

Figure 6.16 shows the profiles of the unit limit shaft resistance q_{sL} estimated using the pile design methods and that obtained from the static load test. The ICP, Purdue and UWA methods are again the most consistent and reliable predictors of the unit shaft

resistance. On the other hand, as shown in Table 6.12, the ultimate base resistance is much overestimated by all the methods (by 3.5 to 5 times the measured $Q_{b,ult}$). This is due to the fact that the pile base was embedded in a thin very dense silt layer, which was underlain by a soft silty clay layer; a detailed discussion on this can be found in Kim et al. (2009). This suggests that caution is required when calculating the base resistance of a pile embedded in a thin, strong layer overlying a weak layer.

6.9 Summary and Conclusions

The chapter presented results of static and dynamic load tests on a closed-ended pipe pile driven in a multilayered soil profile. The test pile was fully instrumented with a combination of vibrating-wire and electrical-resistance strain gauges to measure the axial deformation along the test pile. Since the test pile was fabricated in two segments, a special procedure was developed and followed to protect the strain gauges and gauge cables during driving and welding of the two pipe-pile segments.

Both static and dynamic load tests were performed on the test pile. The test pile load-settlement response, load-

TABLE 6.8

Comparison of the Estimated Average Unit Limit Shaft Resistance, q_{sL} (kPa), with the Measured Values between Each Pair of Neighboring Strain Gauges.

Depth (m)	Soil classification for design	Measured*	Purdue-CPT	ICP	UWA	NGI	Fugro
0-0.82	Sand	1	15	27	7	30	13
0.82-1.82	Sand	2	30	54	26	53	26
1.82-2.82	Sand	35	45	74	51	70	36
2.82-3.92	Sand	20	23	33	26	30	14
3.92-4.92	Sand	10	26	34	32	30	15
4.92-5.92	Sand	60	50	61	74	54	31
5.92-6.92	Sand	115	132	159	189	140	90
6.92-7.92	Sand	35	80	88	118	78	50
7.92-8.92	Sand	37	123	126	188	113	79
8.92-9.92	Sand-Clay	69	107	83	109	89	91
9.92-10.92	Clay-Sand	190	125	117	148	104	103
10.92-11.92	Sand	342	294	256	360	238	220
11.92-12.92	Sand	385	254	218	305	207	213
12.92-13.92	Sand	185	121	109	133	108	128
13.92-14.42	Sand	238	193	176	224	193	287
14.42-14.92	Sand	345	236	203	260	272	463
14.92-15.17	Sand	525	240	193	257	273	155

*Measured values with consideration of the residual loads

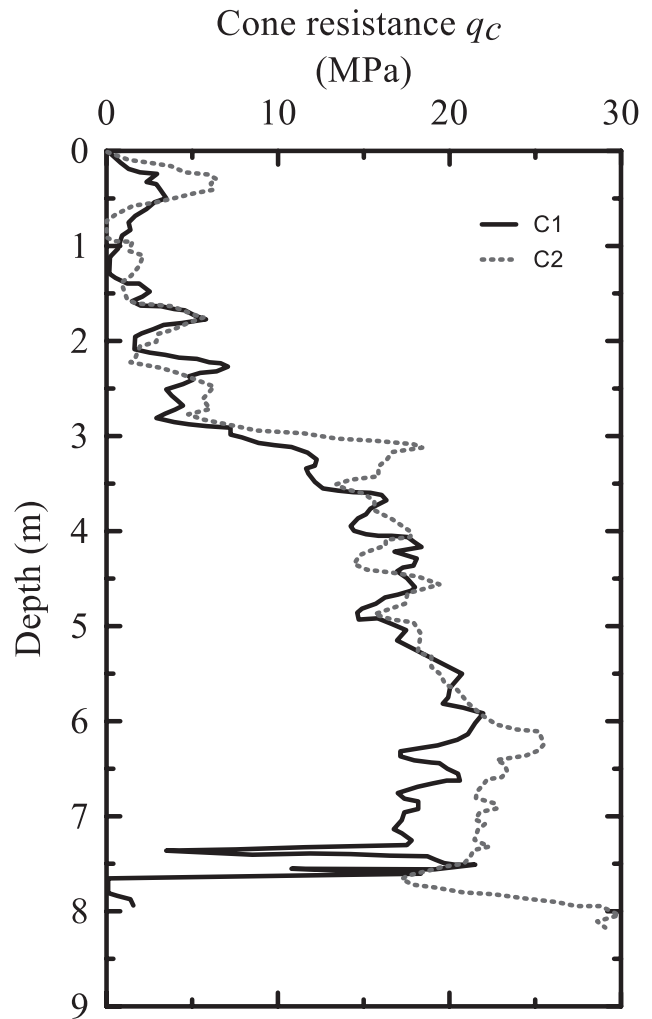


Figure 6.13 Results of CPTs performed at the pile load test site in Lagrange County, Indiana.

transfer curves, residual load and limit shaft resistance profiles were obtained from the data measured by the sensors. When residual loads were considered, the actual base resistance was greater than that directly measured, whereas the shaft resistances were smaller than those directly measured.

The dynamic load tests indicated an increase of the total pile resistance from 1,931 kN at the time of driving to 3,367 kN (757 kip) 22 days after the initial driving, a pile capacity increase resulting mainly from an increase in shaft resistance. Comparisons were made between the bearing capacities obtained from the static and dynamic load tests with those estimated by several well-known CPT-based and property-based pile design methods; additionally, two other static load tests on closed-ended driven pipe piles were used to verify these design methods, most of which yielded satisfactory estimates of pile resistance. However, field test data is still required to continue to validate pile design methods and to elucidate more challenging aspects of pile resistance estimation, such as the evolution of pile capacity and the rate of set up.

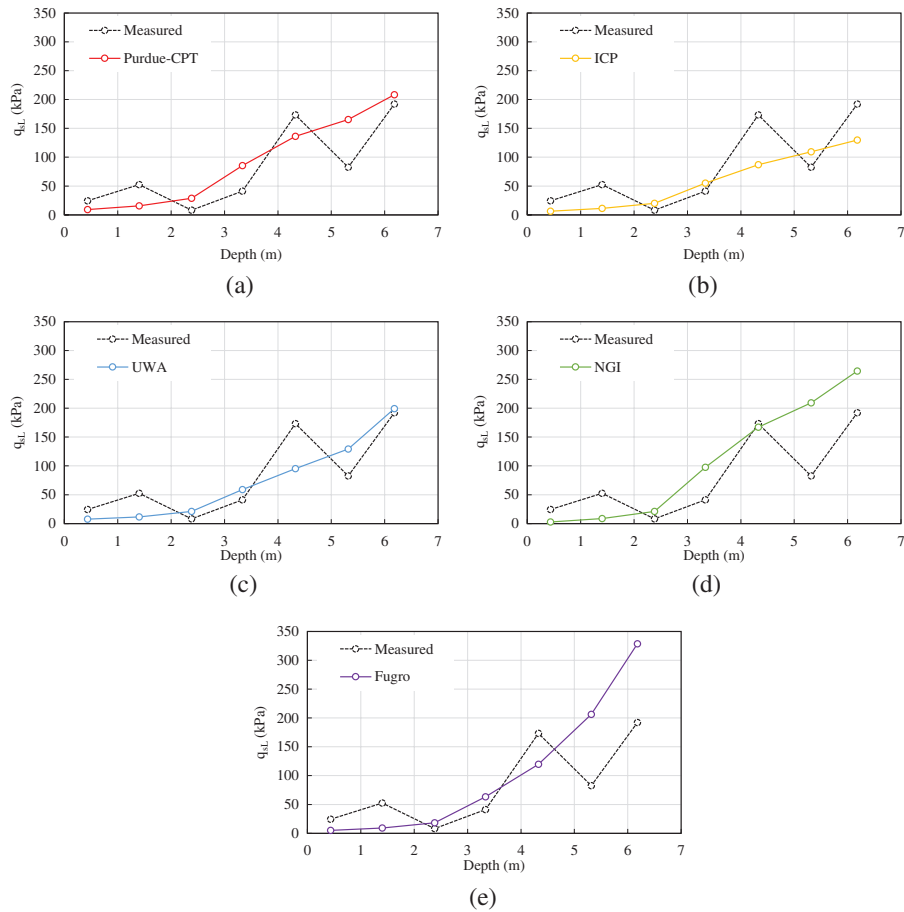


Figure 6.14 Comparison of the unit limit shaft resistance, q_{sL} , obtained from the static load test (not accounting for residual loads) with those estimated using: (a) Purdue-CPT method; (b) ICP method; (c) UWA method; (d) NGI method; and (e) Fugro method.

TABLE 6.9
Soil Profile at the Load Test Site in Lagrange County, Indiana.

Depth (m)	Depth (m)	Soil description	Total unit weight (kN/m ³)	Maximum void ratio	Minimum void ratio	Relative density (%)	Critical-state friction angle (deg)
0–3	0–9.84	Gravelly sand	16.38	0.68	0.41	30	33.3
3–13	9.84–42.7	Gravelly sand	21.20	0.68	0.41	80	33.3

NOTE: Data from Paik et al. (2003).

TABLE 6.10
Comparison of the Predicted Ultimate Base Resistances with the Measured Value of Pile Load Test in Lagrange County, Indiana.

Measured ^a (kN)	Design methods (kN)				
	Purdue-CPT	ICP	UWA	NGI	Fugro
866 (195)	872 (196)	826 (186)	987 (222)	786 (177)	1088 (245)

NOTE: Numbers in parenthesis are in kip.
^aNot accounting for residual loads.

TABLE 6.11
Soil Profile at the Load Test Site in Jasper County, Indiana.

Depth (m)	Depth (ft)	Soil description	Classification of soil type used in pile design	Total unit weight (kN/m ³)	Moisture content (%)	Critical-state friction angle (Deg)	PI (%)	OCR
0–2.9	0–9.5	Organic soil	Clay	13.4	96		89	
2.9–3.7	9.5–12.1	Silty sand	Sand	22	15	31		
3.7–5.7	12.1–18.7	Clayey sandy silt	Clay	21.6	19		8	5.6
5.7–7.3	18.7–24.0	Silt clayey sand	Sand	22	22	29		
7.3–7.8	24.0–25.6	Sandy silty clay	Clay	21	22			8
7.8–9.0	25.6–29.5	Silt clayey sand	Sand	22	22	29		
9.0–10.2	29.5–33.5	Clayey silt	Clay	20.1	25		19	3.2
10.2–12.0	33.5–39.4	Clayey silt	Sand	20.6	23	30		
12.0–14.5	39.4–47.6	Clayey silt	Clay	21.9	15		9	4.9
14.5–17.0	47.6–55.8	Clayey silt	Clay	21.9	11		10	2
17.0–18.4	55.8–60.4	Very dense silt	Sand	21	11	30		

NOTE: Data from Bica et al. (2014) and Kim et al. (2009).

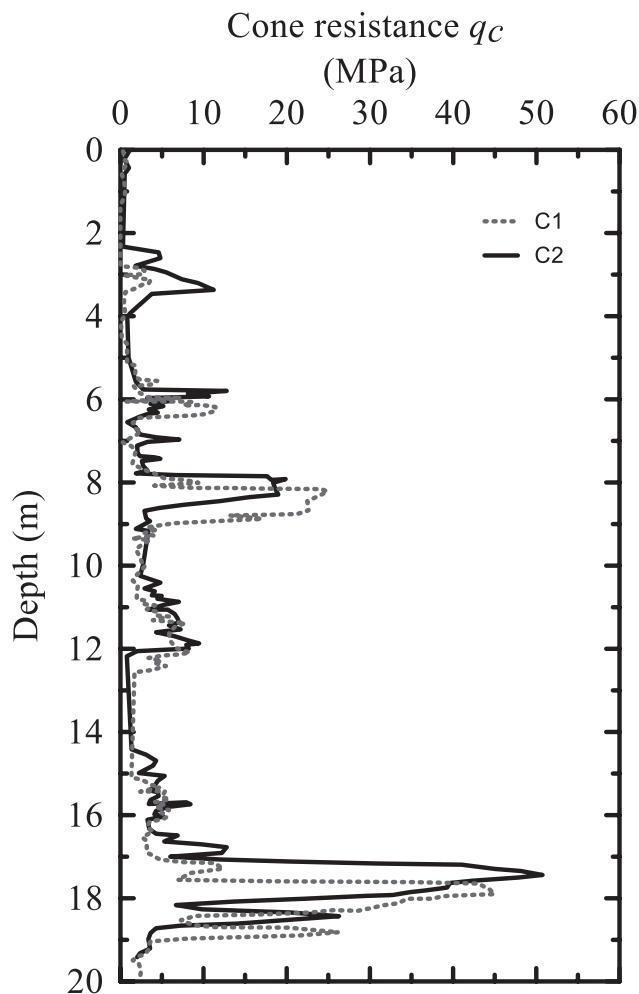


Figure 6.15 Results of CPTs performed at the pile load test site in Jasper County, Indiana.

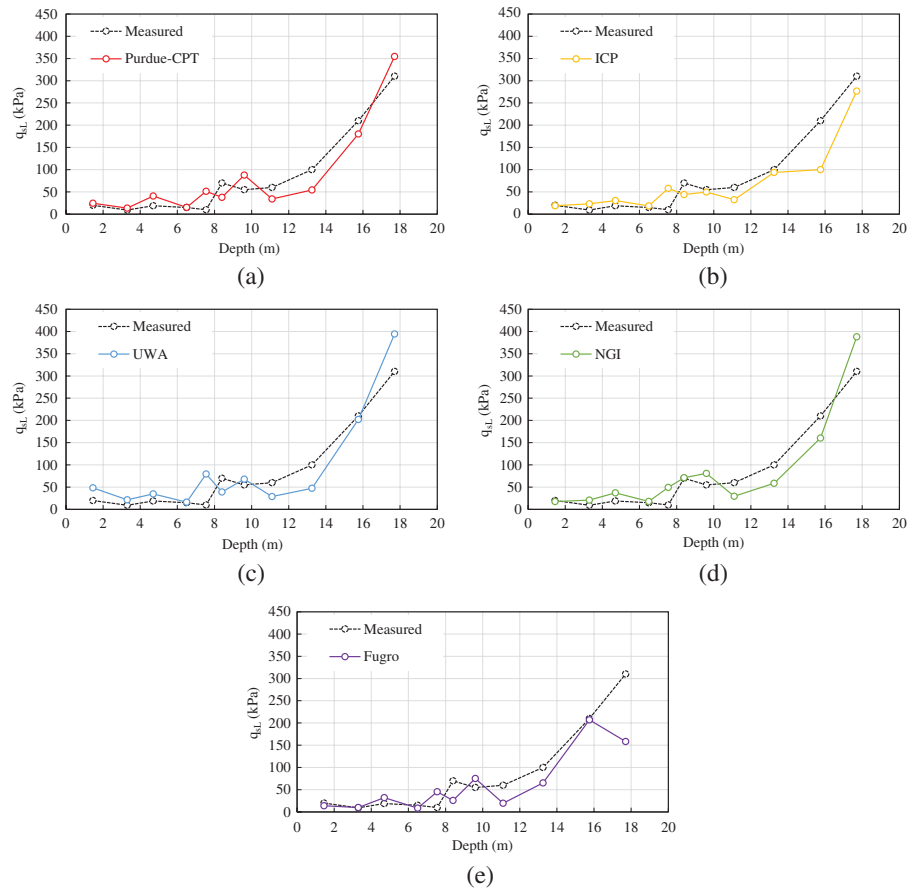


Figure 6.16 Comparison of the unit limit shaft resistance q_{sL} obtained from the static load test (not accounting for residual loads) with those estimated using: (a) Purdue-CPT method; (b) ICP method; (c) UWA method; (d) NGI method; and (d) Fugro method.

TABLE 6.12
Comparison of Predicted Ultimate Base Resistances with the Measured Value of Pile Load Test in Jasper County, Indiana.

Measured ^a (kN)	Design methods (kN)				
	Purdue-CPT	ICP	UWA	NGI	Fugro
399 (90)	1504 (338)	1694 (381)	2023 (455)	1421 (319)	1557 (350)

NOTE: Numbers in parenthesis are in kip.

^aNot accounting for residual loads.

7. LRFD OF PILE GROUPS

7.1 Introduction

The Federal Highway Administration (FHWA) mandate that load and resistance factor design (LRFD) be used for designing the foundations of all bridge structures initiated after September 2007 may have started a trend in the US of change from the traditional Working (or Allowable) Stress Design (WSD or ASD) to LRFD of foundations and geotechnical structures. This is a natural trend because LRFD is conceptually superior to WSD. In LRFD, the

uncertainties associated with the design variables and methodologies can be systematically allocated to factors (the resistance and load factors) that are associated separately with the resistances and applied loads. In contrast, WSD relies on *ad hoc* use of one factor (the factor of safety) that attempts to account for all the uncertainties. Additionally, LRFD allows designing for target probabilities of failure, which is simply not possible in WSD.

LRFD is appropriate for geotechnical design because the variabilities and uncertainties associated with natural systems, the ground in this case, are much greater than

those associated with well controlled engineered systems (Lacasse & Nadim, 1996). Consequently, the development of LRFD methods for various geotechnical problems (e.g., design of foundations, slopes and retaining structures) has been an active field of research since the last decade.

Early efforts toward establishing LRFD codes for geotechnical designs in the US were not sufficiently rigorous. The specifications were calibrated based on a combination of simplistic reliability analysis, fitting to WSD and engineering judgment (Paikowsky, 2004). The lack of rigor followed from the reliance of traditional geotechnical design approaches on *ad hoc* judgment and empirical methods and from the difficulty in quantifying uncertainties associated with geotechnical designs. While that was an acceptable and perhaps necessary approach at the time, future LRFD development can and should be placed on a stronger scientific basis.

A large number of research studies on reliability analysis or LRFD of piles and pile groups have relied on calibrations with respect to field pile load tests to obtain target reliability indices or resistance factors (Allen, Nowak, & Bathurst, 2005; Barker, Duncan, Rojiani, & Ooi, 1991; Paikowsky, 2004; Yoon, Abu-Farsakh, Tsai, & Zhang, 2008; Zhang, Tang, & Ng, 2001). For pile groups, there is an issue of system redundancy, which lowers the possibility of failure of the entire group because the load not carried by one or more piles that fail to correspond to their estimated load-carrying capacity could be transferred to other piles in the group. According to Allen et al. (2005), Barker et al. (1991), Paikowsky (2004), and Zhang et al. (2001), the system redundancy in pile groups would increase the reliability of pile groups with respect to single piles. On the other hand, if pile groups are not extensive, soil conditions should be similar for all piles. That means that, in the absence of construction problems, it is difficult to expect very different response for these piles, precluding the notion that one pile would fail while others remain operational. It is more likely that the piles will respond similarly, eliminating the “redundancy” benefit.

In this report, resistance factors for pile group design using soil variable-based design methods are developed through systematic probabilistic analyses. The present report develops the resistance factors by quantifying individually the uncertainties of basic soil variables appearing in the soil variable-based design equations. By identifying and discriminating the different sources of uncertainties associated with pile group design, more rigorous resistance factors can be suggested for pile groups.

7.2 LRFD Framework

In the LRFD framework, the capacity (total resistance) and demand (applied loads) for an acceptable

design are related through the following inequality:

$$RF \cdot R^n \geq \sum_i LF_i \cdot L_i^n \quad (7.1)$$

where RF = resistance factor, R^n is the nominal (or characteristic) resistance, LF_i = load factor corresponding to the i^{th} nominal (or characteristic) load L_i^n , and the superscript n represents nominal loads and resistances. The nominal loads and resistances indicate the deterministic loads and resistances estimated by design engineers based on design methods or procedures prescribed by codes.

The total resistance developed by a pile group has two components: (1) shaft resistance, $Q_{g,s}$, which is the total shaft resistance available from the interaction of the shafts of the piles in the group and the surrounding soil and (2) base resistance, $Q_{g,b}$, which is the sum of the compressive resistances of the soil below the base of all the piles in the group. Those resistances are developed through totally different mechanisms; near the shaft of an individual pile, soil tends to experience extensive shearing and likely reaches critical state; around the base, soil experiences compressive loading and, as mean stress increases, the shear stress develops to a different degree and at different rates at points around the base. The influence zones of the shaft and base are also very different; the shaft has a relatively small influence zone due to the highly localized deformation near the shaft; the base has relatively large influence zone near the pile base. These different zones of influence lead to different degree of interaction between piles in a group depending on whether the interaction results from base of shaft resistance. It is obvious that shaft and base resistances of pile group are subjected to different sets of uncertainties; this needs to be reflected in two different resistance factors for the shaft and base resistances.

Depending on the type of construction, a great number of load types and load combinations could be considered in LRFD design. In this study, two types of loads, which are dominant and appear in most design situations for pile group are considered: dead load, DL , and live load, LL .

For pile group design, Equation 7.1 can be rewritten as:

$$RF_b Q_{g,b}^n + RF_s Q_{g,s}^n \geq LF_{DL} DL^n + LF_{LL} LL^n \quad (7.2)$$

where $Q_{g,b}^n$ and $Q_{g,s}^n$ are the nominal values for the base and shaft resistances of the pile group, DL^n is the nominal dead load, LL^n is the nominal live load, RF_b and RF_s are resistance factors for base and shaft resistances, and LF_{DL} and LF_{LL} are load factors for dead and live load.

7.3 Pile Group Resistance Equations

7.3.1 Design Criteria

For a single pile, the ultimate load is customarily defined as that load that would cause a settlement of 10% of the pile diameter. For small pile groups (1×2 ,

1 × 3 and 2 × 2 pile groups), the same design criterion, which is 10% of single pile diameter, could be used. However, for larger pile groups, it could be excessively conservative to use 10% of pile diameter as an ultimate limit state criterion and even as a serviceability limit state criterion. Pile groups with a large number of piles behave more like a composite, a block of deep foundation elements with soil between them that would be supporting either an entire structure or, in the case of bridges, a pier that would be at a significant distance from other piers. As pointed out by Salgado (2008), tolerable differential settlements are a function of the span, which is the distance between supported components of the superstructure. Therefore, pile groups can sustain a greater total settlement than a single pile supporting one of many columns that are closer together, as in a residential building, for example.

Ideally, engineers would define the tolerable settlement for each structure specifically. In the absence of that, we rely on the work of Bozozuk (1978) to propose a limiting settlement that should be avoided to prevent serviceability or ultimate limit states from occurring. For small pile groups, we still use a settlement of 10% of the pile diameter as this limiting settlement. For larger pile groups, 50 mm (2 in) is taken as the limiting settlement. This value separates harmful from tolerable vertical movement (see Figure 3.16).

7.3.2 Contribution of Pile Shaft Resistances to Pile Group Resistance

The fraction of the axial resistance of the pile group coming from the shaft resistance of the piles in it can be expressed as:

$$Q_{g,s} = \sum_{i=1}^{N_p} \eta_{shaft,i} Q_{sL,i} \quad (7.3)$$

where $\eta_{shaft,i}$ is the shaft resistance efficiency of i^{th} pile, which can be different depending on the position of the i^{th} pile in the pile group, N_p is the number of piles in the pile group, and $Q_{sL,i}$ is the shaft resistance of the i^{th} pile in the pile group when i^{th} pile is isolated and single; for the i^{th} single pile, in isolation, $Q_{sL} = \sum_j q_{sL,j} A_{s,j}$ where $q_{sL,j}$ is the limit unit shaft resistance along the segment of the i^{th} pile shaft crossing the j^{th} sub-layer, and $A_{s,j}$ is the corresponding shaft surface area. The limit shaft resistance, Q_{sL} , of an isolated single pile can be used as a reference resistance both for small and large pile groups because the shaft resistance of isolated single piles reaches its limit value within 2 to 3% relative settlement, which is smaller than 10% of the pile diameter or 50 mm. In most cases, all piles in the group have the same geometry. In this case, as long as the piles are close enough, Q_{sL} is identical for each pile, and Equation 7.3 can be simplified as:

$$Q_{g,s} = Q_{sL, \text{single}} \sum_{i=1}^{N_p} \eta_{shaft,i} \quad (7.4)$$

where $Q_{sL, \text{single}}$ is Q_{sL} of the isolated single pile.

A shaft resistance group efficiency $\eta_{shaft} \geq 1$ indicates that the interaction between piles in pile group increases the shaft resistance of the individual piles in the group compared with the shaft resistance of an isolated single pile. In this study, η_{shaft} is examined through a number of rigorous numerical simulations. The shaft resistance efficiency, η_{shaft} , changes depending on the settlement level, pile group configuration, center-to-center distance, position of the individual pile in the group (center, side or corner of the group), soil profile and pile length. For small pile groups, with 4 or fewer piles in the group, $\eta_{shaft} \approx 1$. For large pile groups, it varies from 85% to 150% for sand and from 45% to 105% for clay. As far as we know, this is the first time this is investigated, so further research is needed to fully understand and better quantify these effects.

The unit shaft resistance of isolated single piles can be determined by soil variable-based equations depending on pile and soil types. In this study, drilled shafts and driven piles, and sand and clay are considered. Table 7.1 summarizes unit shaft resistance equations for drilled shafts and driven piles in sand or clay.

For CPT-based design, the relative density D_R of sand and the undrained shear strength, s_u , of clay can be calculated from cone resistance, q_c , according to Salgado (2008):

$$\begin{aligned} D_R(\%) &= \frac{\ln\left(\frac{q_c}{p_A}\right) - 0.4947 - 0.1041\phi_c - 0.841 \ln\left(\frac{\sigma'_{ho}}{p_A}\right)}{0.0264 - 0.0002\phi_c - 0.0047 \ln\left(\frac{\sigma'_{ho}}{p_A}\right)} \quad (7.5) \\ &\leq 100\% \end{aligned}$$

and

$$s_u = \frac{q_c - \sigma'_{v0}}{N_k} \quad (7.6)$$

where σ'_{v0} is initial *in-situ* vertical stress, and N_k is the cone factor, which ranges from 11.0 to 13.7 (Salgado, Lyamin, Sloan, & Yu, 2004).

When CPT results are not available but SPT results are, D_R can be estimated by Meyerhof (1957) and Skempton (1987):

$$D_R(\%) = \sqrt{\frac{N_{60}}{A + BC\left(\frac{\sigma'_{v0}}{p_A}\right)}} \quad (7.7)$$

where N_{60} is corrected (standard) SPT blow count, A and B are correlation coefficients, which are $27 \leq A \leq 46$ and $B \approx 27$, and C is a function of the coefficient of earth pressure at rest for normally consolidated soil, $K_{0,NC}$, which is $C = (1 + 2K_0) / (1 + 2K_{0,NC})$. The cone

TABLE 7.1
Unit Shaft Resistance of Drilled Shafts and Driven Piles in Sand or Clay.

Design cases	Unit shaft resistance q_{sL}
Drilled shaft in sand (Salgado, 2008)	$q_{sL} = \left[\frac{K_0}{e^{0.2\sqrt{K_0}-0.4}} C_1 e^{\frac{D_R}{100} [1.3-0.2\ln(\frac{\sigma'_{v0}}{p_A})]} \right] \sigma'_{v0} \tan \phi_c$ <p>where $C_1 = 0.7$ for clean sand in general</p>
Drilled shaft in clay (Chakraborty, Salgado, Basu, et al., 2013)	$q_{sL} = \left(\frac{s_u}{\sigma'_{v0}} \right)^{-0.05} \left[A_1 + (1 - A_1) e^{-\left(\frac{\sigma'_{v0}}{p_A} \right) (\phi_c - \phi_{r,min})^4} \right] s_u$ <p>where $A_1 = 0.75$ for $\phi_c - \phi_{r,min} \leq 5^\circ$, 0.4 for $\phi_c - \phi_{r,min} \geq 12^\circ$ and linearly interpolated value between 0.75 and 0.4 for other cases, and $A_2 = 0.4 + 0.3\ln(s_u / \sigma'_{v0})$.</p>
Driven piles in sand (Randolph, 2003; Salgado et al., 2011)	$q_{sL} = K \sigma'_{v0} \tan \delta_c$ $K = K_{min} + (K_{max} - K_{min}) \exp(-\alpha \frac{h}{B})$ $K_{min} = 0.2$ $K_{max} = 0.02 q_c / \sigma'_{v0}$ <p>where h is the distance from the depth being considered to the pile base; $K_{min} = 0.2$, and $\alpha = 0.05$</p>
Driven piles in clay (Basu et al., 2014)	$q_{sL} = 1.28 \left(\frac{s_u}{\sigma'_{v0}} \right)^{-0.05} \left[A_1 + (1 - A_1) e^{-\left(\frac{\sigma'_{v0}}{p_A} \right) (\phi_c - \phi_{r,min})^4} \right] s_u$ <p>where $A_1 = 0.75$ for $\phi_c - \phi_{r,min} \leq 5^\circ$, 0.4 for $\phi_c - \phi_{r,min} \geq 12^\circ$ and linearly interpolated value between 0.75 and 0.4 for other cases, and $A_3 = 0.64 + 0.4\ln(s_u / \sigma'_{v0})$.</p>

σ'_{v0} = initial *in-situ* vertical effective stress at the depth where q_{sL} is calculated.

ϕ_c = critical-state friction angle of sand.

K_0 = coefficient of earth pressure at rest.

p_A = reference stress (= 100 kPa).

D_R = relative density of sand (%).

s_u = undrained shear strength of clay.

$\phi_{r,min}$ = minimum residual friction angle of clay.

q_c = the representative cone resistance of the soil layer at the depth where q_{sL} is calculated.

δ_c = the interface friction angle ($\delta_c = 0.9 \phi_c$; Foye et al., 2009; Salgado et al., 2011).

resistance, q_c , can be estimated by:

$$q_c = 1.64 p_A e^{0.1041\phi_c + (0.0264 - 0.0002\phi_c) D_R} \left(\frac{\sigma'_{h0}}{p_A} \right)^{0.841 - 0.0047 D_R} \quad (7.8)$$

where σ'_{h0} is initial *in-situ* horizontal effective stress.

7.3.3 Contributions of Pile Base Resistances to Pile Group Resistance

The fraction of pile group axial resistance coming from individual pile base resistances can be expressed as:

$$Q_{g,b} = \sum_{i=1}^{N_p} \eta_{base,i} Q_{b,ult,i} \quad (7.9)$$

where $\eta_{base,i}$ is the base resistance efficiency of i^{th} pile, which can be different depending on the position of the i^{th} pile in the pile group, and $Q_{b,ult,i}$ is the ultimate base resistance of the i^{th} pile in the pile group when i^{th} pile is isolated and single. For the i^{th} single pile, in isolation, $Q_{b,ult} = q_{b,ult} A_b$ where $q_{b,ult}$ is the ultimate unit base resistance of i^{th} pile, and A_b is the area of the pile base. The ultimate base resistance, $Q_{b,ult}$, of the isolated single pile is the load for which the single pile would settle by an amount equal to 10% of the pile diameter.

Based on simulation results for single piles in sand and clay, base resistance increases monotonically as the settlement increases from 30 mm (= 1.2 in = 10% of pile diameter in this study) to 50 mm (= 2 in). The increase ranges from 25% to 30% of base resistance for sand and around 20% for clay. For large pile groups, for which the design criterion is based on a settlement of 50 mm regardless of the diameter of the piles in the group, a factor that may be taken as equal to 1.2 for piles with 0.3 m (= 1 ft) of diameter could be used to correct (by multiplication) for a higher $Q_{b,ult}$ at 50 mm (= 2 in) settlement. This factor likely would be different depending on the pile diameter.

A base resistance group efficiency $\eta_{base} \geq 1$ indicates that the interaction between piles in pile group increases the base resistance of the individual pile in the group compared with the base resistance of isolated single pile. In this study, η_{base} is examined by rigorous numerical simulations. Base resistance group efficiency, η_{base} , depends on the settlement level, pile group configuration, center-to-center distance, position of the individual pile in the group (center, side or corner of the group), soil profiles and the length of the pile. For small pile groups, with 4 or fewer piles in the group, $\eta_{base} \approx 1$. For large pile groups, it varies from 80% to 130% for sand and from 100% to 105% for clay. These

numbers should be considered provisional, with further research needed to arrive at more definitive numbers.

Ultimate unit base resistance for isolated single piles can be determined by soil variable-based equations depending on pile and soil types. In this study, drilled shafts and driven piles, and sand and clay are considered. Table 7.2 presents ultimate unit base resistance equations for drilled shafts and driven piles in sand or clay.

7.4 Live Load/Dead Load Ratio for Transportation Structures

An appropriate range of live to dead load, LL / DL , should be determined for pile group design. Hansell and Viest (1971) reported that LL / DL is a function of dynamic load allowance, IM , and bridge span length L (in meters). IM is a factor converting dynamic load effects into an equivalent static load effect. IM equals to 0.33 based on AASHTO (2012). Mathematically, LL / DL is:

$$LL/DL = \frac{1}{0.0433(1+IM)L} \quad (7.10)$$

In this report, three different ratios of LL / DL are considered: 0.25, 1, and 2. $LL / DL = 0.25$ and 2.0 correspond to bridge span lengths $L = 70\text{m}$ ($= 230\text{ft}$) and 8.5m ($= 28\text{ft}$), respectively.

7.5 Assessment of Uncertainties

7.5.1 Uncertainties of Independent and Dependent Variables

The uncertainties associated with the design variables are quantified by treating each of these variables as a random variable with an associated probability density function (PDF). One measure of variable uncertainty is the sample coefficient of variation (COV). The COV of a random variable x is defined as the ratio of its (estimated) standard deviation, s_x , to its (estimated) mean, \bar{x} :

$$\text{COV} = \frac{s_x}{\bar{x}} \quad (7.11)$$

The COV is a measure of the relative scatter of values of a variable around its mean. The basic idea

behind this quantity is that the absolute measure of scatter around the mean should be proportional to the mean.

Biases often arise in the estimation of the design variables, such as material properties, loads and resistances making the nominal values calculated by the designers different from the corresponding mean values. In such cases, the mean, \bar{x} , and nominal value, $x_{nominal}$, are related through *bias factors* as:

$$\text{bias factor} = \frac{\bar{x}}{x_{nominal}} \quad (7.12)$$

7.5.2 Uncertainties of Models and Transformations

Model and transformation uncertainties arise because the mathematical models (equations) we use are not perfect representation of a process but approximations of the actual behavior based on a set of assumptions.

If a function $y = f(x_1, x_2, \dots, x_n)$ represents a mathematical relationship between y and component variables x_1, x_2, \dots, x_n of function f , the model or transformation uncertainty associated with the function f appears as a difference between realizations (or measurements) y_i and $f(x_{1,i}, x_{2,i}, \dots, x_{n,i})$. A normalized error, w_i^* , can be defined to facilitate the calculations as (Foye, 2005; Lacasse & Nadim, 1996):

$$w_i^* = \frac{y_i - f(x_{1,i}, x_{2,i}, \dots, x_{n,i})}{f(x_{1,i}, x_{2,i}, \dots, x_{n,i})} \quad (7.13)$$

Equation 7.13 can be used to redefine the relationship between y_i and $f(x_{1,i}, x_{2,i}, \dots, x_{n,i})$:

$$\begin{aligned} y_i &= (1 + w_i^*)f(x_{1,i}, x_{2,i}, \dots, x_{n,i}) \\ &= M^{bias} m_i f(x_{1,i}, x_{2,i}, \dots, x_{n,i}) \end{aligned} \quad (7.14)$$

where M^{bias} is deterministic bias in the model f , and m_i is realization of the random variable M representing the random part of the model uncertainty. The bias factor, M^{bias} , is defined as $(1 + \text{the mean value of } w_i^*)$.

The standard deviation, s_w , of w_i can be considered as the standard deviation of the model or transformation f and can be expressed by:

TABLE 7.2
Unit Base Resistance of Drilled Shafts and Driven Piles in Sand or Clay.

Design cases	Unit base resistance $q_{b,ult}$
Drilled shaft in sand (Salgado, 2008)	$q_{b,ult} = 0.23e^{-0.0066D_R} q_c$
Drilled shaft in clay (Salgado, 2006)	$q_{b,ult} = 9.6s_u$
Driven piles in sand (Salgado et al., 2011)	$q_{b,ult} = \min[1, (1.09 - 0.007D_R)]q_c$
Driven piles in clay (Salgado, 2006)	$q_{b,ult} = 10s_u$

D_R = relative density of sand (%).

q_c = the representative cone resistance of the soil layer at the depth where $q_{b,ult}$ is calculated.

s_u is undrained shear strength of clay.

$$s_w = \sqrt{\frac{\sum_{i=1}^n (w_i - \bar{w})^2}{(n-1)}} \quad (7.15)$$

The COV of the model or transformation $f(x_1, x_2, \dots, x_n)$ is:

$$\text{COV} = \frac{s_w}{\bar{w}} \quad (7.16)$$

7.5.3 Summary of Uncertainty Assessments

The uncertainties that we consider in this study are the uncertainties in (a) soil variables, (b) design equations (model uncertainties), (c) applied loads and (d) pile dimensions. We assume pile length, L_p , coefficient of

earth pressure at rest, K_0 , number, N_p of piles in the pile group, and live load-dead load ratio, LL/DL , as deterministic variables. For probabilistic variables, we assume the PDF as either a normal or log-normal distribution and estimate its mean (expected value) and COV. Table 7.3 shows the summary of the assessment of uncertainties. The expected means of the variables are different depending on analysis cases considered in reliability analysis; thus, the means of the variables are not presented in Table 7.3.

7.6 Reliability Analysis

7.6.1 Reliability Index and Most Probable Failure Point

At the limit state, the capacity (the total resistance) equals the demand (the applied loads). Therefore, the

TABLE 7.3
Summary of Uncertainty Assessment (Salgado et al., 2011).

Variables		Quantification	PDF	
Soil variables	Sand	γ	COV = 0.1	normal
		ϕ_c	COV = 0.02	normal
		q_c	COV = 0.08	normal
		N_{60}	COV = 0.3 (optimistic) and 0.5(pessimistic) $A^{mean} = 36.5$, COV = 0.0868	log-normal
		A in Eq.7.7		
	Clay	γ	COV = 0.1	normal
		ϕ_c	COV = 0.03	normal
		$\phi_{r,min}$	COV = 0.044	normal
		q_c	COV = 0.06	normal
Model uncertainties	Drilled shafts in sand	D_R (Eq.7.5)	$\bar{w} = 0.97$, $s_w = 0.1/0.97E(f_{DR})$	normal
		q_{sL}	COV = 0.2	normal
		$q_{b,ult}$	$\bar{w} = 0.97$ for $D_R \leq 50\%$, 1.16 for $D_R \geq 90\%$ and linearly interpolated value for other cases, $s_w = 0.1$	normal
	Drilled shafts in clay	s_u (Eq.7.6)	COV = 0.036	normal
		q_{sL}	COV = 0.1	normal
		$q_{b,ult}$	COV = 0.05	normal
	Driven piles in sand	D_R (Eq.7.5)	$\bar{w} = 0.97$, $s_w = 0.1/0.97E(f_{DR})$	normal
		δ_c	COV = 0.1	normal
		q_{sL}	COV = 0.269	log-normal
		$q_{b,ult}$	COV = 0.217	normal
	Driven piles in clay	s_u	COV = 0.036	normal
q_{sL}		COV = 0.2	normal	
$q_{b,ult}$		COV = 0.05	normal	
Loads	DL	$bias\ factor = 1.05$, COV = 0.1	normal	
	LL		$bias\ factor = 1.15$, COV = 0.18	log-normal
Pile dimension	B	COV = 0.02	normal	

γ = soil unit weight.

$E(f_{DR})$ = mean value of D_R calculated using Equation 7.5.

B = pile diameter.

limit-state performance function can be expressed by:

$$Q_{g,b}^{LS} + Q_{g,s}^{LS} = DL^{LS} + LL^{LS} \quad (7.17)$$

where the superscript LS denotes the limit state. The equation can be rewritten for convenience in mathematical operations as:

$$g(\mathbf{X}) = X_1 + X_2 - X_3 - X_4 = 0 \quad (7.18)$$

where $\mathbf{X} = \{X_1, X_2, X_3, X_4\}$ is the vector of the random variables representing $Q_{g,b}$ ($= X_1$), $Q_{g,s}$ ($= X_2$), DL ($= X_3$), and LL ($= X_4$), respectively. The probability of failure, p_f , is given by:

$$p_f = \int_{g(\mathbf{X}) < 0} f_{\mathbf{X}}(\mathbf{x}) d\mathbf{x} \quad (7.19)$$

where $f_{\mathbf{X}}(\mathbf{x})$ is the joint probability distribution of X_1, X_2, X_3 and X_4 , and \mathbf{x} is the domain of \mathbf{X} .

Based on our assumption that X_1, X_2 and X_3 are normally distributed and X_4 is log-normally distributed (Table 7.3), by performing the Rosenblatt transformation (Ang & Tang, 1975) on X , Equation 7.18 can be expressed in terms of the standard normal variables Y_1, Y_2, Y_3 and Y_4 as:

$$g(\mathbf{Y}) = Y_1\sigma_1 + \mu_1 + Y_2\sigma_2 + \mu_2 - Y_3\sigma_3 - \mu_3 - e^{(Y_4s_4 + m_4)} = 0 \quad (7.20)$$

where $Y_i = (X_i - \mu_i) / \sigma_i$ for $i = 1, 2$ and 3 , $Y_4 = (\ln X_4 - m_4) / s_4$, $s_4 = \sqrt{\ln(1 + \sigma_4^2 / \mu_4^2)}$, $m_4 = \ln \mu_4 - \sigma_4^2 / 2$, and μ_i and σ_i are the mean and standard deviation of X_i (for $i = 1, 2, 3$ and 4). In the standard normal space, p_f is given by:

$$p_f = \int_{g(\mathbf{Y}) < 0} \phi_{\mathbf{Y}}(\mathbf{y}) d\mathbf{y} \quad (7.21)$$

where $\phi_{\mathbf{Y}}(\mathbf{y})$ is the probability density function (PDF) of $g(\mathbf{Y})$, and \mathbf{y} is the domain of \mathbf{Y} . The magnitude of p_f depends on the relative position of the limit-state hyper surface $g(\mathbf{Y}) = 0$ with respect to the origin of the four-dimensional standard normal hyperspace of \mathbf{Y} .

The position of the limit-state surface is often described by the minimum distance, β_{HL} , from the limit state surface to the origin; β_{HL} is commonly known as the Hasofer-Lind reliability index. The greater the value of β_{HL} , the further the limit state surface is from the origin and the smaller the probability of failure. This minimum distance, β_{HL} , is calculated from the origin to a particular point on $g(\mathbf{Y}) = 0$, known as the most probable failure point \mathbf{Y}^* . This point corresponds to the maximum value of the integrand $\phi_{\mathbf{Y}}(\mathbf{y})$. It is important to locate \mathbf{Y}^* because β_{HL} and the corresponding \mathbf{X} , which is $Q_{g,b}^{LS}$, $Q_{g,s}^{LS}$, DL^{LS} , and LL^{LS} in Equation (7.17), depend on it.

For uncorrelated and independent standard nominal variables Y_i with a linear limit-state function, β_{HL} gives

an accurate estimate of the probability of failure as (Basu & Salgado, 2012):

$$p_f = 1 - \Phi(\beta_{HL}) \quad (7.22)$$

where $\Phi(\cdot)$ is the cumulative density function of the standard normal variate. For example, $\beta_{HL} = 3.719, 3.090, 2.326$, and 1.282 for $p_f = 10^{-4}, 10^{-3}, 10^{-2}$, and 10^{-1} , respectively, for standard normal variables with linear limit state functions. The greater β_{HL} is, the smaller is p_f .

7.6.2 Target Probability of Failure for Pile Groups

The target probability of failure, $p_{f,T}$, for pile design has been often taken as 10^{-3} corresponding to a target reliability index, $\beta_{HL,T}$, of 3 (Ellingwood, MacGregor, Galambos, & Cornell, 1982; Foye, 2005). However, it has been argued that, depending on the importance of a structure and the specific type of structure, different $p_{f,T}$ may be required (Fisher, Ravindra, Kulak, & Galambos, 1978; JCSS, 2000).

When we consider single pile designs, a target probability failure, $p_{f,T}$, of 10^{-3} implies that one in every 1,000 piles would fail. This incidence of failures may be too high. It would mean that, in a large project, one pile would likely fail. This would likely be an inconvenience that engineers would rather not have. A $p_{f,T}$ of 10^{-4} , corresponding to one failure in every 10,000, piles would then be more reasonable.

In pile groups, the issue of redundancy has often been raised in advocating for higher acceptable probabilities of failure. As the argument goes, failure of the entire group would be less likely because the load not carried by one or more piles that fail to correspond to their estimated load-carrying capacity could be transferred to other piles in the group. To consider this effect, most researchers have assumed target reliability indices, $\beta_{HL,T}$, to be lower, which correspond to higher $p_{f,T}$, than for single piles (Barker et al., 1991; Kwak, Kim, Huh, Lee, & Park, 2010; Paikowsky, 2004). This view may be overly optimistic, at least for small pile groups.

Since piles in small groups are all in close proximity, variability in the soil is small, so little to no redundancy can be counted on. Save for very large pile groups or piled rafts, it is therefore not advisable to consider a reduction in the p_f on account of redundancy. If pile cap bearing resistance has not been accounted for in pile group capacity calculations, that would offer a cushion of safety, but, again, it should not be considered in determining resistance factors if it is to be considered, but in the geotechnical capacity calculations instead. Finally, the focus of this report is on bridge foundations, which may be harder and more costly to retrofit or reinforce. Therefore, no consideration of redundancy is recommended. Based on these considerations, we decided to use two values of $p_{f,T}$, 10^{-3} and 10^{-4} , in reliability analyses to develop resistance factors for pile group.

7.6.3 Monte Carlo Simulations

Monte Carlo (M-C) simulations are performed to obtain probability distributions of the capacity ($Q_{g,b} + Q_{g,s}$) of the pile group, the demand ($DL + LL$) and their difference. We assumed in our analysis that the capacity and the demand are statistically independent and that all the random variables used in the analysis are uncorrelated.

Depending on the soil type (sand or clay), pile type (drilled shaft or driven pile), and target probability of

failure $p_{f,T}$ (in this study, $p_{f,T} = 10^{-3}$ or 10^{-4}), we can set different sets of input variables for M-C simulations. Input variables consist of deterministic variables (pile length L_p , coefficient of earth pressure at rest K_0 , number of piles N_p in the pile group, and live load-dead load ratio (LL/DL)) and the probabilistic variables in Table 7.3. Figure 7.1 shows the flow chart for M-C simulations.

To obtain a good approximation to the continuous PDFs for $Q_{g,b}$, $Q_{g,s}$, DL , LL and the difference between capacity and demand (capacity – demand), we should

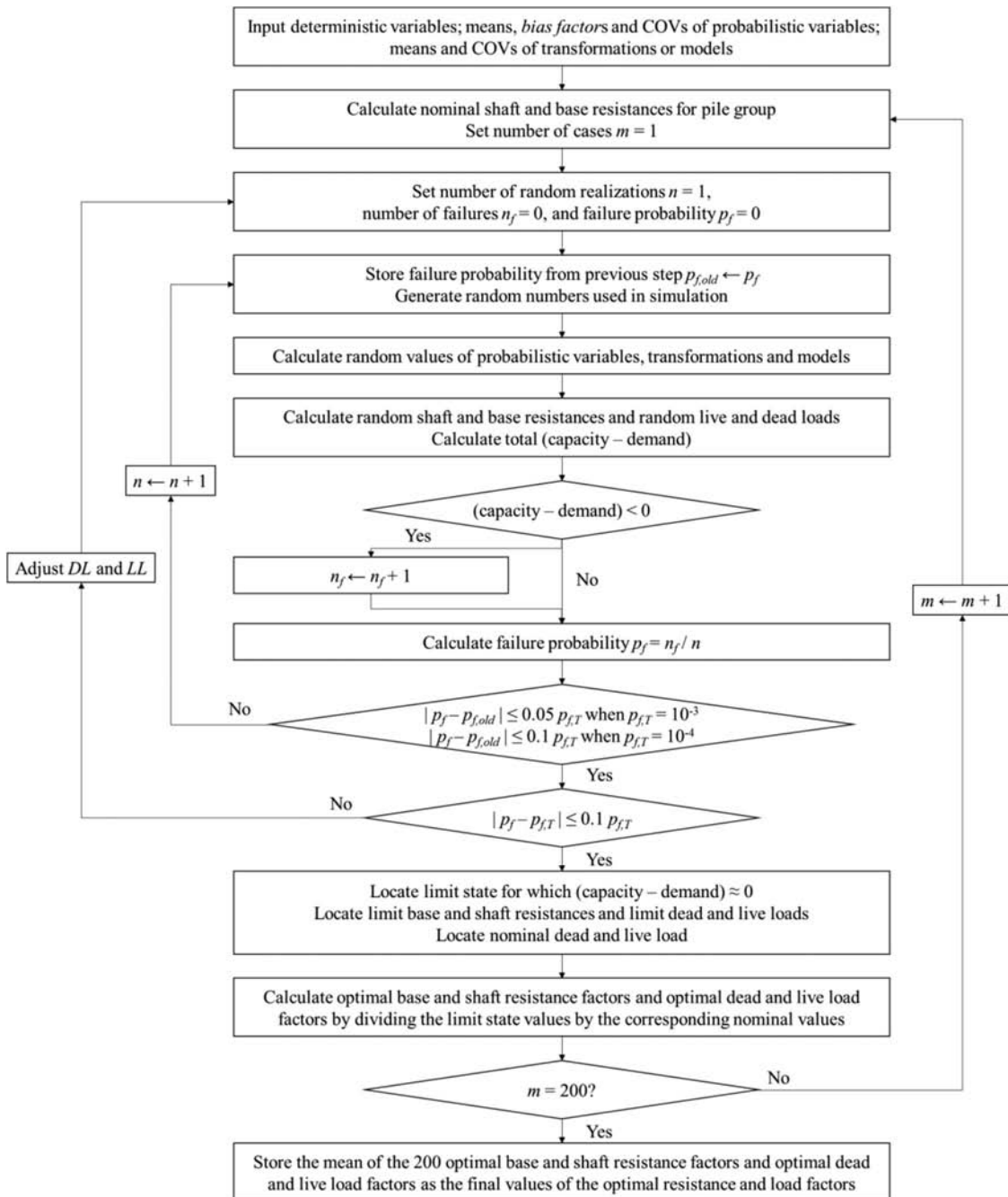


Figure 7.1 Flow chart of Monte Carlo simulations.

generate a sufficient number n of realizations of the random input variables and obtain the corresponding random values of $Q_{g,b}$, $Q_{g,s}$, DL , LL and (capacity – demand). When we have a sufficient number of realizations of the random difference between capacity and demand, we can estimate the probability of failure, p_f , by calculating the ratio n_f/n , where n_f is the number of failure cases, when capacity < demand. To determine if n is sufficiently large, we calculate the ratio n_f/n for each increment of n to evaluate if it has converged. The ratio n_f/n will converge to the theoretical value of p_f as n increases. We determine the convergence of the ratio by evaluating the difference between the ratios at the previous step and the current step. If the difference in calculated p_f is less than $0.05p_{f,T}$ when $p_{f,T} = 10^{-3}$ and $0.10p_{f,T}$ when $p_{f,T} = 10^{-4}$, convergence is assumed.

With the assumed values of DL and LL , the calculated probability of failure p_f will not be equal to $p_{f,T}$. We need to then adjust DL and LL until we obtain p_f approximately equal to $p_{f,T}$. In order to keep the computation time to within reasonable limits, convergence is defined as the calculated p_f being within $\pm 10\%$ of $p_{f,T}$. After the probability of failure has converged to its target value, we find the limit state values of the base and shaft capacities and dead and live loads (for which capacity – demand ≈ 0). The nominal values of resistances and loads are calculated separately and the optimum factors of base and shaft resistances, and dead and live loads are calculated by dividing the ultimate limit state values by the corresponding nominal values according to:

$$RF_b = Q_{g,b}^{LS} / Q_{g,b}^n \quad (7.23)$$

$$RF_s = Q_{g,s}^{LS} / Q_{g,s}^n \quad (7.24)$$

$$LF_{DL} = DL^{LS} / DL^n \quad (7.25)$$

$$LF_{LL} = LL^{LS} / LL^n \quad (7.26)$$

where superscript n denotes the nominal values, and LS denotes the limit state values. Using Equations 7.23 through 7.26, the limit state condition (Eq. 7.17) can be rewritten by:

$$RF_b Q_{g,b}^n + RF_s Q_{g,s}^n = LF_{DL} DL^n + LF_{LL} LL^n \quad (7.27)$$

In design, the equality sign in Equation 7.27 is replaced by “ \geq ” (inequality (Eq. 7.2)), indicating that the sum of the factored resistances must be no less than the sum of the factored loads.

The equality condition (Eq. 7.17) at limit state can be achieved by multiple combinations of limit state values

of resistances ($Q_{g,b}^{LS}$ and $Q_{g,s}^{LS}$) and loads (DL^{LS} and LL^{LS}) depending on different field conditions. Because of this non-uniqueness of the ultimate limit state, the calculations of optimum factors are repeated 200 times and their averaged values (means of the 200 optimal base and shaft resistance factors and dead and live load factors) are used as the final values of the optimal resistance and load factors.

7.6.4 Adjusted Load and Resistance Factors

The resistance and load factors obtained by M-C simulations are optimal factors that satisfy the limit state condition (Equation 7.17). Most pile group designs are done using load factors prescribed in codes. The optimal resistance factors are not compatible with the code-prescribed load factors because their combination does not satisfy the limit state equation (Eq. 7.17). Therefore, the optimal resistance factors should be adjusted to make them compatible with the load factors prescribed in the codes according to Foye et al. (2009):

$$RF^{code} = \min\left(\frac{LF_{DL}^{code}}{LF_{DL}^{opt}}, \frac{LF_{LL}^{code}}{LF_{LL}^{opt}}\right) RF^{opt} \quad (7.28)$$

where RF^{opt} = optimal resistance factor (for either shaft or base resistance) as obtained from the reliability analysis, LF_{DL}^{code} and LF_{LL}^{code} = optimal dead and live load factors obtained from the reliability analysis, and $\min(\cdot, \cdot)$ = minimum of the two arguments within (\cdot). In design, RF^{code} should be used with code-specified load factors; if designs can be done with optimal load factors, RF^{opt} should be used instead. In this study, to obtain the adjusted resistance factors, we used load factors recommended by AASHTO (2012); $LF_{DL}^{code} = 1.25$ and $LF_{LL}^{code} = 1.75$.

7.6.5 Factor of Safety

In order to feel comfortable with Load and Resistance Factor Design, LRFD, framework, some designers like to estimate the equivalent Factor of Safety (FS) of their designs so that they can link their designs by LRFD method with equivalent designs by Working Stress Design method, WSD. Although the traditional factor of safety of the WSD method is not defined in the LRFD framework, a corresponding factor of safety FS can be defined as the ratio of the nominal capacity to the nominal demand ($FS = C^n / D^n$). We calculate the nominal capacity, C^n , by summing up the nominal values of Q_b^n and Q_s^n by using the pile design equations; the nominal demand, D^n , can be defined by the summation of the nominal loads ($D^n = DL^n + LL^n$). Therefore, the factor of safety can be expressed as:

$$FS = \frac{Q_b^n + Q_s^n}{DL^n + LL^n} \quad (7.29)$$

7.7 Practical Cases Considered

To investigate how the optimal load and resistance factors and the corresponding code-adjusted resistance factors depend on various design variables, we consider a range of soil properties, profiles and pile group dimensions that may occur in real field conditions. We focused on single pile cases because use of the pile in a small pile group does not add any significant uncertainty. Uncertainties related to soil profiles, pile dimensions and applied loads are already considered in single pile cases. Based on our rigorous simulation results, group efficiencies (η_{shaft} and η_{base}) for shaft and base pile resistances are close to 1 for small pile groups independently of soil profile, but could deviate significantly from 1 for large pile groups. For the purposes of this report, we use the same resistance factors for large pile groups as for single piles based on the assumption that group efficiencies are deterministic variables. However, more rigorous reliability analyses are needed to clarify the effect of uncertainties related to soil profiles and group efficiency on the resistance factors for large pile groups.

For our analyses, we considered six soil profiles for sand and one soil profile for clay. Figure 7.2 and Figure 7.3 show profiles for sand and clay, respectively. The detailed description on profiles is as follows.

Soil Profiles for Sand

Homogeneous, completely dry deposit of sandy soil with a mean value of relative density, $D_{R,mean}$, equal to 70%. See Figure 7.2(a).

Soil profile (1) with water table located at the ground surface. See Figure 7.2(a).

Completely dry sand deposit with a medium-dense layer, with $D_{R,mean,1} = 50\%$, overlying a dense layer, with $D_{R,mean,2} = 80\%$, that extends to great depth; embedment depth $H_{bearing}$ of pile is twice of mean value of pile diameter B_{mean} , as shown in Figure 7.2(b).

Soil profile (3) with the water table located at a depth of 2 m below the ground surface; $H_{bearing} = 2 B_{mean}$ (Figure 7.2(b)); soil above the water table is assumed to be completely dry

Extremely loose top layer ($D_{R,mean,1} = 20\%$) overlying a dense layer ($D_{R,mean,2} = 80\%$) with the water table located at the ground surface; $H_{bearing} = 2 B_{mean}$ (Figure 7.2(b))

Completely dry four-layer deposits (Figure 7.2(c)):

5 m thickness loose top layer ($D_{R,mean,1} = 30\%$)

5 m thickness medium-dense second layer ($D_{R,mean,2} = 45\%$)

5 m thickness medium-dense to dense third layer ($D_{R,mean,3} = 60\%$)

dense bearing layer ($D_{R,mean,4} = 75\%$) that extends to great depth

Soil Profile for Clay

Homogeneous, completely saturated deposit of normally consolidated (NC) clay with the ratio between mean undrained shear strength $s_{u,mean}$ and mean initial vertical effective stress $\sigma'_{v0,mean}$ equal to 0.17 with water table located at the ground surface. See Figure 7.3(a).

Completely saturated deposit of NC clay with $s_{u,mean} / \sigma'_{v0,mean} = 0.17$ overlying a stiff layer of over-consolidated (OC) clay with OCR = 10 and $s_{u,mean} / \sigma'_{v0,mean} = 1.0$ that extends to great depth; embedment depth $H_{bearing}$ of pile is twice of mean value of pile diameter B_{mean} . The water table is located at the ground surface (Figure 7.3(b)).

As for sand, three different values of mean critical-state friction angle, $\phi_{c,mean}$, and coefficient of earth pressure at rest, K_0 , are considered: $\phi_{c,mean} = 30^\circ, 33^\circ$ and 36° and $K_0 = 0.4, 0.45$ and 0.5 . For clay, three different values of mean minimum residual-state friction angle, $\phi_{r,min,mean}$, equal to $9^\circ, 16^\circ$ and 21° are considered with $\phi_{c,mean} = 21^\circ$.

Mean value of soil unit weight, γ_{mean} , for sand and clay is estimated using:

$$\gamma_{mean} = \frac{G_s + S e_{mean}}{1 + e_{mean}} \gamma_w \quad (7.30)$$

where G_s is the specific gravity of soil solid particles; S is the degree of saturation of soil; γ_w is the unit weight of water ($= 9.81 \text{ kN/m}^3$), and e_{mean} is mean value of void ratio of soil. We assumed G_s to be 2.62 for sand and 2.67 for clay. S is assumed to be 1 below the water table and 0 above the water table. The mean void ratio, e_{mean} , is estimated using different equations for sand and clay. For sand, $e_{mean} = e_{max} - (D_{R,mean} / 100)(e_{max} - e_{min})$ with $e_{max} = 0.9$ and $e_{min} = 0.45$ where e_{max} and e_{min} are maximum and minimum void ratios of sand. For clay, $e_{mean} = N - \lambda \ln(p'_{mean} / p'_A)$ where N is the void ratio of clay at the reference pressure, λ is slope of normal consolidation line in the $e - \ln(p')$ plane, p'_{mean} is the mean effective pressure, and p'_A is the reference pressure ($= 100 \text{ kPa}$).

Table 7.4 shows the various pile dimensions considered in the reliability analyses with respect to soil and pile types.

7.8 Reliability Analyses Results

7.8.1 Drilled Shafts in Sand

Pile resistance of drilled shafts in sand can be estimated using CPT results or SPT results. After performing reliability analyses for the CPT-based design method (see Table 8.1) for drilled shafts in sand for the practical cases that we considered, we found that the optimal load and resistance factors are practically independent of the values of the soil properties, soil profiles and pile dimensions. Figure 7.4 shows optimal factors

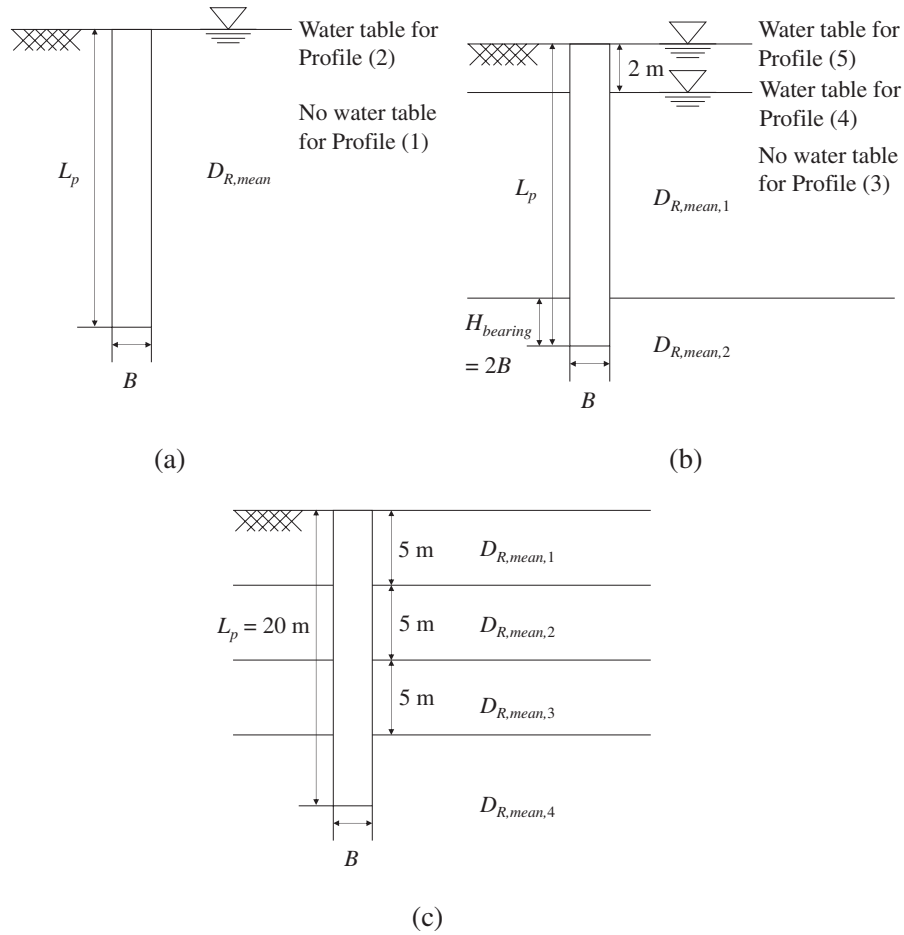


Figure 7.2 Soil profiles for sand: (a) (1) – (2); (b) (3) – (5); and (c) (6) where $D_{R,mean,i}$ = mean relative density of i^{th} layer, B = pile diameter, and L_p = pile length.

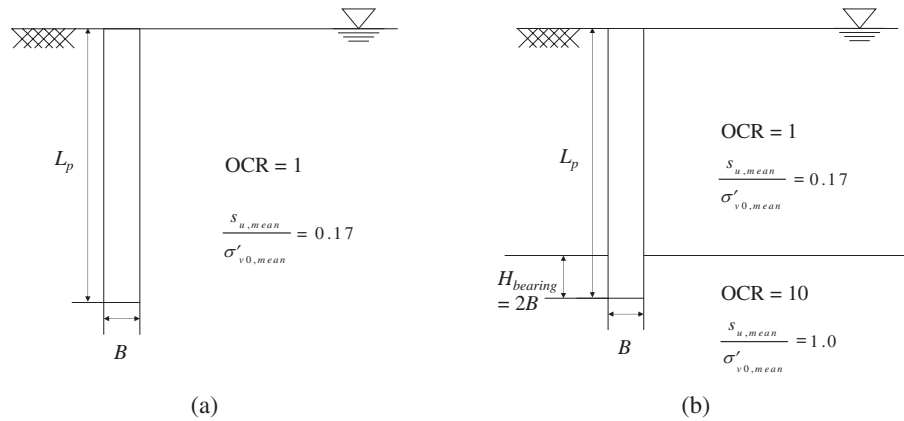


Figure 7.3 Soil profiles for clay: (a) (1); and (b) (2) where $s_{u,mean}$ = mean undrained shear strength of clay, $\sigma'_{v0,mean}$ = mean effective initial vertical stress, OCR = overconsolidation ratio, B = pile diameter, and L_p = pile length.

with various soil properties. Figure 7.4(a) and (b) plot optimal factors versus critical-state friction angle and K_0 , respectively, when a drilled shaft with $B = 1.5$ m (= 4.9 ft) and $L_p = 30$ m (= 98 ft) is installed in soil profile (1) with $LL / DL = 0.25$ and $p_{f,T} = 10^{-3}$.

Similarly to what is observed in Figure 7.4, other analyses with different pile dimensions and soil profiles also showed little change in the optimal factors as soil properties are changed. Figure 7.5 shows optimal factors with various soil profiles when a drilled shaft

TABLE 7.4
Various Pile Dimensions Considered in Reliability Analyses.

Soil type	Pile dimensions
Sand	<i>Drilled shafts:</i>
	$B_{mean} = 0.3 \text{ m} (= 1 \text{ ft})$ and 1.5 m , $L_p = 10 \text{ m} (= 32.8 \text{ ft})$ for CPT-based design in soil profile (1)–(5) and for SPT-based design in soil profile (1)
	$B_{mean} = 0.9 \text{ m}$, $L_p = 10 \text{ m} (= 32.8 \text{ ft})$ for SPT-based design in soil profile (1)
	$B_{mean} = 0.3 \text{ m} (= 1 \text{ ft})$ and 1.5 m , $L_p = 30 \text{ m}$ for CPT-based design in soil profiles (1)–(5)
	$B_{mean} = 1.0 \text{ m}$, $L_p = 20 \text{ m}$ for CPT-based design in soil profile (6)
Clay	<i>Driven piles:</i>
	$B_{mean} = 0.3 \text{ m} (= 1 \text{ ft})$, 0.5 m , 0.7 m and 0.9 m , $L_p = 10 \text{ m} (= 32.8 \text{ ft})$ and 30 m for CPT-based design in soil profiles (1)–(5)
	$B_{mean} = 0.3 \text{ m} (= 1 \text{ ft})$, 0.5 m , 0.7 m and 0.9 m , $L_p = 20 \text{ m}$ for CPT-based design in soil profile (6)
	<i>Drilled shafts:</i>
	$B_{mean} = 0.3 \text{ m} (= 1 \text{ ft})$, 0.9 m and 1.5 m , $L_p = 10 \text{ m} (= 32.8 \text{ ft})$
Clay	<i>Driven piles:</i>
	$B_{mean} = 0.3 \text{ m} (= 1 \text{ ft})$, 0.6 m and 0.9 m , $L_p = 10 \text{ m} (= 32.8 \text{ ft})$

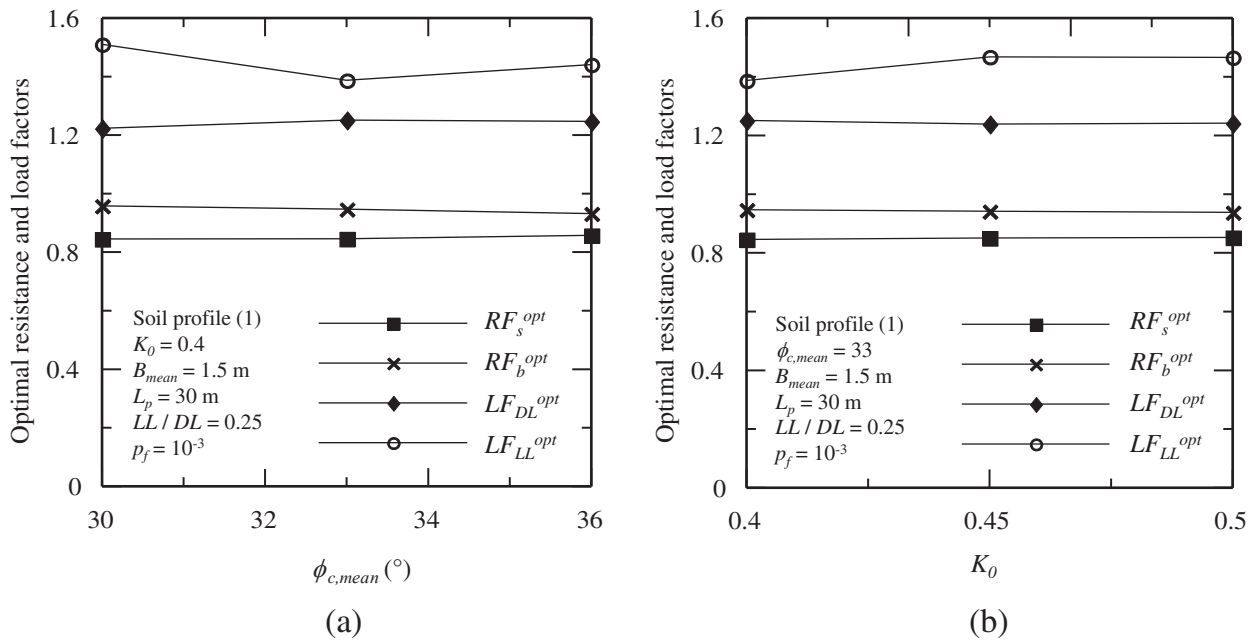


Figure 7.4 Optimal resistance and load factors with various pile dimensions: (a) critical-state friction angle and (b) K_0 for CPT-based design method.

with $B = 1.5 \text{ m} (= 4.9 \text{ ft})$ and $L_p = 10 \text{ m} (= 32.8 \text{ ft})$ is installed in sand with $K_0 = 0.45$, $\phi_c = 33^\circ$, $LL / DL = 1.0$ and $p_{f,T} = 10^{-3}$. Figure 7.6 shows optimal factors for various pile dimensions with soil profile (3) with $K_0 = 0.45$, $\phi_c = 33^\circ$, $LL / DL = 1.0$ and $p_{f,T} = 10^{-4}$.

Figure 7.7 shows optimal load and resistance factors for the CPT-based design method with various LL / DL when a drilled shaft with $B = 1.5 \text{ m} (= 4.9 \text{ ft})$ and $L_p = 30 \text{ m} (= 98 \text{ ft})$ is installed in soil profile (1) with $\phi_c = 33^\circ$, $K_0 = 0.45$ and $p_{f,T} = 10^{-4}$. As shown in Figure 7.7, the optimal load factor for live load LF_{LL}^{opt} is significantly influenced by the live load – dead load ratio LL / DL ; as the ratio LL / DL increases, LF_{LL}^{opt}

increases. These changes in LF_{LL}^{opt} lead to changes in the corresponding factor of safety FS .

Figure 7.8(a) and (b) show FS and optimal load and resistance factors for the CPT-based design method with various values of target probability of failure when a drilled shaft with $B = 0.3 \text{ m} (= 1 \text{ ft})$ and $L_p = 10 \text{ m} (= 32.8 \text{ ft})$ is installed in soil profile (3) with $\phi_c = 33^\circ$, $K_0 = 0.45$ and $LL / DL = 1.0$. As shown in Figure 7.8(a), FS increases as LL / DL increases when p_f is the same. This indicates that the factor of safety is not a true indicator of the reliability of a design. Based on our reliability analysis results, a higher factor of safety is required to achieve the same level of reliability

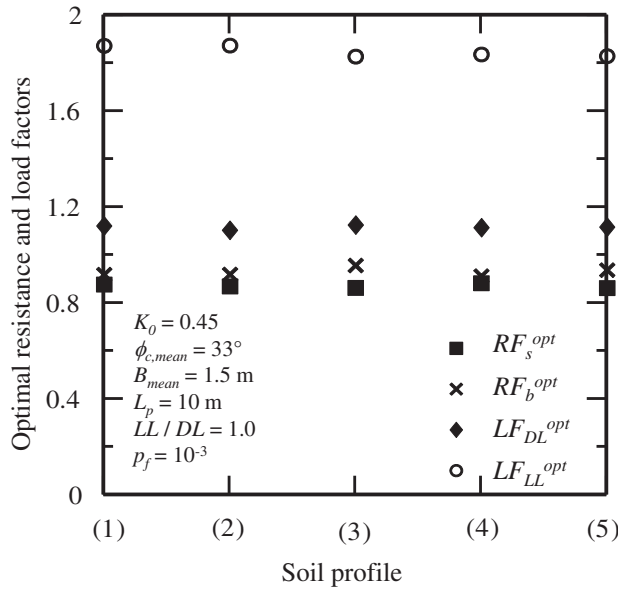


Figure 7.5 Optimal resistance and load factors with various soil profiles for CPT-based design method.

when higher live load – dead load ratio LL / DL is expected in design. Figure 7.8(b) shows that the optimal load factor for live load LF_{LL}^{opt} decreases significantly but other optimal factors do not change much as the probability of failure p_f increases.

The SPT-based design method produced similar trends in optimal load and resistance factors with respect to different soil properties, profiles, pile dimensions, LL / DL and $p_{f,T}$. We can calculate code-adjusted resistance factors, so that they will be compatible with the load factors prescribed by AASHTO (2012), from the obtained optimal load and resistance factors using Equation 7.28. Those load factors are $LF_{DL}^{code} = 1.25$ and $LF_{LL}^{code} = 1.75$. After obtaining code-adjusted resistance factors, we found that they are practically insensitive to soil properties, profiles, pile dimensions and LL / DL and that they are slightly smaller than optimal resistance factors. We found those features of code-adjusted factors both in CPT-based and SPT-based design methods.

Because code-adjusted resistance factors are not very sensitive to soil properties, profiles, pile dimensions and LL / DL , we can consolidate code-adjusted resistance factors for various soil properties, profiles, pile dimensions and LL / DL into a single set of resistance factors with respect to target probability of failure for each design method. As to the CPT-based design method, we first combined resistance factors for different soil properties, pile dimensions and LL / DL and calculated the mean, standard deviation SD and maximum and minimum resistance factors with respect to different soil profiles and target probability of failure $p_{f,T}$ in Table 7.5. As to the SPT-based design method, we consolidated resistance factors for different soil

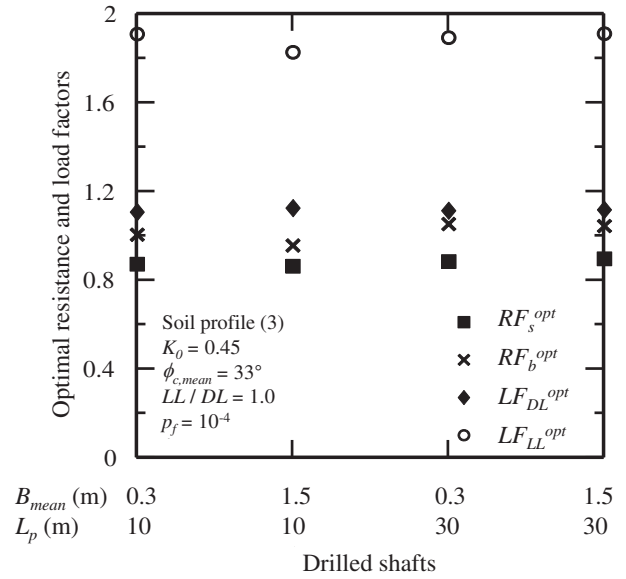


Figure 7.6 Optimal resistance and load factors with various pile dimensions for CPT-based design method.

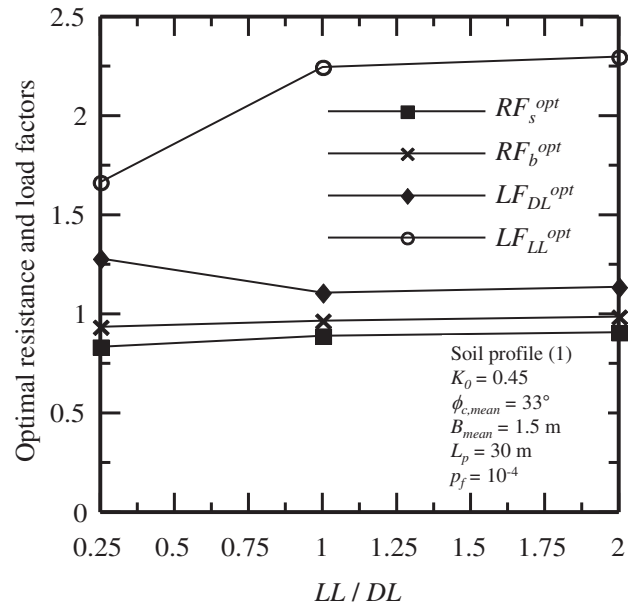


Figure 7.7 Optimal resistance and load factors with various LL/DL for CPT-based design method.

properties and LL / DL and calculated the mean, SD and maximum and minimum resistance factors with respect to different pile dimensions, $p_{f,T}$ and coefficient of variation COV of standard SPT blow count N_{60} in Table 7.6. Table 7.5 and Table 7.6 also contain mean, maximum and minimum values for factors of safety for different soil profiles and $p_{f,T}$. Based on the results in Table 7.5 and Table 7.6, we calculated code-adjusted resistance factors with 99% confidence to provide reasonable and conservative resistance factors: the

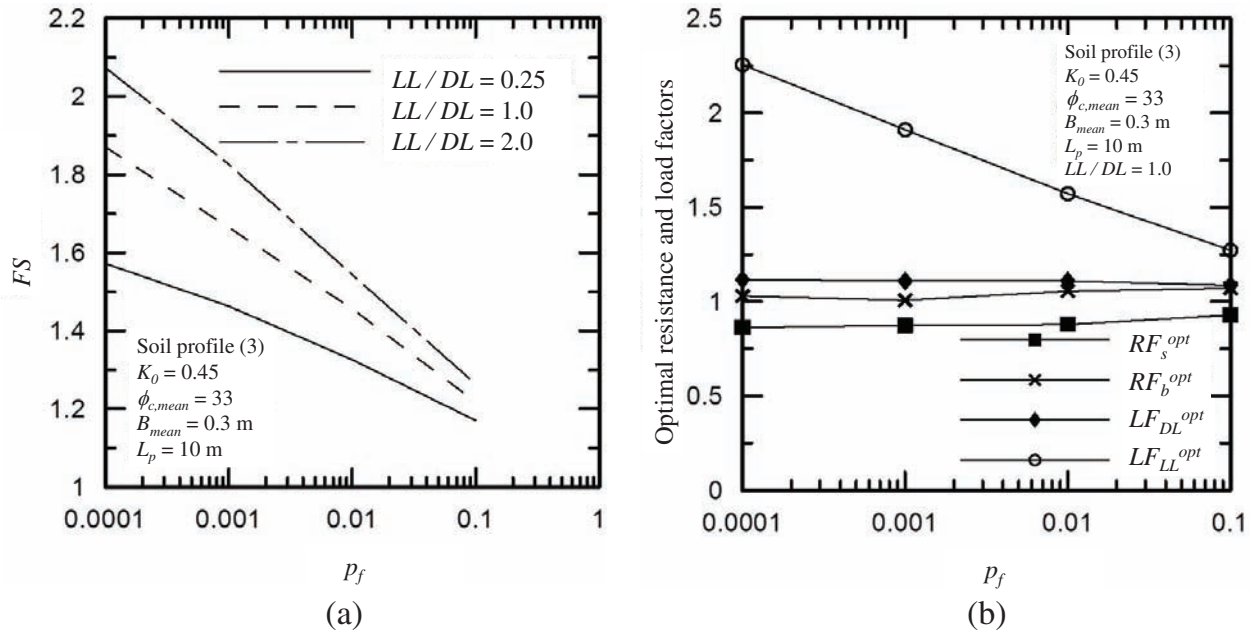


Figure 7.8 (a) Factor of safety and (b) optimal resistance and load factors versus probability of failure for CPT-based design method.

resulting values are $RF_b^{code} = 0.75$ and $RF_s^{code} = 0.70$ with $p_{f,T} = 10^{-3}$ and $RF_b^{code} = 0.70$ and $RF_s^{code} = 0.65$ with $p_{f,T} = 10^{-4}$ for CPT-based design method, $RF_b^{code} = 0.45$ and $RF_s^{code} = 0.60$ with $p_{f,T} = 10^{-3}$ and $RF_b^{code} = 0.35$ and $RF_s^{code} = 0.50$ with $p_{f,T} = 10^{-4}$ for SPT-based method with COV of $N_{60} = 0.3$, and $RF_b^{code} = 0.40$ and $RF_s^{code} = 0.60$ with $p_{f,T} = 10^{-3}$ and $RF_b^{code} = 0.35$ and $RF_s^{code} = 0.50$ with $p_{f,T} = 10^{-4}$ for SPT-based method with COV of $N_{60} = 0.5$. The corresponding factors of safety FS are 1.94 with $p_{f,T} = 10^{-3}$ and 2.08 with $p_{f,T} = 10^{-4}$ for the CPT-based design method, 2.78 with $p_{f,T} = 10^{-3}$ and 3.45 with $p_{f,T} = 10^{-4}$ for the SPT-based method with COV of $N_{60} = 0.3$, and 2.94 with $p_{f,T} = 10^{-3}$ and 3.45 with $p_{f,T} = 10^{-4}$ for SPT-based method with COV of $N_{60} = 0.5$. We recommend the values of resistance factors listed above for pile group design for drilled shafts in sand.

7.8.2 Drilled Shafts in Clay

Pile resistance of drilled shafts in clay can be estimated using CPT results or undrained shear strength s_u results. After performing reliability analyses for cases that we considered for both CPT-based and s_u -based design methods, we found similar trends in optimal load and resistance factors to those for drilled shafts in sand with respect to different soil properties, soil profiles, pile dimensions, LL/DL and $p_{f,T}$: (1) the optimal load and resistance factors are practically independent of soil properties, soil profiles and pile dimensions. (2) The optimal load factor for live load LF_{LL}^{opt} is significantly influenced by LL/DL . (3) LF_{LL}^{opt} decreases significantly but other optimal

factors do not change significantly as probability of failure p_f increases. As for code-adjusted resistance factors, both design methods also yielded similar results to those for drilled shafts in sand: (1) the code-adjusted resistance factors are practically insensitive to soil properties, soil profiles, pile dimensions and LL/DL . (2) The code-adjusted resistance factors are slightly less than optimal resistance factors.

Based on these results, we combined code-adjusted resistance factors for various soil properties, soil profiles, pile dimensions and LL/DL to suggest a set of resistance factors for each pile group design method. Table 7.7 shows the calculated mean, SD and maximum and minimum resistance factors for various soil properties, soil profiles and LL/DL with respect to different pile dimensions and two values of $p_{f,T}$ that should bound values of interest for CPT-based and s_u -based design methods. Table 7.7 also contains mean, maximum and minimum values of factors of safety FS with respect to pile dimensions and $p_{f,T}$ for CPT-based and s_u -based design methods. Based on the results in Table 7.7, we calculated code-adjusted resistance factors with 99% confidence as: $RF_b^{code} = 0.70$ and $RF_s^{code} = 0.75$ for $p_{f,T} = 10^{-3}$ and $RF_b^{code} = 0.65$ and $RF_s^{code} = 0.70$ for $p_{f,T} = 10^{-4}$ for the CPT-based design method, and $RF_b^{code} = 0.50$ and $RF_s^{code} = 0.45$ for $p_{f,T} = 10^{-3}$ and $RF_b^{code} = 0.40$ and $RF_s^{code} = 0.40$ for $p_{f,T} = 10^{-4}$ for the s_u -based method. The corresponding factors of safety FS are 1.94 for $p_{f,T} = 10^{-3}$ and 2.08 for $p_{f,T} = 10^{-4}$ for the CPT-based design method, and 3.05 for $p_{f,T} = 10^{-3}$ and 3.56 for $p_{f,T} = 10^{-4}$ for the s_u -based method. We recommend the resistance factors listed above for pile group design for drilled shafts in clay.

TABLE 7.5
Code-Adjusted Base and Shaft Resistance Factors, RF_b^{code} and RF_s^{code} , for $LF_{DL}^{code} = 1.25$ and $LF_{LL}^{code} = 1.75$, and Different Drilled Shafts in Sand for CPT-Based Design Method.

p_f, T	Soil profile														
	(1)		(2)		(3)		(4)		(5)		(6)				
Statistics	RF_b^{code}	RF_s^{code}	FS	RF_b^{code}	RF_s^{code}	FS	RF_b^{code}	RF_s^{code}	FS	RF_b^{code}	RF_s^{code}	FS	RF_b^{code}	RF_s^{code}	FS
10^{-3}	0.916	0.805	1.65	0.970	0.801	1.64	0.959	0.823	1.66	0.955	0.821	1.68	0.956	0.815	1.69
Mean	0.062	0.027	—	0.050	0.023	—	0.069	0.024	—	0.069	0.022	—	0.069	0.026	—
SD	0.984	0.851	1.96	1.067	0.852	1.80	1.091	0.861	1.81	1.088	0.856	1.82	1.088	0.851	1.85
Maximum	0.789	0.745	1.55	0.890	0.774	1.56	0.867	0.789	1.54	0.862	0.789	1.54	0.856	0.766	1.55
Minimum	0.809	0.704	1.98	0.831	0.715	1.84	0.851	0.723	1.83	0.848	0.721	1.83	0.847	0.713	1.92
10^{-4}	0.077	0.029	—	0.103	0.052	—	0.101	0.053	—	0.101	0.051	—	0.098	0.048	—
Mean	0.947	0.760	2.19	1.036	0.808	2.20	1.062	0.814	2.14	1.059	0.807	2.15	1.057	0.799	2.17
SD	0.708	0.663	1.76	0.706	0.657	1.63	0.734	0.667	1.60	0.729	0.667	1.61	0.730	0.654	1.62
Maximum															
Minimum															

p_f, T = target probability of failure.
SD = standard deviation.

TABLE 7.6
Code-Adjusted Base and Shaft Resistance Factors, RF_b^{code} and RF_s^{code} , for $LF_{DL}^{code} = 1.25$ and $LF_{LL}^{code} = 1.75$, and Drilled Shafts in Sand for SPT-Based Design Method.

p_f, T	COV of $N_{60} = 0.3$												COV of $N_{60} = 0.5$															
	$B / L_p = 0.03$				$B / L_p = 0.15$				$B / L_p = 0.03$				$B / L_p = 0.15$				$B / L_p = 0.03$				$B / L_p = 0.15$							
Statistics	RF_b^{code}	RF_s^{code}	FS	RF_b^{code}	RF_s^{code}	FS	RF_b^{code}	RF_s^{code}	FS	RF_b^{code}	RF_s^{code}	FS	RF_b^{code}	RF_s^{code}	FS	RF_b^{code}	RF_s^{code}	FS	RF_b^{code}	RF_s^{code}	FS	RF_b^{code}	RF_s^{code}	FS	RF_b^{code}	RF_s^{code}	FS	
10^{-3}	0.721	0.808	1.88	0.651	0.888	1.93	0.641	0.791	0.791	0.641	0.791	0.791	0.641	0.791	0.791	0.641	0.791	0.791	0.641	0.791	0.791	0.641	0.791	0.791	0.641	0.791	0.791	0.641
Mean	0.120	0.083	—	0.073	0.123	—	0.114	0.081	—	0.114	0.081	—	0.114	0.081	—	0.114	0.081	—	0.114	0.081	—	0.114	0.081	—	0.114	0.081	—	
SD	1.187	1.081	3.00	0.936	1.360	3.06	1.148	1.010	3.06	1.148	1.010	3.06	1.148	1.010	3.06	1.148	1.010	3.06	1.148	1.010	3.06	1.148	1.010	3.06	1.148	1.010	3.06	
Maximum	0.433	0.530	1.24	0.429	0.528	1.31	0.356	0.503	1.31	0.356	0.503	1.31	0.356	0.503	1.31	0.356	0.503	1.31	0.356	0.503	1.31	0.356	0.503	1.31	0.356	0.503	1.31	
Minimum	0.645	0.725	2.09	0.588	0.806	2.14	0.559	0.697	2.14	0.559	0.697	2.14	0.559	0.697	2.14	0.559	0.697	2.14	0.559	0.697	2.14	0.559	0.697	2.14	0.559	0.697	2.14	
10^{-4}	0.109	0.079	—	0.062	0.117	—	0.103	0.081	—	0.103	0.081	—	0.103	0.081	—	0.103	0.081	—	0.103	0.081	—	0.103	0.081	—	0.103	0.081	—	
Mean	1.000	0.911	3.22	0.774	1.208	3.25	0.914	0.895	3.25	0.914	0.895	3.25	0.914	0.895	3.25	0.914	0.895	3.25	0.914	0.895	3.25	0.914	0.895	3.25	0.914	0.895	3.25	
SD	0.393	0.500	1.48	0.402	0.501	1.53	0.324	0.510	1.53	0.324	0.510	1.53	0.324	0.510	1.53	0.324	0.510	1.53	0.324	0.510	1.53	0.324	0.510	1.53	0.324	0.510	1.53	
Maximum																												
Minimum																												

p_f, T = target probability of failure.
SD = standard deviation.
 B = pile diameter.
 L_p = pile length.
COV = coefficient of variation.
 N_{60} = corrected (standard) SPT blow count.

TABLE 7.7
Code-Adjusted Base and Shaft Resistance Factors, RF_b^{code} and RF_s^{code} , for $LF_{DL}^{code} = 1.25$ and $LF_{LL}^{code} = 1.75$, and Drilled Shafts in Clay.

$p_{f,T}$	Statistics	CPT-based design method						s_u -based design method					
		$B / L_p = 0.03$			$B / L_p = 0.15$			$B / L_p = 0.03$			$B / L_p = 0.15$		
		RF_b^{code}	RF_s^{code}	FS	RF_b^{code}	RF_s^{code}	FS	RF_b^{code}	RF_s^{code}	FS	RF_b^{code}	RF_s^{code}	FS
10^{-3}	Mean	0.902	0.885	1.60	0.861	0.923	1.62	0.756	0.638	2.15	0.674	0.729	2.14
	SD	0.083	0.063	—	0.063	0.079	—	0.109	0.076	—	0.072	0.127	—
	Maximum	1.161	1.041	2.24	1.018	1.150	2.16	1.123	0.935	3.51	0.960	1.275	4.08
	Minimum	0.581	0.676	1.32	0.679	0.684	1.32	0.440	0.414	1.46	0.419	0.317	1.34
10^{-4}	Mean	0.852	0.829	1.78	0.801	0.874	1.79	0.684	0.565	2.40	0.598	0.643	2.42
	SD	0.076	0.057	—	0.058	0.074	—	0.102	0.056	—	0.064	0.093	—
	Maximum	1.065	0.955	2.39	0.939	1.070	2.33	0.995	0.727	3.84	0.809	0.897	3.61
	Minimum	0.627	0.628	1.49	0.615	0.674	1.49	0.396	0.385	1.74	0.407	0.424	1.76

$p_{f,T}$ = target probability of failure.

s_u = undrained shear strength.

SD = standard deviation.

B = pile diameter.

L_p = pile length.

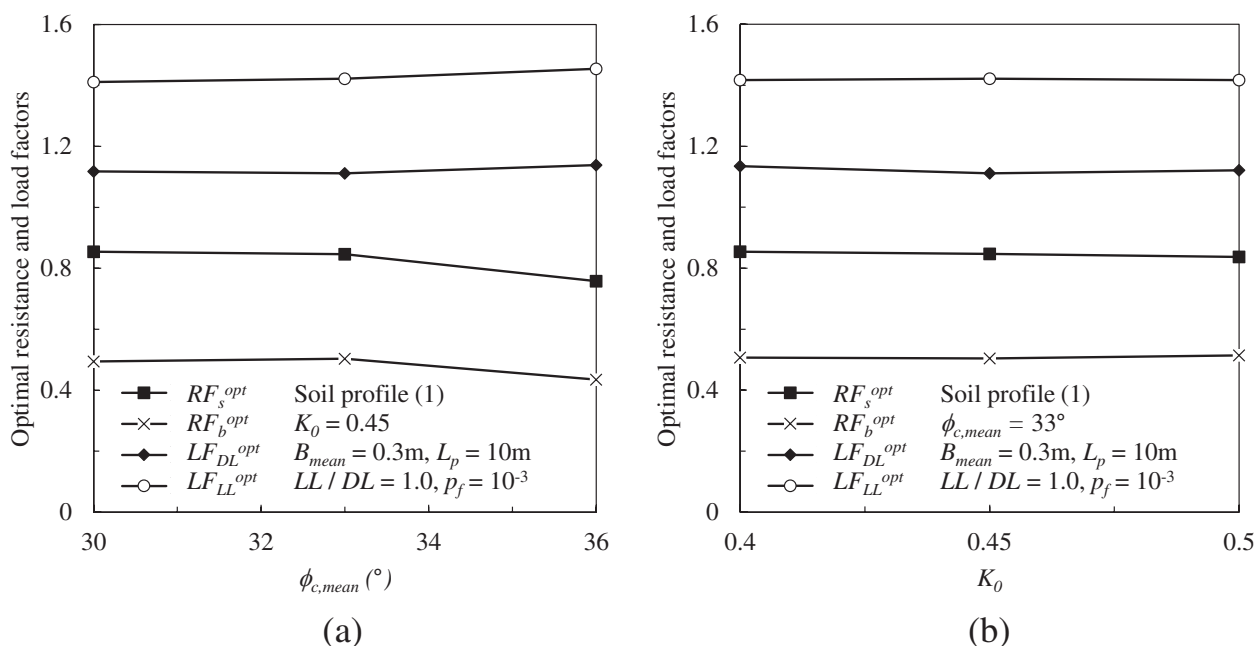


Figure 7.9 Optimal load and resistance factors with various (a) $\phi_{c,mean}$ and (b) K_0 .

7.8.3 Driven Piles in Sand

The resistance of driven piles in sand can be estimated using CPT results or SPT results. In this report, we focus on the CPT-based design method (see Table 8.1) to obtain resistance factors through reliability analyses. After performing Monte Carlo simulations for a range of cases that are expected to represent field conditions, we found that optimal resistance and load factors are

practically insensitive to soil properties and profiles. Figure 7.9 shows optimal load and resistance factors for various values of (a) critical-state friction angle, $\phi_{c,mean}$, and (b) coefficient of earth pressure at rest, K_0 , when a driven pile is installed in soil profile (1) with $B_{mean} = 0.3$ m (= 1 ft), $L_p = 10$ m (= 32.8 ft), $LL / DL = 1.0$ and $p_{f,T} = 10^{-3}$. Similarly, Figure 7.10 shows optimal load and resistance factors for various soil profiles with $\phi_{c,mean} = 33^\circ$, $K_0 = 0.45$, $B_{mean} = 0.3$

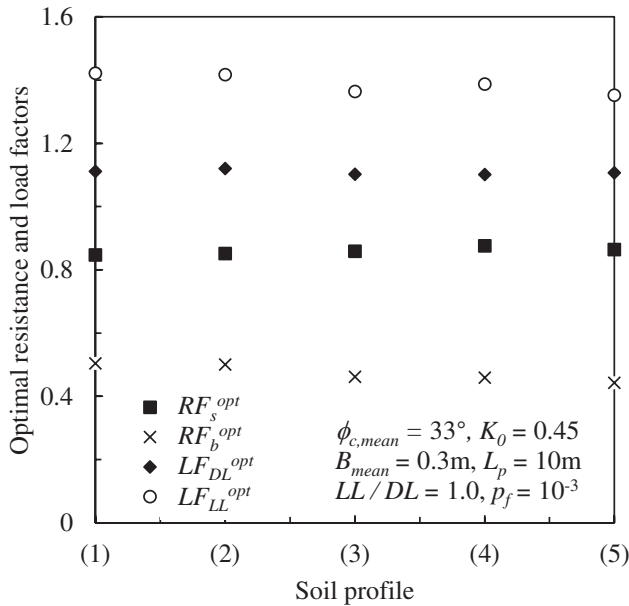


Figure 7.10 Optimal load and resistance factors with various soil profiles.

$m = 1$ ft), $L_p = 10$ m (= 32.8 ft), $LL / DL = 1.0$ and $p_{f,T} = 10^{-3}$.

Figure 7.11 shows optimal load and resistance factors for different pile diameters B_{mean} with $\phi_{c,mean} = 33^\circ$, $K_0 = 0.45$, $LL / DL = 1.0$, and $p_f = 10^{-3}$. Figure 7.11(a) plots optimal values when a 10-m-long driven pile is installed in soil profile (1). Figure 7.11(b) shows optimal values when a 20-m-long driven pile is installed in soil profile (6). Figure 7.11(c) shows optimal values when a 30-m-long (98-ft-long) driven pile is installed in soil profile (1). Based on Figure 7.11, LF_{LL}^{opt} and RF_b^{opt} decrease with increasing B_{mean} up to 15% and 30%, respectively. To figure out the relationship between optimal factors and pile dimensions, we plot optimal load and resistance factors for different aspect ratios B_{mean} / L_p in Figure 7.12. We found that RF_s^{opt} slightly increases and RF_b^{opt} slightly decreases as the aspect ratio increases. The variation ranges are about 30% from $B_{mean} / L_p = 0.01$ to $B_{mean} / L_p = 0.09$.

Optimal factors for driven piles in sand are also slightly sensitive to LL / DL and p_f . Figure 7.13 and Figure 7.14 show the optimal load and resistance factors for various values of LL / DL and p_f . LF_{LL}^{opt} slightly increases as LL / DL increases, and RF_b^{opt} increases as p_f increases.

As for code-adjusted resistance factors: (1) the code-adjusted resistance factors are practically insensitive to soil properties, soil profiles, pile dimensions and LL / DL . (2) The code-adjusted resistance factors are slightly higher than optimal resistance factors.

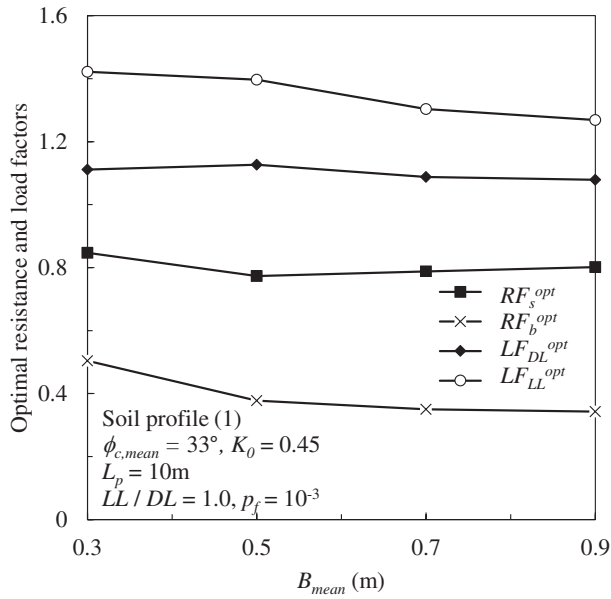
Because code-adjusted resistance factors are not very sensitive to soil properties, profiles, pile dimensions and LL / DL , we combine code-adjusted resistance factors for various soil properties, profiles, pile dimensions and

LL / DL into a single set of resistance factors with respect to target probability of failure $p_{f,T}$. Table 7.8 shows the mean, SD and maximum and minimum resistance factors with respect to different $p_{f,T}$. Table 7.8 also shows the mean, maximum and minimum values of factors of safety FS for different $p_{f,T}$. Based on the results in Table 7.8, we calculated code-adjusted resistance factors with 95% confidence as $RF_b^{code} = 0.32$ and $RF_s^{code} = 0.64$ with $p_{f,T} = 10^{-3}$ and $RF_b^{code} = 0.30$ and $RF_s^{code} = 0.64$ with $p_{f,T} = 10^{-4}$ for CPT-based design method. The corresponding factors of safety FS are 2.85 with $p_{f,T} = 10^{-3}$ and 2.90 with $p_{f,T} = 10^{-4}$. We recommend the values of resistance factors listed above for pile group design for drilled shafts in sand.

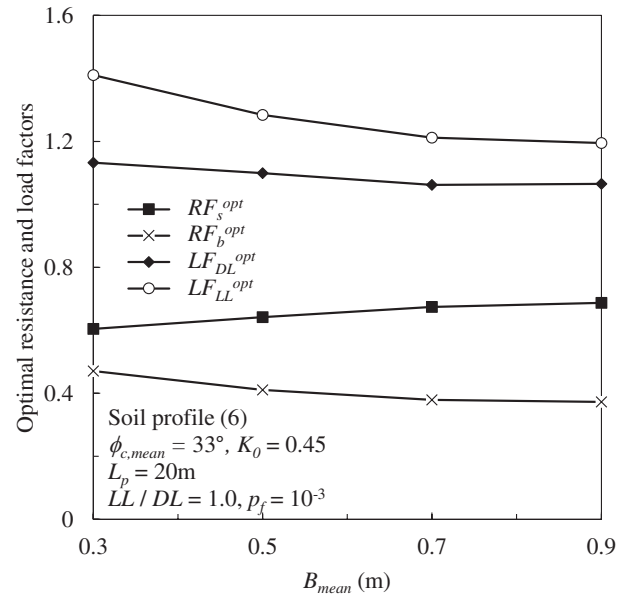
7.8.4 Driven Piles in Clay

Pile resistance of driven piles in clay can be estimated using CPT results or measured undrained shear strength s_u . After performing rigorous reliability analyses for both design methods, we found that (1) the optimal load and resistance factors are practically independent of soil properties, soil profiles and pile dimensions, (2) the optimal load factor for live load LF_{LL}^{opt} is significantly influenced by LL / DL , and (3) LF_{LL}^{opt} decreases significantly but the other optimal factors remain practically unchanged as probability of failure p_f increases. As for code-adjusted resistance factors, both design methods show that (1) the code-adjusted resistance factors are fairly insensitive to soil properties, soil profiles, pile dimensions and LL / DL , and (2) the code-adjusted resistance factors are slightly less than the optimal resistance factors.

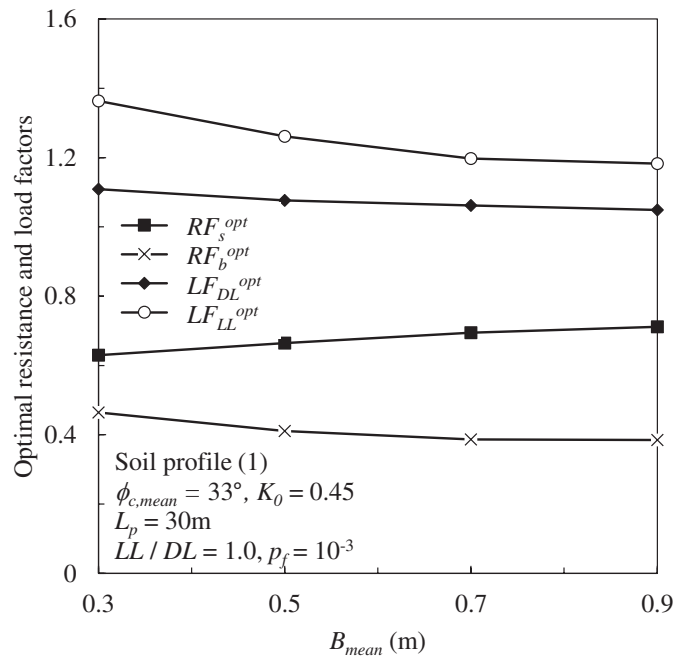
Because code-adjusted resistance factors are fairly insensitive to soil properties, soil profiles, pile dimensions and LL / DL , we combined the code-adjusted resistance factors for different soil properties, soil profiles, pile dimensions and LL / DL to suggest a set of resistance factors for each pile group design method. Table 7.9 presents the calculated mean, SD and maximum and minimum values of code-adjusted resistance factors for various soil profiles and different values of soil properties and LL / DL ; those are calculated for different pile dimensions and $p_{f,T}$ for CPT-based and s_u -based designs, respectively. Table 7.9 also contains mean, maximum and minimum values for factors of safety FS with respect to pile dimensions and $p_{f,T}$ for CPT-based and s_u -based design methods. Based on the results in Table 7.9, we calculated code-adjusted resistance factors with 99% confidence to be: $RF_b^{code} = 0.70$ and $RF_s^{code} = 0.70$ for $p_{f,T} = 10^{-3}$ and $RF_b^{code} = 0.70$ and $RF_s^{code} = 0.65$ for $p_{f,T} = 10^{-4}$ for the CPT-based design method, and $RF_b^{code} = 0.50$ and $RF_s^{code} = 0.45$ for $p_{f,T} = 10^{-3}$ and $RF_b^{code} = 0.45$ and $RF_s^{code} = 0.40$ for $p_{f,T} = 10^{-4}$ for the s_u -based method. The corresponding factors of safety FS are 2.03 for $p_{f,T} = 10^{-3}$ and 2.12 for $p_{f,T} = 10^{-4}$ for the CPT-based design method; and 3.02 for $p_{f,T} = 10^{-3}$ and 3.38 for $p_{f,T} = 10^{-4}$ for the s_u -based method. We recommend the resistance



(a)



(b)



(c)

Figure 7.11 Optimal load and resistance factors for various pile diameter B_{mean} with (a) pile length, $L_p = 10$ m (= 33 ft); (b) $L_p = 20$ m (= 66 ft); and (c) $L_p = 30$ m (= 98 ft).

factors listed above for pile group design for driven piles in clay.

7.8.5 Recommended Resistance Factors for Pile Groups

Table 7.10 summarizes the recommended resistance factors for use in pile group design with $LF_{DL}^{code} = 1.25$ and $LF_{LL}^{code} = 1.75$.

7.9 Conclusions

Systematic probabilistic analyses were performed to develop resistance factors for pile group design considering displacement and nondisplacement piles, a range of soil conditions, and two values of target probability of failure. The higher value of probability of failure (10^{-3}) may be used only for noncritical

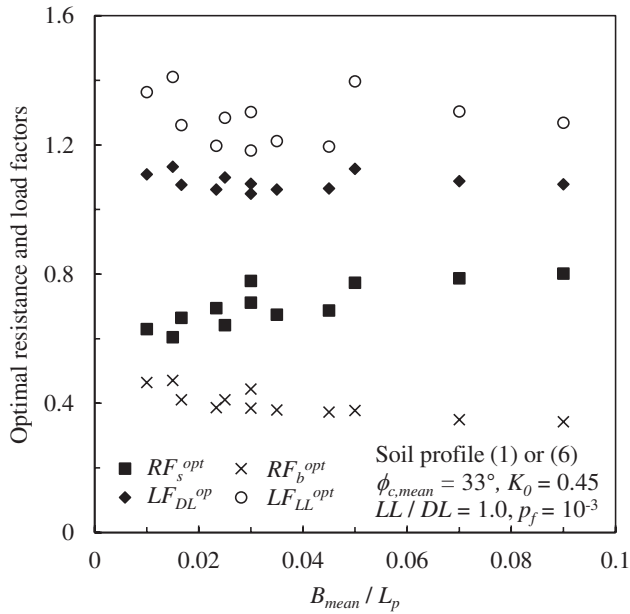


Figure 7.12 Optimal load and resistance factors for various B_{mean}/L_p .

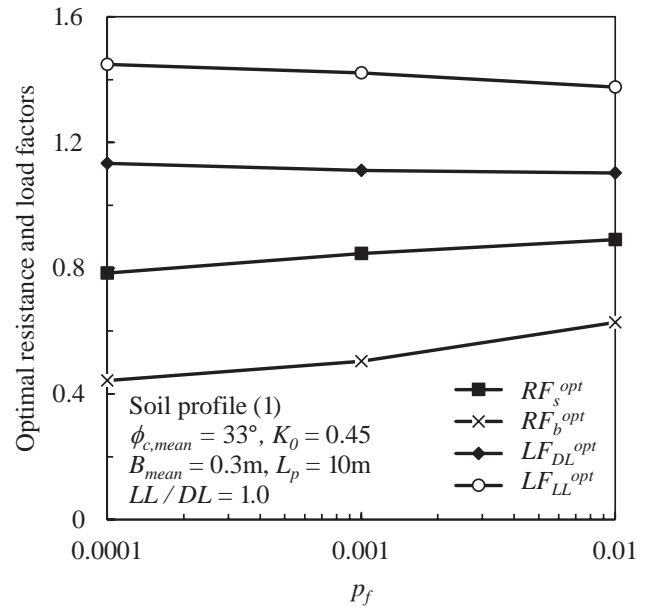


Figure 7.14 Optimal load and resistance factors with various probability of failure, p_f .

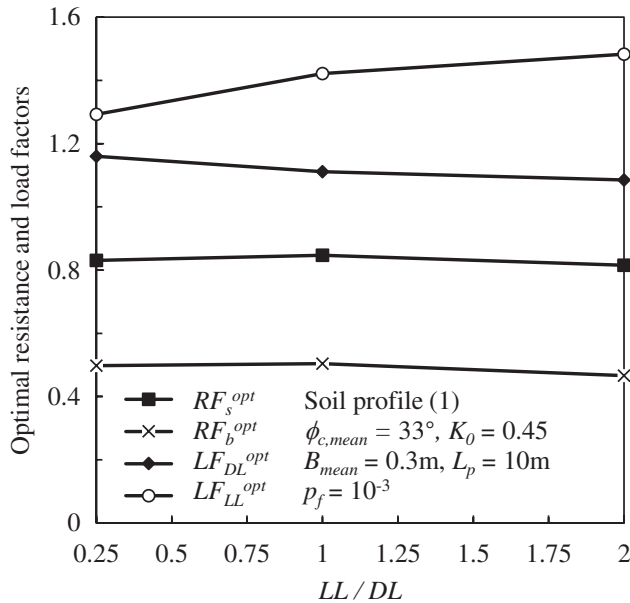


Figure 7.13 Optimal load and resistance factors for various LL/DL .

structures. The analyses involve quantifying uncertainties in design variables and design equations, performing Monte Carlo simulations to estimate probability distributions of base and shaft pile resistances, obtaining limit-state load and resistances and optimal load and resistance factors, and calculating code-adjusted resistance factors that can be used in pile group design together with load factors prescribed in AASHTO

TABLE 7.8
Code-Adjusted Base and Shaft Resistance Factors, RF_b^{code} and RF_s^{code} , for $LF_{DL}^{code} = 1.25$ and $LF_{LL}^{code} = 1.75$, and Driven Piles in Sand.

$p_{f,T}$	Statistics	CPT-based design method		
		RF_b^{code}	RF_s^{code}	FS
10^{-3}	Mean	0.475	0.860	2.32
	SD	0.098	0.136	—
	Maximum	0.866	1.371	4.23
	Minimum	0.283	0.427	1.36
10^{-4}	Mean	0.414	0.795	2.59
	SD	0.082	0.111	—
	Maximum	0.956	1.137	3.89
	Minimum	0.290	0.488	1.40

(2012) code. We considered a typical range of soil properties, profiles and pile dimensions in reliability analyses.

We obtained optimal and code-adjusted resistance factors that are practically insensitive to soil properties, profiles and pile dimensions. Therefore, we combined resistance factors obtained from different analyses cases to suggest one set of resistance factors for each pile group design method for each of the two target probabilities of failure considered. The recommended resistance factors for pile group design in this report can be used in load and resistance factor design, LRFD, of pile groups with load factors recommended by AASHTO (2012) for dead load (1.25) and live load (1.75).

TABLE 7.9
Code-Adjusted Base and Shaft Resistance Factors, RF_b^{code} and RF_s^{code} , for $LF_{DL}^{code} = 1.25$ and $LF_{LL}^{code} = 1.75$, and Driven Piles in Clay.

$p_{f,T}$	Statistics	CPT-based design method						s_u -based design method					
		$B / L_p = 0.03$			$B / L_p = 0.09$			$B / L_p = 0.03$			$B / L_p = 0.09$		
		RF_b^{code}	RF_s^{code}	FS	RF_b^{code}	RF_s^{code}	FS	RF_b^{code}	RF_s^{code}	FS	RF_b^{code}	RF_s^{code}	FS
10^{-3}	Mean	0.927	0.825	1.64	0.888	0.865	1.63	0.807	0.630	2.03	0.717	0.688	2.04
	SD	0.086	0.058	—	0.077	0.081	—	0.125	0.074	—	0.093	0.106	—
	Maximum	1.263	0.994	2.22	1.106	1.117	2.40	1.210	0.838	3.32	1.025	1.119	3.69
	Minimum	0.638	0.650	1.29	0.624	0.624	1.35	0.474	0.430	1.46	0.411	0.402	1.40
10^{-4}	Mean	0.887	0.776	1.73	0.838	0.811	1.73	0.721	0.551	2.24	0.644	0.601	2.32
	SD	0.084	0.052	—	0.067	0.068	—	0.126	0.056	—	0.076	0.078	—
	Maximum	1.093	0.892	2.38	1.012	0.988	2.33	1.137	0.710	3.89	0.852	0.855	3.84
	Minimum	0.643	0.615	1.51	0.633	0.620	1.50	0.383	0.388	1.62	0.401	0.380	1.76

$p_{f,T}$ = target probability of failure.

s_u = undrained shear strength.

SD = standard deviation.

B = pile diameter.

L_p = pile length.

TABLE 7.10
Recommended Code-Adjusted Resistance Factors for Pile Group Design for Drilled Shafts and Driven Piles in Sand and Clay with $LF_{DL}^{code} = 1.25$ and $LF_{LL}^{code} = 1.75$.

Pile-soil combination	Design method	$p_{f,T} = 10^{-3}$		$p_{f,T} = 10^{-4}$	
		RF_b^{code}	RF_s^{code}	RF_b^{code}	RF_s^{code}
Drilled shafts in sand	CPT-based design	0.75	0.70	0.70	0.65
	SPT-based design (COV of $N_{60} = 0.3$)	0.45	0.60	0.35	0.50
	(COV of $N_{60} = 0.5$)	0.40	0.60	0.35	0.50
Drilled shafts in clay	CPT-based design	0.70	0.75	0.65	0.70
	s_u -based design	0.50	0.45	0.40	0.40
Driven piles in sand	CPT-based design	0.32	0.64	0.30	0.64
Driven piles in clay	CPT-based design	0.70	0.70	0.70	0.65
	s_u -based design	0.50	0.45	0.45	0.40

8. DESIGN RECOMMENDATIONS

8.1 Pile Design Equations

The pile design equations for drilled shafts and driven piles in sand or clay are summarized in Table 8.1.

8.2 Recommended Resistance Factors

The recommended resistance factors for pile group of drilled shafts and driven piles in sand and clay are summarized in Table 8.2.

8.3 Pile Efficiencies for Individual Piles in Pile Group

Pile efficiencies for individual piles in the pile group are summarized in Table 8.3 and Table 8.4.

8.4 Pile Group Design Method

Load and resistance factor design (LRFD) of pile groups consistent with the AASHTO (2012) code can be done by following these steps:

Obtain nominal dead and live loads (DL^n and LL^n , respectively) from the superstructure design

Set load factors for dead and live loads as: $LF_{DL} = 1.25$ and $LF_{LL} = 1.75$

Calculate the nominal group resistances $Q_{g,b}^n$ and $Q_{g,s}^n$ coming from base and shaft resistances of individual piles using:

$$Q_{g,b}^n = \sum_{i=1}^{n_p} \eta_{b,i} Q_{b,ult,i} \quad (7.31)$$

TABLE 8.1
CPT-Based Pile Design Equations for Drilled Shafts and Driven Piles in Sand or Clay.

Design cases	Unit shaft resistance q_{sL}	Unit base resistance $q_{b,ult}$
Drilled shafts	<p>Sand</p> $q_{sL} = \left[\frac{K_0}{e^{0.2\sqrt{K_0}-0.4}} C_I e^{\frac{D_R}{100} \left[1.3 - 0.2 \ln \left(\frac{\sigma'_{v0}}{p_A} \right) \right]} \right] \sigma'_{v0} \tan \phi_c$ <p>where $C_I = 0.7$ for clean sand in general; the relative density D_R in sand can be estimated from the CPT data:</p> $D_R(\%) = \frac{\ln \left(\frac{q_c}{p_A} \right) - 0.4947 - 0.1041 \phi_c - 0.841 \ln \left(\frac{\sigma'_{v0}}{p_A} \right)}{0.0264 - 0.0002 \phi_c - 0.0047 \ln \left(\frac{\sigma'_{v0}}{p_A} \right)} \leq 100\%$	$q_{b,ult} = 0.23 e^{-0.0066 D_R} q_{cb,avg}$
	<p>Clay</p> $q_{sL} = \left(\frac{s_u}{\sigma'_{v0}} \right)^{-0.05} \left[A_1 + (1 - A_1) e^{-\left(\frac{\sigma'_{v0}}{p_A} \right) (\phi_c - \phi_{r,min})^2} \right] s_u$ <p>where $A_1 = 0.75$ for $\phi_c - \phi_{r,min} \leq 5^\circ$, 0.4 for $\phi_c - \phi_{r,min} \geq 12^\circ$ and linearly interpolated value between 0.75 and 0.4 for other cases, and $A_2 = 0.4 + 0.3 \ln(s_u / \sigma'_{v0})$.</p>	$q_{b,ult} = 9.6 s_u$
Driven piles	<p>Sand</p> $q_{sL} = K \sigma'_{v0} \tan \delta_c$ $K = K_{min} + (K_{max} - K_{min}) \exp \left(-\alpha \frac{h}{B} \right)$ $K_{min} = 0.2$ $K_{max} = 0.02 q_c / \sigma'_{v0}$ <p>where h is the distance from the depth being considered to the pile base; $K_{min} = 0.2$ and $\alpha = 0.05$</p>	$q_{b,ult} = \min[1, 1.09 - 0.007 D_R] q_{cb,avg}$
	<p>Clay</p> $q_{sL} = 1.28 \left(\frac{s_u}{\sigma'_{v0}} \right)^{-0.05} \left[A_1 + (1 - A_1) e^{-\left(\frac{\sigma'_{v0}}{p_A} \right) (\phi_c - \phi_{r,min})^2} \right] s_u$ <p>where $A_1 = 0.75$ for $\phi_c - \phi_{r,min} \leq 5^\circ$, 0.4 for $\phi_c - \phi_{r,min} \geq 12^\circ$ and linearly interpolated value between 0.75 and 0.4 for other cases, and $A_3 = 0.64 + 0.4 \ln(s_u / \sigma'_{v0})$.</p>	$q_{b,ult} = 10 s_u$

σ'_{v0} = initial *in-situ* vertical effective stress at the depth where q_{sL} is calculated; σ'_{h0} = initial *in-situ* horizontal effective stress; ϕ_c = critical-state friction angle of sand; K_0 = coefficient of earth pressure at rest; p_A = reference stress (= 100 kPa = 1 tsf); D_R = relative density of sand (%); s_u = undrained shear strength of clay; $\phi_{r,min}$ = minimum residual friction angle of clay; q_c = the representative cone resistance of the soil layer; δ_c = the interface friction angle ($\delta_c = 0.9 \phi_c$; Foye et al., 2009; Salgado et al., 2011); $q_{cb,avg}$ is the representative cone resistance at the pile base level; this can be obtained by averaging the cone resistances between $1B$ above and $2B$ below the pile base level.

TABLE 8.2
Recommended Code-Adjusted Resistance Factors for Pile Group Design for Drilled Shafts and Driven Piles in Sand and Clay with $LF_{DL}^{code} = 1.25$ and $LF_{LL}^{code} = 1.75$.

Pile-soil combination	Design method	$p_{f,T} = 10^{-3}$			$p_{f,T} = 10^{-4}$		
		RF_b^{code}	RF_s^{code}	FS	RF_b^{code}	RF_s^{code}	FS
Drilled shafts in sand	CPT-based design	0.75	0.70	1.94	0.70	0.65	2.08
	SPT-based design						
	(COV of $N_{60} = 0.3$)	0.45	0.60	2.78	0.35	0.50	3.45
	(COV of $N_{60} = 0.5$)	0.40	0.60	2.94	0.35	0.50	3.45
Drilled shafts in clay	CPT-based design	0.70	0.75	1.94	0.65	0.70	2.08
	s_u -based design	0.50	0.45	3.05	0.40	0.40	3.56
Driven piles in sand	CPT-based design	0.32	0.64	2.85	0.30	0.64	2.90
Driven piles in clay	CPT-based design	0.70	0.70	2.03	0.70	0.65	2.12
	s_u -based design	0.50	0.45	3.02	0.45	0.40	3.38

For layered clay deposits (soft over stiff layers), 25% and 20% lower code-adjusted resistance factors for base and shaft resistances are recommended, respectively.

TABLE 8.3
Efficiency (as a Percentage) for Individual Piles in a 4 × 4 Pile Group Installed in Sand.

		$D_R = 50\%$			$D_R = 80\%$		
		Center pile	Side pile	Corner pile	Center pile	Side pile	Corner pile
$s = 30\text{mm}$	Base	112	93	82	81	75	75
	Shaft	69	105	112	90	120	104
$s = 50\text{mm}$	Base	131	101	87	112	88	81
	Shaft	87	129	130	118	151	107

TABLE 8.4
Efficiency (as a Percentage) for Individual Piles in a 4 × 4 Pile Group Installed in Normally Consolidated London Clay.

		Center pile	Side pile	Corner pile
$s = 30\text{mm}$	Base	96	101	100
	Shaft	38	77	98
$s = 50\text{mm}$	Base	102	106	103
	Shaft	46	85	103

with
 $\eta_{b,i}$ = base resistance efficiency for individual piles (≈ 1 for small pile groups; see Table 8.3 and Table 8.4 for large pile groups)
 n_p = number of piles in pile group
 $Q_{b,ult,i} = Q_{b,ult}$ of i^{th} pile, with $Q_{b,ult} = q_{b,ult}A_b$
 $q_{b,ult}$ is obtained from Table 8.1

$A_b = \pi B^2 / 4$ where B = pile diameter

$$Q_{g,s}^n = \sum_{i=1}^{n_p} \eta_{s,i} Q_{sL,i} \quad (7.32)$$

with
 $\eta_{s,i}$ = shaft resistance efficiency for individual piles (≈ 1 for small pile groups; see Table 8.3 and Table 8.4 for large pile group)
 n_p = number of piles in pile group
 $Q_{sL,i} = Q_{sL}$ of i^{th} pile where $Q_{sL} = \sum_{j=1,2,\dots} q_{sL,j} A_{s,j}$
 $q_{sL,j} = q_{sL}$ in Table 8.1 at mid-depth of j^{th} sub-layer
 $A_{s,j} = \pi B t_j$, where B = pile diameter and t_j = thickness of j^{th} sub-layer
 Obtain resistance factors RF_b and RF_s for base and shaft resistances from Table 8.2

Check if $RF_b Q_{g,b}^n + RF_s Q_{g,s}^n \geq LF_{DL} DL^n + LF_{LL} LL^n$

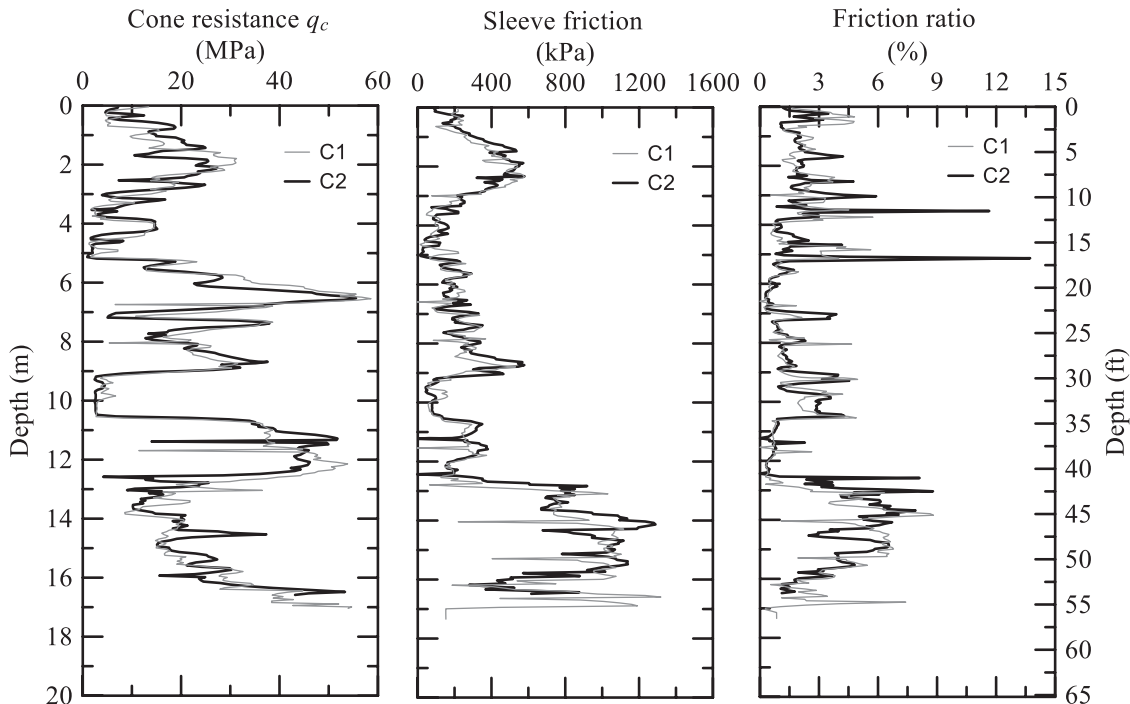


Figure 8.1 Results of CPTs performed at the test site of the project on U.S. 31.

TABLE 8.5
Nominal and Factored Resistances Calculated for a Few Assumed Pile Lengths for Single Pile Design.

Pile length L (m)	Pile length L (m)	Q'_s (kN)	Q'_b (kN)	RF_s	Q'_b (kN)	Q'_b (kN)	RF_b	$RF_s Q'_s + RF_b Q'_b$ (kN)	$RF_s Q'_s + RF_b Q'_b$ (kN)	Corresponding FS
11	36.1	1421	319	0.64	1617	364	0.30	314	314	3.32
12	39.4	1800	405	0.64	1484	334	0.30	359	359	3.59
14	45.9	1919	431	0.64	1151	259	0.30	354	354	3.35
15.4	50.5	1992	448	0.64	1221	274	0.30	369	369	3.51

If true, pile group design is satisfactory; iterate to minimize cost if required by going back to (3); end if cost has been optimized

If false, modify pile group design and go back to (3)

8.5 Design Examples

Two design examples (for a single pile and for a pile group) will be presented in this section to illustrate the steps to follow for LRFD design of individual piles or pile groups.

8.5.1 Single Pile Design

A closed-ended, pipe pile was driven and static-load tested at the intersection of 7th Road with U.S. 31 (Han, Prezzi, Salgado, & Zaheer, 2016) in Marshall County, Indiana. The foundation in reality consisted of a row of piles with center-to-center spacing equal to 8 B which means the interactions between piles are negligible, and therefore each pile may be considered as a single pile. The LRFD design procedure is followed to check the safety/reliability of this foundation.

(1)–(2) Obtain nominal loads and calculate the factored design load by using load factors $LF_{DL} = 1.25$ and $LF_{LL} = 1.75$

The bridge span length $L = 31.7$ m, resulting in $LL/DL = 0.55$ by using Equation 7.10. According to the bridge plan provided by INDOT, the nominal dead load $DL^n = 591$ kN, the nominal live load $DL^n = 325$ kN, and the factored design load is:

$$LF_{DL}DL^n + LF_{LL}LL^n = 1308 \text{ kN (294 kip)}$$

(3) Calculate the nominal base and shaft resistances

The diameter of the pile is $B = 356$ mm (14 inch). The pile was driven to an actual depth of 15.4 m. This actual embedment length, as well as lengths $L = 11, 12$ and 14, are considered for comparison. Figure 8.1 shows the results of the CPTs performed at the test site, which are used to calculate the nominal base and shaft resistances with the design equations for driven pile in sand listed in Table 8.1. The calculated resistances for different pile lengths are summarized in Table 8.5.

(4) Obtain resistance factors RF_b and RF_s

Table 8.1 is used to determine the resistance factors, with the results summarized in Table 8.5. A target probability of failure $p_{f,T} = 10^{-4}$ is used in this example.

(5) Check if $RF_b Q'_{g,b} + RF_s Q'_{g,s} \geq LF_{DL}DL^n + LF_{LL}LL^n$

The pile lengths considered above all produce factored resistances greater than the factored load (1308 kN = 294 kip), which means that this existing pile foundation should

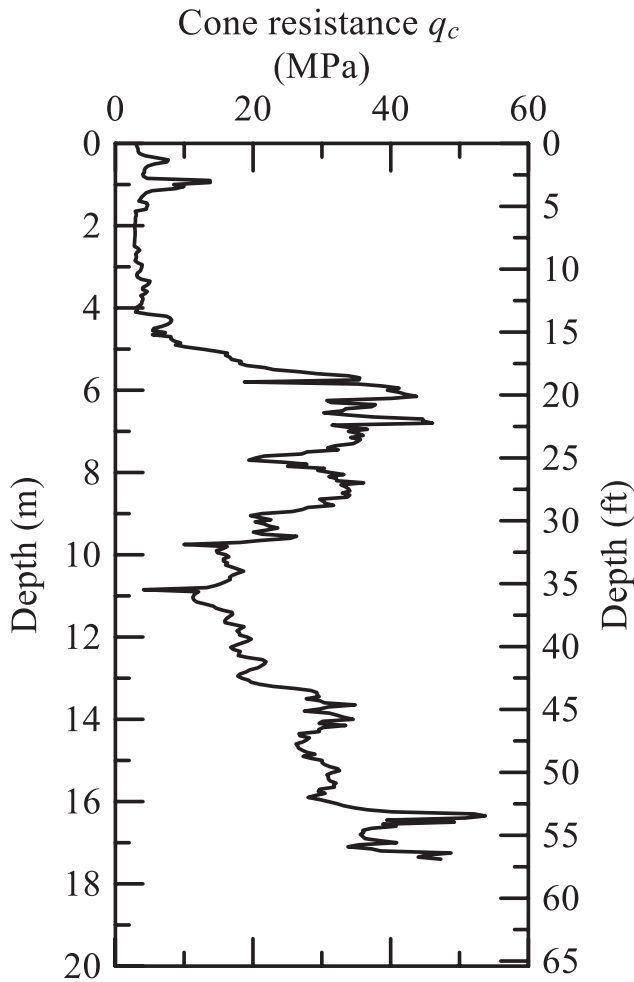


Figure 8.2 Result of CPT performed at the test site of the project on U.S. 52.

be safe/reliable, with a probability of failure less than $p_{f,T} = 10^{-4}$. The corresponding factors of safety are also summarized in Table 8.5 for reference.

8.5.2 Pile Group Design

The project of Replacement of the Bridge on U.S. 52 over Wabash River in Tippecanoe County, Indiana, will be used as a design example of a pile group consisting of driven, closed-ended pipe piles. The design steps would be:

(1)–(2) Obtain nominal loads and calculate the factored design load by using load factors $LF_{DL} = 1.25$ and $LF_{LL} = 1.75$

The bridge span length $L = 45.72$ m (150 ft), resulting in $LL/DL = 0.38$ by using Equation 7.10. According to the bridge plan provided by INDOT, the factored design load:

$$LF_{DL}DL^n + LF_{LL}LL^n = 17791 \text{ kN (4000 kip)}$$

The nominal dead load $DL^n = 9291$ kN (= 2089 kip) and the nominal live load $DL^n = 3530$ kN (= 794 kip).

TABLE 8.6
Nominal and Factored Resistances Calculated for a Few Assumed Pile Lengths for Pile Group Design.

Pile length L (m)	Pile length L (ft)	Q_s^n (kN)	Q_s^n (kip)	RF_s	Q_b^n (kN)	Q_b^n (kip)	RF_b	$RF_s Q_s^n + RF_b Q_b^n$ (kN)	$RF_s Q_s^n + RF_b Q_b^n$ (kip)	Corresponding F:S
14	45.9	160	36	0.64	1172	263	0.30	7338	1650	1.61
15	49.2	414	93	0.64	1185	266	0.30	10829	2434	2.04
16	52.5	725	163	0.64	1436	323	0.30	16141	3629	2.84
17	55.8	1186	267	0.64	1596	359	0.30	23079	5188	3.79

(3) Calculate the nominal base and shaft resistances

Select the diameter of the pile as $B = 356$ mm (14 inch).

For a pile with several lengths $L = 14, 15, 16$ and 17 m, the nominal base and shaft resistances can be calculated by using the design equations for driven pile in sand listed in Table 8.1. Figure 8.2 shows the CPT data used in the calculations. The Pile efficiencies for base and shaft resistance are determined using values for dense sand in Table 8.3. The scour elevation at the site is $Q_{100} = 144.83$ m (475.16 ft) and the ground surface elevation is 158.2 m (519 ft), which means that the shaft resistance for the top segment (13.36 m, or 43.8 ft) of the pile will not be considered for nominal shaft resistance. Table 8.6 summarizes the calculation results of the estimated nominal resistances.

(4) Obtain resistance factors RF_b and RF_s

Table 8.1 is used to determine the resistance factors, which are listed in Table 8.6. A target probability of failure $p_{f,T} = 10^{-4}$ is used in this example.

(5) Check if $RF_b Q_{g,b}^n + RF_s Q_{g,s}^n \geq LF_{DL} DL^n + LF_{LL} LL^n$

Based on calculations summarized in Table 8.6, the pile needs to be at least 17 m long to produce factored resistances greater than the factored load (17791 kN = 4000 kip).

9. IMPLEMENTATION

Implementation of the design methods presented in this research is already underway at INDOT. The pile design equations and the detailed procedures to perform a LRFD design of a single or a pile group are summarized in Chapter 8. Two design examples, one for single pile and one for a pile group, are given to illustrate the calculation steps. INDOT is currently utilizing two design tools that were developed in the course of this project: (i) pile design excel spreadsheet program tool and (ii) a web-based pile design resource.

9.1 Pile Design Excel Spreadsheet Program Tool

The pile design excel spreadsheet program tool is developed in the Microsoft Office Excel environment, which is familiar to most engineers. The user interface is concise and friendly, and the operation is intuitive and straightforward.

Figure 9.1 shows the spreadsheet tool. The user needs to select the unit system (SI or USC units), pile type (closed-ended pipe pile or H pile), design method (WSD or LRFD) and analysis type (CPT-, SPT- or property-based). The load and resistance factors, which can be found in Chapter 8, are required for LRFD design and the factor of safety is required for WSD design. The user

also needs to input the pile geometry, the soil properties, and the *in-situ* test results in each layer.

Next, the user needs to go to the desired analysis tab located at the bottom of the window. After selecting the design equations, the shaft and base resistances will be automatically calculated and displayed on the same page.

9.2 Web-Based Pile Design Tool

Software-based pile design tools require download, installation, licensing and update processes. Additionally, users may be troubled by the incompatibility between different versions of the software. In comparison, the web-based design tool can be accessed from either computers or mobile devices wherever internet connection is available. Moreover, users will always have the up-to-date version of the design program.

The web-based design tool is developed based on two different unit systems: United States customary units (USC units) and International System of units (SI units). Five different types of pile can be considered: drilled shafts, open-ended pipe piles, closed-ended pipe piles, H-piles or concrete piles. For a given pile geometry and soil profiles, nominal base and shaft resistances of single pile can be estimated based on available field test or laboratory test data. CPT or SPT results for sandy soils and CPT or undrained shear strength measures for clayey soils can be used. Template input files with the required data format are provided on the website for users to easily prepare the input files. Depending on the pile and soil types, different design equations can be used (see Figure 9.2). Table 9.1 summarizes available design equations for different pile and soil types.

For drilled shaft designs, factored (design) shaft and base resistances can also be calculated after getting nominal pile resistances by applying the suggested resistance factors that is consistent with AASHTO (2012) load factors within LRFD framework. For concrete piles, the pile integrity check is performed at the end of the calculation by comparing the nominal resistance of the pile divided by the cross-sectional area of the pile, and the compressive strength of concrete. The considered range for the compressive strength is assumed to be $15\text{--}30$ MPa ($156\text{--}314$ tsf).

The web-based pile design tool is available online through the link *Purdue pile design* at <https://engineering.purdue.edu/COFFEE/resources.html>.

Authorization is required to access to the web-based design tool. Figure 9.3 shows the first page of the web-based design tool. On the first page, users can download sample files for the required input data and get basic instructions and information about the program.

Figure 9.4 shows a calculation example for single drilled shaft design. Figure 9.4(a) shows the input tab where input files are uploaded and Figure 9.4(b) shows the result tab, where calculation results are shown.

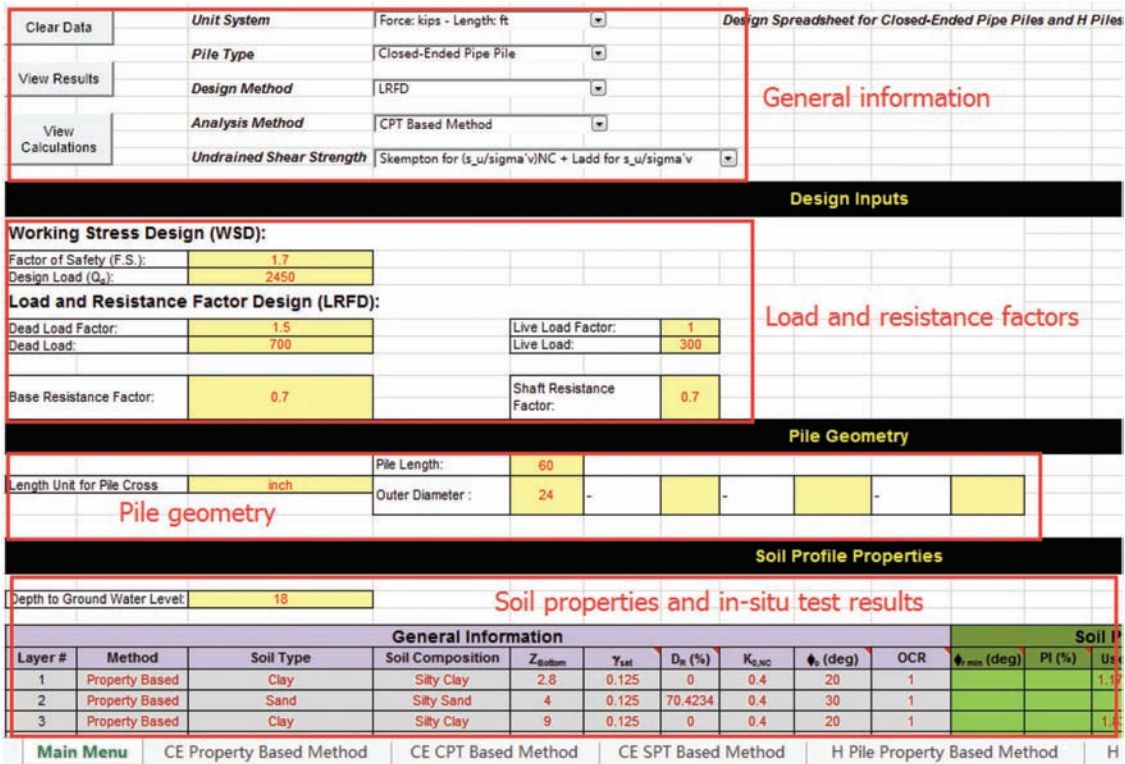


Figure 9.1 Pile design Excel spreadsheet program tool.

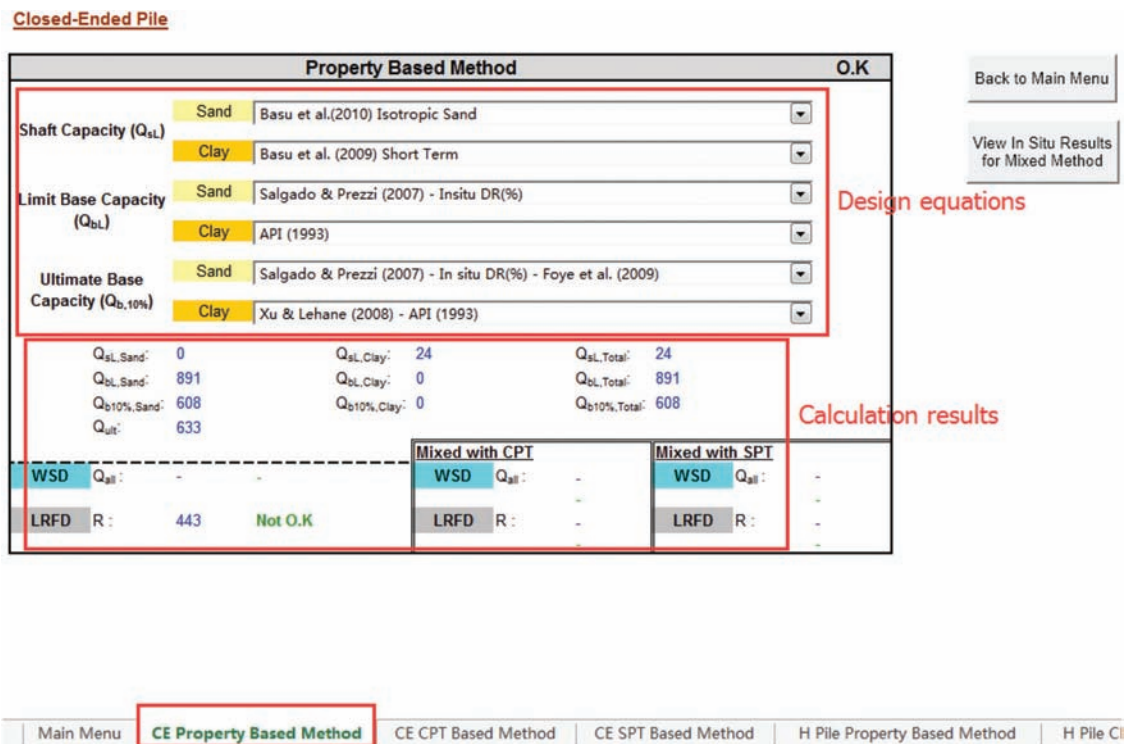


Figure 9.2 Selection of pile design equations and the result output.

Pile Design for Axial Loads

Single Pile

Instructions

1 Upload Input Data

Soil boring log data (soil layers and basic soil properties for each layer) are required. SPT, CPT or unconfined compression data are needed only if the methods that you intend to use rely on those tests. Data must be uploaded using MS Excel files in the required format.

Sample data files:

- Boring Log Data:
- CPT Data
- SPT Data
- Undrained shear strength (s_u) Data

2 Get the Nominal Single Pile Resistances

The unit base and shaft resistances for each layer are calculated using the Purdue Sand Method, the Purdue Clay Method (Salgado et al., 2011; Paik and Salgado, 2003; Basu et al., 2009), NGI (Clausen et al., 2005; Karlsrud et al., 2005), Fugro (Kolk et al., 2005), UWA (Lehane et al., 2005), API (1993) and ICP (Jardine et al., 2005) depending on the pile and soil types.

The unit base resistance is defined as the unit load (base stress) corresponding to a pile base settlement equal to 10% of the pile diameter:
 $q_{b,ult} = q_{b,10\%}$

The unit shaft resistance is the limit unit shaft resistance. Corrections for compressive versus tension loading, friction degradation and other factors are included depending on the calculation method.

Figure 9.3 Web-based pile design tool.

TABLE 9.1
Applicable Design Methods in Web-Based Design Tool.

Pile type	Installed in sand	Installed in clay
Drilled shaft	Purdue Method (Salgado, 2008)	Purdue Method (Chakraborty, Salgado, Basu, et al., 2013; Salgado, 2006)
Open-ended pipe pile	Purdue Method (Randolph, 2003; Salgado et al., 2011) NGI (Clausen et al., 2005) UWA (Lehane et al., 2005) ICP (Jardine et al., 2005) Fugro (Kolk et al., 2005)	NGI (Clausen et al., 2005)
Closed-ended pipe pile	Purdue Method (Randolph, 2003; Salgado et al., 2011) NGI (Clausen et al., 2005) UWA (Lehane et al., 2005) ICP (Jardine et al., 2005) Fugro (Kolk et al., 2005)	Purdue Method (Basu et al., 2014; Salgado, 2006) NGI (Clausen et al., 2005) API (1993) ICP (Jardine et al., 2005)
H-pile	ICP (Jardine et al., 2005)	ICP (Jardine et al., 2005)
Concrete pile	Purdue Method (Randolph, 2003; Salgado et al., 2011) NGI (Clausen et al., 2005) UWA (Lehane et al., 2005) ICP (Jardine et al., 2005) Fugro (Kolk et al., 2005)	Purdue Method (Basu et al., 2014; Salgado, 2006) NGI (Clausen et al., 2005) API (1993) ICP (Jardine et al., 2005)

Purdue University Register Login

Home Input Results Contact

Input Data

1. System of Units

USC Units * SI Units

2. File Properties

File Type: Drilled Shaft
 Diameter: 0.3 m
 Length: 10 m
 File Weight per Length: 18 kN/m

3. Applied Equations

Sand Shaft Resistance: Purdue Sand Method
 Sand Base Resistance: Purdue Sand Method
 Clay Shaft Resistance: Purdue Clay Method
 Clay Base Resistance: Purdue Clay Method

4. Boring Log Data

Depth to Ground Water Table: 12 m
 Capillary Height: 0 m

Choose File: No file chosen

Layer No.	Depth to Top (m)	Depth to Bottom (m)	Soil Type	Dry Unit Weight of Soil (kN/m ³)	Moisture Content (%)	Critical State Friction Angle (°)	Minimum Residual Friction Angle (°)	K ₀	PI (%)	IJ (%)	OCR
1	0	2	Sand	15	12	32		0.45	0	0	1
2	2	5	Sand	16	13	30		0.5	0	0	1
3	5	6	Clay	13	20	15	11	0.4	15	20	1
4	6	10	Clay	14	18	13	12	0.45	15	20	1
5	10	15	Sand	16.5	13	35		0.45	0	0	1

5. Field Data

CPT Data: Upload MS Excel file (Depth (m) vs. Cone penetration resistance (q_c, MPa))
 Choose File: No file chosen

SPT Data: Upload MS Excel file (Depth (m) vs. N₆₀)
 Choose File: No file chosen

Un drained shear strength (s_u) Data: Upload MS Excel file (Depth (m) vs. Un drained shear strength (s_u, kPa))
 Choose File: No file chosen

Reset Calculate

Please check if your input data is correct before you click 'Calculate'. If it is not correct, please click 'Reset' to reload input data.

(a)

Purdue University Register Login

Home Input Results Contact

Results

1. Shaft resistance (q_{sL}, kPa) Export

2. Base resistance (q_{b,ult}, kPa)

q_{b,ult}: 1336.35 kPa (Based on CPT data, q_{bL} = 6999.97 kPa)

3. Load capacity (Q_{ult}, kN)

Q _{sL}	235 kN
Q _{sL} in sand (SPT)	0 kN
RF = 0.6 or 0.5	
Q _{sL} in sand (CPT)	100 kN
RF = 0.75 or 0.6	
Q _{sL} in clay (CPT)	135 kN
RF = 0.75 or 0.7	
Q _{sL} in clay (UC)	0 kN
RF = 0.45 or 0.4	
Q _{sL} in clay (UC)	94 kN
RF = 0.8 or 0.65	
Q _{b,ult}	
Q _{ult} = Q _{sL} + Q _{b,ult}	330 kN

Maximum stress applied to the pile: 4666.82 kPa **Okay!** (< 15,000 kPa)

4. Design load (Q_{design}, kN) Calculate

Probability of failure	10 ⁻³	10 ⁻⁴
Q _{design} = RF _{sL} Q _{sL} + RF _{b,ult} Q _{b,ult}	252 kN	216 kN
Equivalent FS	1.83	2.14

RESET

(b)

Figure 9.4 Calculation example of web-based pile design tool: (a) input data and (b) calculation results.

9.3 Conclusions

The design tools developed to assist INDOT with implementing the results of this research are intuitive and easy to use. Improvements in these methods can be made as additional dynamic and static pile load test data are collected from INDOT projects and additional rigorous pile loading simulations are performed. Ideally, high-quality data should be obtained from static load tests performed on instrumented piles in combination with detailed characterization of the soil profiles at test sites, as done in previous INDOT test sites. Some clear gaps in knowledge regarding axial pile loading remain, including the understanding and quantification of the effects of pile driving on the soil surrounding a pile and the impact of that on pile resistance, the response of large pile groups, negative skin friction in piles, the response of open-ended pipe piles, friction degradation during pile driving and pile set up.

So far, the design tools can be used only for single pile design. Extension to pile group design is desirable after further research is available on the topic. Exhaustive analyses of pile group load response considering various pile diameters, pile lengths, group configurations and layered soil profiles need to be performed to assess pile interaction within a group. The effects of pile installation methods on pile group interaction factors should also be studied and quantified.

It is highly recommended that JTRP support further research on pile design and the further development of the design tools developed for this project.

REFERENCES

- AASHTO. (2012). *AASHTO LRFD bridge design specifications, customary U.S. units (6th edition) with 2012 and 2013 interim revisions; and 2012 Errata*. Washington, DC: American Association of State Highway and Transportation Officials.
- Alawneh, A. S., & Malkawi, A. I. H. (2000). Estimation of post-driving residual stresses along driven piles in sand. *ASTM Geotech Test J*, 23(3), 313–326. <http://dx.doi.org/10.1520/GTJ11053J>
- Allen, T., Nowak, A., & Bathurst, R. (2005). *Calibration to determine load and resistance factors for geotechnical and structural design* (Transportation Research Electronic Circular No. E-C079). Washington, DC: Transportation Research Board.
- Al-Shafei, K. A., Cox, W. R., & Helfrich, S. C. (1994). Pile load tests in dense sand: Analysis of static test results. In *Proceedings of the 14th Offshore Technology Conference, May 2–5, Houston, Texas* (pp. 83–103). <http://dx.doi.org/10.4043/7381-MS>
- Alshibli, K. A., & Sture, S. (1999). Sand shear band thickness measurements by digital imaging techniques. *J Comput Civ Eng*, 13(2), 103–109. [http://dx.doi.org/10.1061/\(ASCE\)0887-3801\(1999\)13:2\(103\)](http://dx.doi.org/10.1061/(ASCE)0887-3801(1999)13:2(103))
- Andresen, L., & Jostad, H. (2002). A constitutive model for anisotropic and strain-softening clay. In G. N. Pande & S. Pietruszczak (Eds.), *Numerical models in geomechanics (NUMOB VIII)* (pp. 79–83). London, UK: Taylor & Francis. <http://dx.doi.org/10.1201/9781439833797-c12>
- Ang, A. H.-S., & Tang, H. W. (1975). *Probability concepts in engineering: Emphasis on applications to civil and environmental engineering, Vol. 1: Basic principles*. New York, NY: John Wiley & Sons.
- API. (1993). *Recommended practice for planning, designing and constructing fixed offshore platforms-working stress design* (API RP 2A, 20th ed.). Washington, DC: American Petroleum Institute.
- Arshad, M. I., Tehrani, F., Prezzi, M., & Salgado, R. (2014). Experimental study of cone penetration in silica sand using digital image correlation. *Geotechnique*, 64(7), 551–569. <http://dx.doi.org/10.1680/geot.13.P.179>
- Axelsson, G. (2000). *Long-term set-up of driven piles in sand* (Doctoral dissertation). Stockholm, Sweden: Royal Institute of Technology.
- Barker, R., Duncan, J., Rojiani, K., & Ooi, P. (1991) *Manuals for the design of bridge foundations* (NCHRP Report 343). Washington, DC: Transportation Research Board.
- Basu, D., & Salgado, R. (2012). Load and resistance factor design of drilled shafts in sand. *J Geotech Geoenvironmental Eng*, 138(12), 1455–1469. [http://dx.doi.org/10.1061/\(ASCE\)GT.1943-5606.0000714](http://dx.doi.org/10.1061/(ASCE)GT.1943-5606.0000714)
- Basu, P., Loukidis, D., Prezzi, M., & Salgado, R. (2011). Analysis of shaft resistance of jacked piles in sands. *Int J Numer Anal Methods Geomech*, 35(15), 1605–1635. <http://dx.doi.org/10.1002/nag.968>
- Basu, P., Prezzi, M., Salgado, R., & Chakraborty, T. (2014). Shaft resistance and setup factors for piles jacked in clay. *J Geotech Geoenvironmental Eng*, 140(3), 04013026. [http://dx.doi.org/10.1061/\(ASCE\)GT.1943-5606.0001018](http://dx.doi.org/10.1061/(ASCE)GT.1943-5606.0001018)
- Bica, A. V. D., Salgado, R., Kim, D., Seo, H., & Prezzi, M. (2014). Instrumentation and axial load testing of displacement piles. *Proc ICE—Geotech Eng*, 167(3), 238–252. <http://dx.doi.org/10.1680/geng.12.00080>
- Bowman, E. T., & Soga, K. (2005). Mechanisms of setup of displacement piles in sand: laboratory creep tests. *Can Geotech J*, 42(5), 1391–1407. <http://dx.doi.org/10.1139/t05-063>
- Bozozuk, M. (1978). Bridge foundations move. *Transp Res Rec*, 678, 17–21.
- Briaud, J., & Tucker, L. (1984). Piles in sand: A method including residual stresses. *J Geotech Eng*, 110(11), 1666–1680. [http://dx.doi.org/10.1061/\(ASCE\)0733-9410\(1984\)110:11\(1666\)](http://dx.doi.org/10.1061/(ASCE)0733-9410(1984)110:11(1666))
- Bullock, P. J., Schmertmann, J. H., McVay, M. C., & Townsend, F. C. (2005). Side shear setup. II: Results from Florida test piles. *J Geotech Geoenvironmental Eng*, 131(3), 301–310. [http://dx.doi.org/10.1061/\(ASCE\)1090-0241\(2005\)131:3\(301\)](http://dx.doi.org/10.1061/(ASCE)1090-0241(2005)131:3(301))
- Chakraborty, T., Salgado, R., & Loukidis, D. (2013). A two-surface plasticity model for clay. *Comput Geotech*, 49, 170–190. <http://dx.doi.org/10.1016/j.compgeo.2012.10.011>
- Chakraborty, T., Salgado, R., Basu, P., & Prezzi, M. (2013). Shaft resistance of drilled shafts in clay. *J Geotech Geoenvironmental Eng*, 139(4), 548–563. [http://dx.doi.org/10.1061/\(ASCE\)GT.1943-5606.0000803](http://dx.doi.org/10.1061/(ASCE)GT.1943-5606.0000803)
- Chow, F. C., Jardine, R. J., Brucy, F., & Nauroy, J. F. (1998). Effects of time on capacity of pipe piles in dense marine sand. *J Geotech Geoenvironmental Eng*, 124(3), 254–264. [http://dx.doi.org/10.1061/\(ASCE\)1090-0241\(1998\)124:3\(254\)](http://dx.doi.org/10.1061/(ASCE)1090-0241(1998)124:3(254))
- Clausen, C. J. F., Aas, P. M., & Karlsrud, K. (2005). Bearing capacity of driven piles in sand, the NGI approach. In M. Cassidy & S. Gourvenec (Eds.), *Proceedings of the*

- International Symposium on Frontiers in Offshore Geotechnics (IS-FOG 2005)* (pp. 574–580). London, UK: Taylor & Francis. <http://dx.doi.org/10.1201/NOE0415390637.ch75>
- Colombi, A. (2005). *Physical modeling of an isolated pile in coarse grained soils* (Doctoral dissertation). Ferrara, Italy: University of Ferrara.
- Dafalias, Y. F., & Manzari, M. T. (2004). Simple plasticity sand model accounting for fabric change effects. *J Eng Mech*, 130(6), 622–634. [http://dx.doi.org/10.1061/\(ASCE\)0733-9399\(2004\)130:6\(622\)](http://dx.doi.org/10.1061/(ASCE)0733-9399(2004)130:6(622))
- DNR. (2015). DNR: Status of ground water levels. Indiana Department of Natural Resources. Retrieved from <http://www.in.gov/dnr/water/4859.htm>
- Ellingwood, B., MacGregor, J. G., Galambos, T. V., & Cornell, C. A. (1982). Probability based load criteria: load factors and load combinations. *J Struct Div*, 108(5), 978–997.
- Fellenius, B. H., Harris, D. E., & Anderson, D. G. (2004). Static loading test on a 45 m long pipe pile in Sandpoint, Idaho. *Can Geotech J*, 41(4), 613–628. <http://dx.doi.org/10.1139/t04-012>
- Fioravante, V. (2002). On the shaft friction modelling of nondisplacement piles in sand. *Soils Found*, 42(2), 23–33. http://dx.doi.org/10.3208/sandf.42.2_23
- Fisher, J. W., Ravindra, M. K., Kulak, G. L., & Galambos, T. V. (1978). Load and resistance factor design criteria for connectors. *J Struct Div*, 104(9), 1427–1441.
- Fleming, K., Weltman, A., Randolph, M., & Elson, K. (2008). *Piling engineering* (3rd ed.). Boca Raton, FL: CRC Press.
- Foye, K. (2005). *A rational, probabilistic method for the development of geotechnical load and resistance factor design* (Doctoral dissertation). West Lafayette, IN: Purdue University. Retrieved from <http://docs.lib.purdue.edu/dissertations/AAI3198165/>
- Foye, K. C., Abou-Jaoude, G., Prezzi, M., & Salgado, R. (2009). Resistance factors for use in load and resistance factor design of driven pipe piles in sands. *J Geotech Geoenvironmental Eng*, 135(1), 1–13. [http://dx.doi.org/10.1061/\(ASCE\)1090-0241\(2009\)135:1\(1\)](http://dx.doi.org/10.1061/(ASCE)1090-0241(2009)135:1(1))
- Halliday, D., Resnick, R., & Walker, J. (2010). *Fundamentals of physics extended* (9th ed.). New York, NY: Wiley.
- Han, F., Prezzi, M., Salgado, R., & Zaheer, M. (2016). Axial resistance of closed-ended steel-pipe piles driven in multi-layered soil. *Journal of Geotechnical and Geoenvironmental Engineering*. [http://dx.doi.org/10.1061/\(ASCE\)GT.1943-5606.0001589](http://dx.doi.org/10.1061/(ASCE)GT.1943-5606.0001589).
- Hansell, W. C., & Viest, I. M. (1971). Load factor design for steel highway bridges. *Eng J, Am Inst Steel Constr*, 8(4), 113–123.
- Hu, Y., & Randolph, M. F. (2002). Bearing capacity of caisson foundations on normally consolidated clay. *Soils Found*, 42(5), 71–77. http://dx.doi.org/10.3208/sandf.42.5_71
- Jardine, R. J., Standing, J. R., & Chow, F. C. (2006). Some observations of the effects of time on the capacity of piles driven in sand. *Géotechnique*, 56(4), 227–244. <http://dx.doi.org/10.1680/geot.2006.56.4.227>
- Jardine, R., Chow, F., Overy, R., & Standing, J. (2005). *ICP design methods for driven piles in sand and clays*. London, UK: Thomas Telford Ltd. <http://dx.doi.org/10.1680/idmfdpisac.32729>
- Joint Committee on Structural Safety (JCSS). (2000). *Probabilistic model code*. Copenhagen, Denmark: Technical University of Denmark. Retrieved from http://www.jcss.byg.dtu.dk/Publications/Probabilistic_Model_Code.aspx
- Karlsruh, K., Clausen, C. J. F., & Aas, P. M. (2005). Bearing capacity of driven piles in clay, the NGI approach. In M. Cassidy & S. Gourvenec (Eds.), *Proceedings of the International Symposium on Frontiers in Offshore Geotechnics (IS-FOG 2005)* (pp. 757–782). London, UK: Taylor & Francis. <http://dx.doi.org/10.1201/NOE0415390637.ch88>
- Kim, D., Bica, A. V., Salgado, R., Prezzi, M., & Lee, W. (2009). Load testing of a closed-ended pipe pile driven in multilayered soil. *J Geotech Geoenvironmental Eng*, 135(4), 463–473. [http://dx.doi.org/10.1061/\(ASCE\)1090-0241\(2009\)135:4\(463\)](http://dx.doi.org/10.1061/(ASCE)1090-0241(2009)135:4(463))
- Kolk, H. J., & der Velde, E. (1996). A reliable method to determine friction capacity of piles driven into clays. *Proceedings of the 16th Offshore Technology Conference, May 6–9, Houston, Texas*. <http://dx.doi.org/10.4043/7993-MS>
- Kolk, H. J., Baaijens, A. E., & Senders, M. (2005). Design criteria for pipe piles in silica sands. In M. Cassidy & S. Gourvenec (Eds.), *Proceedings of the International Symposium on Frontiers in Offshore Geotechnics (IS-FOG 2005)* (pp. 711–716). London, UK: Taylor & Francis. <http://dx.doi.org/10.1201/NOE0415390637.ch80>
- Kulhawy, F. H., & Mayne, P. W. (1990). *Manual on estimating soil properties for foundation design*. Pao Alto, CA: Electric Power Research Institute. Retrieved from <http://www.epri.com/abstracts/Pages/ProductAbstract.aspx?ProductId=el-6800>
- Kwak, K., Kim, K. J., Huh, J., Lee, J. H., & Park, J. H. (2010). Reliability-based calibration of resistance factors for static bearing capacity of driven steel pipe piles. *Can Geotech J*, 47(5), 528–538. <http://dx.doi.org/10.1139/T09-119>
- Lacasse, S., & Nadim, F. (1996). Uncertainties in characterising soil properties. In C. D. Shackelford, P. P. Nelson, & M. J. S. Roth (Eds.), *Uncertainty in the geologic environment: From theory to practice* (Geotechnical Special Publication No. 58) (pp. 49–75). New York, NY: American Society of Civil Engineers.
- Lee, J. (1999). *Design of foundations bearing in sand based on CPT results* (Doctoral dissertation). West Lafayette, IN: Purdue University.
- Lee, J. H., & Salgado, R. (1999). Determination of pile base resistance in sands. *J Geotech Geoenvironmental Eng*, 125(8), 673–683. [http://dx.doi.org/10.1061/\(ASCE\)1090-0241\(1999\)125:8\(673\)](http://dx.doi.org/10.1061/(ASCE)1090-0241(1999)125:8(673))
- Lee, W., Kim, D., Salgado, R., & Zaheer, M. (2010). Setup of driven piles in layered soil. *Soils Found*, 50(5), 585–598. <http://dx.doi.org/10.3208/sandf.50.585>
- Lehane, B. M., Jardine, R. J., Bond, A. J., & Frank, R. (1993). Mechanisms of shaft friction in sand from instrumented pile tests. *J Geotech Eng*, 119(1), 19–35. [http://dx.doi.org/10.1061/\(ASCE\)0733-9410\(1993\)119:1\(19\)](http://dx.doi.org/10.1061/(ASCE)0733-9410(1993)119:1(19))
- Lehane, B. M., Li, Y., & Williams, R. (2013). Shaft capacity of displacement piles in clay using the cone penetration test. *J Geotech Geoenvironmental Eng*, 139(2), 253–266. [http://dx.doi.org/10.1061/\(ASCE\)GT.1943-5606.0000749](http://dx.doi.org/10.1061/(ASCE)GT.1943-5606.0000749)
- Lehane, B. M., Schneider, J. A., & Xu, X. (2005). The UWA-05 method for prediction of axial capacity of driven piles in sand. In M. Cassidy & S. Gourvenec (Eds.), *Proceedings of the International Symposium on Frontiers in Offshore Geotechnics (IS-FOG 2005)* (pp. 683–689). London, UK: Taylor & Francis. <http://dx.doi.org/10.1201/NOE0415390637.ch76>
- Levasseur, S., Malécot, Y., Boulon, M., & Flavigny, E. (2008). Soil parameter identification using a genetic algorithm.

- Int J Numer Anal Methods Geomech*, 32(2), 189–213. <http://dx.doi.org/10.1002/nag.614>
- Lim, J. K., & Lehane, B. M. (2014). Characterisation of the effects of time on the shaft friction of displacement piles in sand. *Géotechnique*, 64(6), 476–485. <http://dx.doi.org/10.1680/geot.13.P.220>
- Ling, H. I., & Yang, S. (2006). Unified sand model based on the critical state and generalized plasticity. *J Eng Mech*, 132(12), 1380–1391. [http://dx.doi.org/10.1061/\(ASCE\)0733-9399\(2006\)132:12\(1380\)](http://dx.doi.org/10.1061/(ASCE)0733-9399(2006)132:12(1380))
- Loukidis, D. (2006). *Advanced constitutive modeling of sands and applications to foundation engineering* (Doctoral dissertation). West Lafayette, IN: Purdue University. Retrieved from <http://docs.lib.purdue.edu/dissertations/AAI3232127/>
- Loukidis, D., & Salgado, R. (2008). Analysis of the shaft resistance of nondisplacement piles in sand. *Géotechnique*, 58(4), 283–296. <http://dx.doi.org/10.1680/geot.2008.58.4.283>
- Loukidis, D., & Salgado, R. (2009). Modeling sand response using two-surface plasticity. *Comput Geotech*, 36(1–2), 166–186. <http://dx.doi.org/10.1016/j.compgeo.2008.02.009>
- Mascarucci, Y., Miliziano, S., & Mandolini, A. (2014). A numerical approach to estimate shaft friction of bored piles in sands. *Acta Geotech*, 9(3), 547–560. <http://dx.doi.org/10.1007/s11440-014-0305-4>
- Meyerhof, G. (1951). The ultimate bearing capacity of foundations. *Géotechnique*, 2(4), 301–332. <http://dx.doi.org/10.1680/geot.1951.2.4.301>
- Meyerhof, G. (1957). Discussion for session 1. *Proceedings of the 4th International Conference on Soil Mechanics and Foundation Engineering, Vol. 3* (p. 110). London, UK: Butterworths Scientific Publications.
- Morgenstern, N. R., & Tchalenko, J. S. (1967). Microscopic structures in kaolin subjected to direct shear. *Géotechnique*, 17(4), 309–328. <http://dx.doi.org/10.1680/geot.1967.17.4.309>
- Morgenstern, N. R., & Tchalenko, J. S. (1969). Microscopic structures in kaolin subjected to direct shear. *Géotechnique*, 19(3), 426–427. <http://dx.doi.org/10.1680/geot.1969.19.3.426>
- Ou, C.-Y. (2006). *Deep excavation: Theory and practice*. Boca Raton, FL: CRC Press.
- Paik, K., Salgado, R., Lee, J., & Kim, B. (2003). Behavior of open- and closed-ended piles driven into sands. *J Geotech Geoenvironmental Eng*, 129(4), 296–306.
- Paikowsky, S. G. (2004). *Load and resistance factor design (LRFD) for deep foundations* (NCHRP Report 507). Washington, DC: Transportation Research Board.
- Pucker, T., & Grabe, J. (2012). Numerical simulation of the installation process of full displacement piles. *Comput Geotech*, 45, 93–106. <http://dx.doi.org/10.1016/j.compgeo.2012.05.006>
- Puzrin, A., Alonso, E., & Pinyol, N. (2010). *Geomechanics of failures*. Dordrecht: Springer Netherlands.
- Qiu, G., Henke, S., & Grabe, J. (2011). Application of a coupled Eulerian–Lagrangian approach on geomechanical problems involving large deformations. *Comput Geotech*, 38(1), 30–39. <http://dx.doi.org/10.1016/j.compgeo.2010.09.002>
- Randolph, M. F. (2003). Science and empiricism in pile foundation design. *Géotechnique*, 53(10), 847–875. <http://dx.doi.org/10.1680/geot.2003.53.10.847>
- Rechenmacher, A., Abedi, S., & Chupin, O. (2010). Evolution of force chains in shear bands in sands. *Géotechnique*, 60(5), 343–351. <http://dx.doi.org/10.1680/geot.2010.60.5.343>
- Robertson, P. K. (2009). Interpretation of cone penetration tests—a unified approach. *Can Geotech J*, 46(11), 1337–1355. <http://dx.doi.org/10.1139/T09-065>
- Rouainia, M., & Muir wood, D. (2000). A kinematic hardening constitutive model for natural clays with loss of structure. *Géotechnique*, 50(2), 153–164. <http://dx.doi.org/10.1680/geot.2000.50.2.153>
- Salgado, R. (2006). The role of analysis in nondisplacement pile design. In W. Wu & H. S. Yu (Eds.), *Modern ends in geomechanics* (pp. 521–540). Heidelberg, The Netherlands: Springer-Verlag Berlin Heidelberg. http://dx.doi.org/10.1007/978-3-540-35724-7_30
- Salgado, R. (2008). *The engineering of foundations*. New York, NY: McGraw-Hill.
- Salgado, R., & Prezzi, M. (2007). Computation of cavity expansion pressure and penetration resistance in sands. *Int J Geomech*, 7(4), 251–265. [http://dx.doi.org/10.1061/\(ASCE\)1532-3641\(2007\)7:4\(251\)](http://dx.doi.org/10.1061/(ASCE)1532-3641(2007)7:4(251))
- Salgado, R., Bandini, P., & Karim, A. (2000). Shear strength and stiffness of silty sand. *J Geotech Geoenvironmental Eng*, 126(5), 451–462. [http://dx.doi.org/10.1061/\(ASCE\)1090-0241\(2000\)126:5\(451\)](http://dx.doi.org/10.1061/(ASCE)1090-0241(2000)126:5(451))
- Salgado, R., Lyamin, A. V., Sloan, S. W., & Yu, H. S. (2004). Two- and three-dimensional bearing capacity of foundations in clay. *Géotechnique*, 54(5), 297–306. <http://dx.doi.org/10.1680/geot.2004.54.5.297>
- Salgado, R., Woo, S. I., & Kim, D. (2011). *Development of load and resistance factor design for ultimate and serviceability limit states of transportation structure foundations* (Joint Transportation Research Program Publication No. FHWA/IN/JTRP-2011/03). West Lafayette, IN: Purdue University. <http://dx.doi.org/10.5703/1288284314618>
- Seo, H., Yildirim, I. Z., & Prezzi, M. (2009). Assessment of the axial load response of an H pile driven in multilayered soil. *J Geotech Geoenvironmental Eng*, 135(12), 1789–1804. [http://dx.doi.org/10.1061/\(ASCE\)GT.1943-5606.0000156](http://dx.doi.org/10.1061/(ASCE)GT.1943-5606.0000156)
- Simonini, P. (1996). Analysis of behavior of sand surrounding pile tips. *J Geotech Eng*, 122(11), 897–905. [http://dx.doi.org/10.1061/\(ASCE\)0733-9410\(1996\)122:11\(897\)](http://dx.doi.org/10.1061/(ASCE)0733-9410(1996)122:11(897))
- SIMULIA. (2012). ABAQUS (Version 6.12-2) [Computer software]. Providence, RI: Dassault Systèmes Simulia Corp.
- Skempton, A. W. (1987). Discussion: Standard penetration test procedures and the effects in sands of overburden pressure, relative density, particle size, ageing and overconsolidation. *Géotechnique*, 37(3), 411–412. <http://dx.doi.org/10.1680/geot.1987.37.3.411>
- Stallebrass, S., & Baudet, B. (2004). A constitutive model for structured clays. *Géotechnique*, 54(4), 269–278. <http://dx.doi.org/10.1680/geot.2004.54.4.269>
- Stamatopoulos, C., & Balla, L. (2010). Modeling clay response along slip surfaces. In O. Martin, X. Zheng, G.-R. Gillich, & R. Cermak (Eds.), *Latest Trends on Engineering Mechanics, Structures, Engineering Technology* (pp. 320–325). Athens, Greece: WSEAS Press.
- Tehrani, F. S., Han, F., Salgado, R., Prezzi, M., Tovar, R. D., & Castro, A. G. (2015). Effect of surface roughness on the shaft resistance of nondisplacement piles embedded in sand. *Géotechnique*, 52(6), 1062–1072. <http://dx.doi.org/10.1016/j.sandf.2012.11.021>
- Thakur, V. (2007). *Strain localization in sensitive soft clays* (Doctoral dissertation). Trondheim, Norway: Norwegian University of Science and Technology.

- Thakur, V. (2011). Numerically observed shear bands in soft sensitive clays. *Geomech Geoengin*, 6(2), 131–146. <http://dx.doi.org/10.1080/17486025.2010.546434>
- Uesugi, M., & Kishida, H. (1987). Tests of the interface between sand and steel in the simple shear apparatus. *Géotechnique*, 37(1), 45–52. <http://dx.doi.org/10.1680/geot.1987.37.1.45>
- Van Dijk, B. F. J., & Kolk, H. J. (2011). CPT-based design method for axial capacity of offshore piles in clays. In S. Gourvenec & D. White (Eds.), *Frontiers in offshore geotechnics II* (pp. 555–560). London, UK: Taylor & Francis. <http://dx.doi.org/10.1201/b10132-73>
- Vesic, A. S. (1967). *A study of bearing capacity of deep foundations*. Atlanta, GA: Georgia Institute of Technology.
- Wang, D., Bienen, B., Nazem, M., Tian, Y., Zheng, J., Pucker, T., & Randolph, M. F. (2015). Large deformation finite element analyses in geotechnical engineering. *Comput Geotech*, 65, 104–114. <http://dx.doi.org/10.1016/j.compgeo.2014.12.005>
- Wang, D., Randolph, M. F., & White, D. J. (2013). A dynamic large deformation finite element method based on mesh regeneration. *Comput Geotech*, 54, 192–201. <http://dx.doi.org/10.1016/j.compgeo.2013.07.005>
- White, D. J., & Bolton, M. D. (2002). Observing friction fatigue on a jacked pile. In S. Springman (Ed.), *Constitutive and centrifuge modelling: Two extremes* (pp. 346–354). Lisse, The Netherlands: A. A. Balkema.
- White, D., & Zhao, Y. (2006). A model-scale investigation into “set-up” of displacement piles in sand. In C. W. W. Ng, Y. H. Wang, & L. M. Zhang (Eds.), *Physical modelling in geotechnics, two volume set: Proceedings of the Sixth International Conference on Physical Modelling in Geotechnics, 6th ICPMG '06, Hong Kong, 4–6 August 2006* (pp. 889–894). London, UK: Taylor & Francis.
- Woo, S. I., & Salgado, R. (2015). Bounding surface modeling of sand with consideration of fabric and its evolution during monotonic shearing. *Int J Solids Struct*, 63(15), 277–288. <http://dx.doi.org/10.1016/j.ijsolstr.2015.03.005>
- Yen, T.-L., Lin, H., Chin, C., & Wang, R. F. (1989). Interpretation of instrumented driven steel pipe piles. In F. H. Kulhawy (Ed.), *Foundation engineering: Current principles and practices, Vol. 2* (Geotechnical Special Publication No. 22) (pp. 1293–1308). New York, NY: American Society of Civil Engineers.
- Yoon, S., Abu-Farsakh, M. Y., Tsai, C., & Zhang, Z. (2008). Calibration of resistance factors for axially loaded concrete piles driven into soft soils. *Transp Res Rec*, 2045, 39–50. <http://dx.doi.org/10.3141/2045-05>
- Zhang, B. L., Tang, W. H., & Ng, C. W. W. (2001). Reliability of axially loaded driven pile groups. *J Geotech Geoenvironmental Eng*, 127(12), 1051–1060. [http://dx.doi.org/10.1061/\(ASCE\)1090-0241\(2001\)127:12\(1051\)](http://dx.doi.org/10.1061/(ASCE)1090-0241(2001)127:12(1051))
- Zhang, Z., & Wang, Y. H. (2015). Examining setup mechanisms of driven piles in sand using laboratory model pile tests. *J Geotech Geoenvironmental Eng*, 141(4), 04014114. [http://dx.doi.org/10.1061/\(ASCE\)GT.1943-5606.0001252](http://dx.doi.org/10.1061/(ASCE)GT.1943-5606.0001252)

About the Joint Transportation Research Program (JTRP)

On March 11, 1937, the Indiana Legislature passed an act which authorized the Indiana State Highway Commission to cooperate with and assist Purdue University in developing the best methods of improving and maintaining the highways of the state and the respective counties thereof. That collaborative effort was called the Joint Highway Research Project (JHRP). In 1997 the collaborative venture was renamed as the Joint Transportation Research Program (JTRP) to reflect the state and national efforts to integrate the management and operation of various transportation modes.

The first studies of JHRP were concerned with Test Road No. 1—evaluation of the weathering characteristics of stabilized materials. After World War II, the JHRP program grew substantially and was regularly producing technical reports. Over 1,500 technical reports are now available, published as part of the JHRP and subsequently JTRP collaborative venture between Purdue University and what is now the Indiana Department of Transportation.

Free online access to all reports is provided through a unique collaboration between JTRP and Purdue Libraries. These are available at: <http://docs.lib.purdue.edu/jtrp>

Further information about JTRP and its current research program is available at: <http://www.purdue.edu/jtrp>

About This Report

An open access version of this publication is available online. This can be most easily located using the Digital Object Identifier (doi) listed below. Pre-2011 publications that include color illustrations are available online in color but are printed only in grayscale.

The recommended citation for this publication is:

Han, F., Lim, J., Salgado, R., Prezzi, M., & Zaheer, M. (2015). *Load and resistance factor design of bridge foundations accounting for pile group–soil interaction* (Joint Transportation Research Program Publication No. FHWA/IN/JTRP-2015/24). West Lafayette, IN: Purdue University. <http://dx.doi.org/10.5703/1288284316009>